

**Adaptive microstructure-informed tractography for
accurate brain connectivity analyses**

by

Matteo Battocchio

Submitted to the Department of Computer Science
in partial fulfillment of the requirements for the degree of

Doctor of Philosophy in Computer Science
S.S.D. ING-INF06
Cycle XXXIV/2018

at the

Università degli Studi di Verona

October 2022

© Università degli Studi di Verona 2022. All rights reserved.

Author
Department of Computer Science
October 24, 2022

Certified by
Prof. Alessandro Daducci
Professor
Thesis Tutor

Certified by
Prof. Maxime Descoateaux
Professor
Thesis Tutor

Accepted by
Prof. Massimo Merro
Chairman of the PhD School Council

This work is licensed under a Creative Commons Attribution-NonCommercial-NoDerivs 3.0 Unported License, Italy. To read a copy of the licence, visit the web page:

<http://creativecommons.org/licenses/by-nc-nd/3.0/>

ⓘ **Attribution** – You must give appropriate credit, provide a link to the license, and indicate if changes were made. You may do so in any reasonable manner, but not in any way that suggests the licensor endorses you or your use.

Ⓒ **NonCommercial** – You may not use the material for commercial purposes.

Ⓓ **NoDerivatives** – If you remix, transform, or build upon the material, you may not distribute the modified material.

Adaptive microstructure-informed tractography for accurate brain connectivity analyses

Matteo Battocchio

PhD Thesis, Verona, October 24, 2022.

ISBN: code

©All rights reserved. This copy of the thesis has been supplied to ensure timely dissemination of scholarly and technical work on condition that anyone who consults it is understood to recognize that its copyright rests with its author and that no quotation from the thesis and no information derived from it may be published without the author's prior consent.

Abstract

Human brain has been subject of deep interest for centuries, given it's central role in controlling and directing the actions and functions of the body as response to external stimuli. The neural tissue is primarily constituted of neurons and, together with dendrites and the nerve synapses, constitute the gray matter (GM) which plays a major role in cognitive functions. The information processed in the GM travel from one region to the other of the brain along nerve cell projections, called axons. All together they constitute the white matter (WM) whose wiring organization still remains challenging to uncover. The relationship between structure organization of the brain and function has been deeply investigated on humans and animals based on the assumption that the anatomic architecture determine the network dynamics.

In response to that, many different imaging techniques raised, among which diffusion-weighted magnetic resonance imaging (DW-MRI) has triggered tremendous hopes and expectations. Diffusion-weighted imaging measures both restricted and unrestricted diffusion, i.e. the degree of movement freedom of the water molecules, allowing to map the tissue fiber architecture in vivo and non-invasively. Based on DW-MRI data, tractography is able to exploit information of the local fiber orientation to recover global fiber pathways, called streamlines, that represent groups of axons. This, in turn, allows to infer the WM structural connectivity, becoming widely used in many different clinical applications as for diagnoses, virtual dissections and surgical planning. However, despite this unique and compelling ability, data acquisition still suffers from technical limitations and recent studies have highlighted the poor anatomical accuracy of the reconstructions obtained with this technique and challenged its effectiveness for studying brain connectivity.

The focus of this Ph.D. project is to specifically address these limitations and to improve the anatomical accuracy of the structural connectivity estimates. To this aim, we developed a global optimization algorithm that exploits micro and macro-structure information, introducing an iterative procedure that uses the underlying tissue properties to drive the reconstruction using a semi-global approach. Then, we investigated the possibility to dynamically adapt the position of a set of candidate streamlines while embedding the anatomical prior of trajectories smoothness and adapting the configuration based on the observed data. Finally, we introduced the concept of bundle-o-graphy by implementing a method to model groups of streamlines based on the concept that axons are organized into fascicles, adapting their shape and extent based on the underlying microstructure.

Keywords: Tractography, White matter structure, Bundle-based tractography, Microstructure informed tractography, MCMC optimization, Diffusion-Weighted Magnetic Resonance Imaging

Sommario

Il cervello umano è oggetto di profondo interesse da secoli, dato il suo ruolo centrale nel controllare e dirigere le azioni e le funzioni del corpo in risposta a stimoli esterno. Il tessuto neurale è costituito principalmente da neuroni che, insieme ai dendriti e alle sinapsi nervose, costituiscono la materia grigia (GM), la quale riveste un ruolo centrale nelle funzioni cognitive. Le informazioni processate nella GM viaggiano da una regione all'altra del cervello lungo estensioni delle cellule nervose, chiamate assoni. Tutti insieme costituiscono la materia bianca (WM) la cui organizzazione strutturale rimane tuttora sconosciuta. Il legame tra struttura e funzione del cervello sono stati studiati a fondo su esseri umani e animali partendo dal presupposto che l'architettura anatomica determini la dinamica della rete funzionale. In risposta a ciò, sono emerse diverse tecniche di imaging, tra cui la risonanza magnetica pesata per diffusione (DW-MRI) ha suscitato enormi speranze e aspettative. Questa tecnica misura la diffusione sia libera che ristretta, ovvero il grado di libertà di movimento delle molecole d'acqua, consentendo di mappare l'architettura delle fibre neuronali in vivo e in maniera non invasiva. Basata su dati DW-MRI, la traggografia è in grado di sfruttare le informazioni sull'orientamento locale delle fibre per ricostruirne i percorsi a livello globale. Questo, a sua volta, consente di estrarre la connettività strutturale della WM, utilizzata in diverse applicazioni cliniche come per diagnosi, dissezioni virtuali e pianificazione chirurgica. Tuttavia, nonostante questa capacità unica e promettente, l'acquisizione dei dati soffre ancora di limitazioni tecniche e recenti studi hanno messo in evidenza la scarsa accuratezza anatomica delle ricostruzioni ottenute con questa tecnica, mettendone in dubbio l'efficacia per lo studio della connettività cerebrale.

Il focus di questo progetto di dottorato è quello di affrontare in modo specifico queste limitazioni e di migliorare l'accuratezza anatomica delle stime di connettività strutturale. A tal fine, abbiamo sviluppato un algoritmo di ottimizzazione globale che sfrutta le informazioni sia micro che macrostrutturali, introducendo una procedura iterativa che utilizza le proprietà del tessuto neuronale per guidare la ricostruzione utilizzando un approccio semi-globale. Successivamente, abbiamo studiato la possibilità di adattare dinamicamente la posizione di un insieme di streamline candidate incorporando il prior anatomico per cui devono seguire traiettorie regolari e adattando la configurazione in base ai dati osservati. Infine, abbiamo introdotto il concetto di bundle-o-graphy implementando un metodo per modellare gruppi di streamline basato sul concetto che gli assoni sono organizzati in fasci, adattando la loro forma ed estensione in base alla microstruttura sottostante.

Parole chiave: Trattografia, Struttura della materia bianca, Trattografia basata su bundle, Trattografia informata dalla microstruttura, Ottimizzazione MCMC, Imaging di risonanza magnetica pesata per diffusione

Acknowledgements

I would first like to thank my research directors, Alessandro for pushing me outside my comfort zone, and Maxime for giving me the chance to experience an amazing collaboration. Together, they have been a source of inspiration, guiding and supporting me throughout all the stages of my doctorate.

I am grateful to have been a part of the DICE and SCIL groups, the exceptional atmosphere I found, made of fruitful conversations and laughs contributed to making these years unique.

Finally, I would like to thank my family for their constant love and support through this adventure whose memory I'll always remember with a smile.

- Matteo

Contents

Abstract	i
Sommario	iii
Acknowledgements	v
Contents	vi
Acronyms	ix
List of Figures	1
Introduction	6
1 Context and Background	14
1.1 The Human Brain	14
1.2 Diffusion-weighted MRI	20
1.2.1 Signal acquisition	22
1.2.2 Signal reconstruction	24
1.3 Tractography	33
1.3.1 Local methods	33
1.3.2 Semi-global methods	40
1.3.3 Global methods	42
1.4 Tractography limitations	52

I	Methodological contributions	59
2	Microstructure-informed geodesic tracking	60
2.1	Methods	61
2.1.1	STEP1: graph-based streamline tractography	61
2.1.2	STEP2: evaluation of the tractogram plausibility	62
2.1.3	STEP3: graph's weights update to improve the evaluation	63
2.1.4	Testing dataset	64
2.2	Results and discussion	66
3	From static to dynamic tracking	69
3.1	Methods	70
3.1.1	Initial set of streamlines	71
3.1.2	Parametric representation of the streamlines	71
3.1.3	Optimization	73
3.2	Results and discussion	76
4	Adaptive bundle-based global tractography	82
4.1	Methods	82
4.1.1	Streamline reduction and simplification	83
4.1.2	Bundle representation	85
4.1.3	Optimization	87
4.1.4	Data and Experiments	91
4.1.5	Evaluation metrics	92
4.2	Results	93
4.3	Discussion	95
4.4	Conclusions	101
5	Hierarchical Bayesian Microstructure Modelling	106
5.1	Methods	107
5.1.1	General Bayesian Microstructure model	107
5.1.2	Models	113
5.1.3	Data	115

5.2 Results and discussion	116
II Clinical applications	120
6 Sensory-motor structural connectivity analysis	121
6.1 Methods	124
6.2 Results and discussion	128
7 Corpus callosum damage in multiple sclerosis	142
7.1 Methods	143
7.2 Results and discussion	145
8 Tract specific connectometry study in Fabry disease	152
8.1 Methods	153
8.2 Results and discussion	156
Conclusion	164
Bibliography	166
A Collaborations and Doctoral activities	191
A.1 Collaborations	191
A.2 Journal publications	192
A.3 Conference abstracts	193
A.4 Attended Conferences and Workshops	194

Acronyms

AD Alzheimer's disease
CNS central nervous system
PD Parkinson's disease
MS Multiple sclerosis
pwMS people with multiple sclerosis
PMS progressive multiple sclerosis
PPMS primary progressive multiple sclerosis
SPMS secondary progressive multiple sclerosis
RRMS relapsing–remitting multiple sclerosis
EDSS Expanded Disability Status Scale
SPSS Statistical Package for the Social Sciences
T25FWT Timed 25-Ft Walk Test
9-HPT Nine-Hole Peg Test
SDMT Brief Visuospatial Memory Test Revised
CVLT California Verbal Learning Test II
BVMT Brief Visuospatial Memory Test Revised
FD Fabry Disease
HC healthy controls
2D two-dimensional
3D three-dimensional
ADC Apparent diffusion coefficient
AD axial diffusivity
MD mean diffusivity
RD radial diffusivity
MNI Montreal Neurological Institute

SMN sensory-motor network
SVD small vessel disease
GMF gray matter fraction
CC Corpus callosum
PrCG Precentral gyrus
SD Spherical deconvolution
CSD Constrained spherical deconvolution
DI Diffusion imaging
DT diffusion tensor
DTI Diffusion Tensor Imaging
ACT anatomical constrained tractography
FA Fractional Anisotropy
ICV intra-cranial volume
LV lesion volume
IVIM intravoxel incoherent motion
fODF fiber Orientation Distribution Function
GM gray matter
HARDI High Angular Resolution Diffusion Imaging
NODDI neurite orientation dispersion and density imaging
SMT spherical mean technique
SIFT Spherical-deconvolution Informed Filtering of Tractograms
COMMIT Convex Optimization Modeling for Microstructure-informed Tractography
LiFE Linear Fascicle Evaluation
MR Magnetic Resonance
MRI Magnetic Resonance Imaging
NMR Nuclear Magnetic Resonance
RF radio-frequency
TE echo time
PGSE pulsed-gradient spin echo
MPRAGE magnetization-prepared rapid gradient echo
FLAIR Fluid Attenuated Inversion Recovery
EPI cho planar imaging

dMRI diffusion Magnetic Resonance Imaging
DSI diffusion spectrum imaging
QBI *Q*-ball imaging
CHARMED composite hindered and restricted models of diffusion
MMWMD the minimal model of white matter diffusion
DW diffusion-weighted
DWI diffusion-weighted imaging
DW-MRI diffusion-weighted magnetic resonance imaging
Dmipy Diffusion Microstructure Imaging in Python
HCP Human Connectome Project
MD Mean diffusivity
ODF Orientation Distribution Function
dODF diffusion orientation density function
fODF fibre orientation density function
FOD Fibre Orientation Distribution
PVE partial volume effect
PDE partial differential equation
PDF probability density function
MRF Markov Random Fields
MCMC Markov chain Monte Carlo
LS least-squares
NNLS non-negative least-squares
GLM Generalized Linear Model
RMSE root mean square error
ROI Regions Of Interest
CST Corticospinal tract
CSF cerebrospinal fluid
SCIL Sherbrooke Connectivity Imaging Laboratory
ISBI International Symposium on Biomedical Imaging
MICCAI Medical Image Computing and Computer Assisted Intervention Society
ISMRM International Society for Magnetic Resonance in Medicine
SNR Signal to noise ratio
SH Spherical harmonics

WM white matter

WMH white matter hyperintensities

NAWM normal appearing white matter

List of Figures

1.1	Brain main sulci and boundaries	15
1.2	Brain structural and multi-tissue coronal view	17
1.3	Neuron structure	18
1.4	Depiction of the human brain dissection	19
1.5	Diffusion of a ink drop	21
1.6	Spin echo sequence	23
1.7	Graphical representation of diffusion tensor	25
1.8	Diffusion tensor vs spherical deconvolution model	28
1.9	Graph network connectivity	34
1.10	Local tracking	34
1.11	Curvature overshoot bias	36
1.12	Gyral bias	37
1.13	Comparison between different local probability density functions	39
1.14	Deterministic vs probabilistic tracking	40
1.15	Geodesic shortest path bottleneck bias	42
1.16	Gibbs global tracking streamline reconstruction	45
1.17	SIFT filtering	47
1.18	COMMIT model	50
1.19	COMMIT framework scheme	51
1.20	Visual inspection of the bottleneck effect	54
1.21	Kissing fibers configuration	55
1.22	Narrow intersection effect	56
1.23	Gyral bias	57

1.24	False positives effect on structural connectivity network metrics	57
2.1	Improved graph-based tracking workflow	62
2.2	Synthetic dataset	66
2.3	Effects of microstructure-informed geodesic tracking	68
3.1	Dynamic adaptation workflow	70
3.2	Comparison of different interpolation approaches	73
3.3	Trajectory sampling scheme	80
3.4	Dynamic adaptation proof of concept	81
3.5	Result of dynamic adaptation of synthetic dataset	81
4.1	Bundle-o-graphy workflow. Given an input tractogram the first step aims to reduce the number of streamlines needed to represent pathways between pairs of regions. Additionally, each streamline is parameterized using a subset of the initial points to approximate their trajectory. The second step is characterized by the shift from streamline to bundle-based representation. Here a volume is assigned to each streamline, allowing to mimic the contribution of a set of aligned fibers centered around the original trajectory. Finally the bundle-based configuration is optimized by adapting their shape and geometry following a MCMC optimization approach.	83
4.2	Streamline reduction workflow: the first step implies separating the input tractogram into subsets based on a cortical and subcortical regions segmentation. FAydogan:2021ig. 4.2A is an example showing a set of projection fibers segmented based on Freesurfer atlas. Each connection is then clustered (Fig. 4.2B) keeping only the representative streamlines for each cluster. These are simplified using Ramer-Douglas-Peucker algorithm (Fig. 4.2C) which reduces the number of points needed to approximate the streamline trajectories. Finally these coordinates are interpolated using cubic b-splines (Fig. 4.2D).	84

4.3	Bundle simulation: the contribution of each original streamline can be modeled as a cylinder centered along the trajectory. The volume can be radially adapted using a blurring function to allow uncertainty as we move outward from the central pathway. The two parameters, σ_C and σ_G regulate the extent of the core and the Gaussian dumping respectively.	86
4.4	On the left is shown the acceptance rates of the four proposals throughout the iterative adaptation, starting with an empty set of connections A. On the right is reported the plot of the corresponding cost function trend driving the optimization process	89
4.5	Impact of the optimization on different reconstruction algorithms on the synthetic phantom. On the first and second row are the intracellular signal fraction maps corresponding to the vertical hard-to-track connection of the input and optimized configurations respectively, viewed from two different perspectives.	93
4.6	Impact of the optimization on the removal of false positives connections. The connectivity graphs show in red the connections between pair of regions if they represent false positives connections or in green if they correspond to true positive ones. In the first row are the connectivity graphs of the input tractograms, while on the second row are the connectivity evaluated after bundle-o-graphy optimization.	94
4.7	Comparison between the voxel-wise RMSE maps corresponding to the input tractograms computed with the three different reconstruction algorithms (first row) and the adapted configurations (second row).	97
4.8	Comparison between the estimated IC maps of the input tractograms (first row) and the adapted configurations (second row).	98

4.9	Comparison between the IC maps, estimated with COMMIT, corresponding to the CC, PyT and AF reconstructed with the three different tractography algorithms. For each method, the first row shows the the connection segmented from the input tractogram while the second reports the connection segmented from the adapted one. The last column shows the corresponding visual inspection of the volume and geometry of the tracts. The visualization is performed in the same way and the thickness is related to the blur extent regulated by σ_C	102
4.10	Comparison between the cortical projections of the CC tracts segmented from the input tractograms computed with the three different reconstruction algorithms (first row) and the respectively adapted connections (second row).	103
4.11	Effects of the priors on the optimization process. On the left the adaptation is driven by the fitting error between the reconstructed and the observed signals, while, on the right, we inject priors to minimize the total number of connections and bundles. First row shows the plots of the corresponding cost functions, in the second row are reported the number of true positive (green) and false positive (red) connections, and last row shows the mean RMSE (red) along with the number of bundles in the configurations(green).	104
4.12	Impact of the spline interpolation, using different number of control points, on the signal fitting error. The average value of 6 control points used in this work is reported as a blue vertical line.	105
5.1	Bayesian hierachical model scheme	108
5.2	Bayesian ball-stick model fit on synthetic dataset	116
5.3	Ball-stick model parameter maps estimated on synthetic dataset	117
5.4	Ball-stick parameter maps estimated on real data	118
6.1	Motor network hubs	134
6.2	Sensory-motor network connectomes	135
6.3	Raw connectomes global graph metrics	136

6.4	Raw connectomes nodes strength of healthy controls (HC)s and progressive multiple sclerosis (PMS)	136
6.5	Raw connectomes nodes efficiency of HCs and PMS	137
6.6	Global graph metrics on Convex Optimization Modeling for Microstructure-informed Tractography (COMMIT)-weighted connectomes	137
6.7	Nodes strenght on COMMIT-weighted connectomes	138
6.8	Nodes efficiency on COMMIT-weighted connectomes	138
6.9	Global network metrics boxplots	139
6.10	Local efficiency barplot	140
6.11	Connectivity strength barplot	141
7.1	Corpus callosum parcellation	144
7.2	Fibre density box plots for patients and controls	147
8.1	Cortico-spinal, the cortico-striatal and thalamo-cortical tracts	156
8.2	Complete list of the demographic and clinical information of the included population	157
8.3	White matter differences in Fabry disease	157
8.4	White matter tractometry metrics	158
8.5	Tract-specific mean values and standard deviations of the diffusion metrics	159
8.6	Tract-specific tractometry analysis	160

Introduction

The brain has been subject of major interest across ages and its study has traversed philosophical, experimental, and theoretical phases. Although its central role has been theorized since ancient Greece ([Gross, 1987](#)), it is only within the last century that the study of brain anatomy and function has been placed on a scientific basis and still they remain largely unknown ([Hofman, 2014](#)).

Its responsibilities comprise controlling and directing the actions and functions of the body as response to external stimuli which also represent a driving force behind its evolution ([Magphail et Bolhuis, 2001](#); [Roth et Dicke, 2012](#)). The brain neural tissue is primarily constituted of neurons and neural stem cells along with glial cells and blood vessels providing physical and metabolic support. The ensemble of neural cell bodies is called soma and, together with dendrites and the nerve synapses, constitute the gray matter ([GM](#)). This can be found in the inner part, called nucleus or subcortical regions, and in the cerebral cortex which composes the outer layer of the brain. This last region is highly folded to increase its surface, and plays a major role in cognitive functions. Together they are responsible of receiving and processing the visual, somatosensory, auditory, gustatory, and olfactory information, enabling the control of the movement, memory, and emotions.

The information processed in the [GM](#) travel from one region to the other of the brain as electric impulses along nerve cell projections, called axons ([Figure 1.3](#)), which are organized into *fascicles*. All together they constitute the white matter ([WM](#)) and represent the subways of information transfer in the brain ([Figure 1.2](#)). The importance of uncovering the network structure underlying the information exchange is crucial from clinical, developmental and evolutionary perspectives.

The relationship between structure organization of the brain and function has

been deeply investigated on humans and animals based on the assumption that the anatomic architecture determine the network dynamics (Hagmann et al., 2008; Honey et al., 2007, 2009; Turk et al., 2016). In recent years this has been extended by studying how neurodegenerative conditions such as Alzheimer’s and Parkinson’s diseases (Manza et al., 2016; Son et al., 2017) and multiple sclerosis (Dobryakova et al., 2017; Petracca et al., 2020; Schiavi et al., 2020b) affect mobility, coordination, strength, sensation, and cognition (Catani, 2006; Ciccarelli et al., 2008).

The first approach to investigate the neural architecture was by cerebral dissection, and, while the methodologies have experienced a notable evolution (Cushing, 1909; Dejerine, 1895; Gray, 1918; Ludwig et Klingler, 1956), the idea of depicting the complex organization of WM pathways remains unfeasible. The introduction of local fiber tracing methods, based on local injection and subsequent observation of the propagation of specific chemicals used as markers (Selden et al., 1998; Ugolini, 2010), yielded to the first high-quality connectivity mapping of cerebral cortex in mammals (Maunsell et van Essen, 1983; Rockland et Pandya, 1979; Scannell et al., 1995).

Over the years the neuroimaging field has adapted toward the necessity to acquire and process data rapidly and non-invasively for clinical purposes (e.g. diagnoses). This gave rise to many different imaging techniques, among which diffusion-weighted magnetic resonance imaging (DW-MRI) (Behrens et al., 2014; Bihan et al., 1986; Jones, 2010; Le Bihan et Breton, 1985) has triggered tremendous hopes and expectations being one of the few capable of mapping the tissue fiber architecture in vivo. Starting from a set of diffusion-weighted (DW) images, Diffusion imaging (DI) estimates the effective scalar diffusivity of water molecules (Le Bihan, 1991), providing a measurement of biological tissue properties. The possibility to non-invasively extract fiber orientations from living biological tissue was revolutionary and the first approach, Diffusion Tensor Imaging (DTI) (Le Bihan, 1991), quickly became a central tool in the modern neuroimaging field and it’s currently exploited for clinical and neurological applications (Catani et al., 2002; Horsfield et Jones, 2002; Johansen-Berg et Rushworth, 2009).

The possibility to reconstruct the global fiber trajectories based on DW data is called tractography (see section 1.3) and it notably contributed to the success of DTI (Basser et al., 2000; Conturo et al., 1999; Mori et al., 1999) but also highlighted

its many limitations. Indeed, first tractography algorithms were based on “*local*” integration procedures of the fiber orientations estimated in each voxel from the measured DW-MRI. This approach is very fast but also rather sensitive to estimation errors of the local orientations (Mori et al., 1999); notably, Maier-Hein et al. (2017) showed that such algorithms tend to follow the easiest path available in crossing regions, which represent the majority of WM voxels (Jeurissen et al., 2012), and thus fail to reconstruct some anatomical bundles, i.e. false negatives.

To deal with this inadequacy of tractography to explore the whole space of brain connections, probabilistic alternatives were proposed that use probability distributions estimated in each voxel to allow uncertainty in the propagation of the trajectories. These methods have demonstrated their ability to recover hard-to-track connections and to cover more adequately the WM (Côté et al., 2013); however, this improved capability of exploring brain anatomy leads also to the reconstruction of implausible fascicles that do not anatomically exist, i.e. false positives.

The effects of such false-negative and false-positive connections in tractography reconstructions has been recently investigated and, in particular, Zalesky et al. (2016) have demonstrated that these spurious connections are detrimental to the study of brain connectivity and can heavily bias all analyses based on this technique.

The advent of the so called “*global*” tractography algorithms marked an important milestone on the road to significantly improving the quality of the reconstructions. These approaches introduced the use of global optimization to reconstruct the set of streamlines, i.e. tractogram, that are most consistent with the acquired DW-MRI data and, indeed, the resulting reconstructions showed improved anatomical accuracy (Christiaens et al., 2015; Close et al., 2015; Fillard et al., 2009; Kreher et al., 2008; Mangin et al., 2013; Reisert et al., 2011).

First solutions were based on Markov chain Monte Carlo (MCMC) optimization procedures for constructing the optimal set of streamlines, but this strategy turned out to be computationally very heavy given the large amount of parameters that need to be optimized. Different approaches have been proposed to speed up convergence, for instance by reducing the number of parameters or their space by forcing anatomical constraints on the reconstructed streamlines (Girard et Descoteaux, 2012; Smith et al., 2012).

One major step to reduce the complexity of this *generative* strategy, while keeping a “global” approach, was made with the introduction of *discriminative* approaches. The idea behind these methods is to identify the optimal subset of streamlines from a pre-computed set of candidates, constructed using standard tractography algorithms, that are most compatible with the measured DW-MRI data; for this reason, they are sometimes referred to as “filtering” methods (Daducci et al., 2016). Different formulations exist; for instance, in Spherical-deconvolution Informed Filtering of Tractograms (SIFT)/SIFT2 (Smith et al., 2013, 2015a) streamlines are selected based on the agreement between their trajectories and the local fiber orientation distributions, whereas the full measured DW-MRI data is considered in COMMIT/COMMIT2 and Linear Fascicle Evaluation (LiFE) (Daducci et al., 2015; Pestilli et al., 2014; Schiavi et al., 2020a). These discriminative methods allowed reducing dramatically the computational cost required to perform global tractography, and showed great potential to further improve the quality of the reconstructions, notably alleviating the problem of false positives as well as improving the biological interpretability of the tractograms (Jbabdi et Johansen-Berg, 2011; Schiavi et al., 2020a).

However, unlike generative methods, they assume a static input configuration, i.e. shape / position of the candidate streamlines is fixed and cannot be adapted, which means that the quality of the reconstructions remains indissolubly bounded to the quality of the algorithm used to build the candidate pathways.

Research goal

The thesis is divided into two parts: methodology (1.4) and clinical applications (5.2). In the first are presented the steps followed to develop a tracking algorithm able to exploit the strengths of both global and generative methods to overcome tractography limitations. Along the path we explored different strategies, starting from a semi-global graph-based method and evolving to a global reconstruction approach.

Semi-global methods represent an interesting option, as they are computationally efficient, robust to noise and their formulation is very flexible. However, they also come with limitations. For instance, the reconstructed streamlines tend to be collapsed and to share part of their path, especially in regions with highly curved

fiber bundles. This can introduce voxels with incorrectly high or low streamline density, which does not correspond to the underlying fiber geometry. To mitigate this problem, in section 2 is introduced an iterative procedure that uses microstructure information and provides feedback to the shortest path tractography algorithm about the plausibility of the reconstructions.

Although the previous method is able to mitigate the limitations of shortest path methods, this class of methods cannot be used for exploratory studies, given their “Regions Of Interest (ROI)-based” nature. In section 3 a method overcoming these restrictions is introduced, exploiting both the flexibility and the strengths of global reconstruction approaches. Global generative methods usually requires delicate and fine-tuning of many parameters representing one of their main limitations. Taking inspiration from the work of Lemkaddem et al. (2014), we exploited a convenient streamline parameterization (described in 3.1.2), drastically reducing the number of variables required and at the same time (intrinsically) preserving some of the real-world properties of the white matter structure. The shaping is performed using a Metropolis Hastings MCMC approach (Chib et Greenberg, 1995; Neal et al., 2011) to randomly search the parameters space. The proposed modification is then accepted or rejected based on an energy minimization function checking the difference between the signal observed and the one predicted from the new model. The goal of this project is to prove that the dynamic adaptation of the spatial configuration of the streamlines during the filtering allows overcoming the limitations due to a static input and further improves the reconstructions.

Next step was the implementation of a global reconstruction algorithm, keeping the “hybrid” nature of the previous one (Battocchio et al., 2019), but tackling tractography reconstruction from a different perspective: the idea was to move away from streamline-based tracking to directly reconstruct bundles of them, hence introducing the term *bundle-o-graphy*. Other bundle-based studies and has proven to improve accuracy representations of specific neural pathways (Rheault et al., 2019; Schilling et al., 2020) thanks to the use of prior knowledge in the form of anatomical constraints. Tractography, implemented as a bundle-segmentation technique, however, can’t be used for whole WM structure reconstructions as well for exploratory studies. The goal of this project was to introduce a method to directly model WM bundles,

i.e. disentangling tractography reconstructions from streamline representation without losing the global perspective.

As conclusion of the methodology part, a [MCMC](#) Bayesian approach is introduced to improve estimation of parameters relating microstructural features, such as diffusivities and tissue compartment fractions. The vast majority of fitting techniques assume that voxels are independent; in other words, the model is separately fitted to the signal in each voxel, usually with nonlinear least squares estimation. An alternative approach is to use a [MCMC](#) algorithm to estimate parameter posterior distributions in each voxel ([Harms et Roebroek, 2018](#)). [Orton et al. \(2014\)](#) introduced a hierarchical Bayesian model fitting approach for the intravoxel incoherent motion ([IVIM](#)) ([Le Bihan et al., 1988](#)) model. Their model breaks the assumption of independent voxels by introducing a Gaussian prior (estimated from the data) over the microstructural model parameters across a [ROI](#).

In [section 5](#) we generalized the Bayesian approach to be applied to any microstructural model. We tested how the data-driven Bayesian hierarchical modelling is capable of properly estimating microstructural properties across distinct neurological tissue while reducing noise effects characterizing voxel-by-voxel fitting methods.

The second part of the thesis is characterized by tractography applications to study brain structural connectivity in both healthy and disease. This gives the opportunity to face tractography limitations ([presented in section 1.4](#)) affecting clinical studies performed with standard analysis pipeline and how these can be mitigated.

Graph theory and network modelling have been applied to characterize structural motor network topology in Multiple sclerosis ([MS](#)), demonstrating a reduced motor network efficiency through the quantification of structural damage in [WM](#) bundles connecting pairs of cortical and subcortical [GM](#) regions ([Pardini et al., 2015](#)). However, topology differences identified with standard tractography in [MS](#) seem to be mainly driven by density, which, in turn, is strongly influenced by the presence of lesions, suggesting caution when interpreting between group differences in connectome properties.

In [section 6](#) we applied [COMMIT](#) ([Daducci et al., 2013, 2015](#)) to move from a qualitative towards a more “quantitative” appraisal of the brain structural con-

nectome. The application of [COMMIT](#) allows the tracking of fibres within [WM](#) lesions, removing the ones deemed implausible according to the chosen microstructural property only after reconstruction. The aim of this project was to investigate differences in density and network topology in the [COMMIT](#)-weighted connectome between patients and [HC](#).

Moving from network to tract specific analysis, in section [7](#) the effects of [MS](#) disruption affecting the Corpus callosum ([CC](#)) tract are investigated. As multitude of studies have clarified over the last decade, damage to specific white matter [WM](#) tracts contributes to different aspects of clinical disability in [MS](#) ([Barone et al., 2018](#); [Bester et al., 2013](#); [Bodini et al., 2013](#); [Margoni et al., 2019](#); [Palotai et al., 2020](#); [Wahl et al., 2011](#)). Amongst [WM](#) tracts, the [CC](#) is one of the preferential sites of clinically eloquent damage ([Barone et al., 2018](#); [Bodini et al., 2013](#); [Granberg et al., 2015](#)), since it is the target of both direct damage from focal lesions/diffuse neurodegenerative processes and indirect damage deriving from Wallerian degeneration of axons transected by hemispheric lesions ([Garg et al., 2015](#)). In all previous studies interhemispheric disconnection has been inferred as a consequence of callosal atrophy (indirect quantification of fibre loss expressed as area, volume or thickness) or callosal microstructural damage (expressed as mean or voxel-wise diffusion metrics). Whilst both these factors probably influence the structural connectivity between the two hemispheres, neither of them provides a direct quantification of such connection.

In this section we investigated how streamline density represents a measure of the interhemispheric connection that accounts not only for the effects of microstructural and macrostructural damage on fibre reconstruction, but also for the anatomical variability in [CC](#) volume, which is particularly relevant when evaluating [MS](#) patients in advanced disease stages.

Finally, in section [8](#) the effects of a rare disease called Fabry are investigated. The pathology is characterized by the inability to metabolize specific glycolipids which, in turn, accumulate in different tissues, including heart, kidney and central nervous system ([CNS](#)), leading to the development of clinical symptoms ([Germain, 2010](#)). Although widespread microstructural alterations of the white matter ([WM](#)) are known to occur in Fabry Disease ([FD](#)) patients, as demonstrated by different [DTI](#) studies ([Albrecht et al., 2007](#); [Cocozza et al., 2018b](#)), to date no information about the

integrity of the cortico-basal ganglia motor loop fibers are available.

The goal of this study is to evaluate the microstructural integrity of the main afferences and efferences of the motor cortices to the basal ganglia motor loop in [FD](#) patients and to investigate the possible presence of structural connectivity changes in these connections.

Chapter 1

Context and Background

1.1 The Human Brain

Considered the central unit of the nervous system, the brain is the most complex and unknown organ of the human body (Hofman, 2014). Its responsibilities comprise controlling and directing the actions and functions of the body as response to external stimuli which also represent a driving force behind its evolution (Magphail et Bolhuis, 2001; Roth et Dicke, 2012). This central unit, along with the spinal cord extending within the neural arches of the vertebral column, form the central nervous system CNS.

The brain can be broadly divided into three main structures: brainstem, cerebellum and cerebrum. The first connect the lower part of the brain with the spinal cord and regulates different autonomous body functions as heart rate, breathing and swallowing. The second is a structure placed at the bottom of the cerebrum, behind the brainstem and making up 10% of the brain volume. While, historically, it has been considered the region responsible of motion-related functions its tasks involves the regulation and coordination of the signals generated in the cerebrum. The latter represents the largest component of the brain, consists of two hemispheres, each divided into five lobes: frontal, parietal, temporal, occipital, and insular (Kubik et al., 1990), showed in Figure 1.1.

The brain neural tissue is primarily constituted of neurons and neural stem cells along with glial cells and blood vessels providing physical and metabolic support. The

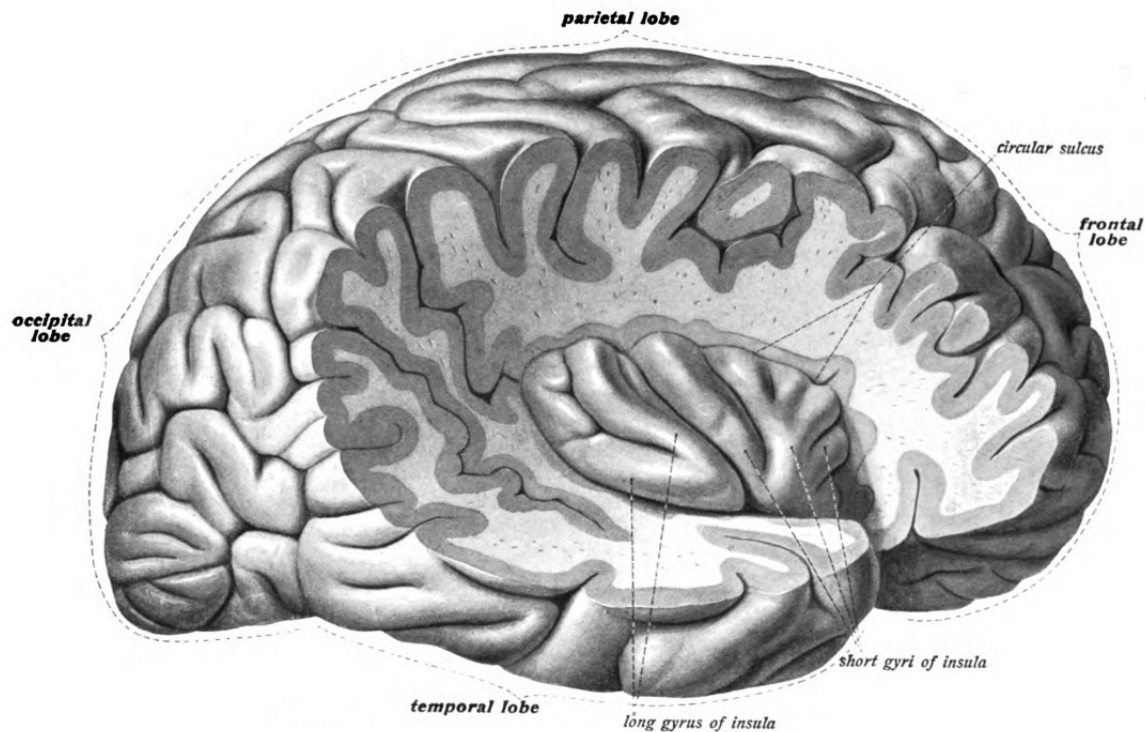


Figure 1.1 – The cortex of the brain is folded into gyri and sulci that are used as references for the analysis of the structure of the brain. Each hemisphere can be divided into five lobes: frontal, parietal, temporal, occipital and insular (Sobotta et Johannes, 1908).

neural cell bodies, or soma, together with dendrites and the nerve synapses constitute the GM that can be found in the outer layer of the brain, the cerebral cortex, and in the inner part, called nucleus or subcortical regions. The importance of uncovering the network structure underlying the information exchange has been of interest from both developmental and evolutionary perspectives. In the last century particular emphasis has been devoted to the investigation of the cerebral cortex, being among the most distinctive morphological features of mammalian brains (Northcutt et Kaas, 1995). This is folded into sulci and gyri increasing the surface area and the causes behind the gyrification process are still debated. Recently Van Essen et al. (2018) summarised the four key mechanisms presented in literature:

1. mechanical tension

2. differential regional proliferation
3. mechanical buckling
4. differential expansion and/or elasticity

The first mechanism suggests that axons physically apply a certain tension causing strongly connected regions to be closer. The second relies on the fact that different regions have different neurons' density: higher concentration produces bulges that then become gyri, whereas reduced proliferation leads to a sulcus or no folding. The third theory has received considerable attention and it's based on the expansion of an initial unfolded sheet over an underlying domain expanding at a slower rate (Tallinen et al., 2016). Lastly, the fourth mechanism promotes the idea that the folding happens by preferential expansion of superficial versus deep layers in regions that become gyri in the first case and sulci in the second.

GM can be divided into regions based on their cytoarchitecture or how the cells are functionally organized. The most widely used is the Brodmann areas classification which includes 51 areas (Garey, 1999) broadly divided into three macro-areas based on their functions: primary sensory areas, primary motor cortex and association areas. Together they are responsible of receiving and processing the visual, somatosensory, auditory, gustatory, and olfactory information, enabling the control of the movement, memory, and emotions (Mercadante et Tadi, 2020).

The information processed in the GM travels from one brain region to the other as electric impulses, i.e. action potentials, along nerve cell projections, called axons. Thanks to the electrically insulating myelin sheaths (formed by glial cells) encasing each neuron, these signals are transmitted more rapidly to other neurons (Figure 1.3). Axons are organized into *bundles* and a set of bundles connecting two regions is called *tract*. All together they constitute the WM and represent the subways of information transfer in the brain (see Figure 1.2).

The relationship between structure organization of the brain and function has been deeply investigated on humans and animals based on the assumption that the anatomical architecture determines the network dynamics (Hagmann et al., 2008; Honey et al., 2007, 2009; Turk et al., 2016). In recent years this has been extended by studying how neurodegenerative conditions such as Alzheimer's and Parkinson's diseases (Manza et al., 2016; Son et al., 2017) and multiple sclerosis (Dobryakova

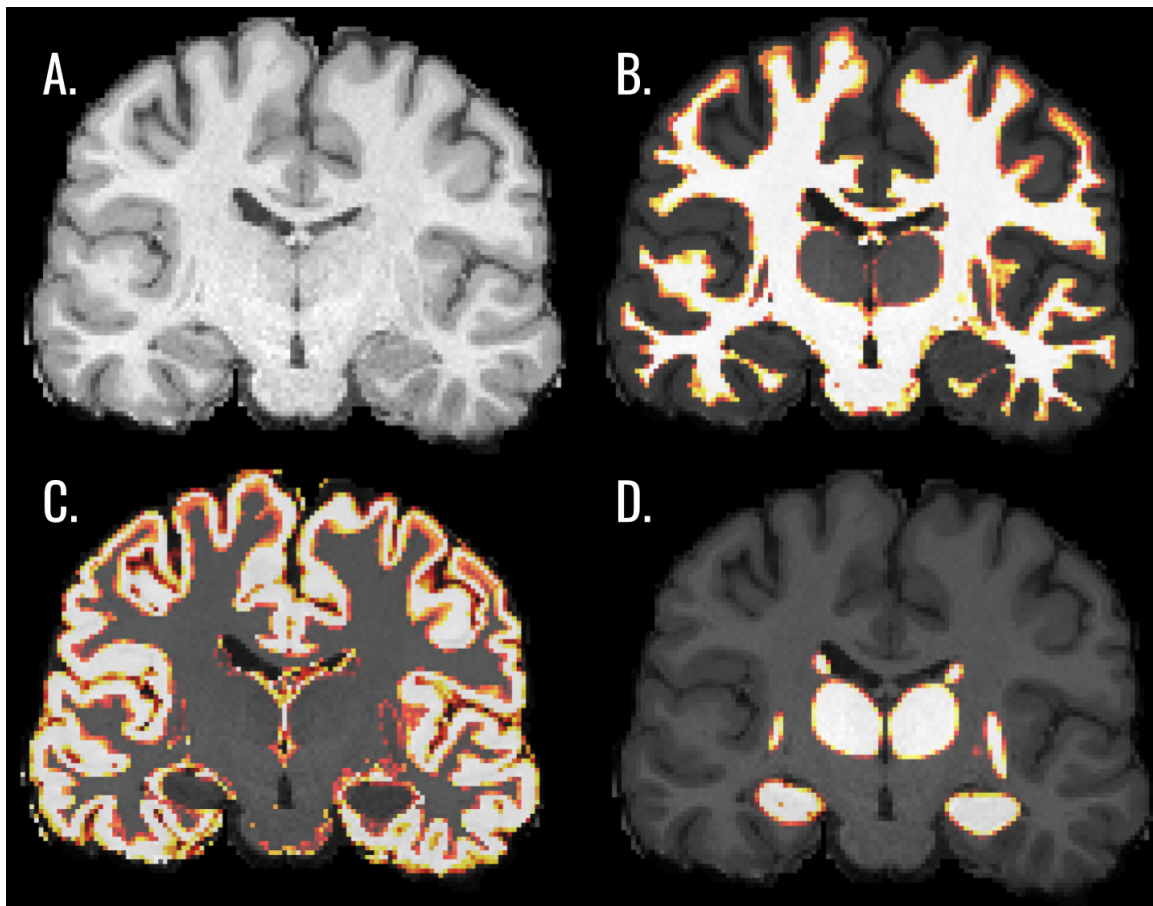


Figure 1.2 – Coronal view of a brain showing a T1 structural image (A), white matter (B), cortical grey matter (C) and subcortical grey matter (D).

[et al., 2017](#); [Petracca et al., 2020](#); [Schiavi et al., 2020b](#)) affect mobility, coordination, strength, sensation, and cognition.

Historically, the only way to access the white matter architecture was by dissection, developed by Arcangelo Piccolhomini in the mid of 16th century, who introduced the terms “cerebrum” for the cerebral cortex and “medulla” for the white matter (Figure 1.4). A century later, Nicolaus Steno introduced the idea of following “the nerve threads through the substance of the brain to find out where they go and where they end” as a way to study the WM structure ([Clarke et O’Malley, 1996](#)).

Since then dissection methodologies have evolved ([Cushing, 1909](#); [Dejerine, 1895](#); [Gray, 1918](#); [Ludwig et Klingler, 1956](#)) but the idea of depicting the complex organi-

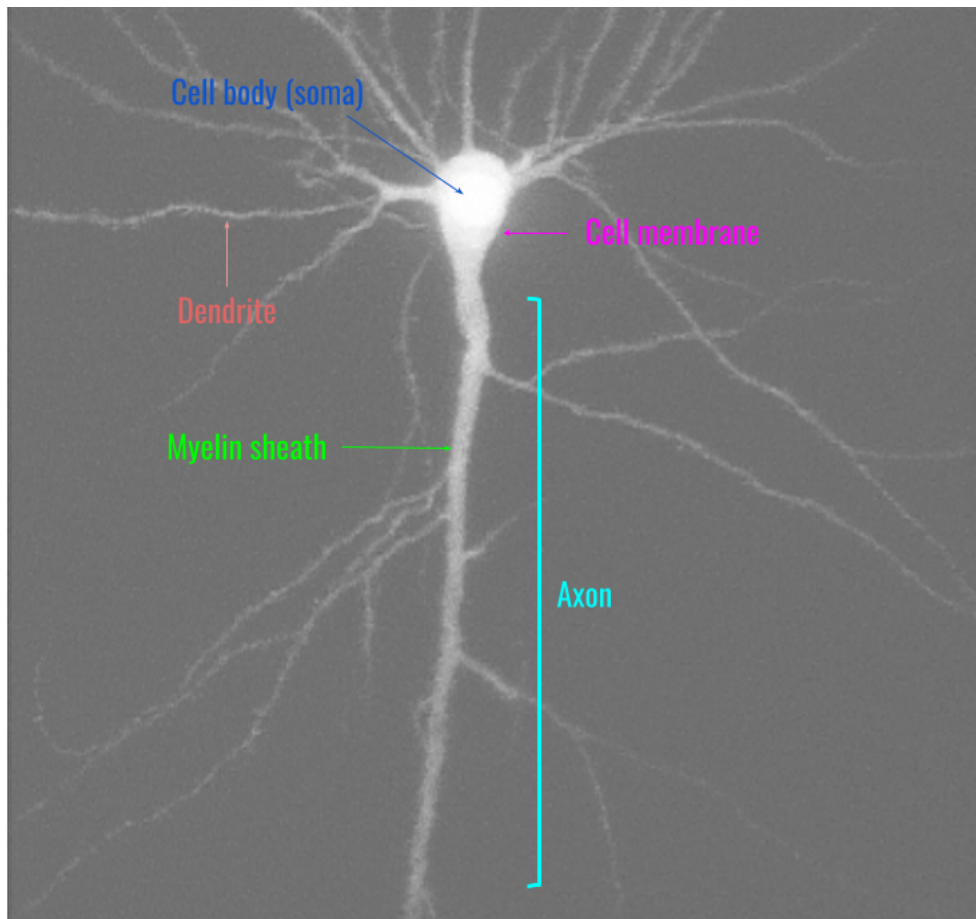


Figure 1.3 – The projections of the three-dimensional (3D) neuron image from confocal stacks of tracing images. Modified from (Al-Kofahi et al., 2002).

zation of WM pathways remains unfeasible. As emphasized by Poliakov et al. (2005), the nature of the body is 3D, so we need 3D imaging techniques to grasp its complexity which cannot be done via dissection since it can only follow planar trajectories.

In this context the ability to map WM pathways has witnessed a notable improvement thanks to the introduction of local fiber tracing methods. These techniques are based on the local injection and the subsequent observation of their propagation (of specific chemicals used as markers) (Selden et al., 1998; Ugolini, 2010). However, the huge amount of labor required, along with the limited population of neurons that can be concurrently studied, strongly restricts the employment of such technique.

Over the years, the neuroimaging field has adapted toward the necessity to acquire

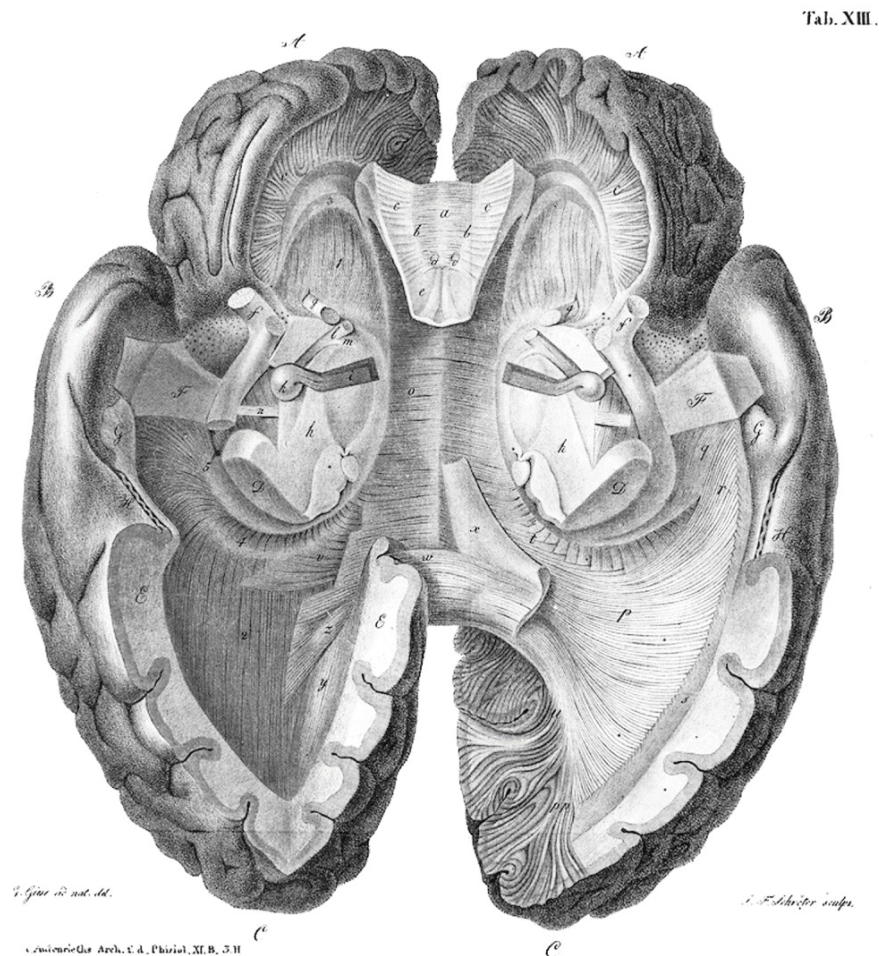


Figure 1.4 – Johann Christian Reil’s depiction of the human brain dissection viewed from below (Schmahmann et Pandya, 2007).

and process data rapidly and non-invasively, for clinical purposes (e.g. diagnoses). This gave rise to many different imaging techniques, among which diffusion-weighted magnetic resonance imaging (DW-MRI) (Behrens et al., 2014; Bihan et al., 1986; Jones, 2010; Le Bihan et Breton, 1985) has triggered tremendous hopes and expectations, being one of the few tools capable of mapping the tissue fiber architecture in vivo. While other methods, such as axonal tracing techniques, are capable to retrieve axonal trajectories with high accuracy, these are more invasive and the application is usually limited to restricted regions.

1.2 Diffusion-weighted MRI

The first characterization of molecular diffusion, a fundamental physical process describing molecules motion in liquid and gas, was made by Brown in 1827 observing pollen grains suspended in water while investigating a fertilization process. In these states particles collide causing random alterations of their motion direction and the temperature is a direct measure of the collisions rate. On average, as the molecules move and bump into each other, they tend to move from areas with higher concentration to areas with lower concentration following a gradient as described by Fick's first law (Fick, 1855):

$$J = -D \frac{dC}{dx}, \quad (1.1)$$

where J is the net flux of molecules in a unit of time, C is the local concentration of molecules, measured in mol/m^3 , and D is the diffusion coefficient, in m^2s^{-1} , which varies based on the medium chemical and physical properties. Fick's second law models how the concentration changes with respect to time:

$$\frac{dC}{dt} = D \frac{d^2C}{dx^2}. \quad (1.2)$$

In particular, for the case of diffusion in two or more dimensions, the ∇ is introduced to generalize the first derivative. Eq. 1.2 becomes:

$$\frac{dC}{dt} = D \nabla^2 C, \quad (1.3)$$

which is known as diffusion equation and can be used to model heat propagation on conductive surfaces as previously introduced by Fourier et al. (1822). Einstein (1905) related the Brownian motion with Fick's formulation showing how particles suspended in a medium experience a displacement in any direction following a probability distribution $p(x, t)$ with variance:

$$\sigma^2 = 2Dt. \quad (1.4)$$

In the case of free diffusivity, i.e., the molecules are free to move with no constraints, the probability to observe a particle at distance r at time t is described by

the Gaussian distribution function:

$$p(r, t) = \frac{1}{\sqrt{4\pi tD}} e^{-\frac{r^2}{4tD}}. \quad (1.5)$$

A well known example of free diffusion is represented by the ink drop spreading in water as time passes, shown in Figure 1.5. At the beginning of the experiment, the particles move away from the center after a certain time, with the same probability along each direction of the 3D space. When the particles are free to move in all the directions, as for the experiment in Figure 1.5, the diffusion is defined as isotropic, anisotropic if the motion is somehow restricted in one or more direction, e.g. in human brain tissues, where the cell membranes hinder or restrict the motion of molecules (Basser et al., 1994; Le Bihan et al., 1993). A direct measure of this anisotropy is the Apparent diffusion coefficient (ADC), which measures the difference between the observed diffusion coefficient of the constrained molecules and the one that would be measured in the same media without obstacles.

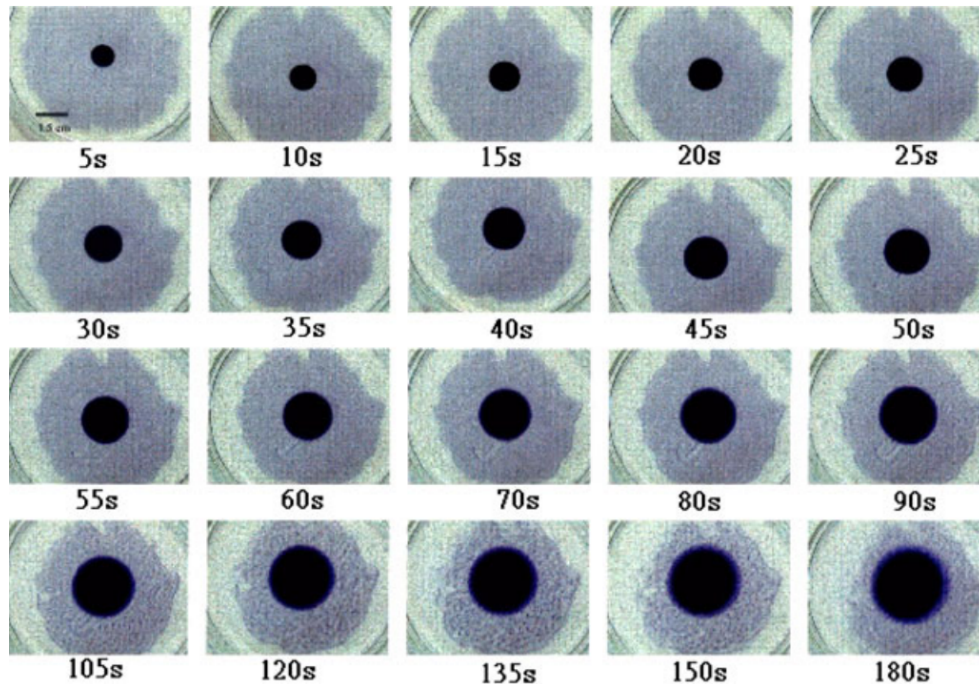


Figure 1.5 – Diffusion of a ink drop in water at different time points (Lee et al., 2004)

The observation that different tissues' microstructure is characterized by different diffusivity properties led to the rise of DWI (Le Bihan et Breton, 1985).

1.2.1 Signal acquisition

The idea of measuring ADC to characterize tissue structures became possible thanks to the introduction of Nuclear Magnetic Resonance (NMR) and the concept of *spin dephasing*. Atom nuclei with odd atomic number are characterized by non-zero spin and charge. If an external magnetic field is applied, an energy transfer is possible between the base energy to a higher energy level. The energy transfer takes place at a wavelength that corresponds to radio frequencies and when the spin returns to its base level, energy is emitted at the same frequency, a process defined as *resonance* (Roberts, 1959). The resonance frequency depends on the magnetic field strength. In particular, what are measured are the *relaxation times* and, more precisely, the source of contrast is the difference in relaxation constants that depends on the tissue chemical and physical properties (Berger, 2002). The spin-lattice relaxation time $T1$, describes the time it takes for the longitudinal magnetization $\mathbf{M}_{z,t}$ to return to the original value, while the spin-spin relaxation time $T2$ measures how the transverse magnetization $\mathbf{M}_{x,y,t}$ goes to zero. As previously mentioned, different acquisition protocols are able to highlight different tissue properties by changing the image contrast, allowing to evaluate both healthy and pathological conditions (Bitar et al., 2006).

The idea to generating images with NMR was firstly introduced by Lauterbur (1973) who observed that spatial variations of the main magnetic field, defined as \mathbf{B}_0 , can be introduced through the use of magnetic field gradients. This makes the spins precess at different frequencies, causing an inhomogeneous dephasing which, in turns, leads to signal artifacts such as magnetic field gradient and a distribution of chemical shifts. The dephasing can be reversed by applying a radio-frequency (RF) pulse of 180° that inverts the magnetic spin vectors, a process called spin echo (Hahn, 1950). The echo time (TE) is the time between the excitation pulse and the peak of the signal.

By applying these gradients in all three dimensions we are able to generate im-

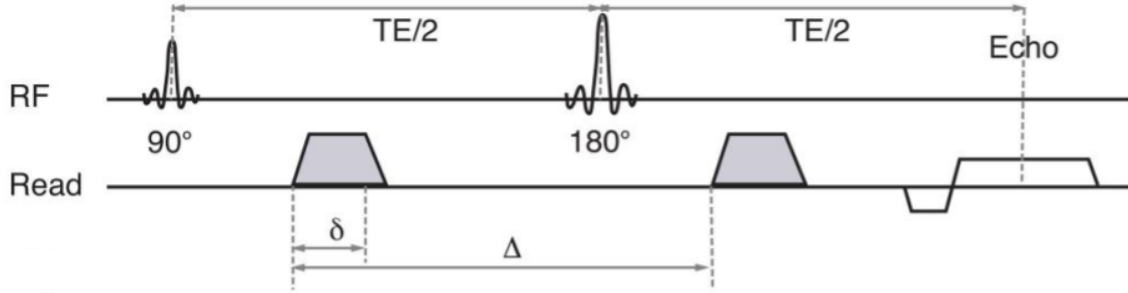


Figure 1.6 – Stejskal-Tanner sequence: the spin echo is formed by applying a 90° RF pulse followed by a 180° RF pulse. Diffusion weighting is obtained by applying a pair of identical unipolar gradient pulses around the slice selective 180° RF pulse (Freidlin et al., 2012).

ages. In particular, these gradients are slice-selection, frequency-encoding, and phase-encoding respectively. Commonly, the first is applied on the same direction of \mathbf{B}_0 field, while the other two gradients are used to generate the signal in the Fourier space, creating the k -space matrix, where the frequency-encoding direction is along one axis, and the phase-encoding direction along the other axis. The Magnetic Resonance (MR) image of a slice is then obtained by performing a two-dimensional (2D) Fourier transform on the k -space matrix. This process is done for each slice which are finally stacked to obtain the 3D volume.

The exploitation of spins phasing-dephasing and related signal attenuation to estimate ADC of different tissues was introduced by Stejskal et Tanner (1965). In their pioneer paper they introduced the pulsed-gradient spin echo (PGSE) MR sequence (shown in Figure 1.6), which still remains a standard scheme to sensitize the NMR signal to diffusion.

The formulation of the signal attenuation related to particle's movement along the direction G is expressed by Stejskal-Tanner equation:

$$S = S_0 \exp(-bD), \quad (1.6)$$

where S_0 is the standard T2 signal intensity acquired without the application of gradient G and b is the diffusion weighting, also called b-value (Bihan et al., 1986). The b-value, measured in mm^{-2} , depends only on the PGSE sequence parameters

and is computed as follows:

$$b = \gamma^2 G^2 \delta^2 \left(\Delta - \frac{\delta}{3} \right), \quad (1.7)$$

where γ is gyromagnetic ratio of the water proton, δ is the duration of the gradient pulse separated by time interval Δ . Different parameters configurations will give us different tissue information and are characterized by distinct levels of signal noise and artifacts.

1.2.2 Signal reconstruction

Diffusion imaging (DI) was first introduced by the pioneer works of Taylor et Bushell (1985) and Le Bihan et Breton (1985) applied to NMR. Starting from a set of diffusion-weighted imaging (DWI), DI estimates the effective scalar diffusivity of water molecules (Le Bihan, 1991), providing a measurement of biological tissue properties.

Diffusion tensor imaging

Based on the work of Douek et al. (1991), Basser et al. (1994) proposed to model the molecular diffusion as a second order positive-defined tensor \mathbf{D} :

$$\mathbf{D} = \begin{pmatrix} D_{xx} & D_{xy} & D_{xz} \\ \cdot & D_{yy} & D_{yx} \\ \cdot & \cdot & D_{zz} \end{pmatrix} \quad (1.8)$$

This diffusion tensor (DT) can be visualized as a 3D ellipsoid whose geometric and diffusion properties are fully described by its three eigenvalues and corresponding eigenvectors. The eigenvector corresponding to the largest eigenvalue represents the principal direction of the DT while the other two span the orthogonal planes as shown in Figure 1.7.

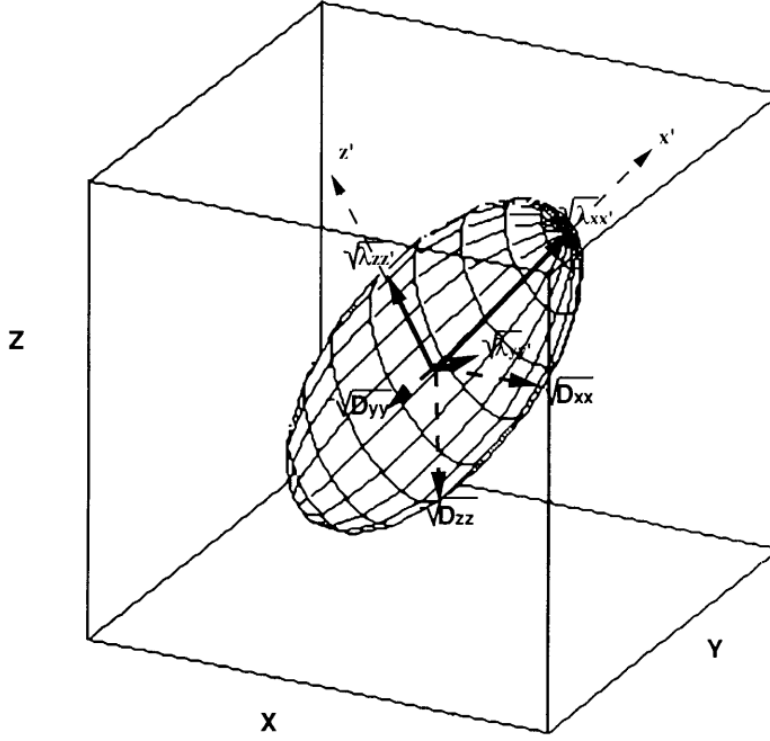


Figure 1.7 – Graphical representation of diffusion tensor (Basser, 1995).

The probability p to find the a molecule at position \mathbf{r} after time t is given by:

$$p(\mathbf{r}, t) = \frac{1}{\sqrt{(4\pi t)^3 |\mathbf{D}|}} \exp\left(-\frac{\mathbf{r}^T \mathbf{D}^{-1} \mathbf{r}}{4t}\right), \quad (1.9)$$

where $|\mathbf{D}|$ is the determinant of \mathbf{D} . As can be seen, the Eq. 1.9, defined Gaussian propagator, approximates the water displacement as a 3-variate normal distribution with zero mean. The diffusion signal equation $S(\mathbf{q}, t)$ is defined as follows:

$$S(\mathbf{q}, t) = S_0 \exp\left(-\frac{T_E}{T_2}\right) \exp(-\mathbf{q}^T \mathbf{D} \mathbf{q}), \quad (1.10)$$

where S_0 is the image without diffusion weighting. It follows that if we want to estimate the six unknown coefficients of 1.8, DTI needs at least six DW images and one S_0 to solve 1.9. In Basser et al. (1994) 1.10 is solved using least-squares (LS) or non-negative least-squares (NNLS) approaches.

Different measures can be extracted from DT, such as its trace, ADC, Fractional

Anisotropy (**FA**), Mean diffusivity (**MD**), axial diffusivity (**AD**), radial diffusivity (**RD**) characterizing different diffusion properties (Pierpaoli et Basser, 1996). For instance, changes in the **AD**, modeling the diffusivity parallel to the fiber population, may reflect myelin loss or reduced axonal packing density. Another example is the case of increased **MD** and **RD** (Basser, 1995; Basser et al., 2000), the first measuring the overall mean-squared displacement of the water molecules while the second measuring the average diffusivity perpendicular to the axonal fibers, which can be symptom of axonal and myelin degradation (Song et al., 2003, 2002, 2005). One of the most famous **DTI** measure is **FA**, which is the fraction on diffusion that is directionally dependent (anisotropic). It is a normalized measure between 0 and 1 and is formulated as follows:

$$FA = \sqrt{\frac{3}{2}} \sqrt{\frac{(\lambda_1 - MD)^2 + (\lambda_2 - MD)^2 + (\lambda_3 - MD)^2}{\lambda_1^2 + \lambda_2^2 + \lambda_3^2}}, \quad (1.11)$$

where $\lambda_1, \lambda_2, \lambda_3$ are the three eigenvalues of 1.8. Changes in its values might reflect changes in axonal packing density or enlarged axonal diameter (Tuch et al., 2005), but it's important to notice that **FA** can be ambiguous, meaning that different tensor configurations can produce the same **FA** values. Features of microstructure, such as cell size, density, permeability and orientation distribution, all affect **DTI** indices, and changes in the indices are impossible to associate with more specific changes in microstructural features (Johansen-Berg et Behrens, 2013).

The possibility to non-invasively extract fiber orientations from living biological tissue was revolutionary and **DTI** quickly became a central tool in the modern neuroimaging field and successfully applied in clinical and neurological studies (Catani et al., 2002; Horsfield et Jones, 2002; Johansen-Berg et Rushworth, 2009). The possibility to reconstruct the global fiber trajectories based on iteratively taking discrete steps in the local principal direction of **DT** is called tractography (presented in section 1.3) and it notably contributed to the success of **DTI** (Basser et al., 2000; Conturo et al., 1999; Mori et al., 1999) but also highlighted its many limitations.

The main disadvantages can be summarised in two main points: (i) inability to model different fiber populations crossing within the same voxel, characterizing up to 90% of the voxels (Jeurissen et al., 2012), and (ii) the inability to discriminate between

fiber coherence and WM microstructural properties (Dell'Acqua et Tournier, 2019; Jones et al., 2013).

Different approaches have been introduced to meet the needs of new reconstruction techniques and higher order models to solve the limitations of DTI. Among them, High Angular Resolution Diffusion Imaging (HARDI) is able to capture more information to estimate the parameters of these advanced models.

As consequence, it requires more measures to recover non-Gaussian diffusion characterizing multiple crossing fibers configurations (Tuch, 1999; Tuch et al., 2002). HARDI computes the average 3D diffusion propagator (Eq. 1.9), that, under narrow-pulse approximation becomes:

$$E(\mathbf{q}, t) = \int_{\mathbb{R}^3} p(\mathbf{r}, t) \exp(-2\pi i \mathbf{q}^T \mathbf{r}) d\mathbf{r}, \quad (1.12)$$

where $E(\mathbf{q}, t)$ is the signal attenuation and \mathbf{q} is the so-called wave vector of displacement, introduced by Callaghan et al. (1988) and later in Callaghan (1993). The \mathbf{q} vector relates width, magnitude and orientation of the diffusion gradient pulse \mathbf{G} of the PGSE sequence as follows:

$$\mathbf{q} = \frac{\gamma}{2\pi} \delta \mathbf{G}. \quad (1.13)$$

The advantage of q -space representation is the possibility to separate diffusion gradient characteristics and diffusion time, allowing to study the evolution of the DW signal according either to the pulse characteristics itself or to the diffusion time.

Q-space vs mixture models

Models based on q -space, often defined “model free”, estimate the so-called diffusion orientation density function (dODF), defined as the radial integral of the diffusion propagator in spherical coordinates (θ, ϕ) :

$$\Psi(\theta, \phi) = \int_0^\infty p(r, \theta, \phi) r^2 dr. \quad (1.14)$$

The first technique based on q -space, called diffusion spectrum imaging (DSI), was introduced by Wedeen et al. (2005) and was based on the full sampling of the

diffusion encoding gradient vector space. In particular, following 1.12, the sampling involves acquiring data on a regular Cartesian grid which, in turn requires very strong imaging gradients and long acquisition time to measure hundreds of diffusion directions. However a good approximation is achieved by acquiring over a dense set of directions at a constant q -value.

A more time-efficient approach is represented by Q -ball imaging (QBI), based on HARDI acquisition protocol. Thanks to the use of Funk-Radon transform, QBI estimates the dODF avoiding the need to the full Fourier transform. Different strategies have been proposed to speed up and improve the reconstruction, as in Descoteaux et al. (2007) where the authors use high order spherical harmonics series coupled with a Laplace–Beltrami regularization method to simplify the Funk–Radon transform.

Spherical deconvolution (SD) has recently emerged as one of the main approaches to model multiple fibre orientations proving to be particularly suited for tractography applications (Dell’Acqua et Tournier, 2019).

Figure 1.8 shows a comparison between signal reconstruction based on DT and SD models. Starting from the observations that (i) DWI signal is similar across different fiber populations and (ii) it will always be low along the main axis of the fibres, we can represent the signal in a given voxel as a linear sum of the signals for all

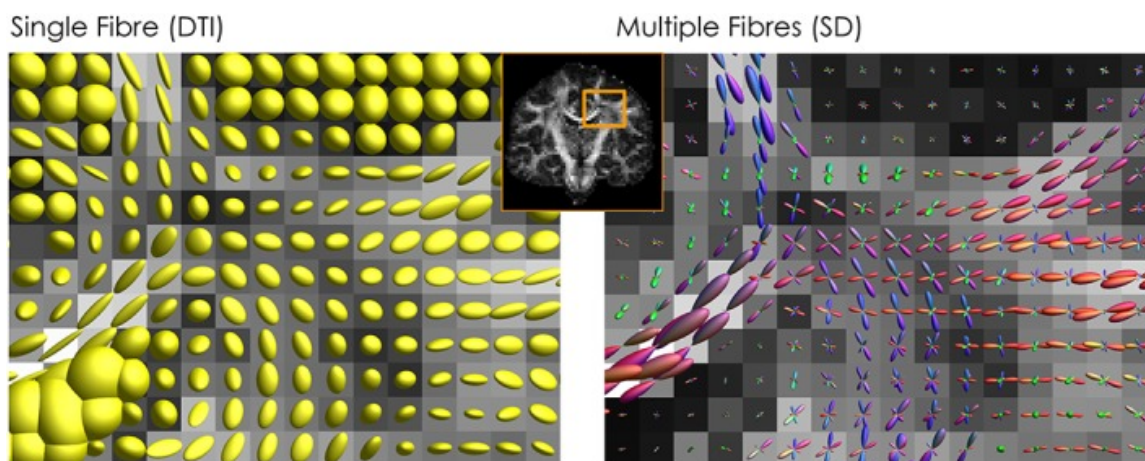


Figure 1.8 – Comparison between local signal reconstruction based on DT model describing voxel the average diffusion profile (left) and a multi-fiber approach based on fODF computed using SD (Dell’Acqua et Tournier, 2019)

the fiber populations present in that voxel. When the operation involves the use of fibre orientation density function (fODF) to represent fiber population orientations, it represents a convolution over the sphere of an fODF with a chosen fibre response function. Given an HARDI signal S , a response function R and the fODF in a voxel, the problem is defined as a multiplication in the frequency space $S = R \cdot F$.

The inverse problem, $F = (R^T R)^{-1} S$ is what SD aims to solve. The direct solution (e.g. using least-squares formulation) can be unstable if ill conditioned, generating negative values (the spherical harmonics contain negative values) and false spurious peaks (Tournier et al., 2007a, 2004), but become stable and unique if the deconvolution algorithms are well regularised. In response to that, Constrained spherical deconvolution (CSD) applies a non-negativity constraint such that, for a given voxel, the coefficients f of the fODF are computed based on least-squares fit of the predicted signal to the data m , while minimizing the sum of squares of the negative amplitudes in the fODF:

$$\hat{f} = \min_f \| Hf - m \|^2 + \lambda \| Af \|^2. \quad (1.15)$$

The DWI signal reconstruction is performed via the matrix $H = MR$, where M maps Spherical harmonics (SH) coefficients to amplitudes along the DW directions sampled, and R is a diagonal matrix of response function coefficients performing the SD in the spherical harmonic domain. The SH coefficients are mapped to a dense set of uniformly distributed directions and $\| \cdot \|^2$ represent the squared norm of the negative components.

One of the main limitations of CSD is that different fiber configurations lead to the same diffusion profile, as shown by Savadjiev et al. (2008).

As opposed to Q -space techniques, mixture models make physical assumptions about the microstructure of white matter tissue, assuming a particular model for the signal that would be measured for a single fibre population. The first approach, proposed by Inglis et al. (2001) and Tuch et al. (2002), was an extension of the DTI to model HARDI signal as a mixture of n Gaussian tensors:

$$p(\mathbf{r}, t) = \sum_{i=1}^n \frac{p_i}{\sqrt{(4\pi t)^3 |\mathbf{D}_i|}} \exp\left(-\frac{\mathbf{r}^T \mathbf{D}_i^{-1} \mathbf{r}}{4t}\right). \quad (1.16)$$

One of the main limitations of this approach is the number of compartments that must be manually defined and that can lead to an over-simplification of the underlying WM structure (Alexander, 2005).

Similarly to the previous approach, *ball & stick* mixture model (Behrens et al., 2007, 2003) assumes two types of diffusion: anisotropic, characterizing molecules restricted within or near fiber structures, and isotropic, characterizing particles not affected by fiber structure barriers.

The restricted diffusion is modeled using an anisotropic Gaussian distribution, with the possibility to extend it to multiple fiber orientations, while a isotropic Gaussian distribution describes the free unrestricted water diffusion. The signal S in the direction i becomes:

$$S_i = S_0 \left(\left(1 - \sum_{j=1}^N f_j \right) \exp(-b_i D) + \sum_{j=1}^N f_j \exp(-b_i d G_i^T R_j A R_j^T G_i) \right), \quad (1.17)$$

where S_0 is the signal without diffusion weighting, D is the diffusion coefficient, b_i and G_i are respectively the b-value and the gradient applied in direction i , f_j and $R_j A R_j^T$ correspond to the signal fraction and the anisotropic diffusion tensor of the j^{th} fiber orientation and N is the total number of fibers.

The signal is computed using a robust Bayesian modeling estimation approach called automatic relevance determination, and has found successful application in clinics (Behrens et al., 2014).

This is the case of composite hindered and restricted models of diffusion (CHARMED) (Assaf et Bassar, 2005; Assaf et al., 2004), a more general multi-compartment model assuming cylinders to have gamma-distributed radii and crossing fiber populations with different orientations. The cylinder radius, along with the parallel and perpendicular diffusivities, determines the intra-axonal signal, while the extra-axonal diffusion is modelled with a general diffusion tensor unconstrained by any tortuosity model.

Based on CHARMED, AxCaliber (Assaf et al., 2008; Barazany et al., 2009) estimates the axon diameter distribution assuming that white matter can be represented by closely packed impermeable cylinders. The method was later improved by Alexan-

der et al. (2010) with their orientation invariant mapping of axon diameter, which led to the the minimal model of white matter diffusion (MMWMD) (Dyrby et al., 2013).

The neurite orientation dispersion and density imaging (NODDI) model simplifies MMWMD by approximating cylinders with sticks and using a Watson distribution to describe the orientation dispersion. The model assumes three compartments to characterize tissue with different microstructural environments: intra-cellular, extra-cellular and isotropic compartments. Following Behrens et al. (2003), the normalized signal of the intra-cellular compartment (i.e. the stick) is given by:

$$S_{ic} = \int_{\mathbb{S}^2} f(\mathbf{n}) e^{-bd_{\parallel}(\mathbf{G}\cdot\mathbf{n})^2} dn, \quad (1.18)$$

where \mathbf{G} and b are the measurement gradient and b-value and $f(\mathbf{n})$ represents the Watson distribution which gives the probability to find a stick oriented along direction \mathbf{n} . Finally, $e^{-bd_{\parallel}(\mathbf{G}\cdot\mathbf{n})^2}$ describes the signal attenuation related to a \mathbf{n} -oriented stick with parallel diffusivity d_{\parallel} . The extra-cellular compartment, modeling the hindered water diffusion in the space around neurites is represented by the orientation-dispersed cylinders signal (Zhang et al., 2011):

$$S_{ec} = e^{-b\mathbf{G}^T(\int_{\mathbb{S}^2} f(\mathbf{n})D(\mathbf{n})dn)\mathbf{G}}, \quad (1.19)$$

where $D(\mathbf{n})$ is a cylindrically symmetric tensor with principal direction of diffusion \mathbf{n} characterized by parallel and perpendicular diffusivity d_{\parallel} and d_{\perp} respectively. Finally, an isotropic Gaussian diffusion model describes the free water compartment characterizing cerebrospinal fluid (CSF). The overall normalized signal S is given by:

$$S = (1 - v_{iso})(v_{ic}S_{ic} + (1 - v_{ic})S_{ec}) + v_{iso}S_{iso}, \quad (1.20)$$

where S_{ic} , S_{ec} and S_{iso} are the signal fractions of the intra, extra and isotropic compartments respectively and v_{ic} is the volume fraction of the intra-cellular compartment.

Models of complex orientation distribution led to the emergence of unified models that aim to represent both WM and GM. The first attempt was made by Jespersen et al. (2007) who exploit this opportunity with an analytical two-compartment model of neurites (dendrites and axons), while (Palombo et al., 2020) recently proposed a new model of brain microstructure where soma of any brain cell type is explicitly

included (Ianuş et al., 2022).

Another notable approach based on mixture models is spherical mean technique (SMT) (Kaden et al., 2016b). The purpose of this technique is to map microscopic features unconfounded by the effects of fibre crossings and orientation dispersion, which are common in the brain (Jeurissen et al., 2012). Based on their previous work (Kaden et al. (2016a)), the method uses microscopic diffusion anisotropy mapping given the assumption that for any fixed gradient magnitude and timing, the spherical mean of the diffusion signal over the gradient directions does not depend on the fibers orientation distribution. In particular, the mean diffusion signal is only a function of the voxel-averaged microscopic diffusion process. SMT assumes that the microscopic tissue geometry is rotationally symmetric around axis $\omega \in S^2$, where $S^2 = \{\omega \in \mathbb{R}^3 : \|\omega\| = 1\}$ is the two-dimensional unit sphere. Given a diffusion weighting factor $b \geq 0$, normalised gradient direction $g \in S^2$ and fixed pulse sequence, the diffusion signal, expressed as

$$h_b(g, \omega) = h_b(\langle g, \omega \rangle) \quad (1.21)$$

depends only on the spherical distance $\langle g, \omega \rangle \in [-1, 1]$ between any two points $g, \omega \in S^2$. Following 1.21 the mean diffusivity becomes:

$$\bar{e}_b = \int_0^{\frac{\pi}{2}} h_b(\cos(\theta)) \sin(\theta) d\theta, \quad (1.22)$$

where θ encodes the angle between the gradient direction and the fiber orientation. The two compartment model proposed in Kaden et al. (2016a) is composed by an intra-neurite compartment that represents the dendrites and axons with cylindrical geometries and the extra-neurite compartment describing neurons, glial cells, astrocytes, and extra-cellular space. The diffusion signal is represented by:

$$h_b(g, \omega) = v_{\text{int}} h_b^{\text{int}}(g, \omega) + (1 - v_{\text{int}}) h_b^{\text{ext}}(g, \omega), \quad (1.23)$$

where h_b^{int} and h_b^{ext} are the signal from the intra and extra-neurite compartment and $v_{\text{int}} \in [-1, 1]$ is the intra-neurite volume fraction.

1.3 Tractography

Thanks to the advanced local reconstruction methods, explained in the previous section, we are now able to discriminate between different fiber populations within a voxel. Based on DWI data, tractography, also known as fibre tracking, is the process of integrating these voxelwise information to extract the structure and organization of WM (Basser et al., 2000; Mori et al., 1999). A pathway connecting two regions is represented by a *streamline*, i.e., an ordered sequence of points $s = \{x_1, x_2, \dots, x_n\}, x_i \in \mathbb{R}^3$, while the set of streamlines is called *tractogram*. It's worth noticing that, given the low resolution of DWI data, a single streamline ends up representing a group of coherently aligned axons (Jones et al., 2013; Schiavi et al., 2020a). Tractography has enabled mapping of the brain's structural connectivity in both healthy and diseased brains, including many neurological applications such as neurosurgical planning, aging and development (Ciccarelli et al., 2008; Essayed et al., 2017). Moreover, inferring structural connectivity permits, for instance, to analytically represent the neural network as a graph where the different regions are represented by nodes and the axons connecting them by edges (see Figure 1.9). The application of graph theory has signed an important step in the study of the innate complexity of white matter structure (Iturria-Medina et al., 2007).

Although tracking methods share the same aim, strategies for achieving it vary greatly from algorithm to algorithm. Tractography methods can be classified into categories depending on how the fiber reconstruction is performed but for the sake of simplicity we usually divide them into “local”, “semi-global” and “global”.

1.3.1 Local methods

The first class encloses the line propagation methods, i.e., algorithms which retrieve the axonal pathways in a step-by-step procedure (see Figure 1.10). First approaches assumed that each imaging voxel is characterized by a single predominant fiber orientation, which is the one corresponding to the gradient of maximum diffusivity (Basser et al., 2000; Mori et al., 1999).

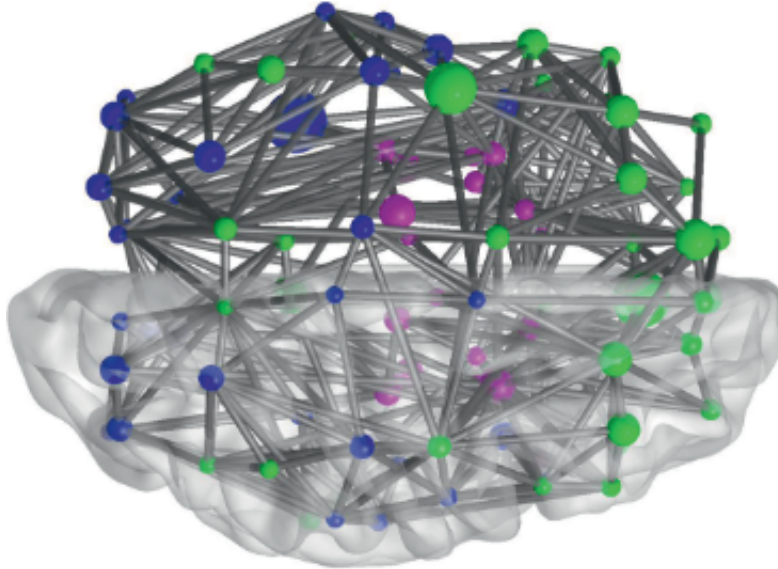


Figure 1.9 – Neural networks can be represented as a graphs to study white matter connectivity(Pereira et al., 2017).

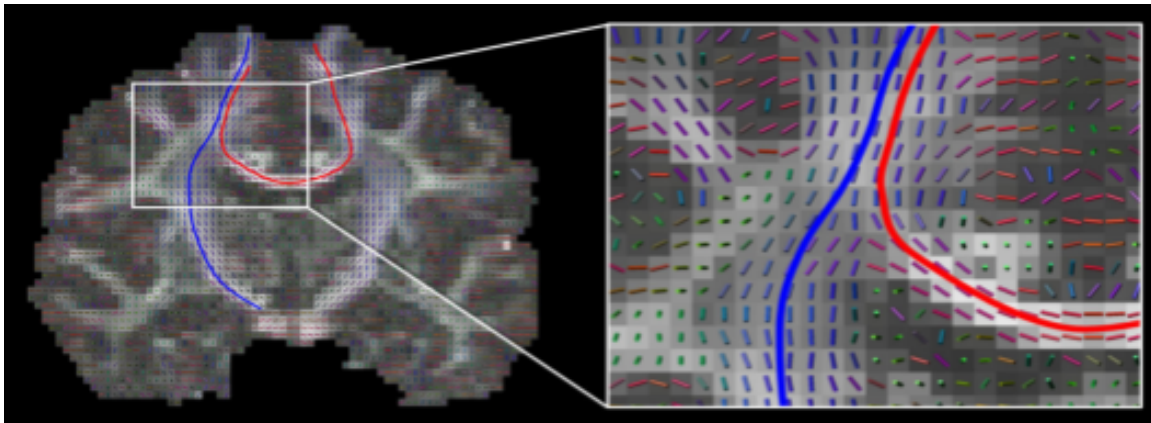


Figure 1.10 – DT tracking following step-by-step the direction of maximum diffusivity. (Jeurissen et al., 2019)

The set of local fiber orientations can be mathematically represented as a 3D vector field and the global fiber trajectories as its streamlines. The equation describing the curve derives from the fact that the tangent to the streamline must be parallel with the vector field, which formally becomes $\mathbf{r}(s) = (x(s), y(s), z(s))$ parameterized by its

arc length s . The equation that must be verified for each voxel, in order to be aligned with the underlying orientation, is therefore:

$$\frac{d\mathbf{r}(s)}{ds} = \mathbf{v}[\mathbf{r}(s)], \quad (1.24)$$

where $\mathbf{r}(s)$ is the relative $[x, y, z]$ location along the streamline at distance s and \mathbf{v} is the vector field first eigenvector of the diffusion tensor. It's worth noticing that Eq. 1.24 is defined in continuous space, whilst the orientations are sampled over the voxel grid. This implies the need of interpolation to “guess” the direction in between voxel boundaries and Lazar et Alexander (2003) showed that, depending on the approach, this can lead to propagation error.

Following Eq. 1.24, streamline reconstruction corresponds to compute the solutions to the first-order differential equation and the most straightforward approach is by performing numerical integration:

$$\mathbf{r}(s) = \int_{s_0} \mathbf{r}[\mathbf{s}] ds, \quad (1.25)$$

where $\mathbf{r}(s_0)$ is the starting point, also called *seed point*. The numerical integration can be performed using Euler integration, proposed by Conturo et al. (1999), using a step-by-step procedure, moving each time by a fixed (and usually short) distance Δ , evaluating the following position $\mathbf{r}_{i+1} = \mathbf{r}_i + \Delta v(r_i)$.

Local reconstruction approaches, even if are still used as a valuable tool in medical imaging applications (Catani et al., 2002; Essayed et al., 2017; Pujol et al., 2015), they presents several limitations. From the mathematical point of view the local integration assumes constant orientation v within the step-size Δ , which, if too large, leads to curvature overshoot (see Figure 1.11).

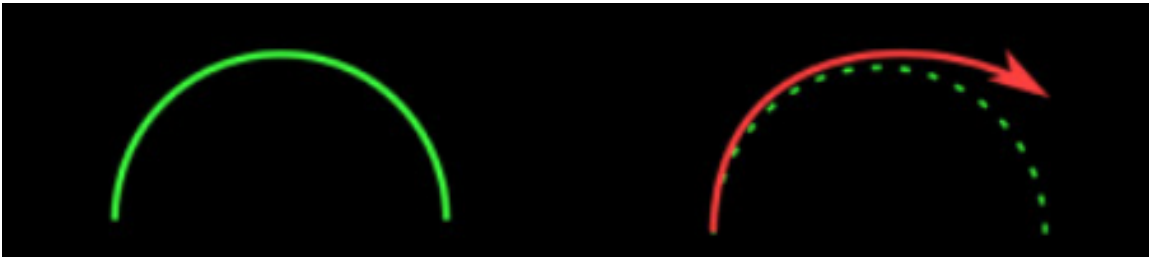


Figure 1.11 – Curvature overshoot bias caused by a step-size too large to follow the ground-truth curvature (Zhang et al., 2022).

Secondly, Euler integration is a first-order integration, meaning is susceptible to local variation between two consecutive steps. The use of higher-order integration scheme, such as Runge-Kutta have proved to be more robust, as implemented by Jeurissen et al. (2019). Another problem often underestimated is the seeding strategy, i.e., where to start the tracking and when to stop. One of the most naive approaches is to uniformly locate the seeding points in the WM and perform the tracking in both the directions. While this ensure a good coverage, it doesn't ensure that both the extremities will end up in regions of GM, and, at the same time, it causes larger bundles to be over represented because, by chance, a greater number of seed points will fall inside their pathways. One way to mitigate this last aspect is to perform the seeding at the boundaries between WM and GM. However, while this strategy ensures that at least one of the two edges of the streamlines are within regions of GM, because of the low spatial resolution of diffusion Magnetic Resonance Imaging (dMRI) and partial volume effect (PVE) tracking techniques have trouble penetrating into gyri and fully exploring the gyrus, as showed in Figure 1.12 (St-Onge et al., 2015).

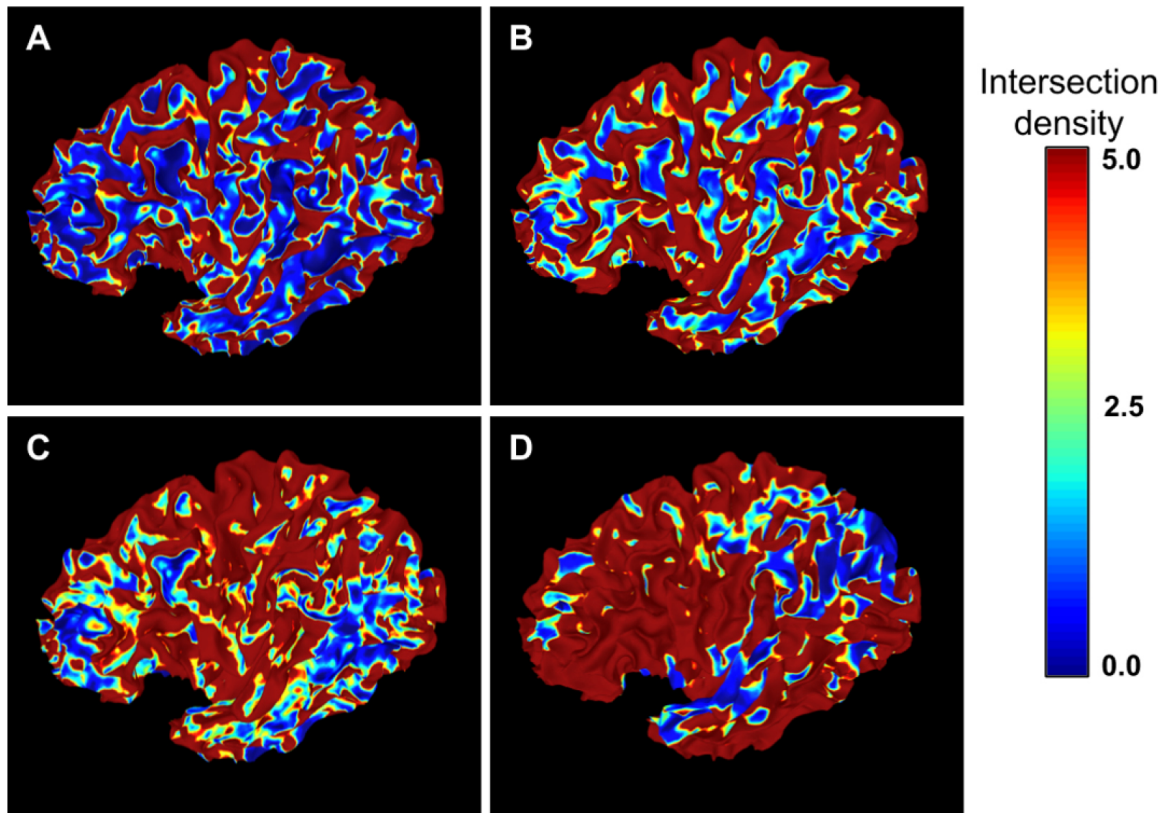


Figure 1.12 – The gyral bias. Cortical coverage (blue := absence of streamlines) of various tractography methods. From the work of [Rheault et al. \(2020\)](#)

With respect to the stopping criteria, the step-by-step orientation integration described above has no mechanism for determining confidence in the next step as the streamline progresses. Nevertheless, by construction the streamline accumulates errors as it extends across regions of high uncertainty. The two main criteria to stop the tracking process are based on heuristics and imply respectively the use of a threshold on the **FA** within the voxel traversed and a maximum curvature threshold. The first relies on the fact that regions of low **FA** tend to be associated with high uncertainty therefore large potential error for the next streamline step. Instead, the second is related to the anatomical plausibility of finding **WM** pathways with high degree of curvature within the voxel.

The tracking method explained above is part of the so called local deterministic approaches. This class of methods struggles to handle voxels where, for instance,

there are crossing fibers. In this kind of scenario the main diffusivity direction is in general tricky to define and the tracking tends to follow the easiest path available in crossing regions, which represent the majority of WM voxels (Jeurissen et al., 2012). Given the limitations, deterministic methods are prone to false negatives, i.e., they fail to recover existing pathways, stopping the reconstruction before reaching the gray matter, and they are often characterized by poor spatial coverage.

To deal with the inadequacy of tractography to explore the whole space of brain connections, probabilistic alternatives were proposed. They use probability distributions estimated in each voxel to allow uncertainty in the propagation of the trajectories. There are three main methods to compute voxel-wise uncertainty: bootstrapping, bayesian methods and calibration methods. The first exploits multi-acquisition dataset to produce bootstrap parameter estimates which serve to quantify the uncertainty (Jones, 2003; Pajevic et Basser, 2003). In Bayesian methods, on the other hand, the diffusion data are combined with a generative model to produce an estimate of the posterior probability density function of the model parameters along with the orientation of the fibers (Behrens et al., 2007, 2003). Finally, calibration methods estimate the noise variance from the data, which is added to the orientations to take care of local inaccuracies and propagation error from the previous tracking steps. Once we have local estimation of uncertainty we can think to compute the probability of two regions being connected by solving the numerical integration along the path. This has been shown to be analytically unfeasible (Behrens et al., 2003) and, instead, a more intuitive step-by-step sampling procedure of the probability distributions has proven to be rather effective (see Figure 1.13).

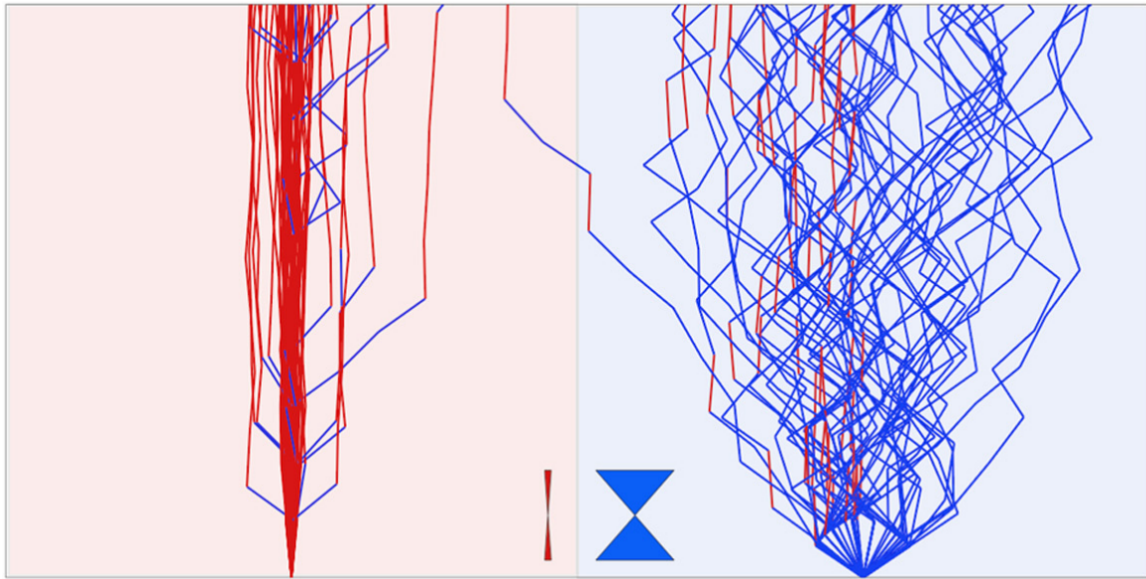


Figure 1.13 – Comparison of sampling schemes on different local probability density functions (Behrens et al., 2014).

Local probabilistic methods have demonstrated their ability to recover hard-to-track connections and to cover more adequately the WM (see Figure 1.14 and Figure 1.13) (Côté et al., 2013). However, this improved capability of exploring brain anatomy leads also to the reconstruction of implausible fascicles that do not anatomically exist, i.e. false positives (Johansen-Berg et Behrens, 2013).

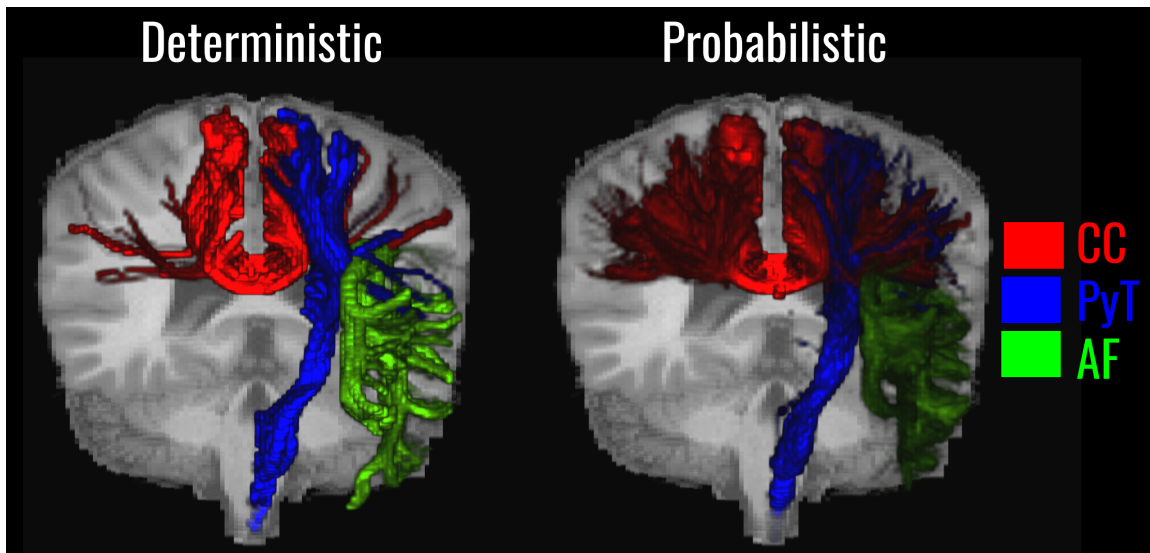


Figure 1.14 – Comparison between the tractography reconstructions performed using deterministic (left) and probabilistic method (right) of three major WM tracts.

1.3.2 Semi-global methods

A top-down strategy on fiber reconstruction can be found in the so-called “geodesic” methods, a class of algorithms in between the local and global ones, where in particular the seek for white matter pathways is modeled as the purse of connections between regions of the brain (Jbabdi et al., 2008; Parker et al., 2002). Usually, geodesic methods rely on the shortest path approach to find the path of minimum length, with respect to a certain metric, connecting the regions of interest. A unique property of geodesic tracking is symmetry, i.e. the recovered pathways between two regions are the same independently from the region where we start the tracking.

The basic idea for constructing a geodesic in a metric space is to build a distance field from a seed region, the very same region one would use as a seed for streamline tractography. This is done by solving the so-called Eikonal equation (Hamilton, 1828), a partial differential equation (PDE) that describes the time of arrival at each point of the space, as a function of the local speed. Formally, the geodesic is found by minimizing the integral:

$$\mathbf{J}(\gamma) = \int \mathbf{F}(s, \gamma, \gamma') ds, \quad (1.26)$$

where, based on the metric \mathbf{M} , $\mathbf{F}(s, \gamma, \gamma') = \sqrt{\gamma'(s)^T \mathbf{M}(\gamma(s)) \gamma'(s)}$ represents an infinitesimal step along the pathway γ . Given Eq. 1.26 the arrival time $u(x)$ becomes the minimum value of the integral $\mathbf{J}(\gamma)$ which satisfies:

$$\begin{aligned} \Delta u^T \mathbf{M}^{-1} \Delta u &= 1, \\ \gamma' &\propto \mathbf{M}^{-1} \Delta u. \end{aligned}$$

Following 1.26, we can deduce that the arrival time is directly proportional to the speed and that this can vary depending on the local metric. This, in turn implies that in a constant speed field, the PDE can be easily integrated, and the geodesics are simply straight lines. Conversely, the geodesic follows bending pathways if it encounters changes of speed, trying to reduce the arrival time. Different methods have been proposed to compute the function u , like the Tsitsiklis's (Tsitsiklis, 1995) method and Sethian's method (Sethian, 2001), both based on optimisation procedures such as gradient descent.

Based on the same concept, graph-based tracking represents the orientation vector field as a weighted graph where each node represent a voxel and the edges the cost of transition from one voxel to its neighbors. Given this representation, a lower cost is assigned to edges that are aligned with fiber trajectories. In this context streamlines reconstruction is performed by following the path with highest coherence in the local orientations and can be found using classic graph algorithms such as Dijkstra.

Both these semi-global approaches are robust and, on average, computationally fast. The main limitation is how the exploration is designed, which is intrinsically constrained. The need of "starting" and "ending" regions, for instance, precludes the use of this strategy for exploratory studies considering that is not always an easy task to provide a parcellation of cortical and subcortical sections. Moreover, as shown in Figure 1.15 the recovered streamlines tend to share the same pathway, especially in proximity of bending regions, with a consequently non-natural representation of neuronal density (Bastiani et al., 2012).

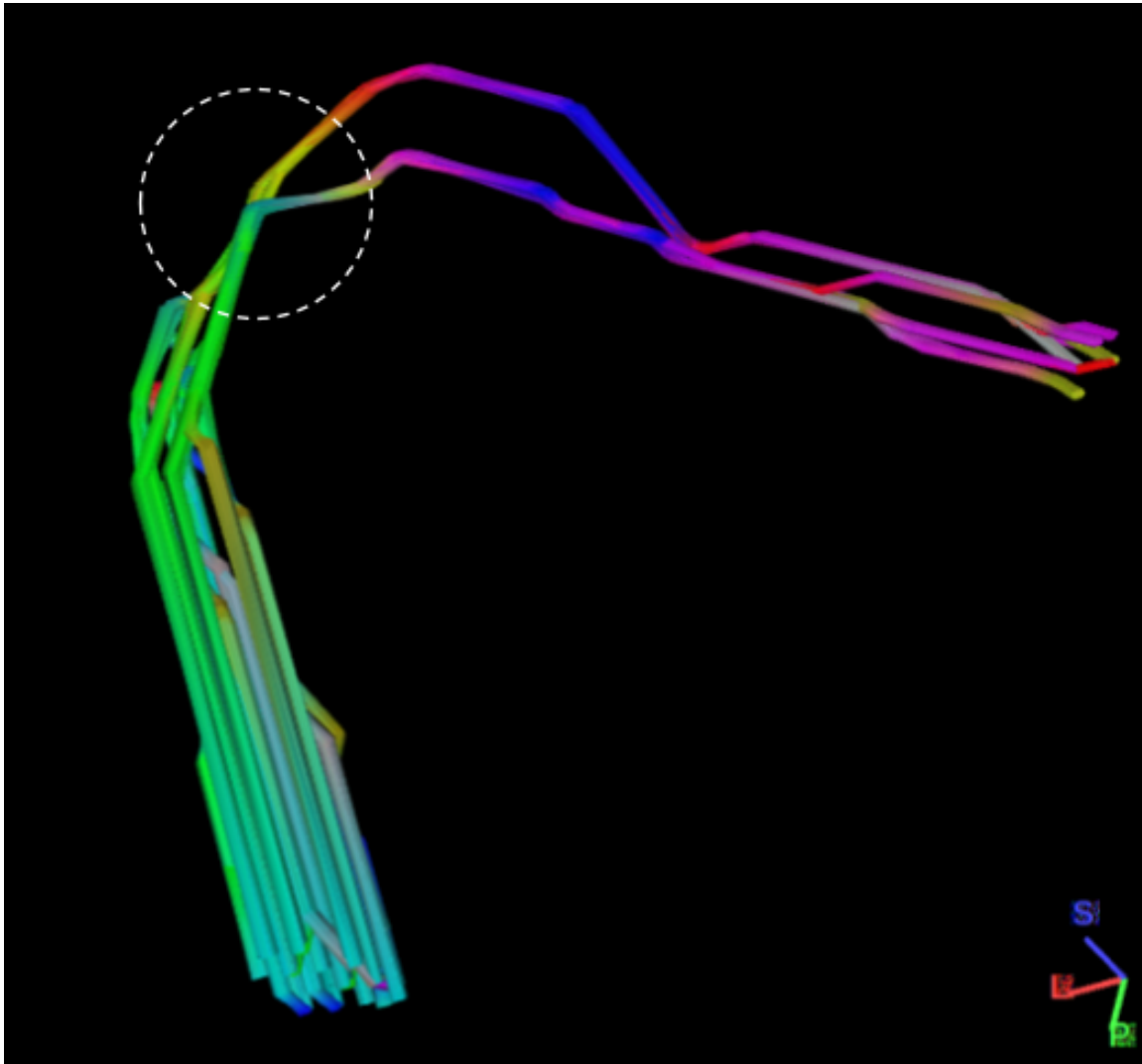


Figure 1.15 – Graph-based tracking in proximity of a bending region. In such configurations minimal-path approaches tend to fail to properly recover streamlines on the outer part of the curve because in most cases they tend to follow the shortest path and share the same trajectories (bottleneck).

1.3.3 Global methods

This brings us to the last and most recent global streamline tracking algorithms, which results outperform any other previous ones (Fillard et al., 2011). As we know, tractography reconstruction is an *ill-posed* problem for two main reasons: first of all,

slight changes in the data heavily affect the result of the tracking and, secondly, the same tracking process cannot deal with error propagation of the local fibre orientations (Mangin et al., 2013). A way to deal with such class of problems and make them numerically affordable is by making assumptions, which are then implemented in the form of constraints. This process is defined as “regularisation” and global tractography provides simple ways to ‘regularise’ the tractography reconstruction problem Mangin et al. (2013). This class of methods can be furthermore divided into *generative* and *discriminative*, depending on the reconstruction strategy adopted.

Global generative methods

The “global” perspective in streamline tracking has been introduced more than two decades ago (Cointepas et al., 2002; Poupon et al., 2001, 1998) and has seen a notable evolution in the last years. First approaches were based on the idea of exploit regions within low ambiguous areas to help the reconstruction in more hard-to-track regions. They relies on two main assumption: axons tend to be organized into coherently aligned fascicles which follows smooth trajectories. In practice, the algorithm recovers pieces of tracts and use their orientation as prior to track through regions with higher ambiguity. The interactions between these segments are modeled by a Markov Random Fields (MRF) which allows to evaluate the different configuration among neighbour segments, looking for the one providing the best explanation for the map of diffusion profiles, based on tensor. Finally, The optimization process was based on curvature-based regularisation and signal explanation.

Following the same idea, Aganj et al. (2011) added the possibility to sample the space looking for the trajectories that are more in agreement with the diffusion signal. The method was based on curve parameterization and was more robust to local inaccuracies but at the same time suffered the high dimensionality of the parameters space that needs to be explored.

Another interesting approach was proposed by Jbabdi et al. (2007), which recalls geodesic methods. Like this class of algorithms, it assumes connections between pair of regions and infers the localization of the tracts and the local fibre Orientation Distribution Function (ODF) at the same time using a Bayesian approach. Although being elegant and computationally efficient with respect to other global approaches,

this method could evaluate one connection at a time and suffered the initialization of connection trajectories which remained an high-dimensional problem.

A notable step forward in terms of reconstruction quality has been made by the introduction of the so-called energy-based tracking algorithms (Kreher et al., 2008; Reisert et al., 2011). The general idea behind these methods is to perform tracking and signal reconstruction at the same time while minimizing a cost function that is often defined as “system energy”. Energy-based methods build the model based on atomic entities (can be, for instance, small segments as in Kreher et al. (2008) and Reisert et al. (2014), spins (Fillard et al., 2009), particles, etc.) which can interact following well-defined behaviors designed to mimic real-world axons. Starting from a random disposition of the segments (see Figure 1.16), covering the whole white matter, the fibers are “assembled” following an energy gradient descent. Usually, this is driven by MCMC simulations (van Lieshout, 2000) to sample from the space of all the possible actions that can alter the organization of the current atoms. At the beginning, the system is characterized by an high energy or “temperature” T which allows to better explore the parameters space. As the process evolves, the temperature decreases, constraining the exploration to promote convergence to the configuration which minimized the total energy, an optimization schedule called simulated annealing (Perrin et al., 2005), borrowed from annealing in metallurgy which implies heating and controlled cooling of materials to alter their physical properties. From the work of Kreher et al. (2008), an example of energy function E , corresponding to a specific segments configuration ω at system temperature T , can be represented as follows:

$$E_T(\omega) = \exp\left(-\frac{1}{T}U_I(\omega)\right) \exp\left(-\frac{1}{T}U_D(\omega, \mathbf{S})\right). \quad (1.27)$$

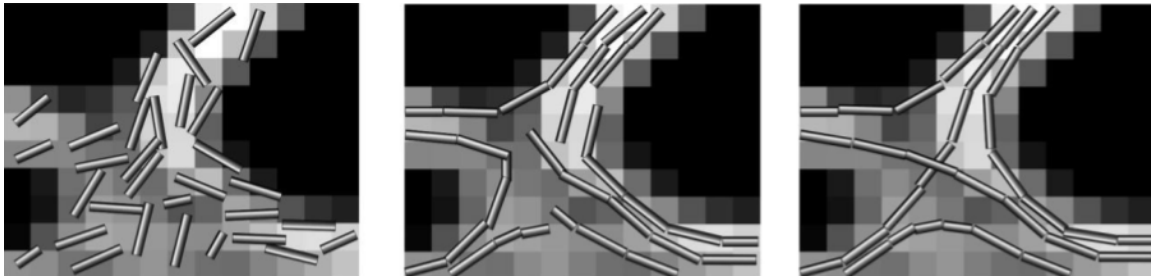


Figure 1.16 – Fiber reconstruction steps in Gibbs global tracking algorithm (Kreher et al., 2008).

Taking inspiration from statistical physics, energy functions like Eq. 1.27 are generally composed of two components. One is responsible to supervise the “quality” of the model, represented here by U_D , looking the configuration that better explain the observed diffusion data S , and how the signal is predicted largely varies among different algorithms. Starting from the simplest “signal fractions” which takes into account only the number of fibers passing through a voxel (basically a measure of density), the most recent techniques assume that the tissue is composed of several different “compartments”, e.g., axons, glial cells, and extra-axonal space, and that the DWI signal measured in each voxel can be explained in terms of the unique diffusion pattern of each of them, hence, taking into account of microstructure characteristics (Panagiotaki et al., 2012). The second component U_I , takes care to produce anatomically reasonable fibers and, depending on the method, this implies different heuristics. Reisert et al. (2011) define an interaction potential such that two segments connect if they are close enough and with similar orientations while Mangin et al. (2013) focus on the angular changes between consecutive segments to promote smooth trajectories.

A key difference between these approaches and the previously described global tractography methods is the bottom-up strategy of the optimization framework in both streamline and signal reconstruction. By construction, energy-based methods tend to recover streamlines at different steps of the optimization before merging in single global connections. In fact, simple configurations are easier to optimize, which implies that most of the computational time is spent disentangling ambiguous regions. From the signal reconstruction point of view, previous methods allows to use any ODF model, which is then used to build a pseudo-likelihood function. This is then applied

to measure the coherence between the streamline segment and the observed data. In this case, the local minima corresponds to the direction with highest probability in the fibre **ODF**. In the work of Reisert and colleagues (Reisert et al., 2011) the signal is estimated in each voxel based on the local segments configuration, meaning that their different orientations and displacement influence the diffusion signal interpretation.

Global generative algorithms have proved to produce good results and they are mostly robust to signal artifacts, but this comes at a price. Facing the reconstruction problem from such an analytical point of view requires a fine-tuning of several parameters (that’s not always straightforward) which can lengthen exponentially the computational time or, in the worst case, cannot converge at all. Different approaches have been proposed to reduce the parameter space, limiting the computational cost: Close et al. (2015) presented a method to direct model groups of streamlines using a bayesian approach, focusing in particular on bundle geometry optimization. While it represents a good solution to reconstruct specific bundles, these class of methods often rely on many empirically tuned parameters to shape the geometry of the fascicle and to compute the corresponding signal. Moreover, the initial setup for each bundle need to be manually defined and they cannot reconstruct multiple bundles at once. Another notable approach, by Lemkaddem et al. (2014), starts from a set of candidate trajectories which is iteratively perturbed to fit the diffusion data using an **MCMC** optimization approach. In this case, the cornerstone is the adoption of splines which dramatically reduce the number of parameters needed to represent anatomically plausible fibers. On the other hand, the method still suffers the cost of the stochastic procedure implied to optimize both geometry and signal contribution at the same time.

Global discriminative methods

One major step to reduce the complexity of this *generative* strategy, while keeping a “global” approach, was made with the introduction of *discriminative* approaches. The idea behind these methods is to identify the optimal subset of streamlines from a pre-computed set of candidates, constructed using standard tractography algorithms, that are most compatible with the observed data; for this reason, they are sometimes referred to as “filtering” methods (Daducci et al., 2016). The results of discriminative

methods are often in the form of a “weight” assigned to each streamline. These weights represent an effective cross-sectional area of each streamline, which can be utilized as a direct measure of connection density (Smith et al., 2020) or to represent the connectivity “strength” by aggregating all the streamlines connecting two regions.

One of the first notable algorithms is presented in Sherbondy et al. (2009), which starts with a massive dataset of 180 billions candidate fibers from different sources looking for the highest resolution and physically plausible projectome, i.e., subset of fascicles, to date. This is accomplished through a heavy search among the possible configurations, called projections, of fibers that minimize the global error which takes into account the intravoxel difference between the signal of the reference diffusion map and the one predicted by that specific projection and the volume cover. As can be easily imagined, this is a computationally tremendous task which also needs to be driven by multiple stochastic restarts to avoid local minima and requires a highly parallelized cluster to converge to a solution.

Recently, more advanced and optimized formulations have been proposed; in SIFT (Smith et al., 2013) and its evolution SIFT2 (Smith et al., 2015a), streamlines are selected based on the agreement between their trajectories and the local fiber orientation distributions, making possible to solve tricky configurations as in voxel with crossing fibers (see Figure 1.17).

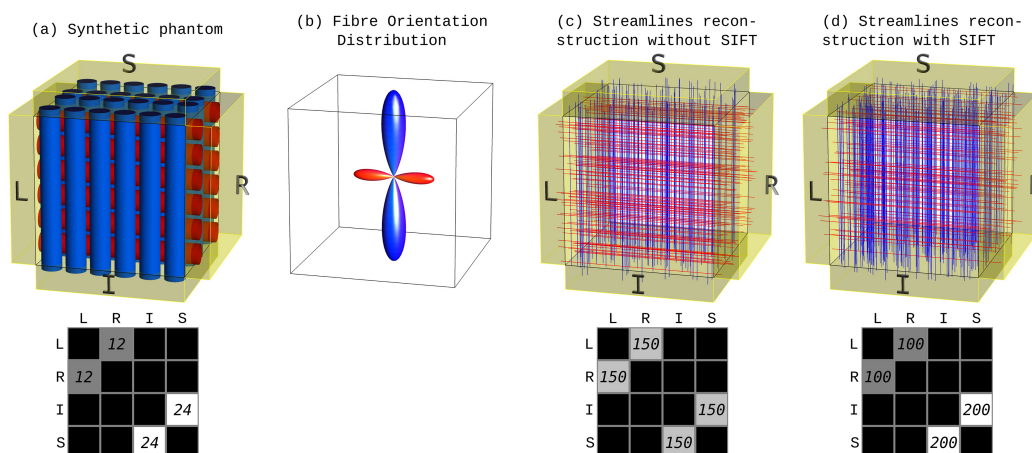


Figure 1.17 – The effect of SIFT on the structural connectome estimated based on the number of streamlines (Smith et al., 2013).

SIFT is based on the assumption that the input tractogram contains all the fibers needed to properly represent the observed track density and each streamline represents some volume of axons per unit length. Following these premises, the streamline density within each voxel V matches the Fibre Orientation Distribution (**FOD**) as follows:

$$\forall \{V : PM_V > 0, l \leq L_V\} : \mu \cdot TD_{V,l} = FOD_{V,l}, \quad (1.28)$$

where PM_V is the corresponding value of voxel V in the processing mask which defines those voxels that should influence the model fit and the degree of influence, l is one of the L_V number of lobes in the voxel, $TD_{V,l}$ is the track density attributed to that particular lobe and $FOD_{V,l}$ is the **FOD** integral of lobe number l in voxel V . Importantly, this assumption holds only if a proportionality coefficient, defined as μ in Eq. 1.28, is applied to convert the streamline density attributed to each **FOD** lobe into a value that can be compared directly with the integral of that lobe, as explained in [Smith et al. \(2020\)](#). Based on Eq. 1.28, the metric for quantifying how well a streamline reconstruction fits the underlying diffusion data becomes:

$$f = \sum_V \left(PM_V \sum_{l=1}^{L_V} (\mu TD_{V,l} - FOD_{V,l})^2 \right) \quad (1.29)$$

The final streamline configuration is recovered by iteratively removing streamlines from the dataset to improve the model fit. Given an initial set of N tracks, the optimal selection of streamlines is a combinatorial optimization problem, with 2^N possible combinations. The solution is found using a gradient descent approach, where streamlines are iteratively removed if this removal improves the cost function value. The process has different stopping criteria: if the cost function reaches a pre-determined threshold, if a certain number of streamlines are kept or if a specific ratio between number of streamlines and density change is met.

Its evolution, **SIFT2**, provides a more efficient implementation. The first difference is how TD_l is defined, i.e., the new formulation allows variable contribution weights from individual streamlines as follows:

$$TD_l = \sum_{s:|s_l|>0} [s_l \cdot e^{F_s}], \quad (1.30)$$

where $|s_l|$ is the length of the streamline s traversing lobe l , F_s is the weighting coefficient for the streamline and e^{F_s} is a weighting factor. Worth to notice is that, differently from [SIFT](#), all streamlines have a non-zero contribution to the model. These weights, instead, are used to scale the contribution such that the streamlines densities match the [FOD](#) lobe integrals throughout the image. The final cost function is similar to [Eq.1.29](#) but with the addition of a second regularisation component:

$$f = \sum_{l=1}^L \left(PM_l \sum_{l=1}^L (\mu TD_l - FOD_l)^2 \right) + A \cdot \lambda_{reg} \cdot \sum_{s=1}^N [f_{reg}(s)]. \quad (1.31)$$

The regularisation term f_{reg} , along with the scaling parameter A , is used to make the effect of the regularisation comparable for different imaging and reconstruction parameters. The regularization function has been proposed in two different version: a conventional Tikhonov regularization and an asymmetric total variation function. The first constraints the weighting coefficients F_s to remain close to zero, such that the weighting factors remain close to unity, while the second forces streamlines traversing the same FOD lobes to have similar weights. Finally the optimization is run using a combination of gradient descent and expectation-maximization approach.

As opposed to [FOD](#) coherence approaches, methods such as [LiFE](#), [COMMIT](#), [COMMIT2](#) and [COMMIT2_{tree}](#) consider the full measured DW-MRI data to evaluate streamlines contributions. All these methods use similar approaches and formulate the problem as a linear system. In particular, [COMMIT](#) framework describes the [DWI](#) signal in each voxel as a linear combination of given basis functions, as follows:

$$\mathbf{y} = \mathbf{A}\mathbf{x} + \eta, \quad (1.32)$$

where $\mathbf{y} \in \mathbb{R}_+^{n_d n_v}$ is the vector containing the n_d q-space samples acquired in all the n_v voxels, η is a parameter to account for noise in the data and modeling errors, $\mathbf{A} \in \mathbb{R}^{n_d n_v \times n_c}$ is the matrix which explicitly contains the multicompartment model for each voxel and \mathbf{x} are the positive weights $x \in \mathbb{R}_+^{n_c}$ are the contributions of the n_c basis functions in \mathbf{A} . The signal associated to the multicompartment model is defined

as follows:

$$S(\mathbf{q}) = \sum_{F_i \in F} \mathbf{f}_i^{IC} R_{(i)}^{IC}(\mathbf{q}) + \sum_{F_i \in F} \mathbf{f}_i^{EC} R_{(i)}^{EC}(\mathbf{q}) + f^{ISO} R^{ISO}(\mathbf{q}). \quad (1.33)$$

Eq. 1.33 describes the observed signal as the sum of intra-cellular, extra-cellular and isotropic water compartment diffusion signals. In particular, f^{IC} represents the product of restricted diffusion arising from fiber $F_i \in F$ by the rotated response function R^{IC} applied to match the local orientation of F_i and scaled by the length of F_i inside the voxel. The same is applied for the extra-cellular compartment.

In Eq. 1.32 the linear operator \mathbf{A} is a block matrix in the form:

$$\mathbf{A} = [\mathbf{A}^{IC} | \mathbf{A}^{EC} | \mathbf{A}^{ISO}], \quad (1.34)$$

containing the three submatrices that encode the restricted, hindered and isotropic contributions respectively (Figure 1.18 shows a visual representation of the COMMIT model and the dictionary structure).

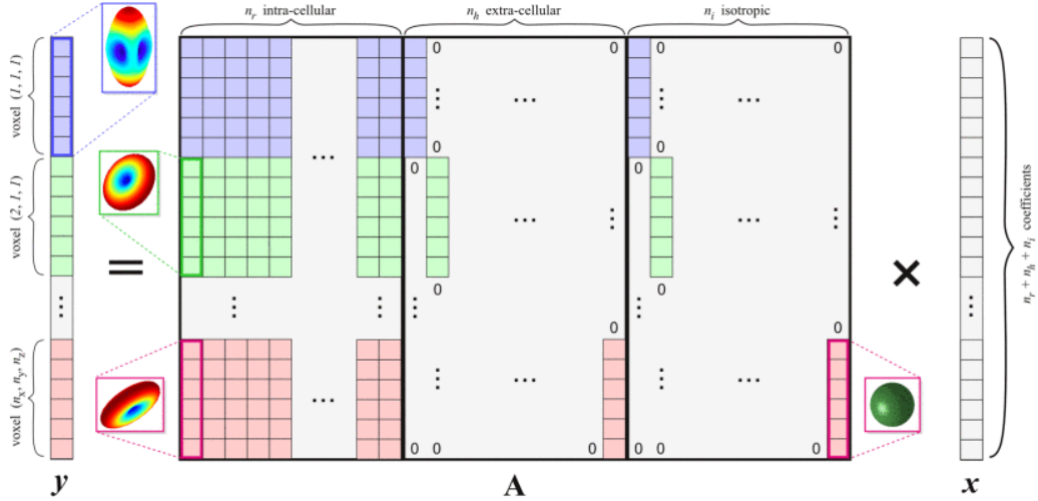


Figure 1.18 – Visual representation of COMMIT model (Daducci et al., 2015). For each voxel the signal is represented as linear combination of water compartments, modeled as tensors of different shape. The response function are pre-computed and stored inside the dictionary matrix \mathbf{A} .

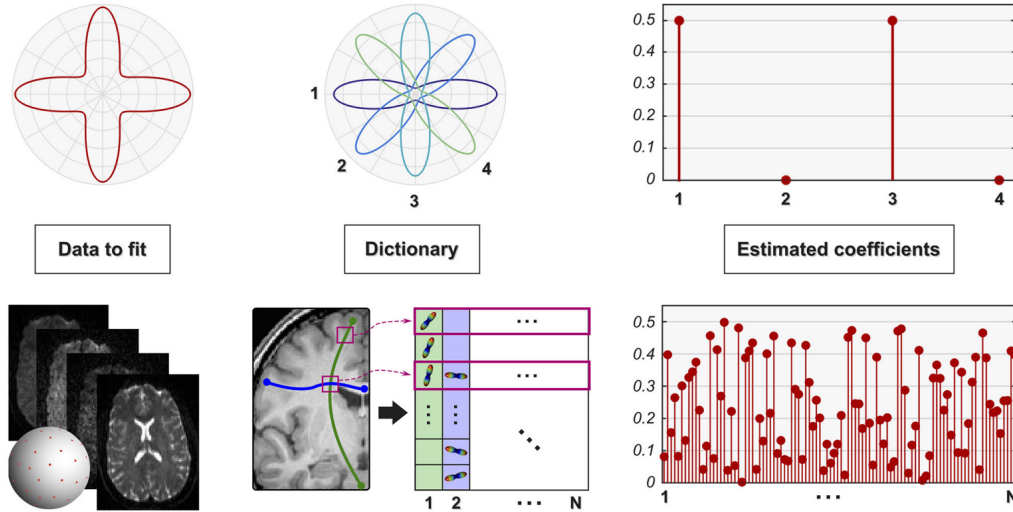


Figure 1.19 – Visual representation of **COMMIT** framework (Daducci et al., 2015).

Following Eq. 1.32, the weights \mathbf{x} are estimated by solving the **NLS** problem:

$$\operatorname{argmin}_{x \geq 0} \|\mathbf{A}x - y\|_2^2, \quad (1.35)$$

where $\|\cdot\|_2$ represents the l_2 norm in \mathbb{R}^n .

The framework, schematically reported in Figure 1.19, is flexible, allowing the user to choose the forward model to adopt to reconstruct the diffusion signal in order to be sensitive to different quantitative properties of the tissue such as axonal diameter or intra-axonal signal fraction. It has been recently demonstrated that the performance of this class of methods can be significantly boosted by combining knowledge and data-driven strategies (Ocampo-Pineda et al., 2021a). Indeed, the flexibility of these formulations allow taking explicitly into account two fundamental assumptions about the connections in the brain: first of all fibers are naturally organized in bundles (Mandonnet et al., 2018; Udin et Fawcett, 1988), secondly, the evolution has promoted a low number of bundles to minimize the overall wiring cost (Bullmore et Sporns, 2012). This prior knowledge helps resolve some of the ambiguities present in the data showing significant improvement of the anatomical accuracy of the connectome as showed by Schiavi et al. (2020a) and Ocampo-Pineda et al. (2021a). This is achieved by organizing the streamlines into groups and seeking for solutions

which explain the measured signal with the minimum number of bundles, using the Group Lasso regularization (Yuan et Lin, 2006), to promote sparsity in the number of connections.

These discriminative methods allowed reducing dramatically the computational cost required to perform global tractography, and showed great potential to further improve the quality of the reconstructions, notably alleviating the problem of false positives as well as improving the biological interpretability of the tractograms (Jbabdi et Johansen-Berg, 2011). However, unlike generative methods, they assume a static input configuration, i.e. shape and position of the candidate streamlines are fixed and cannot be adapted. This means that the quality of the reconstructions remains indissolubly bounded to the quality of the algorithm used to build the candidate pathways.

1.4 Tractography limitations

Tractography represents an invaluable tool to study in vivo a wide spectrum of neurological conditions but suffers from some critical limitations rising from each stage of the DWI processing pipeline, which can be divided into three major steps:

- Acquisition
- Local orientation reconstruction
- Tracking

Differently from invasive approaches, the reconstruction process is based on indirect measures, which is the cause of the ‘ill-posed’ nature of tractography reconstruction (Mangin et al., 2013). For each voxel DW-MRI estimates the average amount of water displacement along the applied gradient meaning that any further information are based on inference over models which often rely upon strong assumptions (Jones et al., 2013). Indeed, inferring tissue microstructural information from DW-MRI data implies solving a difficult inverse problem with non-unique solutions and limited by many factors as the acquisition resolution, the angular sampling of the diffusion space and the number of different gradients used. These inaccuracies influence the quality

of reconstructions performed by tracking algorithms which struggle to recover WM pathways in regions with high ambiguity.

The white matter of the human brain is made up of a large number of individual fiber tracts. Local reconstruction inaccuracies and error propagation have a dramatic impact on the quality of reconstructions (Jbabdi et al., 2011; Mangin et al., 2013), causing tractography to be highly susceptible to false positives (Wassermann et al., 2016). Following are reported the most common biases which particularly affect tracking methods relying on step-by-step procedures.

The so-called *bottleneck* effect is caused by multiple fascicles merging in correspondence of a small region and then separating afterwards. The diffusion signal in that section is likely to be represented by a single orientation, meaning that, once the fibers spread at the exit, the tracking algorithm has to choose among different directions to follow. Without any prior information on the underlying anatomy or constraints, the reconstruction faces a combinatorial problem which, most of the times, leads to the reconstruction of false positive pathways, as clearly demonstrated by Maier-Hein et al. (2017) and reported in Figure 1.20.

The reconstruction of fascicles overlapping is particularly tricky because of the different types of configuration we can encounter in WM. In the case of a *kissing* configuration, streamlines coming from different source regions merge and then split again as showed in Figure 1.21(A) by Rheault et al. (2020). In this case, incoming streamlines bend in proximity of the curve in the overlapping region and then, suddenly, straighten their path due to the blurred single direction of the local model, until they exit the region. Although the true connections are preserved, the streamline coverage is reduced, as shown in Figure 1.21(B).

Narrow intersection effect happens in correspondence of crossing or splitting regions, as schematically showed in Figure 1.22. In such conditions, the streamline reaches a position where multiple directions are considered valid, it is possible that the algorithm simply picks the wrong one and is the main cause of the error propagation in local tractography methods. This bias, along with the fact that the majority of WM voxels are characterized by crossing configurations (Jeurissen et al., 2012), implies that, even if whole-brain tractography reconstructions are able to recover most of the true positive bundles, these are often spatially underrepresented (Maier-Hein

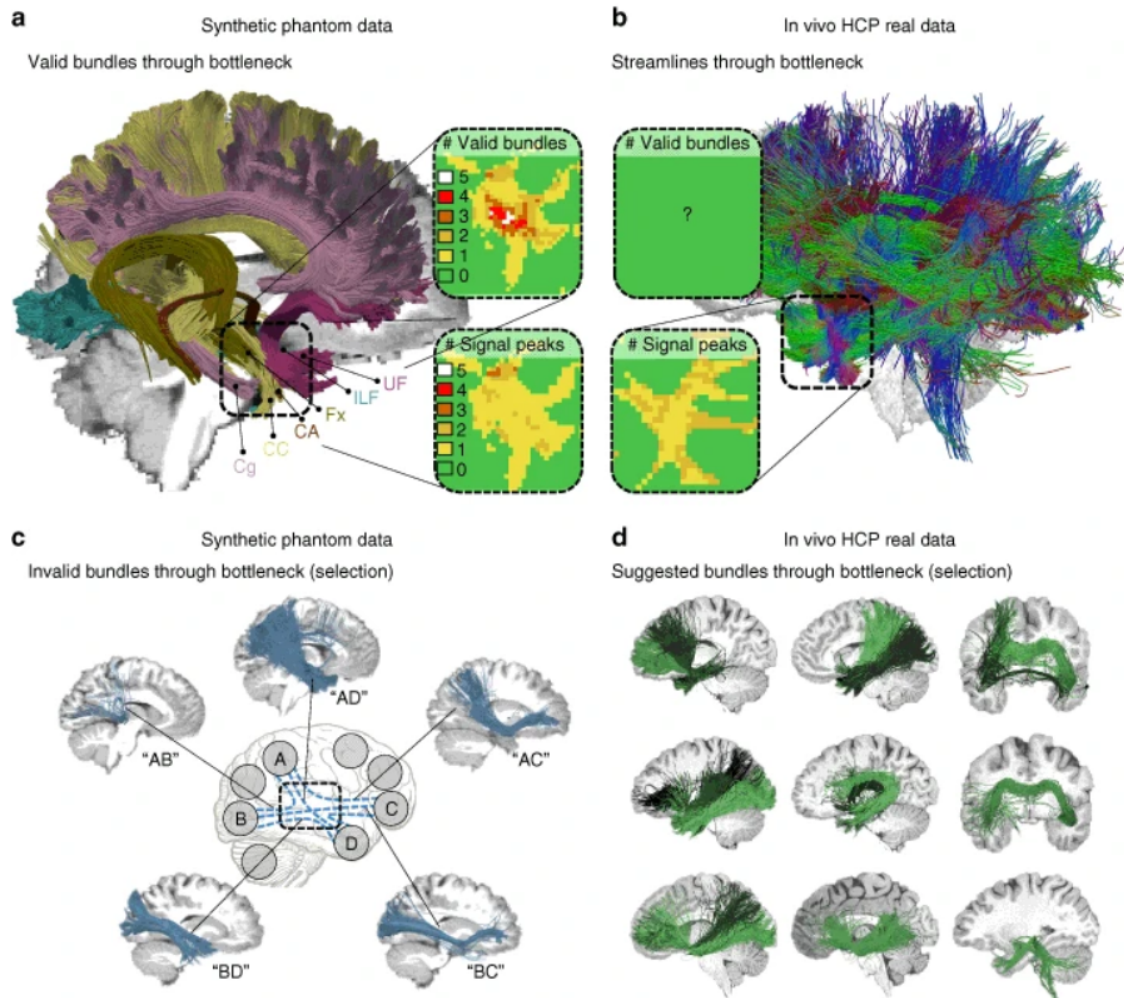


Figure 1.20 – Visual inspection of the bottleneck effect. [Maier-Hein et al. \(2017\)](#) show how in correspondence of merging regions, multiple tracts are represented by a single fiber directions in the diffusion signal, leading to massive combinatorial possibilities of plausible configurations for connecting the associated fascicles endpoints.

[et al., 2017](#)). Different tracking parameters, such as the direction sampling angle and step-size, can alleviate the effect, while in general anatomical-informed approaches are more robust. This effect often occurs in regions close to the cortex, where deep WM tracts projections merge and split as they reach the gyri.

This finally brings us to the *gyral bias*, a well-know termination bias largely stud-

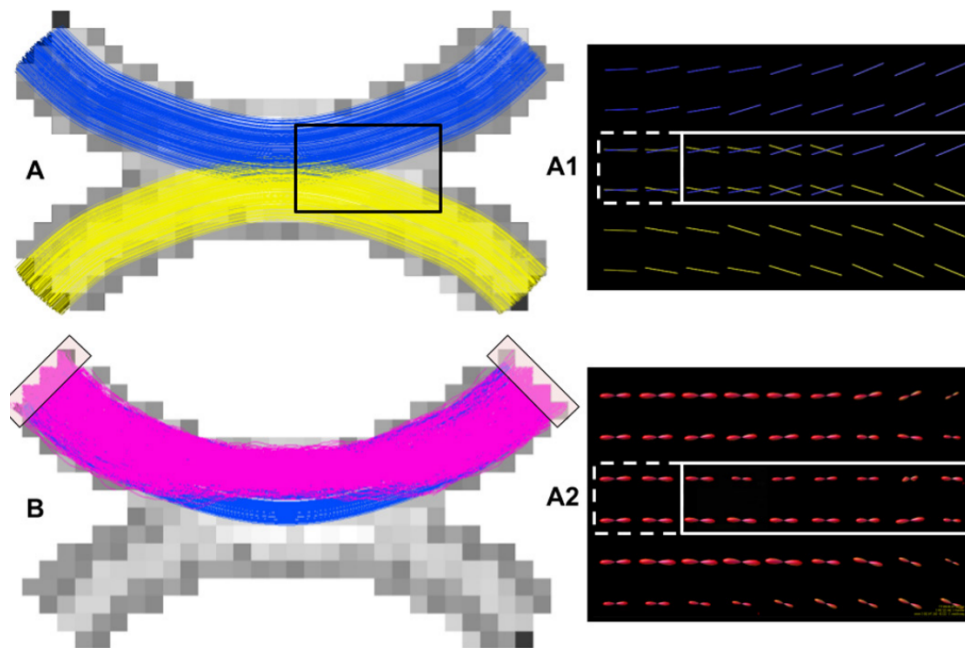


Figure 1.21 – Streamline reconstruction of a kissing fibers configuration, comparing the ground-truth geometry and FOD vector fields (A and A1) with the one recovered using probabilistic tractography and the associated vector fields (B and A2) (Rheault et al., 2020).

ied in the tractography field (Schilling et al., 2018; Van Essen et al., 2014). The low resolution characterizing dMRI acquisitions causes gyral crowns to be prone to partial volume effects. This, in turn, biases orientation estimates along the WM-GM boundary to point in the direction of the adjacent white matter (which is often tangential to the border, as described by Van Essen et al. (2014) and showed in Figure 1.23. Even if these orientation estimates form the input of most tracking algorithms, simplistic tracking methods tend to be particularly biased, causing the crowns to be over-connected while the banks and fundi remain under-represented.

To alleviate the effects of these biases on tractography reconstructions, two strategies can be adopted: whole brain tractography followed by filtering and ROI-based tracking.

In the first case, the spatial coverage is improved by computing a massive amount of streamlines covering the whole WM volume using local or global tractography

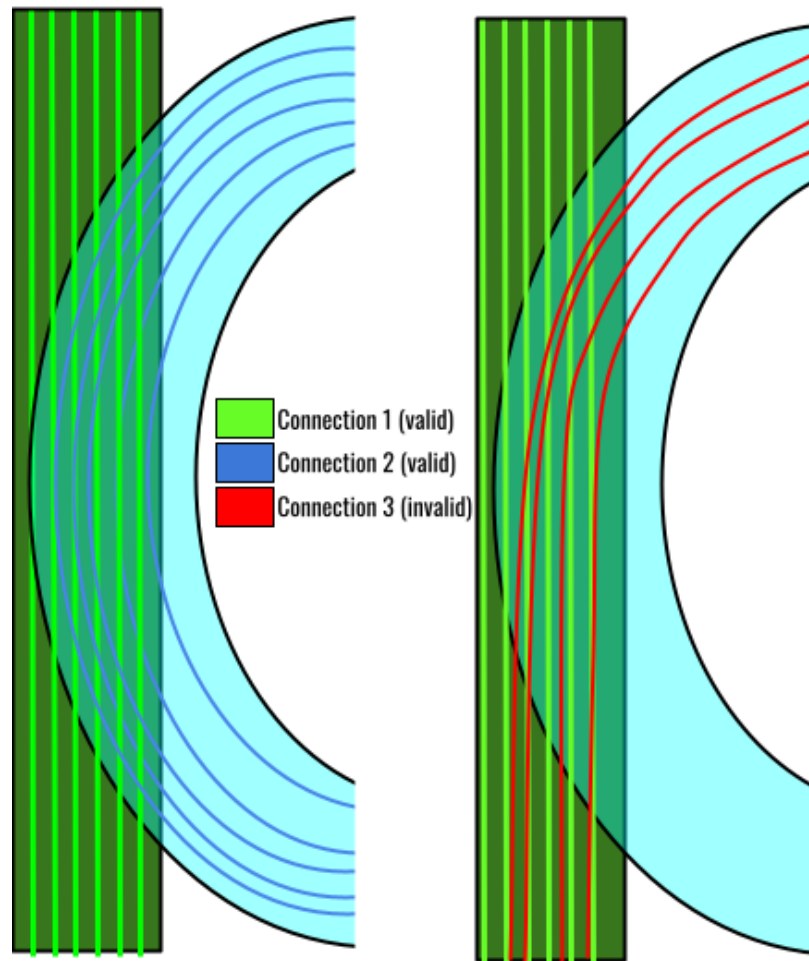


Figure 1.22 – Toy example depicting the narrow intersection effect: on the left is reported the ground-truth configuration with two bundles merging and splitting in a kissing-like configuration. On the right is shown invalid streamlines taking the wrong path in proximity of the crossing region.

algorithms (Jeurissen et al., 2019; Wassermann et al., 2016). The major drawback in this approach is that increasing the number of streamlines leads to a larger number of false positive, resulting in an intrinsic trade-off between sensitivity, i.e. capability of reconstructing real WM bundles, and specificity, i.e. retrieving only true connections (see Figure 1.24).

Advanced filtering methods are able to remove some false positives by exploiting voxel-wise information on fiber orientation distribution, as in SIFT (Smith et al.,

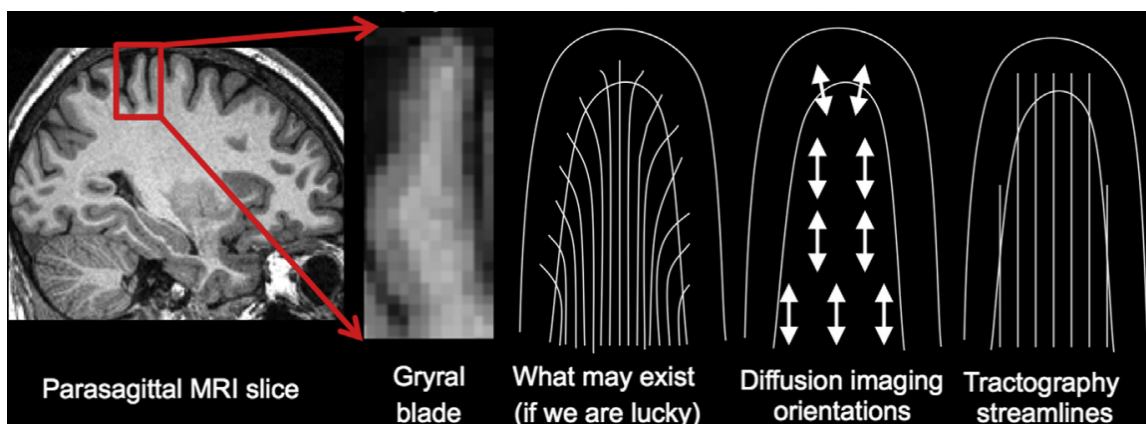


Figure 1.23 – Example of gyral bias showing the effects of local orientation estimation from low-resolution [dMRI](#) data on streamline tracking of a gyral blade ([Van Essen et al., 2014](#)).

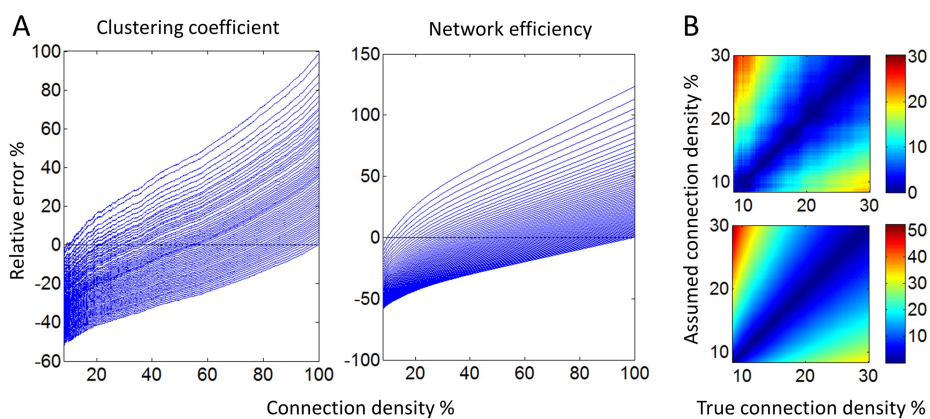


Figure 1.24 – Relative error in the estimation of the clustering coefficient and network efficiency in the human connectome when false positive and false negative connections were added based on the order of streamline counts ([Zalesky et al., 2016](#)).

2013), [SIFT2](#) ([Smith et al., 2015a](#)), or microstructure properties, as in [LiFE](#) ([Pestilli et al., 2014](#)), [COMMIT](#) ([Daducci et al., 2015](#)), [COMMIT2](#) ([Schiavi et al., 2020a](#)) and [COMMIT2_{tree}](#) ([Ocampo-Pineda et al., 2021a](#)), however, the accuracy of the reconstructions is *indissolubly bound to the quality of the input tractogram*. In fact, they assume a static configuration of streamlines throughout the filtering process, whose position and shape is assumed to be correctly estimated by the tractography

algorithm.

The reconstruction of specific bundles can be performed more efficiently using a ROI-based or bundle-specific strategy. The first implementations of this approach implied the use of seeding masks and the tuning of tracking parameters to specifically reconstruct bundles of interest, as in [Basser et al. \(2000\)](#), [Catani et al. \(2002\)](#) and [Behrens et al. \(2007\)](#). Similar approach was used by [Chamberland et al. \(2014\)](#), who were able to improve the output of a tracking method on specific regions by iteratively tuning the tracking parameters. Although ROI-based tractography is more efficient, it does not ensure adequate volume coverage, mainly due to the limitations of the tracking algorithms.

Recently proposed approaches enhance bundle reconstruction by injecting anatomical priors to better guide the recovery of fascicles across hard-to-track regions ([Wasserthal et Neher, 2018](#); [Wasserthal et al., 2019](#)), showing the benefits of using prior information to drive the tracing ([Schilling et al., 2020](#)). [Rheault et al. \(2019\)](#) built a bundle template to scale the FOD, which is then employed to extract streamlines connecting specific regions using a multi-parametric approach. The same bundle-wise approach was explored by [Poulin et al. \(2018\)](#) who used a deep recurrent neural network to learn bundle-specific directional priors.

Although being effective to recover specific tracts, using the same strategy for whole-brain reconstructions is, currently, unfeasible. For such reasons, global tracking algorithms represent a promising strategy which allows exploiting microstructural information and straightforward injection of anatomical priors, but the high demand in computational time is still a hard burden for real-world clinical applications([Jeurissen et al., 2019](#)).

Part I

Methodological contributions

In this part are presented the steps followed to develop a framework able to exploit both microstructural information and anatomical priors to overcome global tractography limitations. This has been achieved by exploring different strategies, from a semi-global graph-based method to a global reconstruction approach. In the last section a [MCMC](#) Bayesian approach is introduced to improve estimation of parameters relating microstructural features.

Chapter 2

Microstructure-informed geodesic tracking

Shortest path tractography, e.g. (Iturria-Medina et al., 2007; Jbabdi et al., 2008; Parker et al., 2002), addresses the reconstruction from a different perspective with respect to local tracking methods: streamlines are reconstructed by seeking for paths of least hindrance to diffusion that connects two regions, defined as the shortest path with respect to a given metric. This yields a good compromise between accuracy and efficiency. For instance, in (Zalesky, 2008), voxels are set as nodes of a graph which are connected to their immediate spatial neighbours by edges. Their weights represent probabilities of transition that are based on the coherence between the corresponding ODFs estimated from DW-MRI. Reconstructing streamlines that connect different brain regions can then be seen as finding the shortest path between the corresponding nodes.

This is an attractive approach for two reasons: (i) it is very efficient as optimized graph search algorithms exist and (ii) the possibility to define ad-hoc metrics makes this formulation flexible and allows for adding additional information into the tracking process. Nonetheless, a major drawback of these approaches is that many reconstructed streamlines tend to be collapsed and to share part of their path, especially in regions with highly curved fiber bundles. This can introduce voxels with incorrectly high or low streamline density, which does not correspond to the underlying fiber geometry (Bastiani et al., 2012).

In this article, we present an iterative procedure that uses microstructure information to provide feedback to the tractography algorithm about the plausibility of the reconstructed streamlines with the aim of mitigating the main limitation of graph-based tractography approaches. In the following sections, we first describe the details of the algorithm and then report results based on numerical simulations to highlight the potential of the proposed method.

2.1 Methods

Our proposed method uses an iterative procedure that alternates between graph-based tractography and evaluation of the plausibility of the reconstructed streamlines. The procedure is illustrated in Figure 2.1. An initial estimate of the graph is constructed from the DW-MRI signal by capturing the structural coherence between neighbouring voxels. Then, the algorithm loops over the following steps:

- **STEP1**: graph-based streamline tractography ;
- **STEP2**: evaluation of the tractogram plausibility;
- **STEP3**: graph’s weights update to improve the evaluation.

This loop is stopped when the root mean square error (RMSE) between the reference streamline density (computed from the DW-MRI data) and the one computed by COMMIT Daducci et al. (2015) reaches a plateau. In other words, it stops when new iterations would not add streamlines that improve the WM volume coverage.

We use DSI-studio¹ to compute the ODFs from the DW-MRI signal. The ODFs are then used to compute the graph’s transition probabilities with the MITTENS software (Cieslak et al., 2018).

2.1.1 STEP1: graph-based streamline tractography

In the graph, WM voxels are represented by nodes that are connected to their immediate spatial neighbours through weighted edges. These weights are based on estimates that the WM structure continues from one voxel into its neighbour. The probability that a voxel is connected to any other voxel is defined as the product of

1. <http://dsi-studio.labsolver.org>

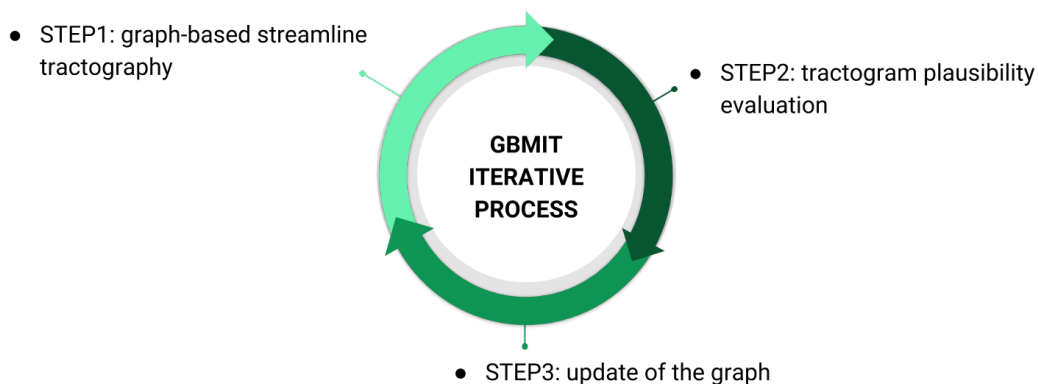


Figure 2.1 – A schematic illustration of the proposed iterative procedure to provide feedback to the tracking algorithm about the plausibility of the current reconstructed streamlines.

the negative logarithm of transition probabilities along the shortest path connecting these two voxels (Zalesky, 2008). This can be computed efficiently using Dijkstra’s algorithm (Dijkstra, 1959), which is implemented in the MITTENS software (Cieslak et al., 2018). The streamlines are constructed as the sequences of nodes corresponding to shortest paths between ROIs. This is made by running Dijkstra’s algorithm (Dijkstra, 1959), iterating over each node from a ROI and looking for the shortest path that connects it with any node of the other ROIs.

We then apply a smoothing function based on splines to preserve the fibers smoothness anatomical prior. To do that we divided each streamline based on the same number of points and then performs an interpolation using a user-defined percentage of them. In this study we interpolate the streamlines using 25% of the points.

2.1.2 STEP2: evaluation of the tractogram plausibility

After reconstructing the streamlines with **STEP1**, the plausibility of the tractogram is evaluated using the **COMMIT** framework (Daducci et al., 2015). In a nutshell, **COMMIT** expresses tractography and tissue microstructure in a unified framework using convex optimization. Given a tractogram \mathcal{F} , the acquired DW-MRI image $\mathbf{I} \in \mathbb{R}_+^{N_x \times N_y \times N_z \times N_d}$, composed of N_d measurements over $N_v = N_x N_y N_z$ voxels, can be modelled as $\mathbf{I} = \mathcal{A}(\mathcal{F}) + \eta$, where $\mathcal{A} : \mathcal{F} \rightarrow \mathbf{I}$ is an operator modelling the

signal contribution of each fiber to every voxel and η is the noise. Notably, if the trajectories and compartment signal patterns are known a priori, \mathcal{A} can be efficiently implemented as a linear operator. The signal in each voxel can be seen as a linear combination of the diffusion arising from the streamlines intersecting the voxel, in addition to local contributions from other tissues; then, the *joint problem* can be expressed as a system of linear equations:

$$\mathbf{y} = \mathbf{A}\mathbf{x} + \eta, \quad (2.1)$$

where $\mathbf{y} \in \mathbb{R}_+^{N_d N_v}$ contains the measured data and $\mathbf{A} \in \mathbb{R}^{N_d N_v \times N_c}$ is the linear operator implementing a generic multi-compartment model for the contribution of the tracts to the signal in each voxel. These contributions $\mathbf{x} \in \mathbb{R}_+^{N_c}$ can be estimated by solving a non-negative least-squares problem:

$$\operatorname{argmin} \|\mathbf{A}\mathbf{x} - \mathbf{y}\|_2^2 \quad \text{such that} \quad \mathbf{x} \geq 0. \quad (2.2)$$

In our case, we used a simple model which accounts for only the restricted (intra-axonal) water pool as represented by the streamlines, and can adequately provide the relative density distribution map and the [RMSE](#) needed for the stopping criterion. The set of streamlines is then filtered according to the weights given by [COMMIT](#), discarding the ones with null contribution to the signal. This is based on the assumption that either a streamline contributes notably to the signal explanation or the following iterations will add more streamlines that will reduce the contributions of the previous ones.

2.1.3 STEP3: graph's weights update to improve the evaluation

The third step is to update the graph using the voxel-wise fitting error. In particular, we focus on the streamlines density distribution of the set of candidate fibers in relation with the reference streamlines density obtained by processing the [DW-MRI](#) data. The graph is modified to improve the density coverage of the [WM](#) structure, promoting or penalizing paths passing through voxels with a streamlines density dif-

ferent from the reference one. In the proposed framework, we iterate over all the edges of the graph, updating their weights using the dissimilarity between the corresponding voxels streamline density and the ones of the reference density. For each edge, the updating function takes as input the original weight (computed based on the [ODFs](#) and geometric constraints) and the average between the differences in streamlines density of the nodes at its ends, and it assigns a new weight. The aim of this new value is to promote or penalize the passing of the streamlines through that specific voxel. This is emphasized using the parameter γ (see [Algorithm 1](#)). Moreover, the value of γ influences the streamline-tracking and the [RMSE](#) rate of decrease which determines the method’s rate of convergence.

To summarize, if we let G be the voxel-graph built starting from the diffusion data, $density_map$ the density map computed by [COMMIT](#) from the set of streamlines retrieved, $GT_density_map$ the reference phantom density map, $ROIs$ the regions among which we want to estimate the streamlines, E the set of edges $E = e_1, e_2, \dots, e_n$ of the graph G , W the set of the corresponding weights $W = w_{e_1}, w_{e_2}, \dots, w_{e_n}$, $Nodes$ the set of nodes and W' the set of weights of the updated graph \tilde{G} , the update-function has been implemented as described in [Algorithm 1](#).

To ensure that the reconstructed streamlines are consistent with the underlying anatomy, we always update the weights of the initial graph, whose edges encode the coherence between neighbouring voxels.

2.1.4 Testing dataset

To evaluate quantitatively our algorithm we used the simulated dataset that prepared for the IEEE International Symposium on Biomedical Imaging ([ISBI](#)) 2013 Reconstruction Challenge ([Caruyer et al., 2014](#)). The phantom consists of 27 known ground-truth fiber bundles, mimicking challenging branching, kissing, crossing structures at angles between 30° and 90° , with various bundle curvature and size (see [Figure 2.2a](#)). The normalized streamlines density of the ground truth is shown in [Figure 2.2b](#), and was obtained computing the number of bundles passing through each voxel and dividing the resulting image by the maximum value.

Algorithm 1 Procedure to update the weights of the graph's edges using microstructure information.

Input: $(G, GT_density_map, density_map)$

Result: $\bar{G} : W \times W \mid (density_map - GT_density_map)$

foreach $n \in Nodes$ **do**

$node_density = density_map[n]$

$GT_n_density = GT_density_map[n]$

$n_density_diff = node_density - GT_n_density$

foreach *neighbour* of n **do**

$average_node_density = (n_density_diff + neighbour_density_diff) \cdot \frac{1}{2}$

$scalar_factor = w_n(n, neighbour) + average_node_density$

if $node_density == GT_n_density$ **then**

 | continue

end

if $node_density > GT_n_density$ **then**

 | $w_n(n, neighbour) = scalar_factor + scalar_factor \cdot \gamma$

else

 | $w_n(n, neighbour) = scalar_factor + scalar_factor \cdot \frac{1}{\gamma}$

end

end

end

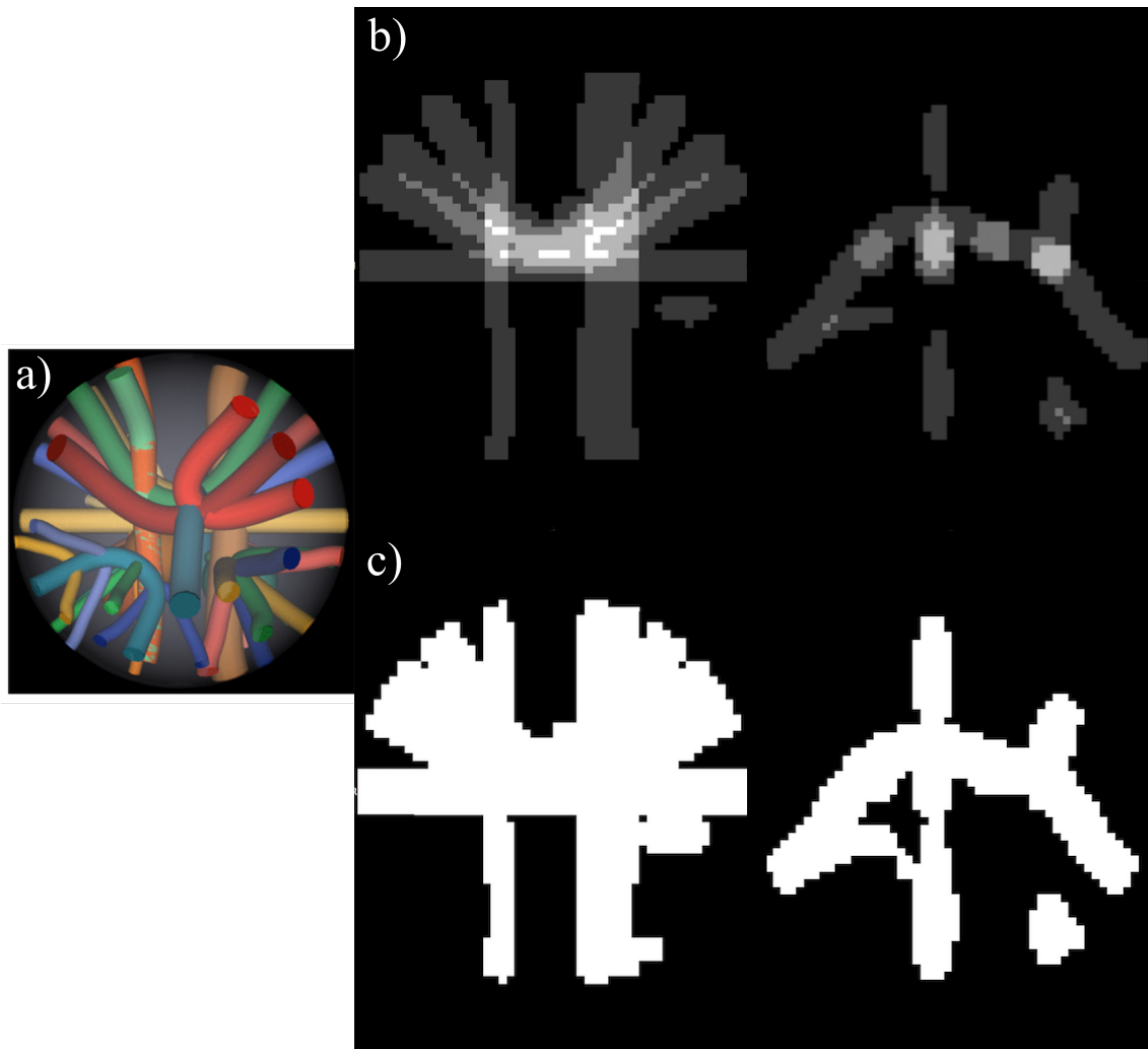


Figure 2.2 – Simulated dataset used for validation: (a) 3D view of the bundles geometry, (b) corresponding normalized streamline density, (c) mask used for tractography.

2.2 Results and discussion

Figure 2.3 shows that the spatial distribution of the streamlines reconstructed with our method is in closer agreement with the underlying ground truth streamline density. The process of flattening the density corresponding to bottlenecks created by the original shortest path algorithm implies that the streamlines do not follow

necessarily the most direct trajectory but the one which, after the graph update step, has the lowest sum of the edge weights along the path that connects the two regions, reflecting the reference WM pathways distribution.

In the first column of Figure 2.3, we can notice how some of the reconstructed streamlines are characterized by local changes of direction. This might be due to a fixed γ value for all nodes when updating the edge weights. This implies that in some cases we are promoting or penalizing excessively the passage through a node, causing local direction changes in streamlines. These erroneous streamlines can be discarded with the COMMIT evaluation. However, the use of the streamline density in the evaluation limits the filtering of all erroneous streamlines. In future work, we plan to use the full DW-MRI signal in our framework to update the edge weights, not solely optimizing for streamline density but also local streamline orientations.

The decrease in the absolute error of the streamline density shown in the third column Figure 2.3 corresponds to a more uniform coverage of the WM volume obtained by the streamlines reconstructed with our proposed approach. We can notice how our algorithm is able to retrieve paths that were poorly reconstructed without the microstructure information while flattening the overall density (see the red arrows).

As all the streamline-tracking methods, graph-based shortest path tractography presents limitations. In this article, we introduced a method to overcome the problem of bottlenecks and consequent incorrect streamline density. This is possible with the graph data structure that allows an easy integration of local microstructure properties estimation. This guides the algorithm to provide a more realistic WM density representation.

Although we presented a method to alleviate geodesic tractography limitations, semi-global methods are still intrinsically constrained by their ROI-based approach. In the next chapter we introduce a global adaptive method overcoming these restrictions.

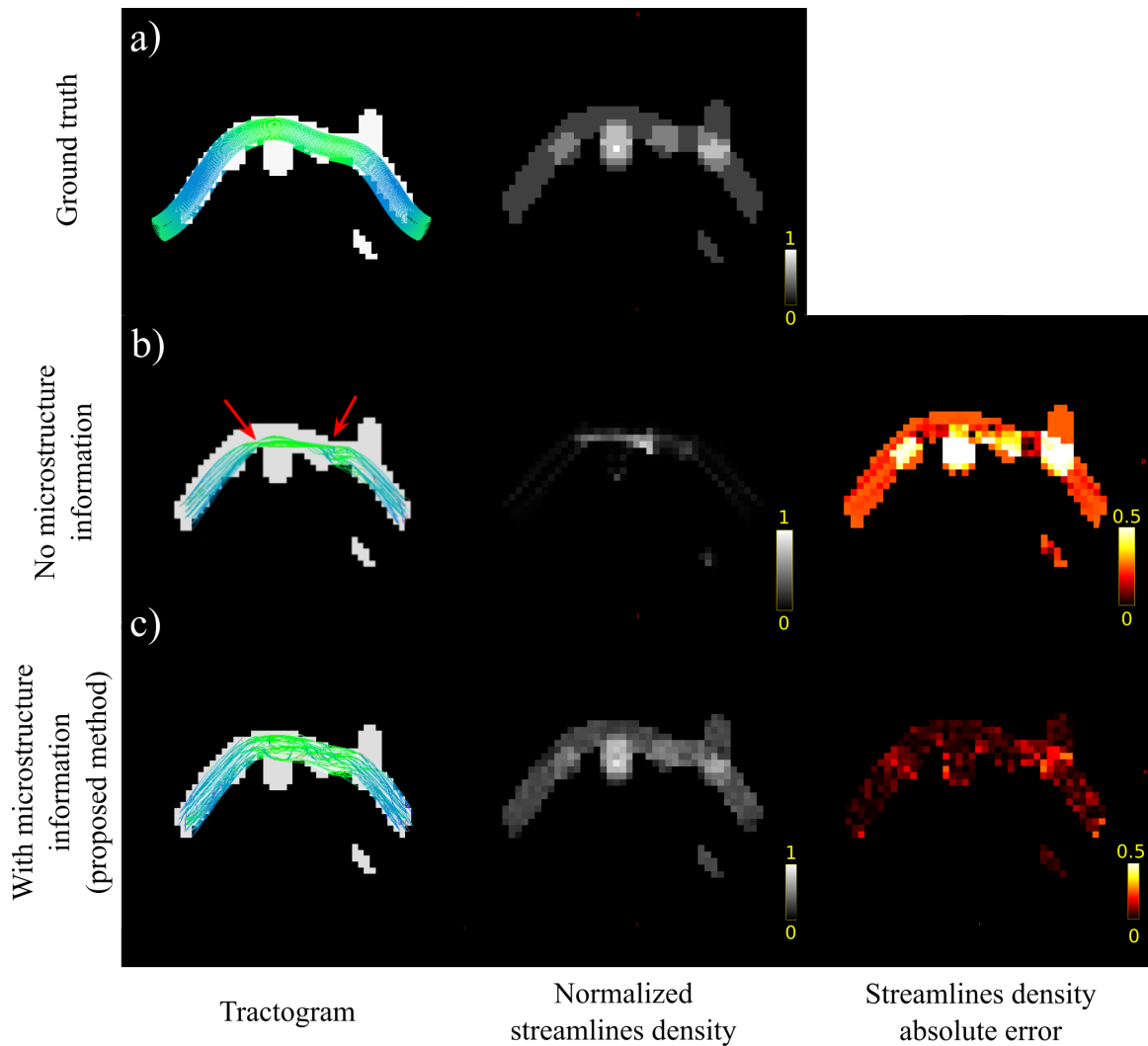


Figure 2.3 – Comparison between: a) ground truth, b) shortest path tractography without microstructure information and c) our proposed method.

Chapter 3

From static to dynamic tracking

In this work we moved from a semi-global to a global approach for tractography reconstructions. Indeed, even if we were able to mitigate the limitations of shortest path methods, this class of methods cannot be used for exploratory studies, given their “ROI-based” nature.

Global discriminative approaches have shown very promising results ([Schiavi et al., 2020a](#); [Smith et al., 2015b](#)) but, unlike generative methods, they assume a static configuration of streamlines throughout the filtering process, whose position and shape is assumed to be correctly estimated by the tractography algorithm.

We propose an *hybrid procedure* with the aim of exploiting the advantages of both filtering and [MCMC](#)-based approaches. Starting from an initial set of streamlines estimated with classical tractography, our method can adapt the configuration of streamlines by alternating the filtering to short runs of classical [MCMC](#)-based techniques. In this work, in particular, we present results obtained using the COMMIT framework.

Our experiments clearly indicate that the possibility to dynamically adapt the spatial configuration of the streamlines during the filtering allows overcoming the limitations due to a static input and further improves the reconstructions. The presented method promotes higher spatial coverage and lower number of invalid bundles while not affecting the valid ones, showing great potential for microstructure-informed filtering and tractography techniques.

3.1 Methods

The proposed method is inspired by the work of Lemkaddem (Lemkaddem et al., 2014) and can be divided in *three main steps* (see flowchart in Figure 3.1):

1. Construction of the initial set of streamlines using tractography. This tractogram is, first, pre-filtered to remove streamlines prematurely stopping inside the WM and, then, randomly divided into two groups: the first group, called M , is the initial set of streamlines to optimize and the other one, called A , is an auxiliary set used as support in the following phase.
2. Parameterization of the streamlines using splines, in order to drastically reduce the complexity for their representation as well as to guarantee smoothness of their trajectories.
3. Alteration and evaluation of the streamline configuration following an MCMC-based optimization approach.

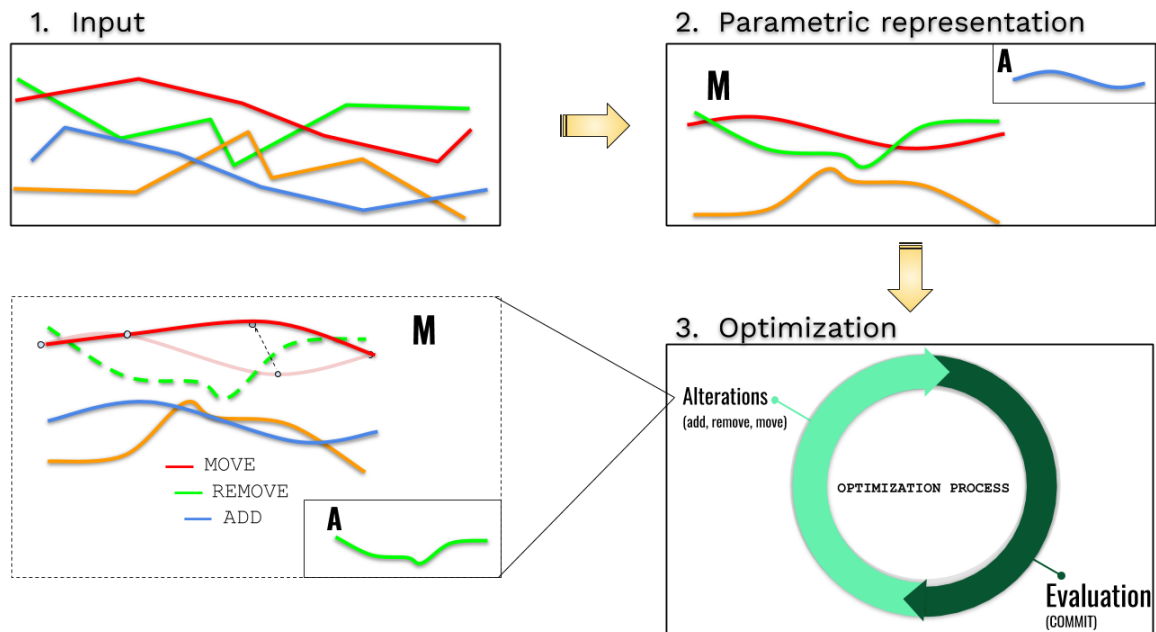


Figure 3.1 – Schematic representation of the 3 main steps of the proposed approach.

3.1.1 Initial set of streamlines

The input tractogram for the proposed approach can be reconstructed with any arbitrary tracking technique. In this work, I've used local deterministic SD_STREAM tracking, implemented in the MRtrix3 toolbox (Tournier et al., 2012). As mentioned above, the first operation is the removal of streamlines that do not reach any cortical and/or subcortical structures. Practically, this is done using labeled ROIs.

3.1.2 Parametric representation of the streamlines

Global generative algorithms have introduced different parameterization approaches. The most famous comprehend the adoption of small segments covering the whole white matter volume, as in (Reisert et al., 2014, 2011), or the use of spin glass model as in (Fillard et al., 2009). These approaches, however, need a large number of parameters and fine tuning to drive the spatial optimization. Among the different parameterizations that have been proposed, B-splines has proven to be a valuable alternative and they have been exploited in different ways, starting from Jbabdi et al. (2007) until the more recent approach of Lemkaddem et al. (2014).

We recall that a B-spline of degree d is a piece-wise concatenation of polynomial curves joining in correspondence of $n + 1$ control points, called knots, $\{\mathbf{Q}_i\}_{i=0}^n$ as follow:

$$X(t) = \sum_{i=0}^n N_{i,d}(t) \mathbf{Q}_i \quad (3.1)$$

where $N_{i,d}(t)$ are B-spline basis functions computed recursively using a sequence of scalars t_i along the curve such that:

$$N_{i,n}(t) = \begin{cases} 0 & \text{if } t \leq t_i \text{ or } t \geq t_{i+n} \\ \neq 0 & \text{otherwise} \end{cases} . \quad (3.2)$$

One of the main advantages of this formulation is the possibility to *reduce the number of points* needed to represent the original input set of streamlines. Indeed, instead of using all the original points, the streamlines can be represented by setting an a-priori number of knots (equal for all the streamlines) and using Eq. 3.1 to

uniquely determine each curve. To compute the sequence of knots for each streamline, Douglas-Peucker reduction algorithm (H et K, 1973) has been employed, which minimizes the number of knots needed to represent the curve. In particular, this minimization is efficiently performed by recursively checking that the distance between the original curve and the simplified one is below a certain imposed threshold defined as “smoothing error”. Among the variety of different spline functions, I chose to adopt cubic B-splines, named Catmull-Rom (Catmull et Rom, 1974). This class of splines is characterized by the fact that the knots are a subset of the points composing the original streamline and, in particular, the first and the last knots coincide with the first and last point of the streamline. The fact that the control points are chosen along the streamline, combined with the use of cubic polynomial curves for the interpolation, ensures that the corresponding spline has a similar shape of the original streamline. This, in turn, permits to discard curves that lie outside the WM or that do not connect GM regions. Besides being easy to handle, the Catmull-Rom’s splines presents also other convenient characteristics: they are able to approximate a large variety of smooth trajectories, making them particularly suitable to represent anatomically plausible WM pathways (see Figure 3.2 and, at the same time, they are fast to compute.

Adapting shape and position of streamlines.

Three different proposals have been implemented to alter the configuration of streamlines:

1. Move streamline’s control points
2. Add a streamline to the set M from the set A
3. Remove a streamline from the set M and add it to A

With the first proposal a streamline is randomly chosen from the set M and its trajectory is altered. This is performed in two possible ways: either by moving one control point or by translating the whole streamline (i.e. simultaneously translate all the control points). In the first case, to find the new spatial position of the control point, the new coordinates are sampled from a Gaussian distribution centered around the original position of that point. To reduce the degrees of freedom of this step, the

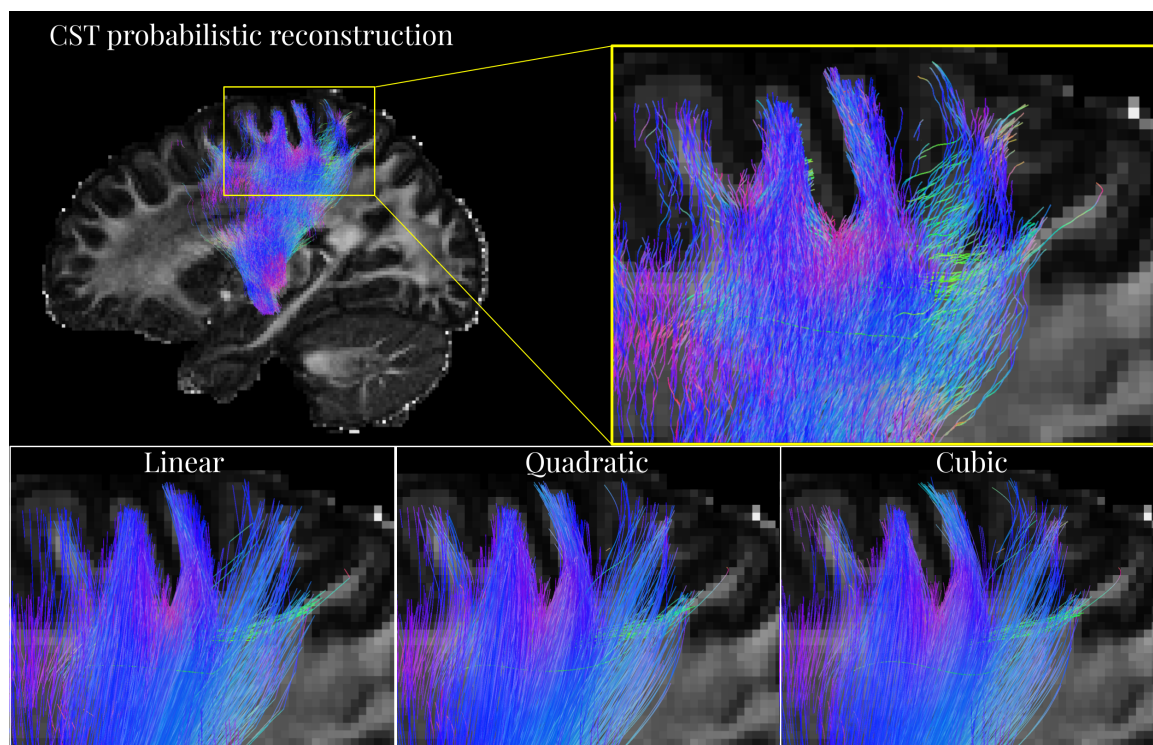


Figure 3.2 – Visual comparison of the interpolation using linear, quadratic and cubic splines for the reconstruction of the Corticospinal tract (CST).

magnitude of the movement has been fixed to half of the voxel dimension and, at the same time, limited to the surface perpendicular to the direction the streamline as shown in Figure 3.3.

The second proposal consists in randomly choosing a streamline from the auxiliary set A and append it to M . Vice versa, the third proposal removes a random streamline from M and add it to A .

3.1.3 Optimization

The optimization step is driven by a Bayesian approach which allows to exploit global information to guide the streamlines adaptation. Given the observed data d and a set of competing models for the data $\{M_i | i = 1, 2, 3, \dots\}$, each defined by a set of parameters θ^i , we can compute the posterior probability distribution function (PDF) following the Bayes' theorem:

$$p(M_i|d) = \frac{p(d|M_i)p(M_i)}{p(d)}, \quad (3.3)$$

where $p(d|M_i)$ represents the likelihood of observing the experimental data given the model M_i , $p(M_i)$ is the prior probability of the model parameters and $p(d)$ is a normalizing constant.

Given a pre-computed set of streamlines the idea is to adapt their shape and trajectory to better represent the underlying neural pathways structure.

In this context, M_i represents the parametric representation of a set of streamlines defined by θ^i control points coordinates in the 3D space, and $p(d|M_i)$ scores how well the configuration M_i explain the measured diffusion data d .

The probability of a given configuration is defined by the following distribution:

$$f_T(M) = \exp\left(-\frac{E_D(M, d)}{T}\right) \exp\left(-\frac{E_P(M)}{T}\right), \quad (3.4)$$

where, according to 3.3, f_T represents the non-normalized joint distribution

$$p(d|M_i)p(M_i) \propto p(M_i|d), \quad (3.5)$$

at the system temperature T . The first term, $e^{-\frac{E_D(M, d)}{T}}$, defines the likelihood function, while the second is independent from the measure data and defines the prior probability. The likelihood function scores how well a specific configuration M explains the data observed, and it can be defined as the difference between the measured and the simulated signal as follow:

$$E_D(M, d) = \sqrt{\left(\frac{1}{V}\right) \sum_{v=1}^V (S_v - d_v)^2}, \quad (3.6)$$

where V is the number of voxels in the WM volume.

In our case, the signal S_v for each voxel v , of the white matter (WM) volume is simulated as follow:

$$S_v = \sum_{i=1}^N x_i L_i, \quad (3.7)$$

where N is the number of streamlines passing through voxel v , x_i is a unique weight, assigned to streamline i , that is used to scale the contribution of all its segments and L_i is the segment length inside v .

Our prior knowledge is represented by $E_P(M)$ as follow:

$$E_P(M) = |M|, \quad (3.8)$$

where $|M|$ represents the number of streamlines in the configuration M . To maximize the posterior probability we adopted a [MCMC](#) Metropolis-Hastings-Green ([Green, 1995](#); [Hastings, 1970](#); [Metropolis et al., 1953](#)) sampling approach and Simulated Annealing ([Perrin et al., 2005](#)) optimization to explore the space of parameters.

Given the current configuration M_i , a new configuration M_{i+1} is accepted with probability:

$$p_{\text{accept}} = \min(1, R) \quad (3.9)$$

where R is the Green's ratio

$$R = \frac{f_T(M_{i+1}) p(M_i|M_{i+1}) q(M_{i+1})}{f_T(M_i) p(M_{i+1}|M_i) q(M_i)}, \quad (3.10)$$

with p describing the probability density functions associated to the proposal to move from configuration M_i to configuration M_{i+1} , and q is the probability to choose one among the three proposals introduced in the previous section:

1. add or remove streamline
2. move one control point
3. move entire streamline

Regarding the first proposal, a new streamline is added to the configuration by drawing randomly and uniformly from a set A of pre-computed streamlines, i.e. the associated probability density takes the form $p(M_{i+1}|M_i) = |A|^{-1}$ where $|A|$ is the number of streamlines in A . On the other way, the removal of a streamline from the configuration is equal to the probability of picking a streamline randomly and uniformly from the current configuration M_i , meaning $p(M_i|M_{i+1}) = |M_i|^{-1}$. The corresponding Green's ratio becomes:

$$R = \frac{f_T(M_{i+1}) |M_i|^{-1} q_r}{f_T(M_i) |A|^{-1} q_a}, \quad (3.11)$$

where q_r and q_a are, respectively, the probabilities for choosing the *Remove* and the *Add* transitions.

While, for the first proposal, the probability density functions are asymmetric, meaning that $p(M_i|M_{i+1}) \neq p(M_{i+1}|M_i)$ for the other proposals we adopt a gaussian distribution as probability density functions, usually defined as random walk sampling step.

Given these symmetric proposals, the acceptance probability becomes proportional to how likely each of the current state M_i and the proposed state M_{i+1} are under the full joint density. Hence, the Green's ratio for these proposals is given by:

$$R = \frac{f_T(M_{i+1})}{f_T(M_i)}. \quad (3.12)$$

Based on the simulated annealing approach, at the beginning, the system is characterized by a high temperature (T), which decreases as the process advances. High values of T imply that “bad” configurations are accepted, allowing the system to explore a wider range of configurations. In previous works, it has been shown how a geometric lowering schedule of the temperature ensures the convergence (Lieshout, 1994) and, at the same time, improves the chances to sample from maxima of $P(M|D)$. Starting from a model M , the space of its parameters is explored by altering the configuration.

3.2 Results and discussion

Data

To show the effectiveness of the method, I've tested its performances on two different synthetic configurations created with Phantomas¹, an open source software that allows manually defining 3D geometries of fiber bundles as well as generating the corresponding DW-MRI signal. In both cases, I've simulated an acquisition protocol with 64 directions at b -value = 3000 s/mm², 1 mm isotropic voxel and signal-to-noise ratio of 30.

1. <http://www.emmanuelcaruyer.com/phantomas.php>

Dataset 1. As a proof of concept, I've created a simple configuration consisting of a single straight bundle without noise. The input tractogram was composed by 10000 streamlines, keeping only those covering the superior part of the WM volume (see Figure 3.4 left).

Dataset 2. I've then assessed the performance on a more challenging bundle configuration represented by the dataset provided for the IEEE ISBI 2013 Reconstruction Challenge. This dataset consists of 27 bundles arranged in a configuration mimicking the majority of the troublesome scenarios that can be found in the brain. These include branching, kissing, crossing structures with various diameters and at different angles. From the signal reconstruction point of view, the phantom reproduces both partial volume effects, given by the presence of multiple fiber compartments within the same voxel and CSF contamination. As for the previous dataset, the input tractogram was reconstructed using SD_STREAM with standard parameters, discarding streamlines shorter than 5 mm. To quantitatively evaluate the performances of the method on this phantom, I carried out also the connectivity analysis, comparing the configurations against the known ground-truth (GT); in particular, the number of valid bundles (VBs), i.e., bundles connecting regions known to be connected has been assessed, as well as the invalid bundles (IBs), i.e., those connecting regions known to be disconnected. I also report the WM volume coverage based on the valid streamlines for each input tractogram and the associated RMSE.

Results

The single bundle configuration allows to highlight the potential of the method in adapting the position of the streamlines in order to better cover the WM volume. Starting from a set of streamlines covering only the superior part of the created phantom (see Figure 3.4 left), COMMIT finds the contributions for each one, discarding some of the redundant that are not necessary to explain the diffusion signal. However, this does not improve the RMSE because the streamline spatial configuration remains fixed, which, in this case, implies that the bundle remains under-represented, as shown by the underlying RMSE map. The result of the optimization performed by the method is reported in Figure 3.4 right. The output set of streamlines has been moved and adapted to better cover the entire volume of the bundle which, in turn,

decreases the differences between the observed and the reconstructed signals shown by the [RMSE](#) map below.

Results of the optimization on the second dataset are reported in [Figure 3.5](#). At the top of the first column, is shown the geometry of the dataset and, at the bottom, the plot of the [RMSE](#) values across the optimization process. The descending trend of the error shows that the streamlines adaptation leads to a configuration that better explain the observed signal. In the second column the [RMSE](#) map of the input configuration filtered by COMMIT and the one computed from the optimized tractogram are compared. In the third column is reported the corresponding configurations, highlighting the impact of the presented approach on the framed vertical bundle in particular. Starting from an underrepresented bundle, the method is able to better distribute the streamlines inside the [WM](#) volume, reducing the difference between the reconstructed and the observed diffusion signal.

[Table 3.1](#) shows the potential of the presented method with respect to connectivity analysis and compared the quality of the input tractogram, after filtering it with [COMMIT](#) and with the presented method. The results show that the method is able to simultaneously reduce the complexity of the entire tractogram while improving the reconstruction quality. In fact, by increasing the quality of the reconstructions, it's also able to better discriminate between valid and invalid connections, consequently promoting the removal of more false positives. Also, besides decreasing the fitting error, the optimized configuration has a better [WM](#) volume coverage, less IBs, stable VBs with 75% less streamlines.

Finally, it is worth to notice that the introduced formulation is completely independent on how the signal reconstruction is performed, meaning that also other state-of-the-art filtering approaches, e.g., [SIFT](#), [SIFT2](#), [LiFE](#) and [COMMIT2](#), may benefit from the proposed hybrid procedure.

Nowadays, the ability of state-of-the-art filtering techniques to improve the accuracy of the tractograms heavily depends on the quality of input tractograms themselves. We showed how the possibility of adjusting the streamlines configuration during the filtering allows improving further the quality of the tractography reconstruction, both from the qualitative and the quantitative point of view.

We believe that this method could support microstructure-informed techniques

Tractograms	VBs	IBs	WM coverage	# streamlines	RMSE
raw	27	94	73.4%	50205	
COMMIT	27	88	72.7%	20366	0.049 ± 0.056
COMMIT + Dynamic Filtering	27	83	92.8%	12444	0.028 ± 0.031

Table 3.1 – Quantitative comparison between the input tractogram (first row), after filtering it with COMMIT (middle) and with the proposed method (bottom row).

by increasing the quality of the reconstruction and helping in the characterization of the brain structural connectivity.

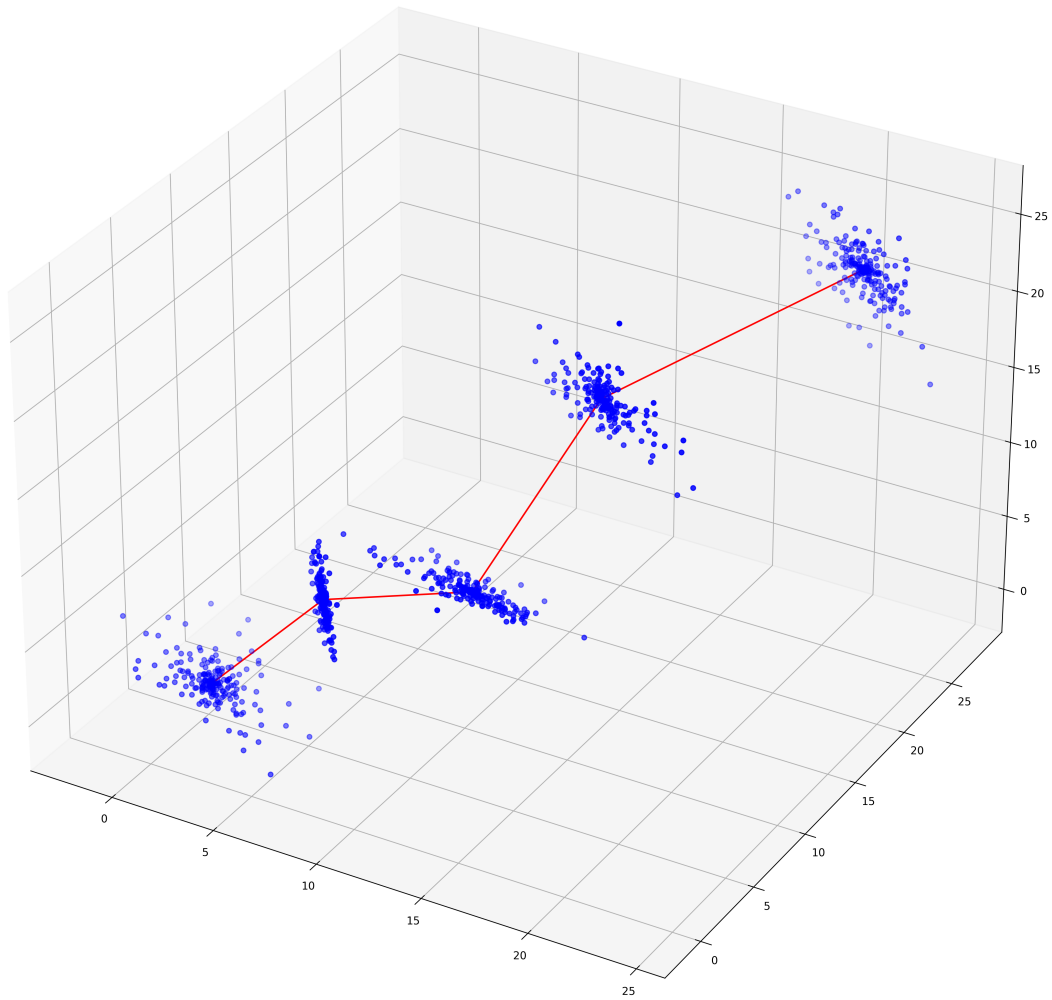


Figure 3.3 – Probability distribution on the plane tangent to the direction of the streamline.

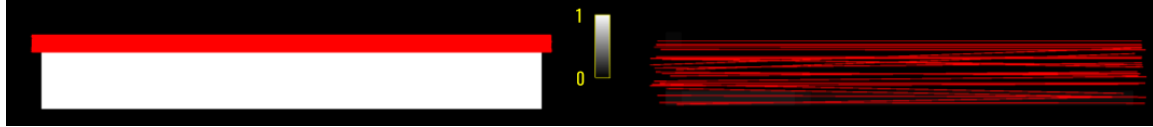


Figure 3.4 – Single bundle dataset: on the left is shown the input tractogram. The tractogram is composed by a set of packed streamlines covering only the superior part of the bundle. The underlying map represents the **RMSE** computed between the corresponding reconstructed diffusion signal and the observed one. On the right is shown the resulting configuration after optimization with our method and the corresponding **RMSE** map.

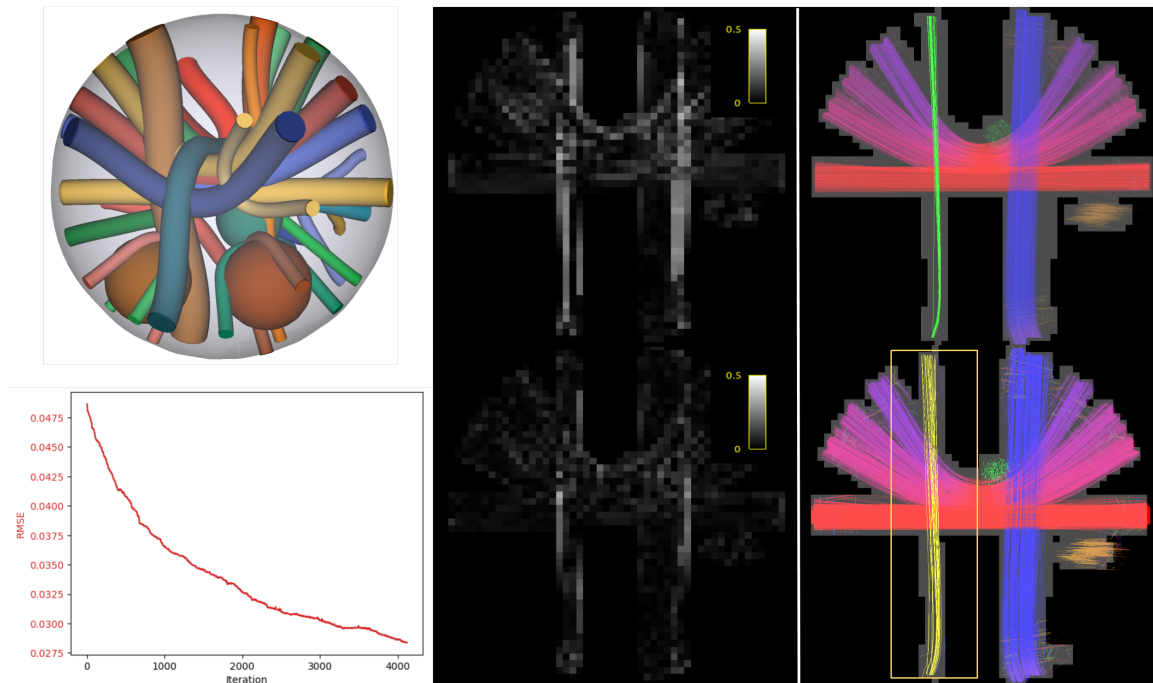


Figure 3.5 – **ISBI** 2013 dataset: at the top of the first column is shown the geometry of the phantom and at the bottom the plot of the **RMSE** values across the optimization process. The second and the third columns shows, respectively the **RMSE** maps and streamline configurations corresponding to the input tractogram filtered by **COMMIT** (top) and to the optimized configuration (bottom).

Chapter 4

Adaptive bundle-based global tractography

Following the work presented in 3.1, we implemented a global reconstruction algorithm, keeping the “hybrid” nature of the previous one (Battocchio et al., 2019) but tackling tractography reconstruction from a different perspective: the idea is to move away from streamline-based tracking with the aim to directly reconstruct bundles of them; for this reason we call it *bundle-o-graphy*. Thanks to a convenient parameterization, we can model groups of coherent streamlines using a minimal set of parameters which, in turn, allows us to extend a state-of-the-art *discriminative* method, i.e. COMMIT (Daducci et al., 2015), with the possibility of *efficiently adapting* the configuration of the bundles as in *generative* approaches. Our experiments conducted both on synthetic and real data clearly indicate the potential of our solution for improving the anatomical accuracy of the reconstructions.

4.1 Methods

The general structure of the algorithm is presented in Fig. 4.1 and the general workflow takes inspiration from our previous work (Battocchio et al., 2021). Bundle-o-graphy takes as input a tractogram that can be computed using any tractography algorithm, or it can be the combination of different reconstructions. As first step, we divide the input tractogram based on a GM parcellation. Each connection is then

clustered to reduce the number of streamlines by keeping only the most representative ones, which are parameterized using splines. As second step, the resulting fibers are used as prior to represent fascicles of coherent streamlines aligned along each pathway, hence introducing the concept of bundle-based representation. The set of bundles constitutes the configuration to optimize using an MCMC iterative approach, that allows to adapt their shape and extent along with the possibility to add and remove entire connections. The configuration is globally evaluated and the process is driven by a Bayesian framework to find the optimal configuration that best explains the observed signal.

In the following, we provide more details about each stage of the algorithm.

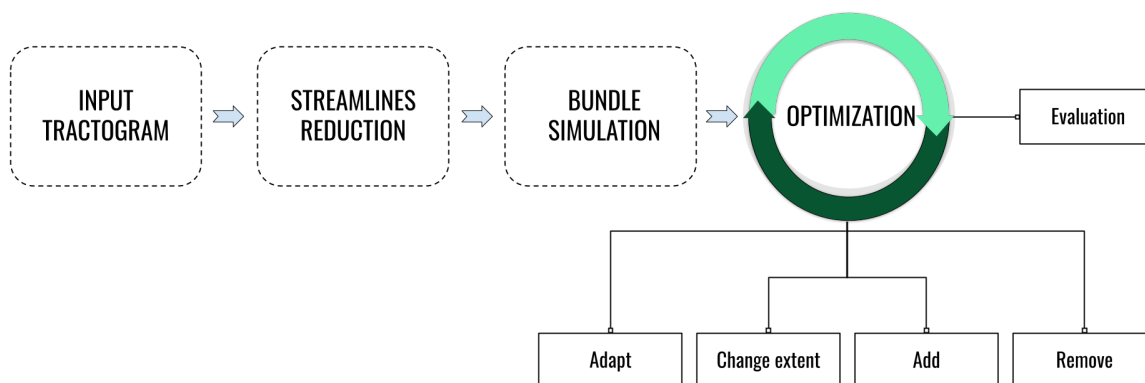


Figure 4.1 – Bundle-o-graphy workflow. Given an input tractogram the first step aims to reduce the number of streamlines needed to represent pathways between pairs of regions. Additionally, each streamline is parameterized using a subset of the initial points to approximate their trajectory. The second step is characterized by the shift from streamline to bundle-based representation. Here a volume is assigned to each streamline, allowing to mimic the contribution of a set of aligned fibers centered around the original trajectory. Finally the bundle-based configuration is optimized by adapting their shape and geometry following a MCMC optimization approach.

4.1.1 Streamline reduction and simplification

Streamline reduction is performed based on hierarchical clustering, following the approach implemented by [Schiavi et al. \(2020a\)](#). We first divide the streamlines with respect to anatomical information, in particular based on the regions they connect

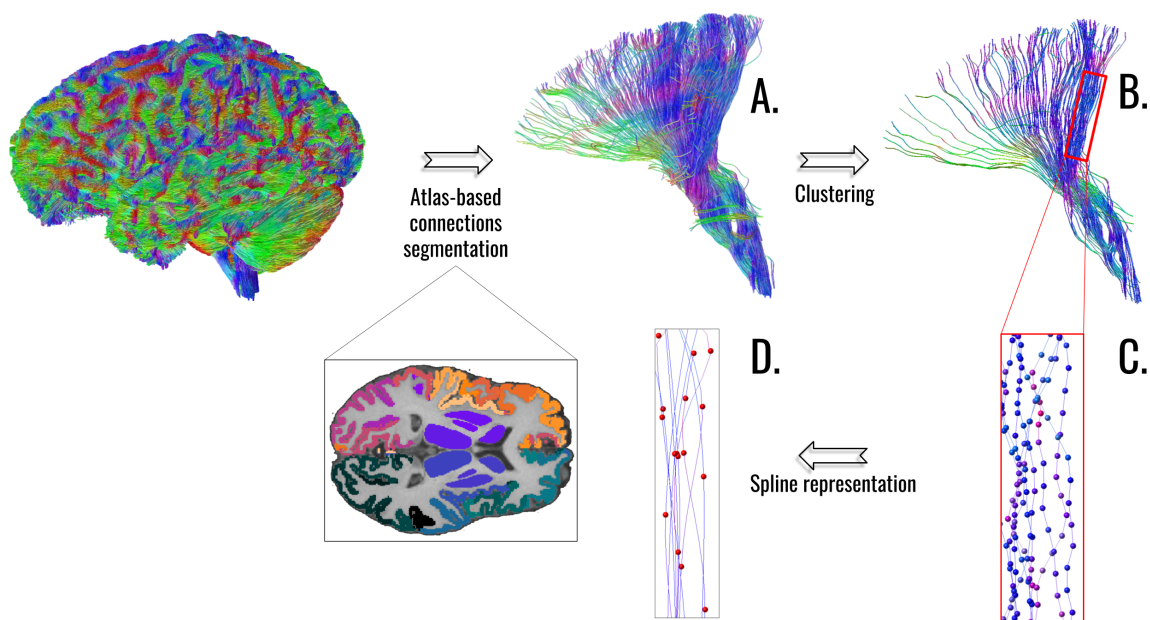


Figure 4.2 – Streamline reduction workflow: the first step implies separating the input tractogram into subsets based on a cortical and subcortical regions segmentation. FAYdogan:2021ig. 4.2A is an example showing a set of projection fibers segmented based on Freesurfer atlas. Each connection is then clustered (Fig. 4.2B) keeping only the representative streamlines for each cluster. These are simplified using Ramer-Douglas-Peucker algorithm (Fig. 4.2C) which reduces the number of points needed to approximate the streamline trajectories. Finally these coordinates are interpolated using cubic b-splines (Fig. 4.2D).

given a cortical and sub-cortical brain parcellation (Fig. 4.2A). Secondly, each group of streamlines is clustered based on geometrical criterion, in our case represented by their average euclidean distance. To this aim, we exploit QuickBundle (Garyfallidis et al., 2012) (Fig. 4.2B) to reduce the number of streamlines needed to represent connections between regions. The clustering threshold can be manually chosen by the user and for our tests, we set it to 3 mm. Thanks to this procedure we can simplify the bundle representation and reduce the tractogram complexity. In particular, by removing unwanted redundancy we are able to downsize the input tractogram using, on average, only the 2% of the initial set of streamlines.

The resulting streamlines are then simplified to minimize the number of parameters needed to represent each trajectory, as in the work of Lemkaddem et al. (2014),

using the Douglas-Peucker reduction algorithm (H et K, 1973), which selects the minimal subset of coordinates given an approximation threshold (Fig. 4.2C). Jbabdi et al. (2007); Lemkaddem et al. (2014) We reduce the number of coordinates to represent each streamline using between 4 and 6 control points, in line with previous works (Jbabdi et al., 2007; Lemkaddem et al., 2014). The set of points is then interpolated using a particular class of cubic B-splines, named Catmull-Rom (Catmull et Rom, 1974) (Fig. 4.2D), characterized by several desirable properties. First of all, they preserve the starting and ending points, i.e. the first and last points remain the original ones, meaning that the original connectivity is preserved giving the fact that the reduced streamlines connect the same regions. Secondly, the interpolated trajectories intersect all the control points, which permits a better supervision of their spatial position and to avoid the reconstruction of pathways outside white matter regions.

4.1.2 Bundle representation

Once the input tractogram has been reduced and simplified, we assign a volume to each streamline by exploiting a feature embedded in COMMIT. In particular, each tract is considered as the centroid of a cylinder, with constant radius, extending along the whole trajectory. Following COMMIT formulation, the signal contribution of a streamline can be computed based on the trajectory, i.e the voxel it traverses, and the response function adopted. To extend the contribution of a streamline to the neighbor voxels we create a set of replicas displaced equidistantly over concentric circles of increasing radius centered around each point of the fiber. These are computed internally, meaning that no further streamlines are added to the configuration. Starting in correspondence of the initial point, all circles lie on a plane that is always orthogonal to the streamline direction. Each point of the replicas is then computed based on Frenet-Serret frames (Frenet, 1852; Serret, 1851) which allows to compute the displacement of the replicas' following points along the streamline trajectory. The circles discretization, i.e., the number of replicas created, and the number of circles used to sample the space are empirically fixed. The signal contribution corresponding to the bundle is computed considering all the voxels traversed by the centroid and its

replicas. While the signal contribution is constant along the trajectory, it can vary as we move outward from the center to take care of uncertainty at the boundaries of the bundle. To do so we implemented a *blurring function*, used to radially scale the signal contribution, shown in Fig. 4.3 and defined as follows:

$$P(x) = \begin{cases} 1 & \text{if } x < \sigma_C, \\ \exp\left(-\frac{(x-\sigma_C)^2}{2\sigma_G^2}\right) & \text{otherwise.} \end{cases} \quad (4.1)$$

Based on Eq. 4.1, the signal contribution of the bundle core, which extent is modulated by the parameter σ_C , is not scaled, while the signal corresponding to the replicas falling farther is exponentially reduced depending on the distance x from the center according to a Gaussian damping function regulated by σ_G . A more detailed description of the bundle creation process can be found in [Daducci et al. \(2021\)](#). Following this implementation, bundle simulation turns into modeling the space of influence of a streamline which requires only the parameter σ_C while σ_G is empirically fixed.

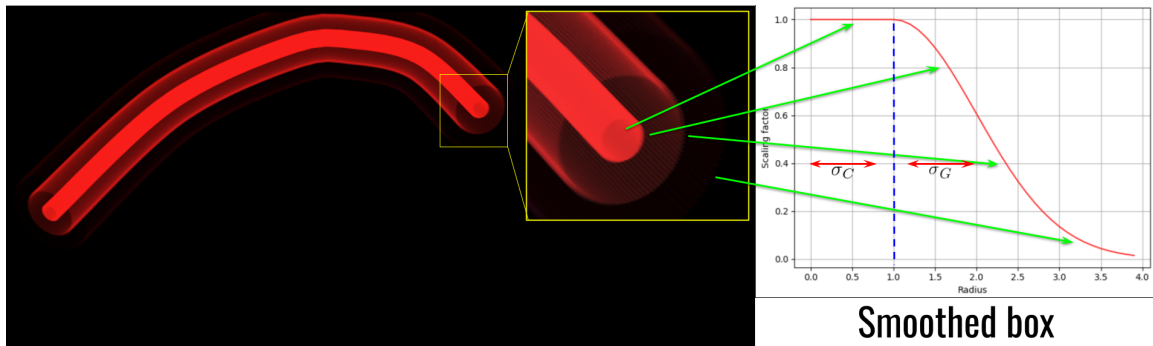


Figure 4.3 – Bundle simulation: the contribution of each original streamline can be modeled as a cylinder centered along the trajectory. The volume can be radially adapted using a blurring function to allow uncertainty as we move outward from the central pathway. The two parameters, σ_C and σ_G regulate the extent of the core and the Gaussian dumping respectively.

4.1.3 Optimization

The resulting set of bundles constitutes the initial configuration to adapt. More specifically, the collection of control points representing each bundle trajectory, along with their corresponding blur extent, controlled by σ_C , represent the parameters to optimize. In particular, the shape and the volume of each bundle is adapted following a generative approach, based on MCMC, which permits to exploit global information to better adapt the reconstruction with respect to the underlying WM structure. Given the observed data d and a set of competing models for the data $\{M_i | i = 1, 2, 3, \dots\}$, each defined by a set of parameters θ^i , we can compute the posterior probability distribution function following the Bayes' theorem:

$$p(M_i|d) = \frac{p(d|M_i)p(M_i)}{p(d)}, \quad (4.2)$$

where $p(d|M_i)$ represents the likelihood of observing the experimental data given the model M_i , $p(M_i)$ is the prior probability of the model parameters and $p(d)$ is a normalizing constant.

In this context, M_i represents the parametric representation of a set of bundles defined by θ^i control points coordinates in the 3D space along with the corresponding blur extent σ_C , and $p(d|M_i)$ scores how well the configuration M_i explain the measured diffusion data d .

At iteration i , the probability of a given configuration is defined by the following distribution:

$$f_T(M_i) = \exp\left(-\frac{E_D(M_i, d)}{T_i}\right) \exp\left(-\frac{E_P(M_i)}{T_i}\right), \quad (4.3)$$

where, in our case, f_T represents the non-normalized joint distribution

$$p(d|M_i)p(M_i) \propto p(M_i|d). \quad (4.4)$$

In particular, the first term, $e^{-\frac{E_D(M_i, d)}{T_i}}$, defines the likelihood function, while the second is independent from the measured data and defines the prior probability. Finally, T_i is the system temperature at iteration i , a parameter used to speed up the convergence. The likelihood function scores how well the bundles configuration ex-

plains the observed data. This is computed as the differences between the original and the reconstructed signal computed based on a local forward model. In our case, instead of the full DW signal, we choose to fit the Intra-cellular (IC) signal fraction using a simple forward model that assigns a contribution, i.e., volume or cross-sectional area, to each bundle i of the input tractogram proportionally to its length L_i inside each voxel v . The voxel-wise signal can be expressed as:

$$S_v = \sum_{i=1}^N x_i L_i, \quad (4.5)$$

where N is the number of bundles passing through the voxel and x_i represents the actual contributions of the bundle i , estimated with COMMIT, needed to explain the acquired data d . Based on Eq. 4.5, the likelihood become:

$$E_D(M_i, d) = \sqrt{\left(\frac{1}{V}\right) \sum_{v=1}^V (S_v - d_v)^2}, \quad (4.6)$$

where V is the number of voxels in the WM volume and d_v the measured voxel signal.

Our prior knowledge is represented by $E_P(M_i)$ as follows:

$$E_P(M_i) = \lambda |B_i| + \beta |M_i|, \quad (4.7)$$

where $|B_i|$ represents the number of connections, in the configuration M_i , between pairs of regions of the cortical and subcortical parcellation and $|M_i|$ the total number of blurred streamlines, i.e. bundles, constituting these connections. Finally, λ and β are fixed parameters to control the regularization terms to balance likelihood and priors in the cost function.

To maximize the posterior probability we adopted an MCMC Metropolis-Hastings-Green (Green, 1995; Hastings, 1970; Metropolis et al., 1953) sampling approach and Simulated Annealing (Perrin et al., 2005) optimization to explore the space of parameters (see Fig. 4.4).

Given the current configuration M_i , a new configuration M_{i+1} is accepted with probability:

$$p_{\text{accept}} = \min(1, R) \quad (4.8)$$

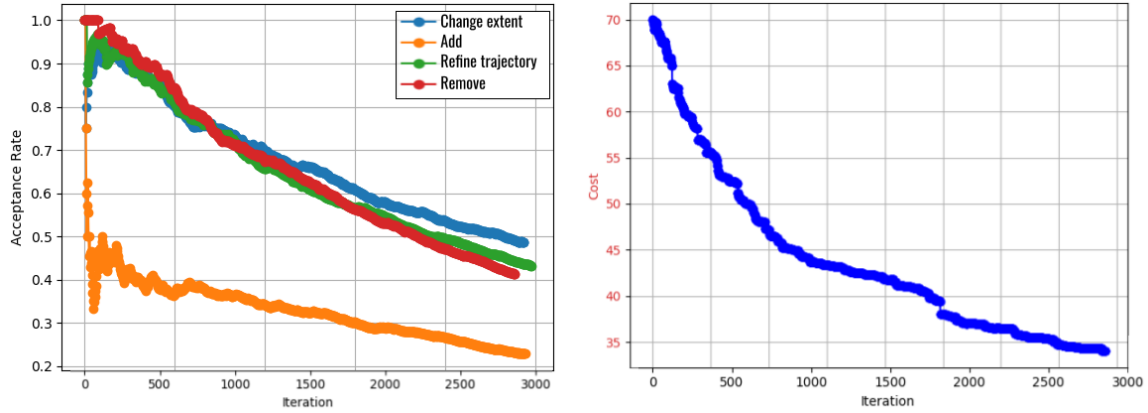


Figure 4.4 – On the left is shown the acceptance rates of the four proposals throughout the iterative adaptation, starting with an empty set of connections A . On the right is reported the plot of the corresponding cost function trend driving the optimization process

where R is the Green's ratio

$$R = \frac{f_T(M_{i+1}) p(M_i|M_{i+1}) q(M_{i+1})}{f_T(M_i) p(M_{i+1}|M_i) q(M_i)}, \quad (4.9)$$

with p describing the probability density functions associated to the proposal to move from configuration M_i to configuration M_{i+1} , and q is the probability to choose one among the four proposals listed below:

1. add connection
2. remove connection
3. refine trajectory
4. change blur extent

Regarding the first proposal, a new connection is added to the configuration by drawing randomly and uniformly from the set of connections A , which is composed by all the connections removed from M during the optimization. The associated probability density takes the form $p(M_{i+1}|M_i) = |A|^{-1}$ where $|A|$ is the number of connections in A . Conversely, the removal of a connection from the configuration is equal to the probability of uniformly sampling from the current configuration M_i , meaning $p(M_i|M_{i+1}) = |B_i|^{-1}$. The corresponding Green's ratio becomes:

$$R = \frac{f_T(M_{i+1}) |B_i|^{-1} q_r}{f_T(M_i) |A|^{-1} q_a}, \quad (4.10)$$

where q_r and q_a are, respectively, the probabilities for choosing the *Remove* and the *Add* transitions.

While, for the first and second proposals, the probability density functions are asymmetric, meaning that $p(M_i|M_{i+1}) \neq p(M_{i+1}|M_i)$, refining the trajectory and change the blur extent rely on normal probability density functions, which are symmetric. In particular, the trajectory can be adapted in two ways: by moving a single control point or by moving the whole bundle. The first consists in sampling the plane orthogonal to the bundle direction from a normal distribution of points centered around the coordinates of each control point. For the movement of an entire bundle we use the same sampling approach, but extended to all the control points. The last proposal randomly picks a bundle from M and adapts its blur extent, i.e the bundle cross-sectional area, by sampling the new value of σ_C from a normal distribution. Given these symmetric proposals, the acceptance probability becomes proportional to how likely each of the current state M_i and the proposed state M_{i+1} are under the full joint density. Hence, the Green's ratio for these proposals is given by:

$$R = \frac{f_T(M_{i+1})}{f_T(M_i)}. \quad (4.11)$$

Based on the simulated annealing approach, at the beginning, the system is characterized by a high temperature (T), which decreases as the process advances. High values of T imply that "bad" configurations are accepted, allowing the system to explore a wider range of configurations. In previous works, it has been shown how a geometric lowering schedule of the temperature ensures the convergence (Lieshout, 1994; Perrin et al., 2005) and, at the same time, improves the chances to sample from maxima of $P(M_i|D)$. Starting from a model $M_{i=0}$, the space of its parameters is explored by altering the configuration.

To better assess convergence we run two separate optimizations. In the first case, the system is allowed only to add or remove connections while, in the second, all four proposals are adopted.

4.1.4 Data and Experiments

To show the effectiveness of the method, we tested it on both synthetic and real data.

Synthetic data. We used the dataset provided for the IEEE International Symposium on Biomedical Imaging (ISBI) 2013 Reconstruction Challenge (Caruyer et al., 2014), which simulates an acquisition protocol with 64 directions at b -value=3000 s/mm², 1 mm isotropic voxel and signal-to-noise ratio of 30. This dataset consists of 27 fascicles arranged in a configuration mimicking most of the challenging bundle configurations that can be found in the brain, like bundles with various diameters branching, kissing and crossing at different angles. From the signal reconstruction point of view, the phantom reproduces both partial volume effects, given by the presence of multiple fiber compartments within the same voxel and cerebrospinal fluid (CSF) contamination. We performed streamline reconstruction with three different tractography algorithms iFOD2 (Tournier et al., 2010), SDStream (Tournier et al., 2012), Trekker (Aydogan et Shi, 2021), generating 1 million streamlines using default parameters for each. We divide the tractograms into bundles based on the parcellation provided with the dataset and then performed clustering to reduce the number of streamlines used to represent each connection.

In vivo brain data. We also evaluated bundle-o-graphy on in vivo human data from the “HCP test-retest” dataset (Van Essen et al., 2013). We downloaded the preprocessed diffusion data corresponding to subject 172332 and the structural T1-weighted image with the corresponding standard Desikan-Killiany (Desikan et al., 2006) parcellation in 85 gray matter ROIs performed with FreeSurfer (Fischl et al., 2004a). To do so, we first segment the T1-weighted image using FMRIB’s automated segmentation tool (Zhang et al., 2001) to derive the multi-tissue image. This allowed performing the tissue-informed multi-shell spherical deconvolution and to recover the fiber orientation distributions (Jeurissen et al., 2014). We performed three whole brain reconstructions, using SDStream, iFOD2 and Trekker. For the deterministic and probabilistic methods we perform anatomically constrained tractography (Smith et al., 2012) with default parameters, generating 3 million streamlines, while, for Trekker, we used the white matter mask as the seed region for the tracking, generating 1 million streamlines.

4.1.5 Evaluation metrics

For each dataset we computed the IC signal fraction maps in each voxel. Different models can be used for the estimation, as standard models like neurite orientation dispersion and density imaging (NODDI) (Zhang et al., 2012) or spherical mean technique (SMT) (Kaden et al., 2016b), implemented as open-source available at ¹. We believe that the choice of the model to use does not affect the validity of our method and, in our case, we arbitrarily decided to use the SMT.

For the synthetic dataset we processed the three input tractograms and computed the total white-matter overlap based on the corresponding IC maps, i.e., the total percentage of WM volume covered by the streamlines. For all the reconstructions, we investigated the connectivity, reporting the strength and the L1- and L2-distances between estimated and ground-truth (GT) connectivity matrices. In our case, a matrix entry reflects the connectivity strength between two regions, defined as the sum of the bundles cross-sectional area each multiplied by the corresponding weight estimated by COMMIT from the fiber density map. We assessed the number of true positive connections (TPCs), i.e., number of connections between pair of regions known to be connected and the false positives connections (FPCs), i.e., the number of those connecting regions known to be disconnected. We also reported the connectivity estimation focusing on a well known hard-to-track connection along with the WM coverage computed by segmenting the the WM mask to isolate that specific connection. Then, we carried the same analysis on the resulting configuration showing the effects of bundle-o-graphy optimization.

For the in vivo brain dataset, we compared the estimated IC maps computed by COMMIT and the signal fitting root-mean-square-error (RMSE) corresponding to the three reconstruction before and after the application of bundle-o-graphy. We also carried out analysis focusing on three major connections, Corpus Callosum (CC), Pyramidal Tract (PyT) and Arcuate Fasciculus (AF), reporting the corresponding estimated IC maps before and after the optimization along with their WM coverage.

1. <https://github.com/ekaden/smt>

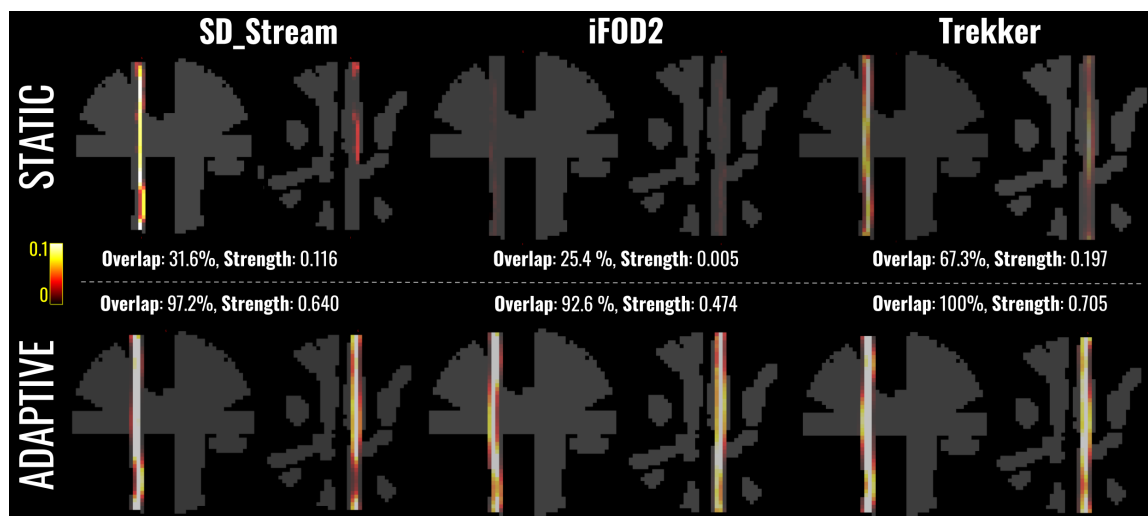


Figure 4.5 – Impact of the optimization on different reconstruction algorithms on the synthetic phantom. On the first and second row are the intra-cellular signal fraction maps corresponding to the vertical hard-to-track connection of the input and optimized configurations respectively, viewed from two different perspectives.

4.2 Results

A visual inspection of the impact of bundle-o-graphy is shown in Fig. 4.5. The first row shows the IC maps estimated by COMMIT from the static reconstructions, performed with the three tractography algorithms, of a well known hard-to-track connection. We also reported the respective connectivity strength and WM overlap. On the second row the corresponding results of the optimization with bundle-o-graphy. Starting from an underrepresented connection, the method is able to better distribute the streamlines inside the WM volume and adapt their spatial extent, converging to the same connectivity value across tractograms computed with different methods. Table 4.1 is a summary of the results on the synthetic dataset. Quantitatively, bundle-o-graphy allows to reach full coverage of WM using less than 2% of the input streamlines. The impact is particularly notable on the hard-to-track connection between region 5 and 6, where the WM coverage increases by almost three fold for SD_STREAM after the adaptation. This, in turn, allows to better estimate its connectivity strength, which converges to similar values across the three adapted configurations. At global level, the presented method drastically reduces the number

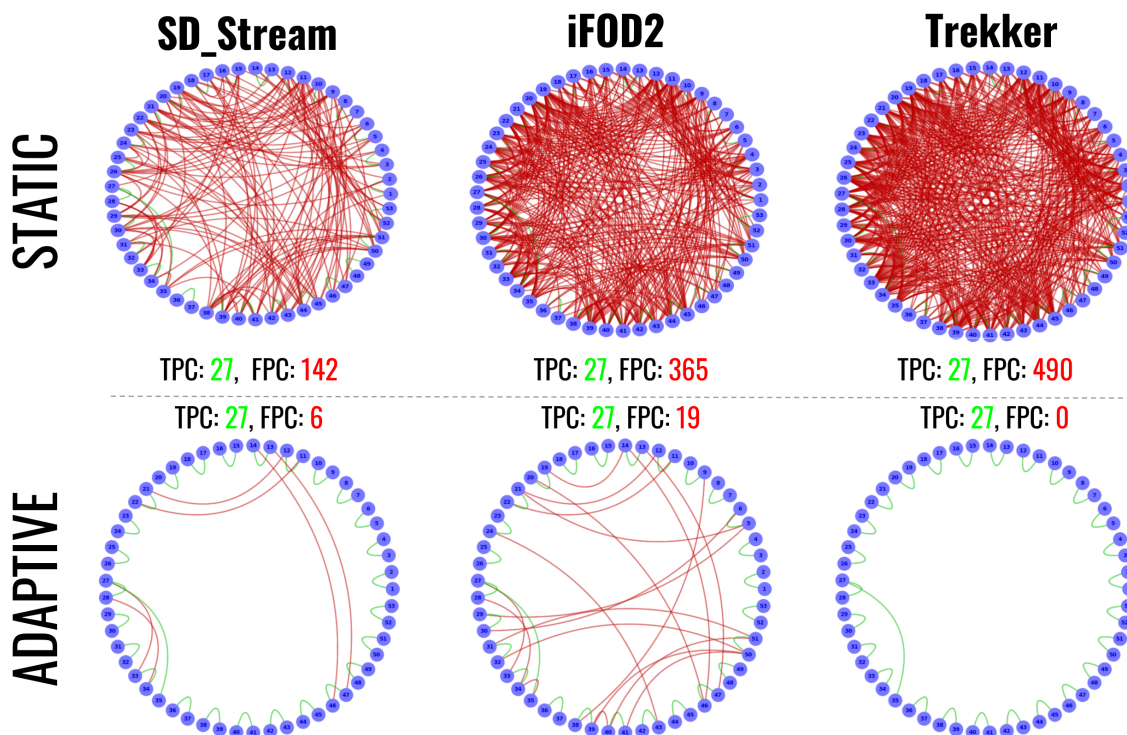


Figure 4.6 – Impact of the optimization on the removal of false positives connections. The connectivity graphs show in red the connections between pair of regions if they represent false positives connections or in green if they correspond to true positive ones. In the first row are the connectivity graphs of the input tractograms, while on the second row are the connectivity evaluated after bundle-o-graphy optimization.

of false positives while all the true positives connections are preserved (see Fig. 4.6), which, in turn, is reflected by the decrease in L1 and L2 connectivity distances with respect to the GT.

Results on in vivo dataset are shown in Fig. 4.7 and Fig. 4.8. The first shows a comparison between the signal fitting error associated to the three input tractograms before (first row) and after bundle-o-graphy optimization (second row). In all three optimized tractograms, the reduction in the RMSE is coupled with an improved streamlines density estimation, as can be see in Fig. 4.8 (second row). Thanks to bundle-o-graphy we are able to increase the overall WM coverage while improving density homogeneity at the same time. Fig. 4.9 shows the results focusing on three specific tracts, comparing the reconstructions before and after the application

of bundle-o-graphy. For each connection we computed the IC maps using COMMIT, reporting in the first row those corresponding to the input and in the second row the adapted configurations. The bundles adaptation allows to improve the tracts WM coverage while better representing the underlying anatomy, converging to connections that shares similar signal density patterns along their trajectories. For the deterministic tractogram, bundle-o-graphy increases the tracts volume by three folds, while, for the input tract recovered using iFOD2 and Trekker, the improvement is by two folds on average. As for the synthetic dataset, bundle-o-graphy complexity reduction allows to achieve these results using a fraction of the initial number of streamlines, in particular around 7% for SD_STREAM, 32% for iFOD2 and 16% for Trekker. Finally, Fig. 4.10 shows the comparison between the cortical surface projections of the CC tract corresponding to the input reconstruction (first row) and the respective optimized connections. The results show how subcortical WM volume coverage is coupled with a significantly improved cortical projection extent.

4.3 Discussion

Results on both synthetic and real data show the impact of our bundle-based approach. Bundle-o-graphy is able to improve the sensitivity/specificity trade-off of tractography by considering two fundamental observations, as previously done by [Schiavi et al. \(2020a\)](#), about brain anatomy to drive the adaptation process: (i) Streamlines can be “quantified” based on the underlying microstructure, and (ii) the WM structure is organized into bundles ([Rheault et al., 2019](#); [Schilling et al., 2020](#); [Wasserthal et Neher, 2018](#); [Wasserthal et al., 2019](#)). To achieve that we exploit two priors: the first, $|B_i|$, minimizing the total number of connections and the second, $|M_i|$, to specifically leverage the ability of the blur to reduce the complexity of the problem. In fact, the empirical image data can be equally explained using a configuration with many streamlines without blur, or using a configuration with fewer streamlines which have a blur associated to them (i.e. bundles). Clearly, this configuration requires less parameters to be estimated, and this second priors promotes this type of solutions (see Fig. 4.11). In this context, it’s important to notice that adding/removing a connection and changing the σ_C value of a bundle does not have

Table 4.1 – Summary table of the comparison between SD_STREAM, iFOD2 and Trekker reconstructions before and after the optimization on the synthetic dataset. The size corresponds to the number of input streamlines for the static case, where only those connecting were kept, while it refers to the number of bundles for the adaptive one. The metrics include the total WM overlap and the one corresponding to a hard-to-track connection along with its estimated connectivity strength. Bundle-ography improves overall white matter coverage and improves connection-specific and global connectivity estimation. The optimized tractograms present a reduced number of FPCs, while keeping all the TPCs.

	size	Total WM overlap	Bundle 5-6 WM overlap	Bundle 5-6 WM conn. strength	TPCs/FPCs	L1 conn. distance	L2 conn. distance	Computational time hh:mm	
SD_STREAM									
Static	772'793	80.21%	32.34%	0.116	27/142	0.36	0.105		
Adaptive	3'798	99.89%	97.25%	0.640	27/6	0.23	0.094	1:40	
iFOD2									
Static	503'371	99.81%	42.78%	0.005	27/365	0.59	0.178		
Adaptive	3'398	99.77%	92.61%	0.474	27/19	0.35	0.134	2:27	
Trekker									
Static	453'233	98.51%	67.35%	0.197	27/490	0.48	0.120		
Adaptive	8'848	99.95%	100%	0.709	27/0	0.01	0.003	4:31	

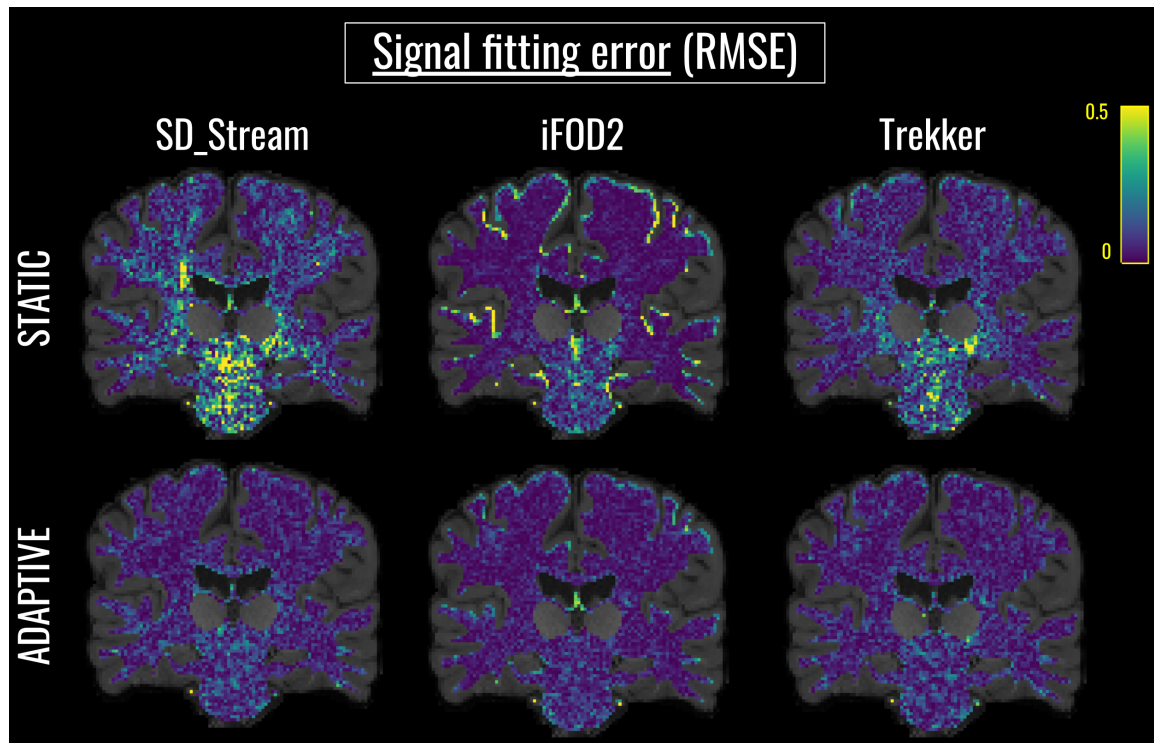


Figure 4.7 – Comparison between the voxel-wise RMSE maps corresponding to the input tractograms computed with the three different reconstruction algorithms (first row) and the adapted configurations (second row).

the same effect because they act at two different levels. The first allows for the addition or removal of the whole set of bundles representing a connection between two regions, while the second adapts the extent of an already existing bundle. For instance, a missing connection can be recovered only by adding a bundle, because the overlap between bundles belonging to a neighbor connection is limited and does not cover the whole extent of a connection.

With COMMIT2, [Schiavi et al. \(2020a\)](#) achieve notable results by using a linear optimization approach but, differently from their work and discriminative methods in general, bundle-o-graphy is capable of improving tractography reconstructions by adapting the shape and the position of each bundle. The adaptation performed by the presented method has many benefits, both qualitatively and quantitatively. The first advantage is crucial in the case of WM pathways poorly reconstructed and hence

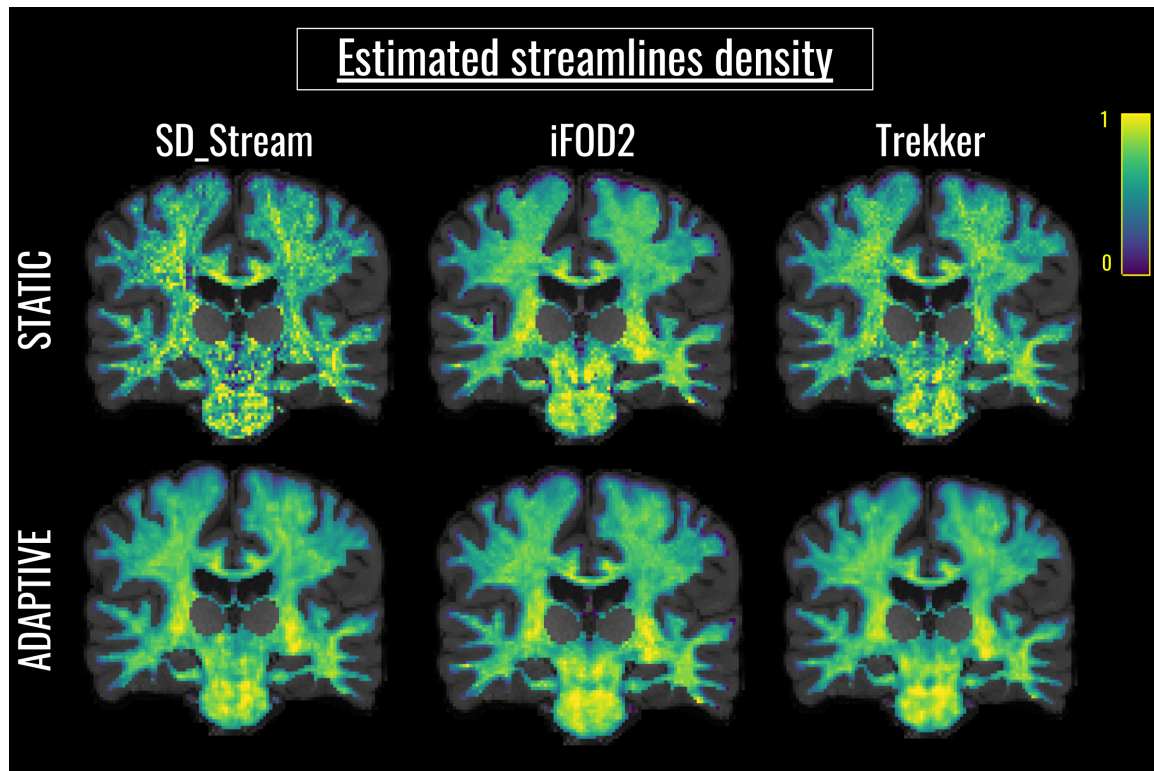


Figure 4.8 – Comparison between the estimated IC maps of the input tractograms (first row) and the adapted configurations (second row).

underrepresented, as shown in Fig. 4.5, where, thanks to bundle-o-graphy, we were able to isolate and improve the reconstruction of the connection. In the second case, the removal of invalid connections and the bundles adaptation in terms of geometry and extent, allows to be remarkably independent from the tractography algorithm used to compute the initial set of streamlines, converging to similar connectivity estimates. Moreover, the possibility to represent groups of streamlines as set of packed and aligned fascicles leads to a more homogeneous and smooth tract density (see Fig. 4.8), which reduces the variability introduced by tracking algorithms. This is particularly evident for connections going through or passing by hard-to-track regions, where tractography algorithms are known to have challenges (see Fig. 4.7).

The idea of direct modeling groups of streamlines has been already explored in previous works, as in [Close et al. \(2015\)](#). However these methods often rely on many empirically tuned parameters to shape the geometry of the bundle and to compute

the corresponding signal as well as the fact that the initial setup for each bundle need to be manually defined and they cannot reconstruct multiple bundles at once.

In our case, we don't aim to represent complex configurations with single bundles but, instead, modeling groups of streamlines by adopting a convenient parameterization. Following our approach, a connection between two regions is reconstructed using a set of bundles that, in the case of complex architecture, e.g fanning, allows to properly represent the whole extent of the tract. One of the crucial step to reducing the number of parameters is represented by the streamlines reduction, described in section 4.1.1, coupled with the blur function that allows us to model groups of similar streamlines with much fewer parameters. The amount of streamlines kept, constituting the configuration we need to adapt, is influenced by three main factors: the input tractogram, the parcellation used and the clustering threshold applied. The amount of pathways reconstructed, either true or false positives, highly depends from the tracking algorithm used to compute the initial tractogram (see Fig.4.6 first row). This fact, along with the adoption of atlases with different parcellation resolution, affects the initial total number of connections. Lastly, the clustering threshold used affects the number of representative streamlines extracted for each connection. In our experiments, using standard Desikan-Killiany atlas and clustering threshold of 3 mm, we reported a drop of 98% in the number of streamlines. The reduction in the number of coordinates to represent the streamlines is another fundamental step. This is combined with the interpolation using polynomial curves that closely follow the original anatomical trajectory. In Fig. 4.12 we show how the fitting error changes with respect to the number of control points used to simplify the input streamlines on the synthetic phantom. In particular, we can see how the fitting error increases exponentially as we progressively reduce the number of control points. In our case, we chose an average number of 6 control points per streamline, shown by the blue vertical line, which represents a good trade-off between fitting error and parameters reduction. Control point reduction is crucial for bundles trajectory adaptation. In fact, the possibility to model a pathway with few control points reduces notably the parameters space that need to be explored, speeding up the convergence. To furthermore reduce the computational cost, we empirically fixed some of the parameters. In particular, the Gaussian dumping, represented by σ_G , the two parameters controlling

the regularization terms λ and β and the initial system temperature T . The first is used to model uncertainty on the borders of a bundle and, if set to zero it means that all the segments within the extent of the bundle contribute in the same way. The parameters λ and β are used to balance likelihood and priors in the cost function, while the initial temperature T is used to regulate the speed of convergence of the optimization process. Although moving to a simplified parametric representation of the input tractogram could affect the quality of the reconstruction, our results show how, thanks to the bundle simulation and adaptation, we were able to equivalently fit the data (see Fig. 4.7 and 4.8).

While the reconstruction method used to compute the initial set of streamlines still influences the performances, our approach allows to converge to similar connectivity and WM density patterns as shown in Fig. 4.5 and 4.9. The differences between the resulting bundles configurations can be explained by two main factors: initial number of false positive connections and reconstruction quality of the valid ones. While the first mostly impact the computational time, requiring more iterations to filter out the implausible connections, the second can affect the quality of the reconstruction. In our case, iFOD2 has a better initial coverage compared to SD_STREAM but it's polluted by a greater amount of false positives, while true positives connections are still poorly reconstructed in correspondence of hard-to-track regions. In the case of valid connections particularly underrepresented, this implies that to cover the WM regions some of the invalids need to be kept to explain the signal, even if this is notably alleviated thanks to the adaptation and consequent improvement of the true positives coverage. The input tractogram computed using Trekker, although being characterized by a huge amount of false positives, provides a better support by properly recovering the true positives connections, allowing the algorithm to successfully identify and discard all the false ones. This is possible thanks to a global discriminative approach that allows to evaluate the bundle configuration as it is adapted throughout the optimization process. In our case we adopted COMMIT framework but bundle-o-graphy supports any global discriminative method that returns a fitness measure between the reconstructed and the observed signal. Moreover, thanks to its formulation, bundle-o-graphy facilitates the embedding of prior information to drive the reconstruction. For instance, these information can be exploited

to introduce hierarchies between streamlines belonging to the same connection, as in COMMIT2tree [Ocampo-Pineda et al. \(2021b\)](#), further improving our ability to filter out false positives connections. Currently, the algorithm starts from a large precomputed set of streamlines. Although efficient, this approach requires that the initial configuration contains all the true positive connections, a condition that is not always satisfied. A solution is to combine reconstructions computed with different techniques to avoid false negatives or to add a module that performs on-the-fly tracking, as the one implemented by [Aydogan et al. \(2021\)](#). This is part of future works, including the exploitation of priors coming from different imaging modalities, as in the work of [Schiavi et al. \(2022\)](#), that can be integrated in different ways.

4.4 Conclusions

Although tracking algorithms have shown a notable evolution, state-of-the-art streamline reconstructions are still anatomically inaccurate and difficult to reproduce, limiting their potential to study white matter connectivity which is fundamental to characterize the healthy structure of the human brain, as well as its perturbation in disease. Thanks to a convenient parameterization, bundle-o-graphy allows to combine both the potential of filtering techniques with the flexibility of generative global optimization approaches. We demonstrated the feasibility and the effectiveness of bundle-o-graphy both on synthetic and in vivo data, showing how bundle-o-graphy can improve the biological accuracy of the reconstruction regardless the input data.

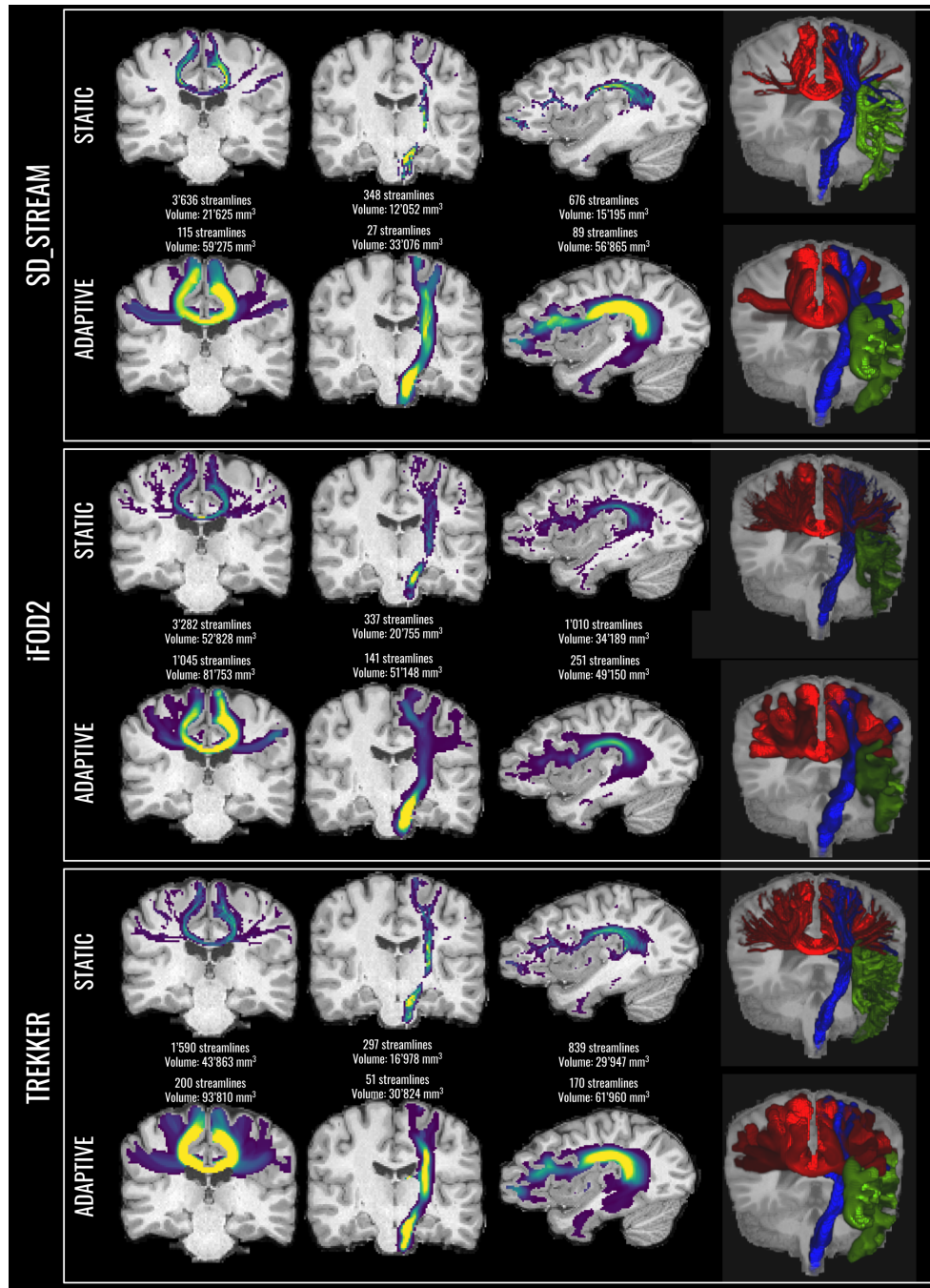


Figure 4.9 – Comparison between the IC maps, estimated with COMMIT, corresponding to the CC, PyT and AF reconstructed with the three different tractography algorithms. For each method, the first row shows the the connection segmented from the input tractogram while the second reports the connection segmented from the adapted one. The last column shows the corresponding visual inspection of the volume and geometry of the tracts. The visualization is performed in the same way and the thickness is related to the blur extent regulated by σ_C .

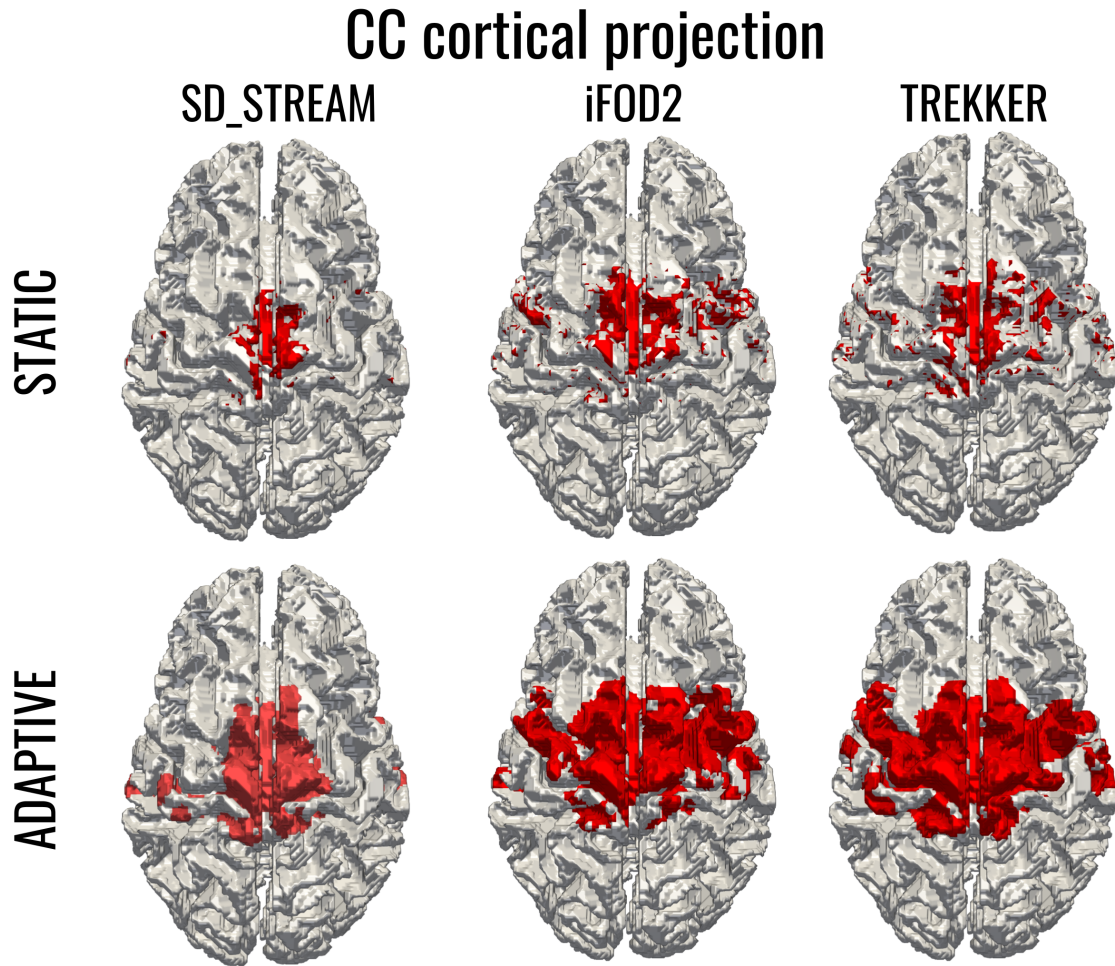


Figure 4.10 – Comparison between the cortical projections of the CC tracts segmented from the input tractograms computed with the three different reconstruction algorithms (first row) and the respectively adapted connections (second row).

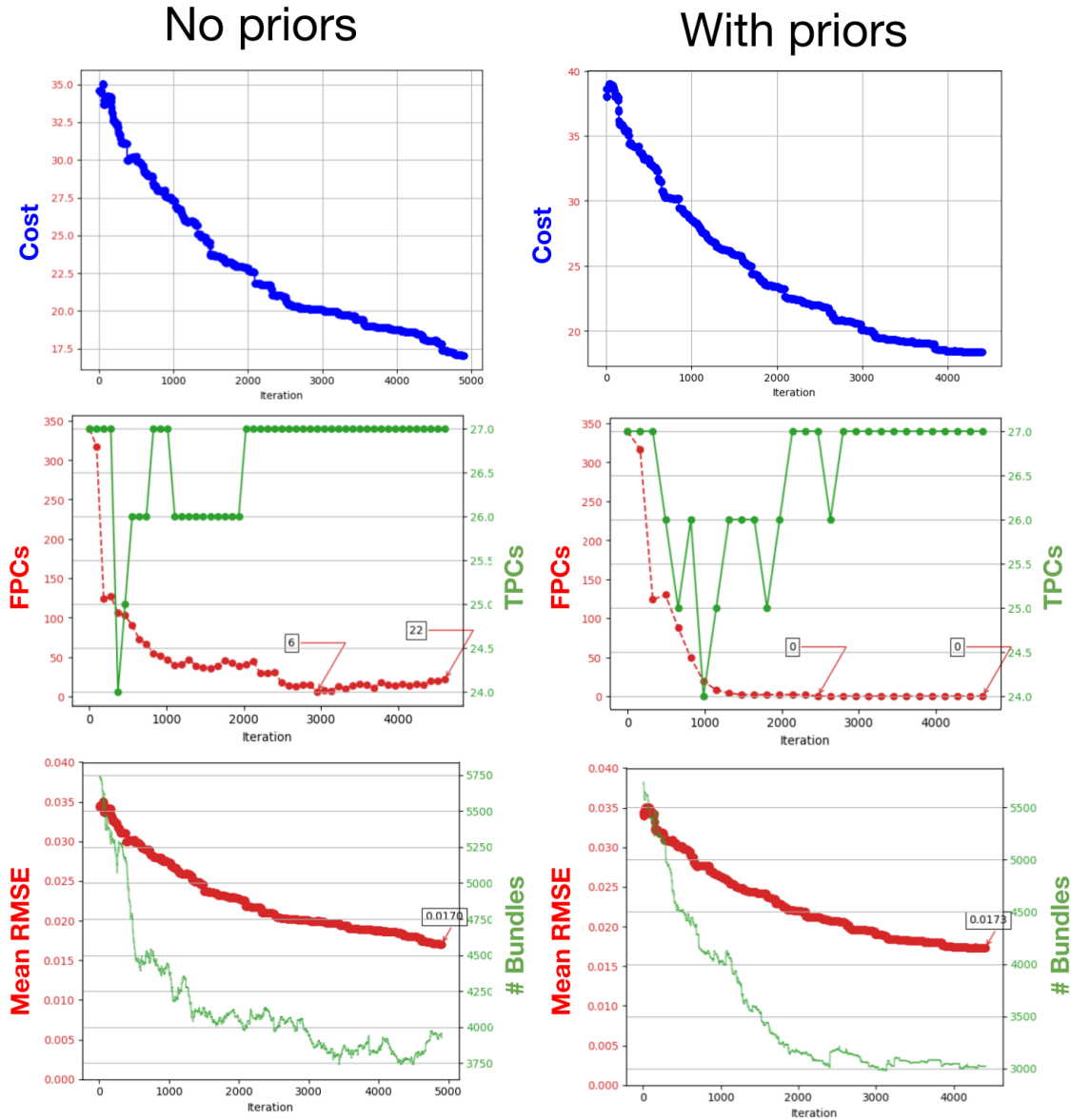


Figure 4.11 – Effects of the priors on the optimization process. On the left the adaptation is driven by the fitting error between the reconstructed and the observed signals, while, on the right, we inject priors to minimize the total number of connections and bundles. First row shows the plots of the corresponding cost functions, in the second row are reported the number of true positive (green) and false positive (red) connections, and last row shows the mean RMSE (red) along with the number of bundles in the configurations (green).

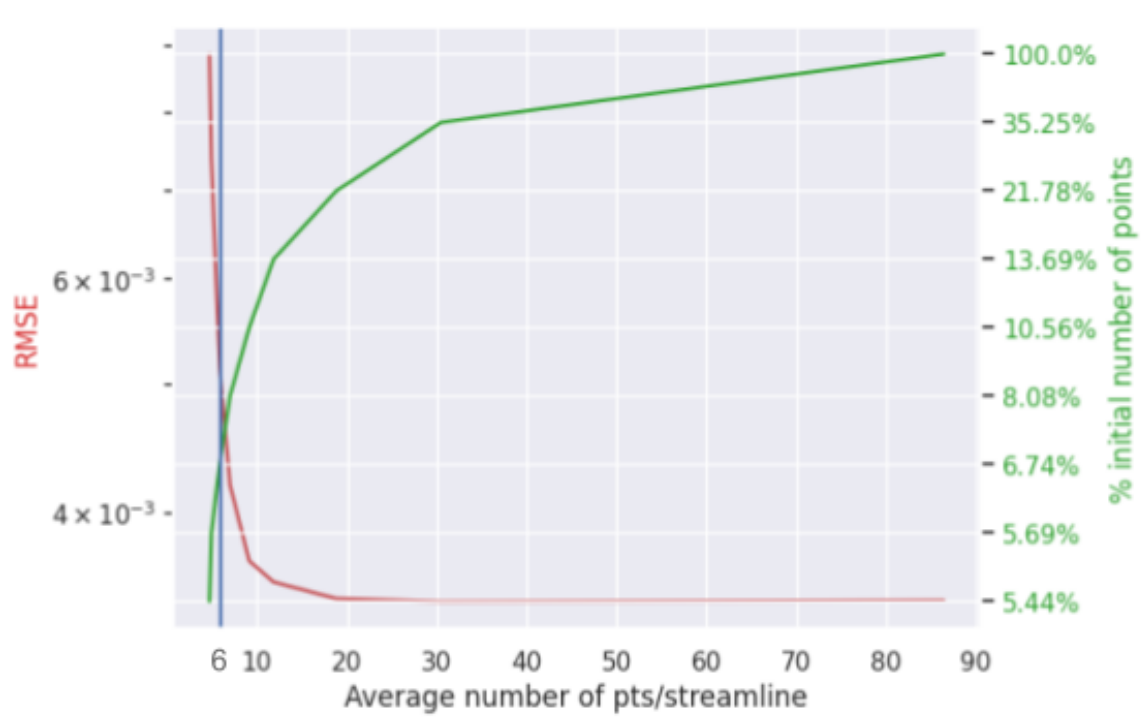


Figure 4.12 – Impact of the spline interpolation, using different number of control points, on the signal fitting error. The average value of 6 control points used in this work is reported as a blue vertical line.

Chapter 5

Hierarchical Bayesian Microstructure Modelling

[DW-MRI](#) measures the microscopic motion of water molecules, and is hence sensitive to tissue microstructure. Microstructural modelling combines specifically-designed [dMRI](#) acquisitions with a tissue model to enable estimation of parameters relating to tissue microstructure. These techniques have been widely applied in neuroimaging, with prominent examples of brain microstructure imaging including [NODDI](#) ([Zhang et al., 2012](#)), the standard model of diffusion in neuronal tissue ([Novikov et al., 2019](#)) and the spherical mean technique ([Kaden et al., 2016b](#)). Microstructural modelling has also provided insights into body Magnetic Resonance Imaging ([MRI](#)) ([Koh et al., 2011](#)), for example in prostate cancer ([Panagiotaki et al., 2015](#)).

The core fitting procedure in microstructure imaging estimates model parameters given the observed [dMRI](#) signal (Figure 5.1, top panel). The vast majority of fitting techniques assume that voxels are independent; in other words, the model is separately fitted to the signal in each voxel, usually with nonlinear least squares estimation. An alternative approach is to use a [MCMC](#) algorithm to estimate parameter posterior distributions in each voxel ([Harms et Roebroek, 2018](#)). [Orton et al. \(2014\)](#) introduced a hierarchical Bayesian model fitting approach for the [IVIM](#) ([Le Bihan et al., 1988](#)) model. Their model breaks the assumption of independent pixels by introducing a Gaussian prior (estimated from the data) over the microstructural model parameters

across a **ROI**. By using a **MCMC** algorithm to fit the Bayesian model, they showed an improvement in **IVIM** parameter maps of the liver. This approach has also been applied to combined T₂- **IVIM** modelling in the placenta (Flouri et al., 2020).

In this work, we generalise the Bayesian approach to apply to any microstructural model, derive the corresponding **MCMC** algorithm, and implement arbitrary upper and lower parameter bounds. We also utilise regional priors, which may be more appropriate than a global prior for fitting across distinct neurological tissue types. The **MCMC** algorithm is implemented in Python by utilising the Diffusion Microstructure Imaging in Python (**Dmipy**) (Fick et al., 2019) software package. We demonstrate our algorithm on simulations and on Human Connectome Project (**HCP**) data, and show clear advantages over the standard least squares fitting technique.

5.1 Methods

5.1.1 General Bayesian Microstructure model

The approach of Orton et al. (2014) is extended to a general multi-compartment microstructural model. A schematic of the hierarchical Bayesian framework is shown in Figure 5.1.

We consider a general multi-compartment model of N_{comp} compartments, with a set of underlying microstructure-related parameters θ . For notational convenience we group θ by parameter type as

$$\theta = \left\{ \left\{ f_k \right\}_{k=1}^{N_{comp}-1}, \left\{ x_j \right\}_{j=1}^J \right\}, \quad (5.1)$$

where f_k denotes compartment signal fractions and x_j the other parameters, e.g. diffusivities, orientations, radii, etc. Assuming that relaxation times are fixed across compartments, the signal fractions sum to 1, i.e. $\sum_{k=1}^{N_{comp}} f_k = 1$, meaning that $f_{N_{comp}}$ is not a free parameter but fixed as $1 - \sum_{k=1}^{N_{comp}-1} f_k$.

A general microstructural model comprises a mapping - or *signal equation* - between underlying tissue-related parameters θ and acquisition parameters t_n (typically b-value and gradient direction), and a **dMRI** signal intensity S_n , i.e.

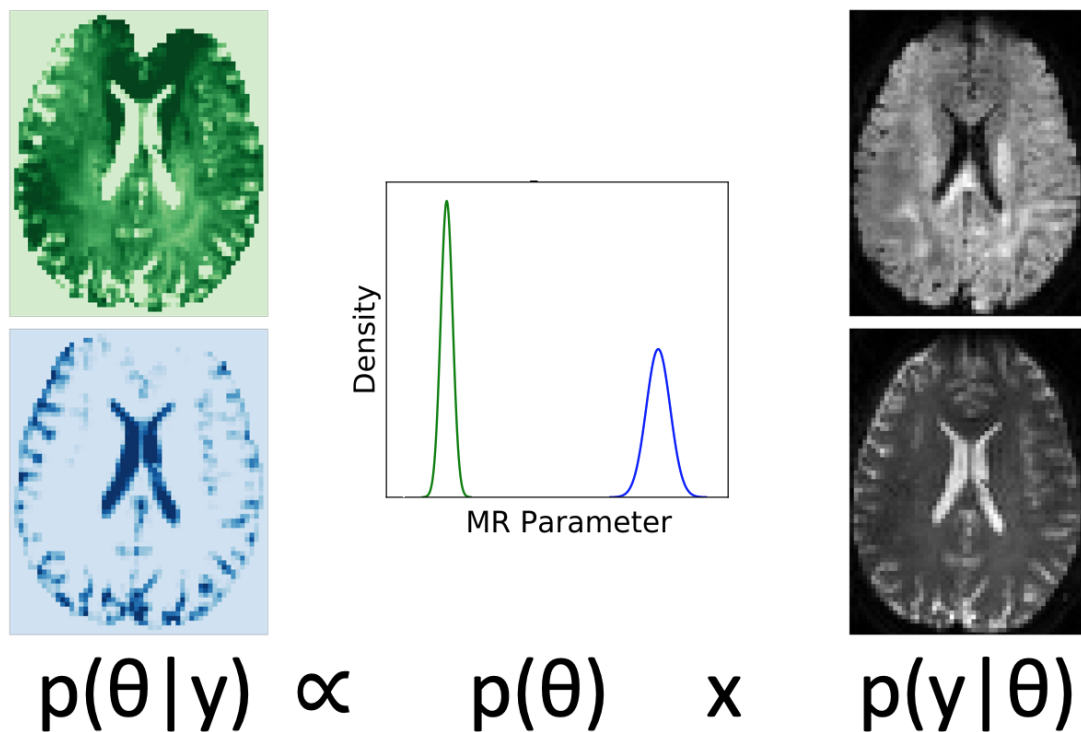


Figure 5.1 – Schematic of Bayesian hierarchical model for a general microstructure model. Top panel defines a general microstructure model, g that maps microstructure-related parameters θ and acquisition parameters \mathbf{t} to **dMRI** signal S . The microstructure parameters can be grouped by parameter type as $\theta = \left\{ \{f_k\}_{k=1}^{N_{comp}-1}, \{x_j\}_{j=1}^J \right\}$ where f_k are the compartment signal fractions and x_j are the other parameters. Second panel defines the voxelwise likelihood function. Third panel displays the **ROI**-wide Gaussian priors, note that θ_μ and Σ are learnt from the data for all **ROIs**. Fourth panel displays the voxelwise parameter posterior distributions and corresponding parameter maps.

$$S_n = S_0 g_n(\theta, t_n), \quad (5.2)$$

where S_0 is the signal intensity without diffusion weighting. The experimentally-measured signal in the presence of noise is hence modelled as

$$y_n = S_n + \epsilon_n = S_0 g_n(\theta, t_n) + \epsilon_n, \quad (5.3)$$

where y_n is the measured signal and ϵ_n is noise.

We now consider all measurements for a voxel i , i.e. the signal intensities at all acquisition parameters $\mathbf{t} = \{t_1, \dots, t_N\}$ - which we denote $\mathbf{y}_i = [y_1, \dots, y_N]^T$. The likelihood, assuming normally distributed noise with variance σ_y^2 , is therefore

$$p(\mathbf{y}_i | \theta_i, S_0, \sigma_y^2) = (2\pi\sigma_y^2)^{-N/2} \exp\left(\frac{-1}{2\sigma_y^2} \sum_{n=1}^N (y_n - S_0 g_n(\theta_i, t_n))^2\right), \quad (5.4)$$

where θ_i denotes the microstructural model parameter values in voxel i . [Orton et al. \(2014\)](#) demonstrated that the “nuisance parameters” S_0 and σ_y^2 can be marginalised out from Eq. (5.4) to give the following marginalised likelihood:

$$p(\mathbf{y}_i | \theta_i) \propto \left[\mathbf{y}_i^T \mathbf{y}_i - (\mathbf{y}_i^T \mathbf{g}_i)^2 / \mathbf{g}_i^T \mathbf{g}_i \right]^{-N/2}, \quad (5.5)$$

where $\mathbf{g}_i = [g_1(\theta_i, t_1), \dots, g_N(\theta_i, t_N)]$ are the model predicted signals for voxel i .

Parameter Transforms

Microstructure model fitting needs to enforce physically reasonable minimum and maximum values of parameters; for example, diffusivities need to be positive. Here we generalise the transforms used by [Orton et al. \(2014\)](#) to enable arbitrary minimum and maximum constraints. For a parameter p , we define a transform

$$p' = \log(p - p_{min}) - \log(p_{max} - p), \quad (5.6)$$

which maps the interval (p_{min}, p_{max}) to \mathbb{R} . By defining the Bayesian prior on the transformed parameter p' , we therefore constrain p between p_{min} and p_{max} . Default

values for p_{min} and p_{max} are set as the minimum and maximum values defined in the `Dmipy` variable “model.parameter_ranges”; however, they can also be manually defined by the user.

Bayesian shrinkage priors

[Orton et al. \(2014\)](#) used a multivariate Gaussian Bayesian shrinkage prior on the `IVIM` model parameters, with the prior defined over a single user-defined `ROI`. The Bayesian fitting method is generalised here to the multiple `ROI` case simply by running the derived `MCMC` algorithm separately on the voxel-wise `dMRI` data from each `ROI`; however, note that here and throughout the methods section we consider the single `ROI` case for brevity, without loss of generality. The prior generalised for any microstructural model is denoted

$$p(\theta|\theta_\mu, \Sigma) = N(\theta; \theta_\mu, \Sigma)' \quad (5.7)$$

where θ_μ is a vector whose elements encode the prior means of the parameters, Σ is their covariance and $N(\theta; \theta_\mu, \Sigma)$ denotes the multivariate normal probability density function (`PDF`) with variable θ , mean θ_μ and covariance Σ . Again, we emphasise that θ_μ and Σ are estimated from the data.

To generalise from [Orton et al. \(2014\)](#) two-compartment model to an arbitrary multi-compartment model, all signal fractions must to sum to one. We enforce this (following [Harms et Roebroek \(2018\)](#)) by modifying the prior to

$$p(\theta_i|\theta_\mu, \Sigma) = \begin{cases} N(\theta_i; \theta_\mu, \Sigma) & \text{if } \sum_{j=1}^{n-1} f_j \leq 1 \\ 0 & \text{otherwise} \end{cases} \quad (5.8)$$

To complete the model we define a hyper-prior on θ_μ and Σ as a non-informative Jeffrey’s prior

$$p(\theta_\mu, \Sigma) = |\Sigma|^{-1/2}. \quad (5.9)$$

Posterior Distributions

Each `ROI` has its own posterior distribution, which can be written as in [Orton et al.](#)

(2014)

$$p(\theta_{1:M}, \theta_\mu, \Sigma | \mathbf{y}_{1:M}) \propto p(\mathbf{y}_{1:M} | \theta_{1:M}) p(\theta_{1:M} | \theta_\mu, \Sigma) p(\theta_\mu, \Sigma)$$

where $\theta_{1:M} = \{\theta_1, \theta_2, \dots, \theta_M\}$ are the parameters and $\mathbf{y}_{1:M} = \{\mathbf{y}_1, \dots, \mathbf{y}_M\}$ the **dMRI** data for all voxels in the **ROI**. Substituting in equations (5.5), (5.7), (5.9) gives

$$p(\theta_{1:M}, \theta_\mu, \Sigma | \mathbf{y}_{1:M}) \propto \left(\prod_{i=1}^M [\mathbf{y}_i^T \mathbf{y}_i - (\mathbf{y}_i^T \mathbf{g}_i)^2 / \mathbf{g}_i^T \mathbf{g}_i]^{-N/2} \right) \left(\prod_{i=1}^M N(\theta_i; \theta_\mu, \Sigma) \right) |\Sigma|^{-1/2}$$

from which we can draw samples with a **MCMC** algorithm.

MCMC Monte Carlo Markov chain algorithm

The **MCMC** algorithm is derived here, and given as pseudocode in Algorithm 2. Following Orton et al. (2014), the **MCMC** updates for the **ROI**-wide prior parameters θ_μ and Σ are Gibbs moves. The conditional distributions are (up to proportionality)

$$p(\theta_\mu | \theta_{1:M}, \Sigma, \mathbf{y}_{1:M}) \propto \prod_{i=1}^M N(\theta_i; \theta_\mu, \Sigma) = N(\theta_\mu; m, V)$$

where $m = M^{-1} \sum_{i=1}^M \theta_i$ $V = M^{-1} \Sigma$, and the second line comes from rearranging the multivariate normal PDF so that θ_μ is the variable. The **MCMC** update is therefore sampled as follows

$$\theta_\mu \sim N(m, V) \tag{5.10}$$

where $N(m, V)$ is a multivariate normal distribution with mean m and covariance V . Following the same steps for Σ (see Orton et al. (2014) for full details) gives the **MCMC** update for Σ

$$\Sigma \sim W^{-1}(\Phi, M - 3) \tag{5.11}$$

where $\Phi = \sum_{i=1}^M (\theta_i - \theta_\mu u)(\theta_i - \theta_\mu u)^T$ and W^{-1} is the inverse-Wishart distribution.

Voxelwise parameters

For the non-signal fraction voxelwise parameters the posterior distribution up to proportionality is

$$p(x_{i,j}|x_{i,-j}, \{f_{i,k}\}_{k=1}^{N_{comp}-1}, \theta_\mu, \Sigma) \propto [\mathbf{y}_i^T \mathbf{y}_i - (\mathbf{y}_i^T \mathbf{g}_i)^2 / \mathbf{g}_i^T \mathbf{g}_i]^{-N/2} N(\theta_i; \theta_\mu, \Sigma) \quad (5.12)$$

where $x_{i,j}$ is the value of parameter x_j in voxel i , $x_{i,-j} = \{x_{i,1}, \dots, x_{i,j-1}, x_{i,j+1}, \dots, x_{i,J}\}$ denotes the set of all non-signal fraction parameters except $x_{i,j}$, and $\{f_{i,k}\}_{k=1}^{N_{comp}-1}$ are the signal fractions for voxel i .

As in [Orton et al. \(2014\)](#), we sample from this with a Metropolis-Hastings algorithm. Proposed parameters are first sampled from Gaussian distributions as

$$x_{i,j}^* \sim N(x_{i,j}, w_{x_{i,j}}), \quad (5.13)$$

where $x_{i,j}$ is the current value of the parameter, $x_{i,j}^*$ is the proposed parameter value and $w_{x_{i,j}}$ is the variance of the proposal distribution, which should reflect the scale of the parameter and can be tuned for optimal algorithm performance.

The acceptance probability utilises the ratio of the posterior distributions for $x_{i,j}$ and $x_{i,j}^*$

$$\alpha(x_{i,j} \rightarrow x_{i,j}^*) = \min \left\{ 1, \frac{p(x_{i,j}^*|x_{i,-j}, \{f_k\}_{k=1}^{N_{comp}-1}, \theta_\mu, \Sigma)}{p(x_{i,j}|x_{i,-j}, \{f_k\}_{k=1}^{N_{comp}-1}, \theta_\mu, \Sigma)} \right\}, \quad (5.14)$$

where the values on the right of the posterior are the current parameter values in the [MCMC](#) algorithm.

The signal fraction parameters [MCMC](#) moves are the same, except that the posterior distributions now contain the terms enforcing $\sum_{k=1}^{N_{comp}} f_k = 1$, i.e.

$$p(f_{i,k}|x_{i,1}, \dots, x_{i,J}, f_{i,-k}, \theta_\mu, \Sigma) \propto \begin{cases} [\mathbf{y}_i^T \mathbf{y}_i - (\mathbf{y}_i^T \mathbf{g}_i)^2 / \mathbf{g}_i^T \mathbf{g}_i]^{-N/2} & \text{if } \sum_{k=1}^{N_{comp}-1} f_k \leq 1 \\ 0 & \text{otherwise,} \end{cases} \quad (5.15)$$

where $f_{i,-k} = \{f_{i,1}, \dots, f_{i,k-1}, f_{i,k+1}, f_{i,K}\}$ are the other signal fractions apart from $f_{i,k}$. Again we sample proposed values as

$$f_{i,k}^* \sim N(f_{i,k}, w_{f_{i,k}}) \quad (5.16)$$

where $f_{i,k}$ is the current signal fraction. The acceptance probabilities are

$$\alpha(f_{i,k} \rightarrow f_{i,k}^*) = \min \left\{ 1, \frac{p(f_{i,k}^* | x_{i,1}, \dots, x_{i,J}, f_{i,-k}, \theta_\mu, \Sigma)}{p(f_{i,k} | x_{i,1}, \dots, x_{i,J}, f_{i,-k}, \theta_\mu, \Sigma)} \right\}. \quad (5.17)$$

Metropolis-Hastings Acceptance Ratio.

We tuned the Metropolis-Hastings jumping variances w_{θ_i} during the burn-in period to achieve an acceptance ratio that samples the posterior distribution efficiently. Following [Orton et al. \(2014\)](#), at every 100 [MCMC](#) steps we applied the update rule

$$w_{\theta_i} = w_{\theta_i} 101 / (2(101 - R_{\theta_i})) \quad (5.18)$$

where R_{θ_i} is the number of times the proposed parameter update was accepted in the previous 100 steps. This scheme aims to adjust the jumping variances such that an acceptance rate of approximately 50% is achieved.

5.1.2 Models

The [MCMC](#) algorithm was tested using the ball-stick model, defined as

$$g(\theta, t) = f_{par} \exp(-bD_{par}(\mathbf{n} \cdot \mathbf{g})) + (1 - f_{par}) \exp(-bD_{iso}), \quad (5.19)$$

where b is the b-value, \mathbf{g} is the gradient direction and \mathbf{n} is the stick orientation, which is parameterised by two angles ϕ_1 and ϕ_2 constrained such that $\phi_1 \in (0, \pi)$ and $\phi_2 \in (-\pi, \pi)$.

The signal fractions were constrained as $f_k \in (0.01 - 0.99)$ and the diffusivities as $D_{par}, D_{iso} \in (0.1 - 3) \mu\text{m}^2/\text{ms}$.

Algorithm 2 MCMC algorithm for Bayesian model fitting of a general microstructural model. This pseudocode describes the algorithm for a single ROI. For multiple ROIs, the algorithm is simply run separately on each ROI.

```

for voxels  $i = 1$  to  $i = N$  do
    Calculate initial values for voxelwise parameters:  $\{x_{i,j}\}_{j=1}^J, \{f_{i,k}\}_{k=1}^{N_{comp}}$  with least
    squares estimation
end for
 $S \leftarrow$  number of MCMC steps
for MCMC steps  $s = 1$  to  $s = S$  do
     $\theta_\mu^{(s)} \leftarrow$  sample from Equation (5.10)
     $\Sigma^{(s)} \leftarrow$  sample from equation (5.11)
    for voxels  $i = 1$  to  $i = N$  do
        for non-signal fraction parameters  $j = 1$  to  $j = J$  do
             $\epsilon_{x_{i,j}} \leftarrow N(x_{i,j}^{(s-1)}, w_{x_{i,j}})$ 
             $x_{i,j}^* \leftarrow x_{i,j}^{(s-1)} + \epsilon_{x_{i,j}}$ 
            calculate  $\alpha(x_{i,j} \rightarrow x_{i,j}^*)$  from Equation (5.14)
             $u \leftarrow$  sample from  $\text{unif}(0, 1)$ 
            if  $u < \alpha$  then
                 $x_{i,j}^{(s)} \leftarrow x_{i,j}^*$ 
            else
                 $x_{i,j}^{(s)} \leftarrow x_{i,j}^{(s-1)}$ 
            end if
        end for
        for signal fraction parameters  $k = 1$  to  $k = N_{comp} - 1$  do
             $\epsilon_{f_{i,k}} \leftarrow N(f_{i,k}^{(s-1)}, w_{f_{i,k}})$ 
             $f_{i,k}^* \leftarrow f_{i,k}^{(s-1)} + \epsilon_{f_{i,k}}$ 
            calculate  $\alpha(f_{i,k} \rightarrow f_{i,k}^*)$  from Equation (5.17)
             $u \leftarrow$  sample from  $\text{unif}(0, 1)$ 
            if  $u < \alpha$  then
                 $f_{i,k}^{(s)} \leftarrow f_{i,k}^*$ 
            else
                 $f_{i,k}^{(s)} \leftarrow f_{i,k}^{(s-1)}$ 
            end if
        end for
         $f_{i,N_{comp}}^{(s)} \leftarrow 1 - \sum_{k=1}^{N_{comp}-1} f_{i,k}^{(s)}$ 
        if  $s \bmod 100 = 0$  then
            for voxels  $i = 1$  to  $i = N$  do
                Update  $\{w_{x_{i,j}}\}_{j=1}^J$  and  $\{w_{f_{i,k}}\}_{k=1}^{N_{comp}-1}$  using Equation (5.18)
            end for
        end if
    end for
end for

```

Algorithm implementation

Note that while all distributions have been presented in the linear scale, they were calculated in log-scale for numerical convenience. Parameter values were initialised with a voxel-wise least squares fit, estimated using the `Dmipy` `brute2fine` option (Fick et al., 2019). The `MCMC` algorithm was then run for 2000 steps with a burn-in of 1000 steps; weights were updated every 100 steps during the first half of the burn-in period. In our experience this was sufficient to sample the posterior distributions, and aligns with the work of Harms et Roebroek (2018). We calculated model parameter posterior distributions and representative statistics from the 1000 `MCMC` samples after the burn-in. Parameter maps were generated using the mean of the posterior distributions in each voxel.

5.1.3 Data

To test the `MCMC` algorithm’s ability to infer correct model parameter values, we ran simulations using the Shepp-Logan phantom. We generated synthetic images with a matrix size of 128×128 and defined ground truth parameters in each major region (see Figure 5.3A, top row). We then simulated the signal in each voxel using `Dmipys` `simulate_signal` function with the same acquisition parameters as the `HCP` data (see below), added Gaussian noise to give a Signal to noise ratio (`SNR`) of 10 in the $b = 0$ data, and ran the `MCMC` algorithm on these synthetic datasets. We perturbed initial parameter values to verify that the algorithm could find the global minimum. Bayesian priors were defined over the whole phantom excluding the background (i.e. one `ROI`).

We then applied our Bayesian model fitting approach on publicly-available data provided by the `HCP` WU-Minn Consortium (48 Subjects Test Retest Data Release, release date: Mar 01, 2017, available online at humanconnectome.org) `HCP` data neuroimaging. Data from a single subject was used. The `WM`, `GM`, sub-cortical `GM` and ventricle `ROIs` derived from the Freesurfer T_1 segmentations (these provided the best contrast between tissues) were transformed into diffusion space via linear and non-linear registration between the subject’s T_1 -weighted image and the $b = 0$ `dMRI` data. The `MCMC` algorithm was applied with the Bayesian priors defined over these

four ROIs.

5.2 Results and discussion

Figure 5.2 displays the output of several runs of the MCMC algorithm for a single voxel in the Shepp-Logan data. The MCMC chains and posterior distributions demonstrate that voxel-wise parameter estimates converged to the ground truth value under a range of perturbations. Figure 5.3 compares the least squares and Bayesian parameter maps with the ground truth. The Bayesian approach more accurately replicated the ground truth and provided lower errors than least squares approach, particularly in low SNR cases.

Figure 5.4 shows the MCMC algorithm results on the HCP data. The Bayesian fit clearly removed some apparent outlier voxels when compared to the least squares fit (see arrows).

In this work we present an extension to previous approaches that enables Bayesian

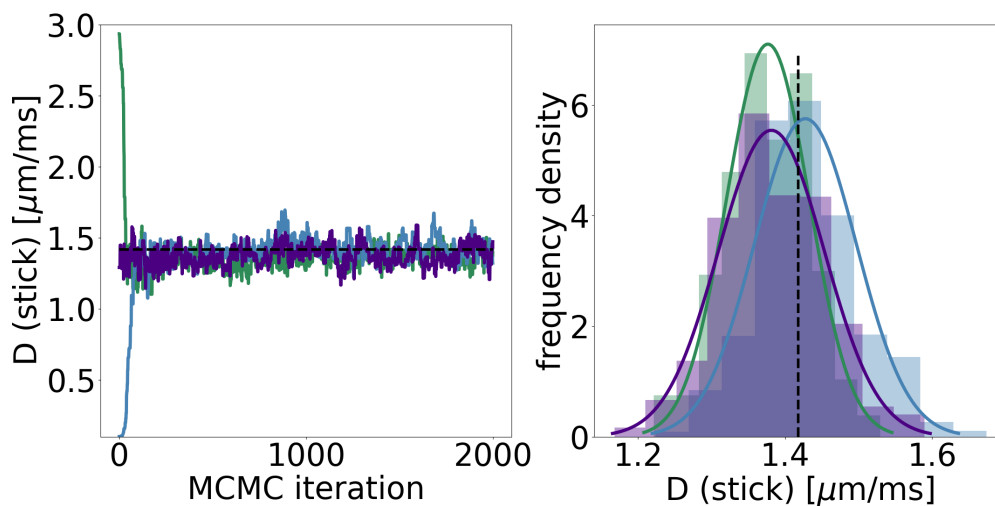


Figure 5.2 – MCMC output from the Bayesian ball-stick model fit on the Shepp-Logan phantom data. The left panel shows three MCMC chains for the stick parallel diffusivity in a single voxel; the initial parameter value in each run was given a different perturbation. The right panel shows the posterior distribution from each run, calculated on all samples after the burn-in of 1000 steps. The ground truth parameter value is indicated by the black lines.

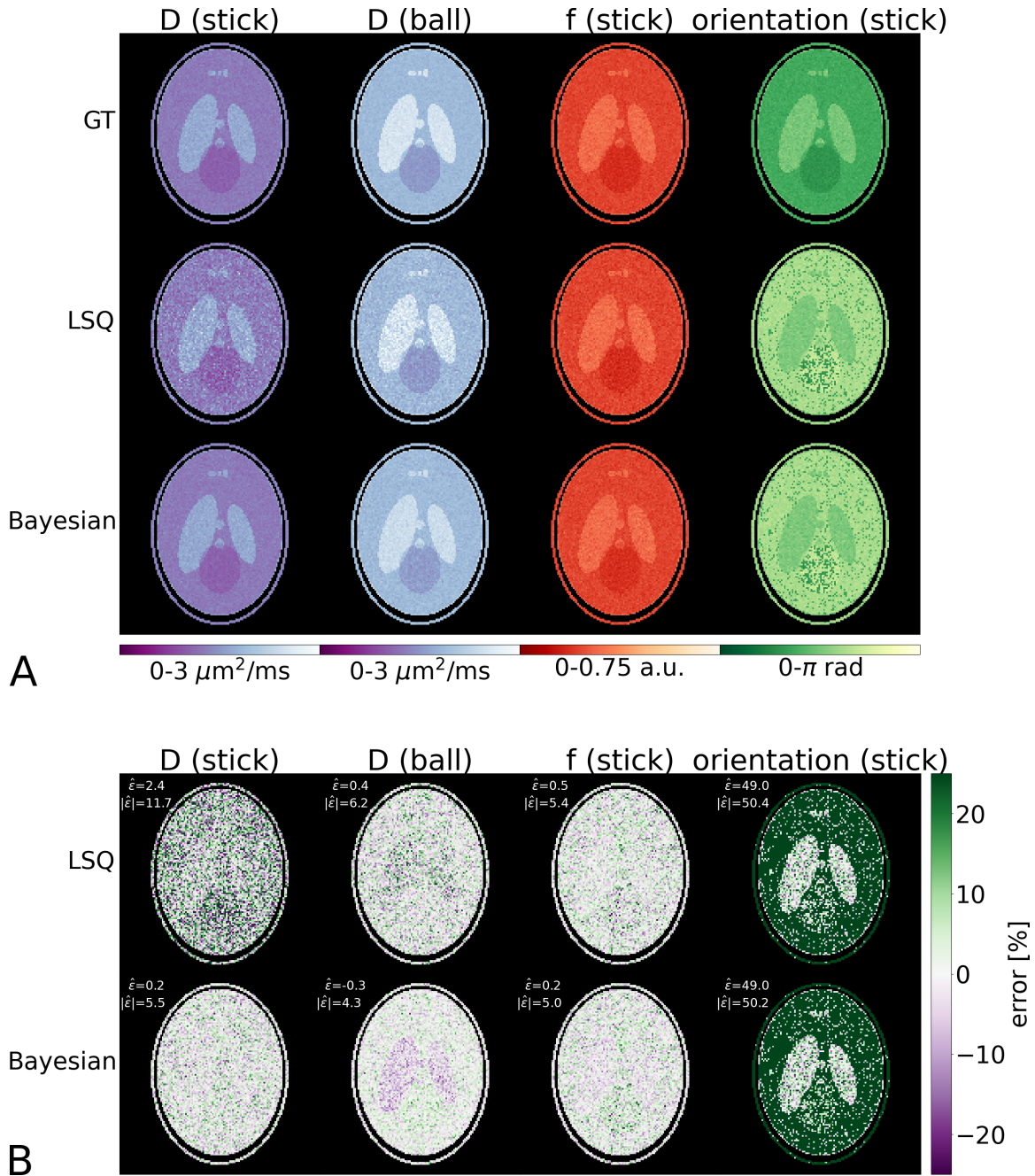


Figure 5.3 – Ball-stick model parameter maps in the Shepp-Logan phantom synthetic images. A. Ground truth (top row), least-squares derived (middle row) and Bayesian derived (bottom row) parameter maps for the stick parallel diffusivity (D_{par}) in $\mu\text{m}^2\text{s}^{-1}$, ball isotropic diffusivity (D_{iso}) in $\mu\text{m}^2\text{s}^{-1}$, stick signal fraction (f_{par}) and elevation orientation parameter (ϕ_1) in radians. B. Relative error maps for the least-squares fits (top row) and Bayesian fits (bottom row). Bayesian priors were defined over the whole image. The mean relative error ($\hat{\epsilon}$) and mean absolute relative error ($|\hat{\epsilon}|$) are displayed for each fitted parameter (both in %). Computation time for the Bayesian method was approximately 1 hour.

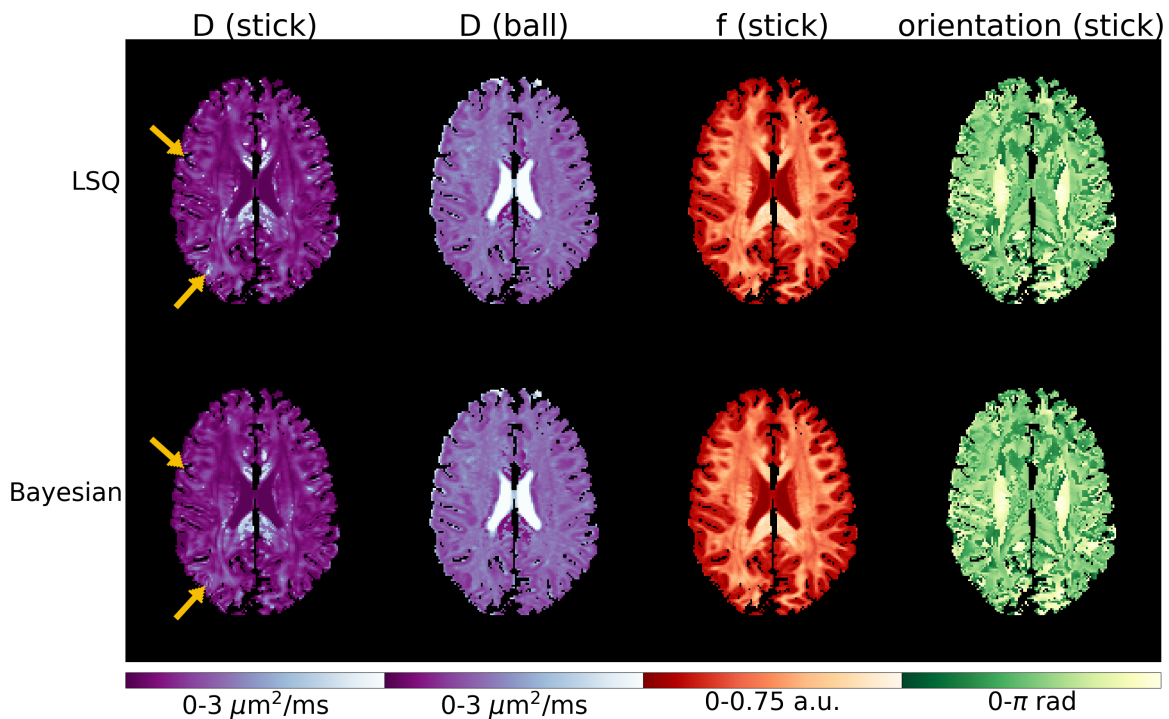


Figure 5.4 – Ball-stick parameter maps in the HCP data for the least squares fit (top row) and Bayesian fit (bottom row). Parameters as Figure 5.3. The Bayesian priors were defined over four ROIs as described in Methods section 5.1.3. Computation time for the Bayesian method was approximately 3.5 hours.

hierarchical model Bayesian hierarchical model fitting for a general microstructural model with arbitrary parameter constraints and regional priors. The algorithm is implemented by utilising and adapting the [Dmipy](#) software package, and is made publicly available¹. On synthetic data, we show that Bayesian fitting of the ball-stick model more accurately recovered ground truth maps than least squares fitting, particularly for parameters more susceptible to noise such as the stick parallel diffusivity. On [HCP](#) data, the algorithm reduced the appearance of apparent outlier voxels.

Although high [SNR](#) images from the [HCP](#) were used as the test data here, we anticipate the biggest gains of this approach will be seen in lower [SNR](#) data and more complex models. This may enable estimation of richer microstructural detail in a greatly reduced acquisition time.

The algorithm has limitations that motivate future work. The Bayesian approach assumes Gaussian noise, which may not be appropriate in all cases, particularly in low [SNR](#) cases. We also assumed that a Gaussian prior is suitable for all parameters; however, this may not be the optimal choice, particularly for orientation parameters where a flat prior may be more appropriate and could enable improved orientation parameter maps over LSQ (see Figures 5.3 and 5.4). Alternative prior choices are an avenue for future work. Utilising probabilistic segmentations, rather than the current hard-thresholded [ROIs](#) which may bias parameter estimation in partial volume voxels, is possible, but may complicate the [MCMC](#) inference. More complex model choices, as well as comparisons with alternative model fitting methods (e.g. [Harms et Roebroek \(2018\)](#)), should also be explored to better quantify the benefits of our Bayesian approach.

To conclude, we derive a general Bayesian hierarchical microstructural model Bayesian hierarchical model and a [MCMC](#) algorithm for model inference given [dMRI](#) diffusion MRI data. The algorithm, and corresponding open-source software, newly enables Bayesian model fitting for a wide range of microstructure microstructure imaging techniques.

1. github.com/PaddySlator/dmipy-bayesian

Part II

Clinical applications

The second part of the thesis is characterized by tractography applications to study brain structural connectivity in subjects affected by **MS** and **FD**. This gives the opportunity to face tractography limitations (presented in section 1.4) affecting clinical studies, carried with standard analysis pipeline, and how these can be mitigated. In the first case, a network connectivity study has been performed, where metrics were investigated taking in account microstructural features, while another analysis inspects the effects of **MS** disruption affecting the **CC** tract specifically.

In the context of **FD**, the microstructural integrity of the tracts connecting the motor cortices to the basal ganglia is inspected, investigating the possible presence of structural connectivity changes in these connections.

Chapter 6

Sensory-motor structural connectivity analysis

Graph theory and network modelling have been applied to characterize structural motor network topology in [MS](#), demonstrating a reduced motor network efficiency through the quantification of structural damage in white matter [WM](#) bundles connecting pairs of cortical and subcortical grey matter [GM](#) regions ([Pardini et al., 2015](#)). More broadly, graph analysis of the structural connectome ([Sporns et al., 2005](#)) (i.e. the set of white-matter pathways between pairs of grey matter regions) has been successfully used to discriminate [MS](#) patients from [HC](#) and to classify [MS](#) clinical phenotypes ([Kocevar et al., 2016](#); [Li et al., 2013](#); [Llufriu et al., 2017](#); [Nigro et al., 2015](#)). However, such between-group differences may be primarily driven by discrepancy in network density ([Van Wijk et al., 2010](#)), which is likely to be reduced in pathologic conditions as a consequence of macroscopic damage and fibres loss. Thus, resulting in a less accurate tracking of streamlines ([Ozturk et al., 2010](#)). In the framework of graph analysis, methods such as the minimum spanning tree have been applied to account for differences in density, by reducing networks to a backbone structure insensitive to alterations in connection strength or linked density ([Tewarie et al., 2015](#)). An alternative and indirect way to deal with group-differences in density is to extract connectivity metrics from an atlas of bundles built from healthy subjects keeping network density constant ([Pagani et al., 2020](#)). Tracing fibres in [HC](#) offers the additional advantage to avoid inaccuracy in tract reconstruction related to the

presence of WM lesions. Therefore, in MS studies, tractography is often performed in the control group (or a subset of it) and the reconstructed tracts are subsequently registered to patients' data to derive the metrics of interest ((Pagani et al., 2020; Pardini et al., 2015; Steenwijk et al., 2015). Although the underlying idea is the same, its implementation is slightly different in each of these works. Pagani et al. (2020) first co-registered the diffusion tensor images of healthy controls to the standard Montreal Neurological Institute (MNI) space; then they used the average of those data to perform tractography saving only the tracts connecting pairs of cortical areas with more than five streamlines as voxel maps. Finally, registered all the remaining subjects to MNI space and they used the common tractogram to compute the individual connectomes. Pardini et al. (2015) instead performed tractography in each individual healthy subject's space and then registered the recovered track density images to the MNI space to create a population-averaged maps for each tracts of interest. They then co-registered these maps to each subject involved in the study to compute the connectomes. Finally Steenwijk et al. (2015) implemented a similar method of Pardini et al. (2015), but they computed for each subject and tract separately the average of weighted lesion volume and weighted average of FA in normal appearing white matter. When tractography is conducted directly in MS patients, an FA threshold is set during fibre reconstruction and a minimum number of fibres is selected to define single bundles in order to reduce the risk of false-positive connections (Nigro et al., 2015; Shu et al., 2011). The shortcoming of this approach is the drastic reduction in reconstructed fibres, especially in those bundles that are rich in crossing fibre (Sinke et al., 2018). More recently, a SIFT (Smith et al., 2013) has been employed to reduce reconstruction bias and improve biological plausibility (Koubiyr et al., 2019), but the accuracy of SIFT application to pathological brains is still under debate (Zalesky et al., 2019).

Furthermore, the characterization of the structural connectome in MS has to take into account the impact of WM lesions on connectivity which is usually assessed through correlation analysis between graph metrics and lesion loads (He et al., 2009; Romascano et al., 2015). A more specific disconnection analysis can also be conducted, quantifying dedicated graph measures that estimate the indirect, compensatory connections between two regions developed after the transection of the direct

connection between them (Li et al., 2013). More recently, the impact of macroscopic lesions on structural connectivity was modelled assuming transection of all fibres passing through WM lesions (Pagani et al., 2020).

Finally, the quantification of the connection strength in structural connectomes is an open issue. Typically, the connection strength between each pair of grey-matter regions is “quantified” by counting the number of streamlines connecting them, i.e. streamline count, but this approach is not quantitative (Jones et al., 2013). Microstructure informed tractography (Daducci et al., 2016) was recently proposed as a means to improve the estimation of structural connectivity by combining tractography with local microstructural features of the tissue and fitting the actual contributions of the streamlines to the measured diffusion MRI data. These contributions do not allow to estimate the microscopical fibre count, but this approach has the potential to provide a more “physically quantitative” assessment of the connectivity than the simple streamline count. In fact, as the contributions of the streamlines (or weights) are estimated such that they explain the diffusion MRI data and the connectivity is “physically quantified” based on these weights. This possibility to extract more “quantitative” metrics from the reconstructed connectomes may allow for a fair comparison of network properties despite density discrepancies. However, to the best of our knowledge, this approach has never been proposed in clinical studies.

In this proof of concept study, we investigated the topology of the “physically quantitative” sensory-motor network (SMN) (i.e. the network whose weights are estimated through microstructure informed tractography) in MS using the COMMIT (Daducci et al., 2013, 2015). COMMIT allows the tracking of fibres within WM lesions and removes the ones deemed implausible according to the chosen microstructural property only after reconstruction. The goal of this study was to test if abnormalities in network topology are still identifiable when focusing on more “quantitative” network properties. We focused on patients with PMS, who present the highest lesion loads, atrophy degree and, presumably, density reduction among MS clinical phenotypes. Specifically, we evaluated if (i) COMMIT can improve the detection of differences in structural connectome density between MS patients and HC compared to the raw connectome; (ii) differences in network density affect between-group comparisons of connectome properties; (iii) WM lesions and GM atrophy influence

connectome properties; (iv) **SMN** network properties are related to clinical disability.

6.1 Methods

Subjects

Forty-two patients with **PMS** (22 primary and 20 secondary progressive 28F, mean age 51.4 ± 11.4 years, mean disease duration 15.6 ± 13.3 years), and 24 **HC** (11F, mean age 50.3 ± 8.5 years) were prospectively enrolled. Inclusion criteria for patients with **MS** were: age between 18 and 70 years, **MS** diagnosis fulfilling the revised McDonald criteria (Polman et al., 2011) and Expanded Disability Status Scale (**EDSS**) score ≤ 7.0 . Exclusion criteria were: coexistence of any major systemic condition, diagnosis of psychiatric disorders, contraindications to undergo an MRI scan, pregnancy, history of head trauma, alcoholism, drug addiction or neurological disorders other than **MS**. Clinical examination, performed within 1 week from the MRI scan, included **EDSS**, Timed 25-Foot Walk Test (T25FW) and 9-Hole Peg Test (9-HPT). Written informed consent was obtained from all participants before the beginning of the study procedures, according to the Declaration of Helsinki. The protocol was approved by the Institutional Review Board of the Icahn School of Medicine at Mount Sinai.

MRI acquisition All subjects underwent MRI on a Siemens Skyra 3T scanner (Siemens, Erlangen, Germany) with a 32-channel head coil. The MRI protocol included the following sequences: axial T2-weighted 3D (repetition time (TR): 8000 **MS**, TE: 95 **MS**, spatial resolution $0.5 \times 0.5 \times 3.0$ mm³); sagittal T1-weighted 3D magnetization-prepared rapid gradient echo (**MPRAGE**) (TR/TE: 3000/2.47 **MS**, inversion time (TI): 1000 **MS**, spatial resolution $0.8 \times 0.8 \times 0.8$ mm³; GRAPPA with acceleration factor $R = 2$); twice-refocused spin echo cho planar imaging (**EPI**) sequence for diffusion MRI with b-values of 1000 and 2000 s/mm² and 30 directions each (repeated twice), in addition to b=0 images (TR/TE: 4700/100 **MS**, flip angle 80deg, spatial resolution $1.8 \times 1.8 \times 2$ mm³).

Lesion and cortical segmentations

Quantification of T2-hyper-intense and T1-hypo-intense lesion volume was performed in each patient by a single experienced observer unaware of subject identity, employing a segmentation technique based on user-supervised local thresholding (Jim 7.0, Xinapse System, Leicester, UK ¹) as described in [Petracca et al. \(2018\)](#). The corresponding T1-images were then accordingly filled using T1-hypo-intense lesion mask and FSL ².

For all subjects, we processed T1-filled images with FreeSurfer ³ and we automatically segmented them ([Fischl et al., 2002, 2004b](#)) using the standard Desikan-Killiany atlas ([Desikan et al., 2006](#)) which allowed obtaining a cortical parcellation in 85 ROIs. From this parcellation we retrieved the nodes of the motor network comparing FreeSurfer ROIs and the Harvard-Oxford cortical and subcortical structural atlas included in FSL ([Smith et al., 2004](#)). In particular, the primary sensory motor cortex (S-M1) was defined by the post central and precentral gyrus ROIs; the secondary motor cortex (M2) by the paracentral gyrus ROI; the secondary sensory cortex (S2) by the supramarginal gyrus; the posterior associative sensory cortex (AS Sens C) by the precuneus and superior parietal gyrus ROIs; the prefrontal cortex (PFC) by the lateral orbitofrontal, medial orbitofrontal, rostral middle frontal and superior frontal ROIs; the deep GM by the union of the thalamus, caudate, putamen and pallidum ROIs acting as relay for projection tracts and, finally, the cerebellum (cerebellum) as itself. The obtained nodes for one of the healthy subjects included in our analyses are shown in [Figure 6.1](#).

SMN gray matter fraction (GMF) was computed as the sum of the volumes of all above listed areas divided by intra-cranial volume (ICV).

Diffusion MRI processing

Diffusion MR images were corrected for motion and eddy currents ([Andersson et Sotiropoulos, 2016](#)) using FSL. To perform whole brain anatomically constrained trac-

1. <http://www.xinapse.com>
2. <https://fsl.fmrib.ox.ac.uk>
3. <http://surfer.nmr.mgh.harvard.edu>

tography (Smith et al., 2012), we first co-registered the T1 and diffusion images using FLIRT (Jenkinson et al., 2002) of FSL with boundary based cost function (Greve et Fischl, 2009). Then we computed the fiber orientation distribution functions using the multi-shell multi-tissue constrained spherical deconvolution approach (Jeurissen et al., 2014; Tournier et al., 2007a) and generated 1 million streamlines using the iFOD2 (Tournier et al., 2010) tractography algorithm implemented in MRtrix⁴. In light of the discussion in Zalesky et al. (2019), we processed the resulting tractograms using COMMIT (Daducci et al., 2013, 2015) with stick and zeppelin ball model (Alexander et al., 2010). COMMIT is a powerful framework that allows to decompose a signal in contributions coming from different compartments. The main assumption of the framework is that the contribution of a streamline is constant along its path, while the remaining components can be different in each voxel. In this case, we applied COMMIT to dMRI signal and we decomposed the signal in intra-axonal, extra-axonal and isotropic contributions according to the stick and zeppelin ball model (Alexander et al., 2010). Indeed, with this model we imposed that the intra-axonal diffusion signal was constant along each tract and (when needed) we indirectly accounted for the presence of free water due to a lesion with the zeppelin and ball compartments.

Finally, for each subject, both the raw (i.e. obtained using the number of streamlines as entries) and the COMMIT-weighted connectomes (i.e. obtained using COMMIT weights as entries) were built using the motor network parcellation described above (Figure 6.2). As entries (a_{ij}) of COMMIT derived matrices we used the weighted average intra-axonal signal contribution of each bundle:

$$a_{ij} = \frac{\sum_{k=1}^{N_{ij}} x_{ij}^k \cdot l_k}{\sum_{k=1}^{N_{ij}} l_k}, \quad (6.1)$$

where i, j are the indices of ROIs connected by the bundle, N_{ij} is bundle's number of streamlines, x_{ij}^k is the weight of the streamline k obtained by COMMIT and l_k its length. In this way, each entry contained the total signal fraction associated to the bundle, which was given by the weighted average of the streamline contribution

4. <http://www.mrtrix.org>

(obtained with [COMMIT](#)) multiplied by its length and divided by the average length of the bundle.

In light of the recent results showed in ([Buchanan et al., 2020](#)), in the supplementary material, we also report additional results obtained by thresholding the number of streamlines in the raw connectomes according to two widely used techniques: proportional and consistency thresholding. For further details we refer the reader to the online supplementary material.

Graph analysis

As it was done in previous works ([Pagani et al., 2020](#); [Pardini et al., 2015](#); [Steenwijk et al., 2015](#)), for each subject we computed six global network measures from the obtained connectomes using the Brain Connectivity Toolbox ([Rubinov et Sporns, 2010](#)): modularity (reflecting the segregation of the network), global efficiency (corresponding to the average inverse shortest path length in the network, and inversely related to the characteristic path length), clustering coefficient (reflecting the degree to which the nodes tend to cluster together), mean strength (corresponding to the average of all the nodal strengths, where the nodal strength is the sum of the weights of links connected to the node), assortativity (reflecting if nodes tend to be connected to other nodes with similar strengths) and density (corresponding to the fraction of present connections to possible connections). For each node of the subjects' connectome we also computed local efficiency and local nodal strength to investigate which node of the [SMN](#) was more affected by the disease.

Statistical Analysis

All analyses were performed using Statistical Package for Social Science (SPSS V.25.0).

Between-group comparisons were performed via ANCOVA analysis, entering age and gender as covariates. In order to assess differences in density estimation related to the application of [COMMIT](#), we performed between-group comparisons both on results from raw connectomes and [COMMIT](#)-weighted connectomes, and repeated

the analysis entering density as additional covariate.

The relationship between network global properties, T2 lesion load and GM atrophy were tested via partial correlation accounting for age and gender.

The relationship between network properties and clinical disability was tested with stepwise regression models, entering age and gender in the first block and network global/local properties in the second block.

Results were considered significant for $p < 0.05$ (Bonferroni corrected < 0.008 for global properties [0.05/6 as the number of network global properties considered]; Bonferroni corrected < 0.003 for local properties [0.05/14 as the number of nodes considered]).

6.2 Results and discussion

Raw connectomes

Mean values and standard deviations of the global network metrics are reported in 6.3. After Bonferroni correction for multiple comparisons, modularity, global efficiency and mean strength were significantly different between the two groups of subjects when accounting for age and sex. When controlling also for density only the difference in modularity was still present. Of note, no significant differences in density were identified between the two groups.

Mean values and standard deviations of the local network metrics are reported in Tab. 6.4 (strength) and 6.3 (efficiency). After Bonferroni correction for multiple comparisons, significant differences were identified in 5 nodes in terms of strength and in 9 nodes in terms of efficiency between the two groups of subjects when accounting for age and sex. When controlling also for density, significant differences were still identified in 2 nodes in terms of strength and in 6 nodes in terms of efficiency.

COMMIT-weighted connectomes

Mean values and standard deviations of the global network metrics are reported in Tab. 6.6. After Bonferroni correction for multiple comparisons, all the explored

metrics, except the clustering coefficient, were significantly different between the two groups of subjects when controlling for age and sex. When controlling also for density the difference in assortativity disappeared.

Mean values and standard deviations of the local network metrics are reported in Tab. 6.7 (strength) and 6.8 (efficiency). After Bonferroni correction for multiple comparisons, significant differences were identified in 6 nodes in terms of strength and in 7 nodes in terms of efficiency between the two groups of subjects when accounting for age and sex. When controlling also for density significant differences were still identified in the same nodes in terms of strength and in 7 nodes in terms of efficiency.

Relationship between raw connectome global properties, WM lesions and GM atrophy

Accounting for age and gender, significant correlations were identified between T2 lesion volume and global efficiency ($r = -0.655$, $p < 0.0001$), clustering coefficient ($r = -0.469$, $p = 0.002$), modularity ($r = 0.640$, $p < 0.0001$), density ($r = -0.696$, $p < 0.0001$), mean strength ($r = -0.630$, $p < 0.0001$). No correlations were identified between [SMN GMF](#) and global metrics.

Relationship between COMMIT-weighted connectome global properties, WM lesions and GM atrophy

Accounting for age and gender, significant correlations were identified between T2 lesion volume and global efficiency ($r = -0.431$, $p = 0.005$), modularity ($r = 0.507$, $p = 0.001$) and density ($r = -0.738$, $p < 0.0001$) as well as between [SMN GMF](#) and mean strength ($r = 0.425$, $p = 0.006$).

Clinical impact of raw connectome abnormalities

The models including demographic variables and network global properties accounted for 40% of variance in 9HPT scores (for density $R^2=0.40$, $p=0.001$, Beta=-0.57, $p=0.003$) and 32% of variance in 25FWT (for density $R^2=0.32$, $p=0.004$, Beta=-

0.51, $p=0.001$; for assortativity $R^2=0.32$, $p=0.004$, $\text{Beta}=0.51$, $p=0.001$). No significant results were yielded by the model including demographic variables and node local properties.

Clinical impact of COMMIT-weighted connectome abnormalities

The models including demographic variables and network global properties accounted for 27% to 35% of variance in 9HPT scores (for modularity $R^2=0.27$, $p=0.018$, $\text{Beta}=0.45$, $p=0.007$; for density $R^2=0.35$, $p=0.003$, $\text{Beta}=-0.53$, $p=0.001$). The model including demographic variables and node local properties accounted for 58% of variance in 9HPT scores (for right prefrontal cortex local efficiency $R^2=0.58$, $p=0.008$, $\text{Beta}=-0.53$, $p=0.003$); and 66% of variance in T25FWT scores (for associative sensory cortex local efficiency $R^2=0.66$, $p=0.001$, $\text{Beta}=1.12$, $p<0.001$).

Notwithstanding all previous efforts in investigating structural connectivity and disconnection in MS, in this study we propose a methodological approach - COMMIT - that accounts for the presence of lesions and fibres loss and provides a means to directly compare connectomes with different density.

Thanks to its capability of decomposing the intrinsic signal contribution of each streamline in the tractogram, COMMIT may represent an effective method to cope with density discrepancies between healthy subjects and patients. The main idea behind this method is to assume that one (or more) microstructure feature does not vary along the length of a tract and therefore it is possible to effectively estimate its value for the entire tract (rather than only voxel-wise). This estimation is done simultaneously for all the streamlines by fitting them to a map related to the selected microstructure feature. If only dMRI data are available, it is reasonable to assume that the intra-axonal diffusion signal is constant along the tract and COMMIT uses any predefined microstructural model to estimate it. Similarly to what was recently found in Lipp et al. (2020), using the recently introduced multi-shell multi-tissue spherical deconvolution (Jeurissen et al., 2014) and the probabilistic algorithm (Tournier et al., 2010) to generate streamlines, we were able to propagate the tracking also inside MS lesions to build the input tractograms. We then applied COMMIT to decide if a streamline passing through a lesion is essential to explain the signal or not and con-

sequently keeps or discards it to construct the final tractogram. In the present work, we employed as microstructural model the stick and zeppelin ball model (Alexander et al., 2010) which indirectly accounts for the presence of free water due to a lesion with the zeppelin and ball compartments. Finally, to construct the COMMIT-weighted connectomes we chose not to use the traditional number of streamlines connecting two cortical regions of interest (streamlines count), which was shown not to be quantitative (Jones et al., 2013). Conversely, we considered the more informative total signal fraction associated to the bundle, which is given by the weighted average of the streamline contribution (obtained with COMMIT) multiplied by its length and divided by the average length of the bundle. This approach offers two main advantages. First, by forcing fibre tracking within lesions and subsequently filtering them according to the signal preservation along the streamline, COMMIT retains in the tractogram only fibres whose microstructure is not irredeemably damaged by lesions or subtle inflammatory/neurodegenerative processes ongoing in the normal appearing WM (Lassmann, 2018). Thus, producing a weighted network composed by “healthy” and partly damaged fibres whose signal is not irreversibly compromised and can be fitted with a stick. As a consequence of COMMIT’s filtering, in the COMMIT-weighted connectomes we observed a reduction in density in comparison with the raw connectomes both in patients and controls (Figure 6.9).

A number of implausible connections, related to tractography intrinsic limitations, as well as the fact that our control group presumably presented age-related subtle WM abnormalities, were removed in healthy controls. As expected though, the number of implausible connections removed in patients was even higher, which explains why differences in terms of density between patients and controls became apparent only after COMMIT application. Second, by giving the possibility to compare more “quantitative” metrics rather than measures derived from the non-quantitative streamline number (Jones et al., 2013), COMMIT offers the possibility to assess differences in network properties beyond changes driven by density discrepancy. This is supported by the results of our between-group comparison, which shows that, while topology differences identified with standard tractography were mainly driven by density, differences in global and local properties derived from the COMMIT-weighted connectomes were insensitive to density correction (Figure 6.9, 6.10, 6.11). Finally,

it is worth highlighting that although COMMIT estimates the actual weight of the edges in the network by fitting the corresponding streamlines to the white-matter signal, normalization may still be required to account for ROI size differences in the chosen parcellation (Sotiropoulos et Zalesky, 2019). In fact, larger ROIs may be connected with more streamlines simply because of their size. Note, however, that this applies to raw and COMMIT-weighted connectomes alike, and hence it does not bias our results. Future studies will investigate the possibility to COMMIT to account also for this aspect.

Differences in connectome global properties estimated after COMMIT application suggest that also the COMMIT-weighted connectome presents the topology abnormalities previously described in MS (Kocevar et al., 2016; Li et al., 2013; Llufriu et al., 2017; Nigro et al., 2015; Pardini et al., 2015). Indeed, the COMMIT-weighted SMN was less efficient, more dispersed and weaker in MS than in HC, supporting the notion that also seemingly intact connections are not sufficient to preserve brain structure. As COMMIT retains also connections partly affected by WM lesions, WM bundles entered in the COMMIT-weighted connectome still suffer the consequences of smouldering inflammation, axonal and neuronal damage within focal lesions, and periventricular damage sustained by detrimental soluble factors (Lassmann, 2018). Fibres damage and loss above a certain threshold could eventually leave a vulnerable structure, not able to sustain efficient network function. Assortativity was the only network property still affected by density after COMMIT application, suggesting that nodes' connection strength in the COMMIT-weighted connectome depends on the presence of preserved connections. The strong link between density and assortativity is also highlighted by their comparable predictive power on clinical disability. Locally, strength and efficiency were decreased in the prefrontal cortex, primary sensory-motor areas, associative sensitive cortex and deep GM, confirming the diffuse involvement of cortical and deep GM regions reported in the progressive phenotypes (Eshaghi et al., 2018) (Figure 6.10, 6.11). COMMIT-weighted SMN global properties showed strong to moderate associations with WM lesion load and atrophy, confirming that brain topological organization is related to the accrual of macrostructural damage (Pagani et al., 2020), with lesion load playing a predominant role in progressive MS (Steenwijk et al., 2015). Of note though, raw SMN global properties showed even stronger

relationships with WM lesion load, once again supporting the notion that network properties derived from raw connectomes are substantially influenced by the presence of lesions. On the other hand, the effects of atrophy were not detectable, possibly because of the dominant influence of WM lesion load itself. As per the clinical impact of network topology, raw connectomes properties were not predictive of clinical status, while among COMMIT-weighted connectomes properties the main role was played by nodes' local efficiency, which predicted a large amount of variance in motor disability. Prefrontal cortex efficiency was particularly relevant for manual dexterity performance, highlighting the importance of motor planning for the execution of fine motor movements, while efficiency of associative sensory cortex was significantly correlated with the ambulation performance. Interestingly, it seems that the efficiency of integrative rather than primary areas is particularly relevant for clinical function preservation within the weighted connectome, highlighting the compensatory role of these regions in advanced disease stages.

Topology differences identified with standard tractography in MS seem to be mainly driven by density, which, in turn, is strongly influenced by the presence of lesions, suggesting caution when interpreting between group differences in connectome properties. Moving from a qualitative towards a more “quantitative” appraisal of the brain structural connectome, COMMIT application allowed the identification of a significant difference in density between patients and HC and the exploration of network topology in the COMMIT-weighted connectome. Differences observed in network global and local properties suggest that preserved connections undergo a topological reorganization in MS. Within such reorganization of the brain connectome, decreased local efficiency in key areas of the SMN represent the most relevant correlates of motor disability. Based on these results, we believe that COMMIT may help characterize the topological organization of structural networks in pathological conditions, allowing a fair comparison of connectomes which takes into account discrepancies in network density. More importantly, our study shows that discrepancy-corrected network properties are clinically meaningful and, therefore, may help guide prognosis assessment and treatment choice.

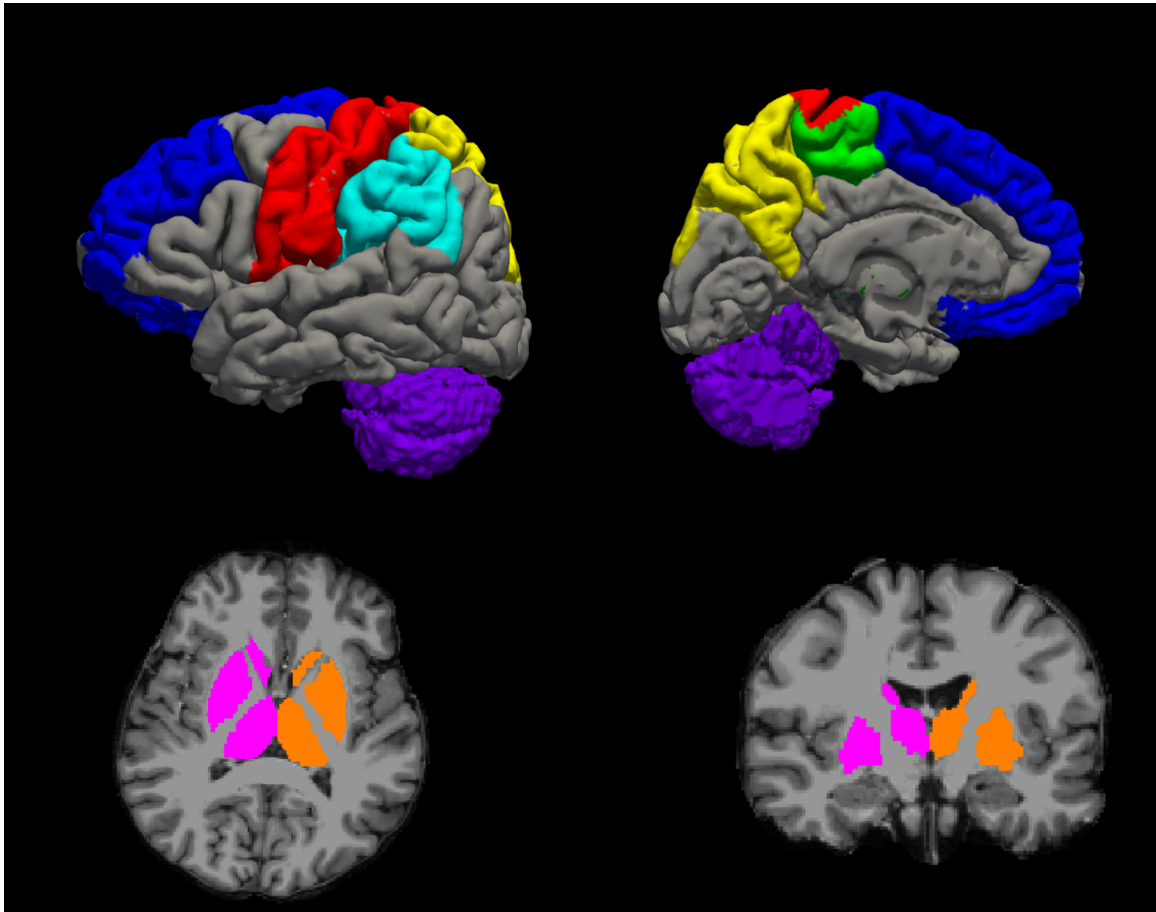


Figure 6.1 – Motor network hubs used in our analysis in a representative healthy subject. The primary sensory-motor cortex (S-M1) is shown in red; the secondary motor cortex (M2) in green; the secondary sensory cortex (S2) in light blue; the posterior associative sensory cortex (AS Sens C) in yellow; the prefrontal cortex (PFC) in blue; the deep grey matter (Deep GM) in pink (for the right hemisphere) and orange (for the left hemisphere) and the cerebellum in purple.

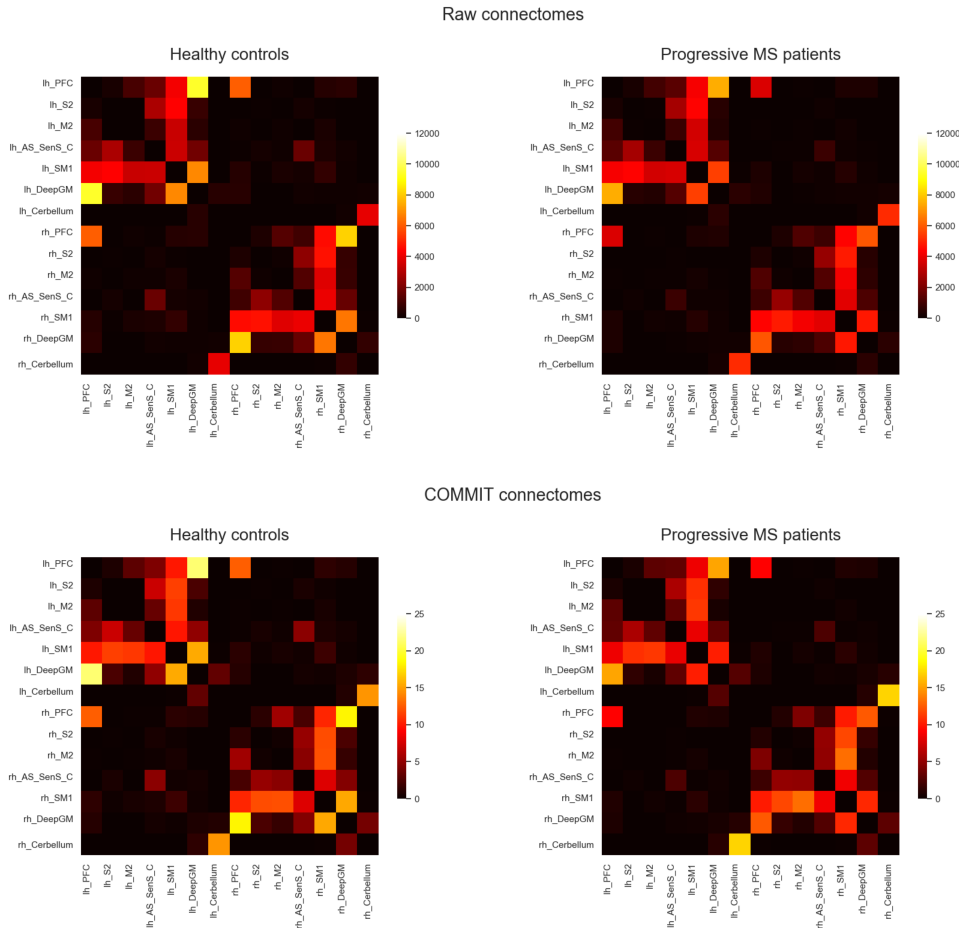


Figure 6.2 – Matrix representation of the connectomes obtained with the two different methods: counting the number of streamlines connecting two pairs of grey matter regions (top); or assigning the quantitative measures obtained with **COMMIT** (bottom). For both method we report the average connectomes obtained for the two groups of subjects: healthy controls (left) and **PMS** patients (right). In both cases (raw and **COMMIT**), the pattern of connections is similar, but while in the upper case the information contained in the connectomes is non-quantitative, in the bottom ones it represents the intra-axonal signal fraction associated to each connection. We also observe that some interhemispheric connections present in the raw connectomes disappear after the application of **COMMIT**.

	HC (n = 24)	PMS (n = 42)	p^a	p^b
Modularity	0.39 ± 0.03	0.46 ± 0.06	<.001	<.001
Global efficiency	1997.23 ± 242.51	1,716.31 ± 379.93	.003	.024
Clustering coefficient	2,376.28 ± 281.07	2,340.14 ± 385.03	.958	.327
Mean strength	14,726.32 ± 1,742.35	12,701.39 ± 2,682.28	.002	.017
Assortativity	-0.13 ± 0.02	-0.12 ± 0.03	.113	.208
Density	0.94 ± 0.02	0.91 ± 0.08	.055	-

Figure 6.3 – Global graph metrics of HCs and PMS patients computed on the raw connectomes.

	Side	HC (n = 24)	PMS (n = 42)	p^a	p^b
PFC	R	22,763.00 ± 3,061.27	17,223.40 ± 5,448.31	<.001	<.001
	L	24,068.79 ± 3,684.92	19,031.62 ± 6,314.12	.001	.010
S2	R	8,730.58 ± 1,326.41	8,490.48 ± 1832.01	.685	.417
	L	8,847.83 ± 1,428.36	8,494.86 ± 1819.53	.508	.651
M2	R	8,164.50 ± 1,553.38	7,556.55 ± 1,558.34	.129	.428
	L	6,648.67 ± 1,451.18	6,142.43 ± 1,421.49	.201	.452
As Sens C	R	12,782.87 ± 2,542.15	10,918.00 ± 3,097.91	.029	.216
	L	13,511.79 ± 2027.72	11,186.31 ± 3,014.71	.002	.018
S-M1	R	25,710.50 ± 3,185.54	23,091.50 ± 4,319.22	.025	.215
	L	24,168.08 ± 3,993.54	22,589.05 ± 4,580.20	.219	.866
Deep GM	R	19,671.92 ± 3,032.35	14,175.50 ± 5,019.85	<.001	<.001
	L	21,266.62 ± 3,421.53	16,600.62 ± 5,764.56	.001	.004
Cerebellum	R	5,024.42 ± 2,200.44	6,222.33 ± 2,177.42	.037	.059
	L	4,808.92 ± 2,198.79	6,096.78 ± 2,301.40	.037	.061

Figure 6.4 – Nodes strength of HCs and PMS patients computed on the raw connectomes.

	Side	HC (n = 24)	PMS (n = 42)	p^a	p^b
PFC	R	709.40 ± 103.54	546.64 ± 171.56	<.001	.001
	L	707.44 ± 124.48	556.60 ± 190.01	.002	.012
S2	R	401.98 ± 53.94	385.79 ± 100.87	.398	.073
	L	379.30 ± 62.29	370.41 ± 89.42	.766	.274
M2	R	434.33 ± 76.70	352.43 ± 83.17	<.001	.002
	L	401.06 ± 67.52	335.49 ± 88.80	.002	.006
As Sens C	R	620.74 ± 111.40	479.05 ± 131.44	<.001	<.001
	L	656.76 ± 110.77	492.80 ± 122.97	<.001	<.001
S-M1	R	839.94 ± 128.53	674.43 ± 172.13	<.001	.001
	L	783.84 ± 138.19	654.77 ± 171.33	.004	.028
Deep GM	R	646.60 ± 109.95	498.40 ± 159.60	<.001	.001
	L	658.61 ± 107.49	537.86 ± 161.56	.002	.014
Cerebellum	R	163.01 ± 61.32	153.46 ± 50.50	.608	.911
	L	130.99 ± 52.71	129.97 ± 44.51	.977	.602

Figure 6.5 – Nodes efficiency of **HC** and **PMS** patients computed on the raw connectomes.

	HC (n = 24)	PMS (n = 42)	p^a	p^b
Modularity	0.41 ± 0.02	0.46 ± 0.05	<.001	.005
Global efficiency	5.27 ± 0.62	4.35 ± 0.52	<.001	<.001
Clustering coefficient	5.67 ± 0.81	5.18 ± 0.70	.024	.025
Mean strength	38.15 ± 4.22	31.64 ± 3.88	<.001	<.001
Assortativity	-0.16 ± 0.03	-0.13 ± 0.04	.006	.188
Density	0.88 ± 0.26	0.82 ± 0.09	.004	-

Figure 6.6 – Global graph metrics of **HCs** and **PMS** patients on **COMMIT**-weighted connectomes.

	Side	HC (n = 24)	PMS (n = 42)	p ^a	p ^b
PFC	R	53.16 ± 9.33	40.86 ± 8.78	<.001	<.001
	L	54.88 ± 7.22	42.81 ± 10.57	<.001	.001
S2	R	22.19 ± 5.71	19.53 ± 4.47	.064	.235
	L	23.20 ± 4.95	19.21 ± 4.66	.002	.011
M2	R	25.54 ± 6.42	24.68 ± 6.77	.587	.500
	L	19.69 ± 5.61	18.60 ± 4.99	.425	.107
As Sens C	R	31.19 ± 4.43	26.55 ± 6.54	.005	.079
	L	36.77 ± 7.37	27.43 ± 6.34	<.001	<.001
S-M1	R	62.95 ± 11.77	56.30 ± 9.03	.027	.129
	L	62.66 ± 13.90	52.03 ± 8.32	<.001	.002
Deep GM	R	49.71 ± 6.63	34.08 ± 10.30	<.001	<.001
	L	52.55 ± 14.48	36.69 ± 9.90	<.001	<.001
Cerebellum	R	20.35 ± 7.87	22.26 ± 7.73	.232	.698
	L	19.30 ± 7.30	21.88 ± 7.72	.174	.676

Figure 6.7 – Nodes strength of HCs and PMS patients computed on COMMIT-weighted connectomes.

	Side	HC (n = 24)	PMS (n = 42)	p ^a	p ^b
PFC	R	1.84 ± 0.34	1.48 ± 0.23	<.001	<.001
	L	1.71 ± 0.28	1.43 ± 0.31	.001	.022
S2	R	1.12 ± 0.22	1.23 ± 0.52	.349	.233
	L	1.10 ± 0.20	1.10 ± 0.49	.918	.007
M2	R	1.25 ± 0.25	1.19 ± 0.36	.456	.022
	L	1.12 ± 0.20	1.19 ± 0.57	.531	.060
As Sens C	R	1.59 ± 0.18	1.41 ± 0.35	.026	.001
	L	1.82 ± 0.26	1.46 ± 0.45	.001	<.001
S-M1	R	2.12 ± 0.32	1.78 ± 0.41	.001	.001
	L	2.12 ± 0.36	1.69 ± 0.36	<.001	<.001
Deep GM	R	1.72 ± 0.21	1.37 ± 0.23	<.001	<.001
	L	1.72 ± 0.28	1.37 ± 0.32	<.001	<.001
Cerebellum	R	0.76 ± 0.26	0.67 ± 0.18	.095	.080
	L	0.79 ± 0.26	0.70 ± 0.20	.094	.140

Figure 6.8 – Nodes efficiency of HCs and PMS patients computed on COMMIT-weighted connectomes.

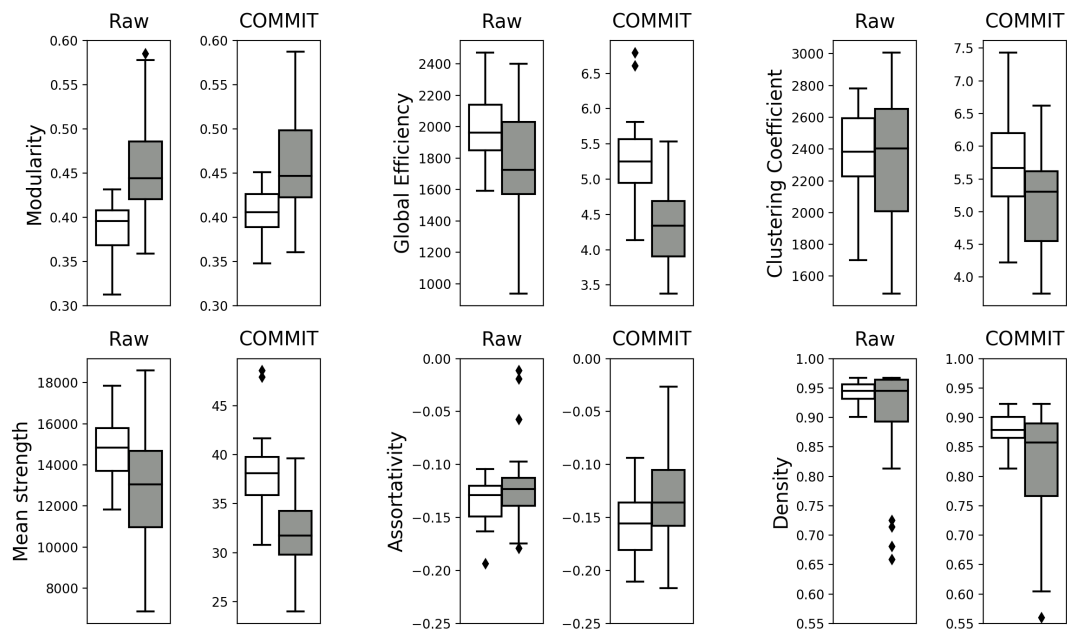


Figure 6.9 – Boxplots showing the differences in global network measures between HCs (white) and PMS patients (grey) for both raw and COMMIT tractograms. We observe that after the application of COMMIT the differences between HC and PMS patients are more pronounced. Also, the presence of outliers is often mitigated when COMMIT is applied.

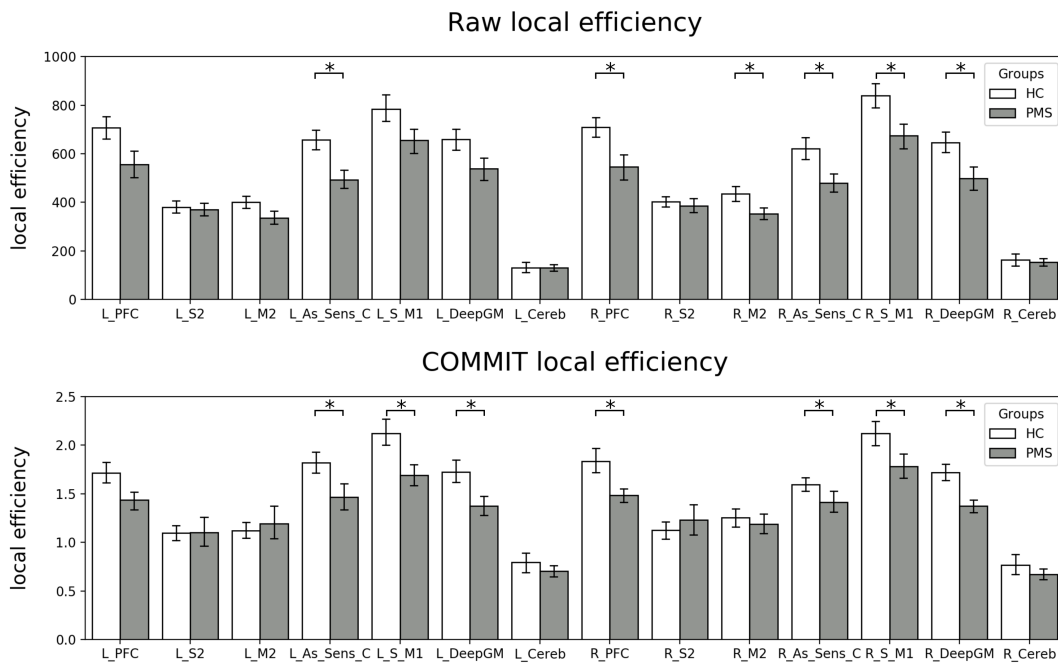


Figure 6.10 – Barplot showing the local efficiency of all the hubs of the motor network for both raw and COMMIT connectomes. The statistically significant differences between HCs in white and PMS patients in grey and accounting for discrepancies in age, sex and density are marked with an asterisk.

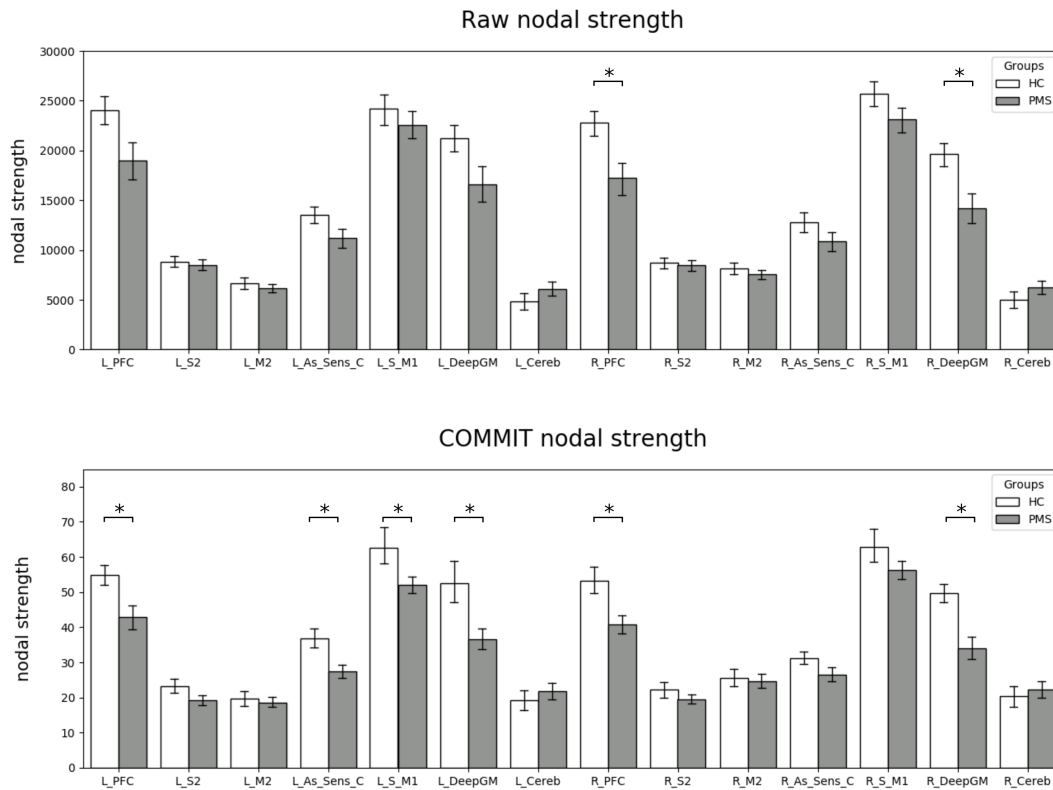


Figure 6.11 – Barplot showing the strength of all the nodes of the motor network for both raw and **COMMIT** tractograms. The statistically significant differences between **HCs** in white and **PMS** patients in grey and accounting for discrepancies in age, sex and density are marked with an asterisk. With the application of **COMMIT** differences in the left associative sensory cortex, sensory-motor and right deep grey matter strength appears.

Chapter 7

Corpus callosum damage in multiple sclerosis

Over the last decades, the application of advanced neuroimaging techniques and new processing methods (Inglese et al., 2018) has clarified that damage of specific white matter WM tracts contributes to different aspects of clinical disability in MS (Barone et al., 2018; Bester et al., 2013; Bodini et al., 2013; Margoni et al., 2019; Palotai et al., 2020; Wahl et al., 2011). Amongst WM tracts, the CC is one of the preferential sites of clinically eloquent damage (Barone et al., 2018; Bodini et al., 2013; Granberg et al., 2015), since it is the target of both direct damage from focal lesions/diffuse neurodegenerative processes and indirect damage deriving from Wallerian degeneration of axons transected by hemispheric lesions (Garg et al., 2015). So far, the relevance of CC damage has been documented in relapsing–remitting multiple sclerosis (RRMS) (Barone et al., 2018; Bester et al., 2013; Bodini et al., 2013; Wahl et al., 2011), benign (from a physical disability standpoint) MS (Bester et al., 2013) and primary progressive multiple sclerosis (PPMS) (Bodini et al., 2013) but a characterization of the interhemispheric disconnection across the entire disease spectrum is still lacking. From a methodological standpoint, in all previous studies interhemispheric disconnection has been inferred as a consequence of callosal atrophy (indirect quantification of fibre loss expressed as area, volume or thickness) or callosal microstructural damage (expressed as mean or voxel-wise diffusion metrics). Whilst both these factors probably influence the structural connectivity between the two

hemispheres, neither of them provides a direct quantification of such connection.

Here the streamlines passing through the CC were quantified with a tractography-based approach, and the density of interhemispheric connection accounting for the number of reconstructed streamlines and volume of the CC was computed. Streamline density represents a measure of the interhemispheric connection that accounts not only for the effects of microstructural and macrostructural damage on fibre reconstruction but also for the anatomical variability in CC volume, which is particularly relevant when evaluating people with multiple sclerosis (pwMS) in advanced disease stages. Specifically, CC damage was assessed in five callosal subregions, and it was investigated whether (i) damage was evenly distributed along the CC; (ii) a phenotype specific pattern of CC damage could be identified indifferent MS phenotypes; (iii) a relationship could be established between CC density, hemispheric/ CC macroscopic lesions and GM atrophy; (iv) CC damage could account for the motor and cognitive status of pwMS.

7.1 Methods

Participants

Fifty-five pwMS [13 RRMS, 20 s secondary progressive multiple sclerosis (SPMS), 22 PPMS, diagnosed according to the revised McDonald criteria (Polman et al., 2011) and 24 HCs were prospectively enrolled (Tab. 7.1). Written informed consent was obtained from all participants before the beginning of the study procedures, according to the Declaration of Helsinki. The protocol was approved by the Institutional Review Board of the Icahn School of Medicine at Mount Sinai. Clinical examination, performed within 1 week from the MRI scan, included the EDSS, the Timed 25-Ft Walk Test (T25FWT), the Nine-Hole Peg Test (9-HPT) and the Brief International Cognitive Assessment of Multiple Sclerosis battery [Brief Visuospatial Memory Test Revised (SDMT), Brief Visuospatial Memory Test Revised (BVMT), California Verbal Learning Test II (CVLT)] (Tab. 7.2).

Magnetic resonance imaging data acquisition and processing

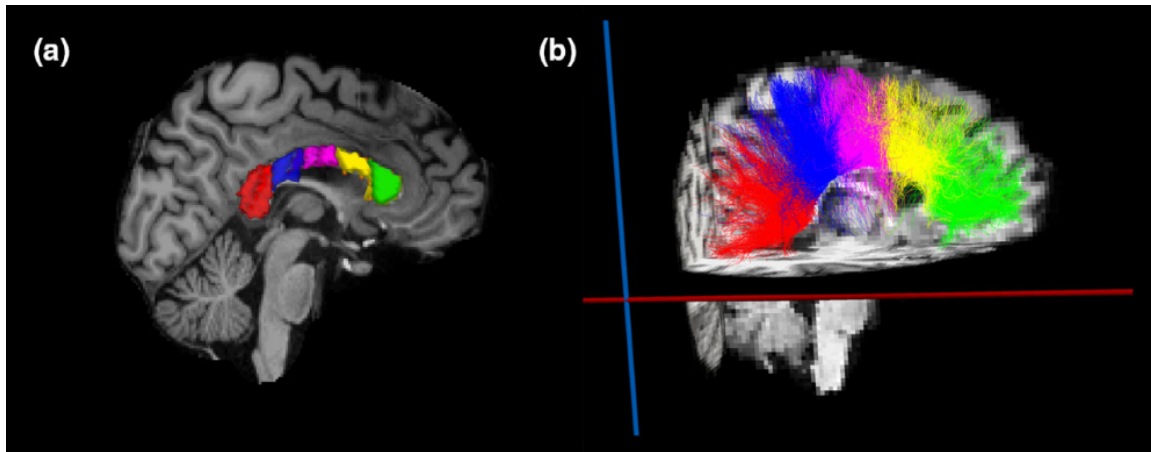


Figure 7.1 – From left to right, images taken from a healthy subject participating in our study: (a) sagittal view of the T1-weighted image with the corpus callosum parcellation in anterior, mid-anterior, central, mid-posterior and posterior; (b) all the streamlines passing through the corpus callosum coloured according to the corpus callosum region they cross.

Images were acquired using a 3-T MRI scanner. T1 images were segmented using the standard FreeSurfer Desikan–Killiany atlas (Desikan et al., 2006) and the CC was divided into five ROIs: anterior, mid-anterior, central, mid-posterior and posterior (Figure 7.1). The volume of each ROI was obtained and the portion affected by T2 hyperintense lesions was quantified, as well as the hemispheric lesion volume (LV). The GM fraction was computed. Whole-brain anatomically constrained tractography (Smith et al., 2012) was performed and the streamlines passing through each CC ROI were extracted. The CC density was computed as the ratio between the number of streamlines and the volume of the considered CC portion in each subject. See Appendix S1 for more details.

Statistical analysis

All analyses were performed using the Statistical Package for the Social Sciences¹. Between-group comparisons were performed with ANCOVA, accounting for age, gender and disease duration. The relationship between CC density, hemispheric/CC macroscopic lesions and GM atrophy as well as the relationship between MRI vari-

1. SPSS V.25.0, SPSS Inc., Chicago, IL, USA

ables and motor/cognitive disability were assessed with hierarchical linear regression models. See Appendix S1 for more details.

7.2 Results and discussion

	HCs	RRMS	SPMS	PPMS	(a) <i>P</i>	(b) <i>P</i>	(c) <i>P</i>	(d) <i>P</i>	(1) <i>P</i>	(2) <i>P</i>	(3) <i>P</i>	(4) <i>P</i>
Age, years	46.46 ± 10.57	46.85 ± 11.25	55.30 ± 8.47	52.36 ± 9.76	<i>0.015</i>	0.910	<i>0.004</i>	0.048	0.058	0.018	0.110	0.331
Gender (M:F)	12:12	5:8	5:15	10:12	0.371	0.373	0.082	0.495	0.382	0.329	0.482	0.145
Disease duration, years	–	14.92 ± 8.54	23.05 ± 13.67	8.91 ± 5.26	–	–	–	–	<i>0.0001</i>	0.027	0.092	<i>0.00003</i>
CC anterior density	13.15 ± 3.04	13.11 ± 1.79	11.56 ± 3.31	11.98 ± 2.27	0.235	0.893	0.064	0.189	0.239	0.092	0.380	0.399
CC mid-anterior density	15.04 ± 3.60	15.48 ± 3.45	12.29 ± 4.71	13.05 ± 3.28	0.050	0.830	0.019	0.096	0.107	0.038	0.160	0.473
CC central density	14.69 ± 3.66	15.95 ± 4.51	12.16 ± 4.75	14.28 ± 4.36	0.029	0.471	0.015	0.544	0.041	0.015	0.430	0.080
CC mid-posterior density	13.58 ± 2.64	11.63 ± 4.82	9.62 ± 4.71	11.25 ± 4.44	0.024	0.165	<i>0.003</i>	0.060	0.668	0.488	0.397	0.866
CC posterior density	16.64 ± 3.49	14.32 ± 4.53	12.93 ± 4.45	12.82 ± 3.91	0.009	0.066	<i>0.003</i>	<i>0.003</i>	0.447	0.514	0.226	0.552
CC anterior LV, ml	–	0.006 ± 0.008	0.065 ± 0.138	0.021 ± 0.038	–	–	–	–	0.116	0.040	0.366	0.226
CC mid-anterior LV, ml	–	0.030 ± 0.045	0.059 ± 0.104	0.046 ± 0.101	–	–	–	–	0.660	0.371	0.545	0.767
CC central LV, ml	–	0.032 ± 0.054	0.056 ± 0.103	0.046 ± 0.129	–	–	–	–	0.772	0.478	0.656	0.785
CC mid-posterior LV, ml	–	0.014 ± 0.017	0.061 ± 0.111	0.015 ± 0.029	–	–	–	–	0.048	0.037	0.966	0.030
CC posterior LV, ml	–	0.019 ± 0.036	0.048 ± 0.089	0.021 ± 0.048	–	–	–	–	0.375	0.171	0.620	0.367
Hemispheric LV, ml	–	4.81 ± 5.88	5.74 ± 8.77	3.73 ± 4.59	–	–	–	–	0.965	0.813	0.981	0.827
GM fraction	0.419 ± 0.042	0.387 ± 0.019	0.386 ± 0.051	0.371 ± 0.025	<i>0.002</i>	0.006	0.026	<i>0.0003</i>	0.220	0.302	0.522	0.086

Table 7.1 – (a) *P* values of the ANCOVA analysis for the between-group comparison **HCs** versus **RRMS** versus **SPMS** versus **PPMS**, corrected for age and gender. (b)–(d) *P* values of the post hoc subgroup comparisons **RRMS** versus **HCs** (b), **SPMS** versus **HCs** (c), **PPMS** versus **HCs** (d). (1) *p* values of the ANCOVA analysis for the between-group comparison **RRMS** versus **SPMS** versus **PPMS**, corrected for age, gender and disease duration. (2)–(4) *p* values of the post hoc subgroup comparisons **SPMS** versus **RRMS** (2), **PPMS** versus **RRMS** (3), **PPMS** versus **SPMS** (4). For age and gender, *p* values of the chi-squared/Fisher test and ANOVA comparison are reported. Significant *p* values are highlighted in bold. Results that would survive Bonferroni correction (demographics $0.05/3 = 0.02$, **MRI** variables $0.05/12 = 0.004$) are shown in italics. All values are reported as mean ± standard deviation.

Demographic and clinical assessment

Differences in demographic and clinical features are reported in Tab. 7.1 and 7.2.

Topology of **CC damage and phenotypic pattern: between-group comparisons** Differences in streamline density were detected between **pwMS** and **HCs** in the mid-anterior ($p = 0.050$), central ($p = 0.029$), mid-posterior ($p = 0.024$) and posterior ($p = 0.009$) **CC**. A post hoc analysis revealed no differences in **CC** density between people with **RRMS** and **HCs**, with a trend present only for the posterior **CC** ($p = 0.066$). People with **SPMS** showed a widespread decrease in density in comparison

	RR-MS	SP-MS	PP-MS	P ¹	P ²	P ³	P ⁴
EDSS, median (range)	2 (0-6)	6 (2-6)	6 (2-6)	<i>.0000</i>	<i>.0000</i>	<i>.0000</i>	.830
				<i>3</i>	<i>8</i>	<i>4</i>	
T25FWT, seconds	4.02 ± .33	8.25 ± 3.20	11.18 ± 15.75	.306	.349	.127	.504
9-HPT, seconds	21.97 ± 3.37	31.39 ± 8.45	28.87 ± 7.11	<i>.002</i>	<i>.001</i>	<i>.009</i>	.588
BVMT	21.55 ± 7.50	18.84 ± 8.45	16.30 ± 9.41	.328	.499	.141	.389
CVLT	52.91 ± 10.22	52.63 ± 11.94	53.80 ± 16.68	.730	.809	.448	.582
SDMT	52.27 ± 9.30	45.95 ± 11.14	48.10 ± 14.79	.557	.316	.375	.899

Table 7.2 – Clinical features of the study population. p -values of the ANCOVA analysis for the between-group comparison **RRMS** vs **SPMS** vs **PPMS**, corrected for age, gender and disease duration are reported in (1), as well as p -values of the post-hoc subgroup comparisons **SPMS** vs **RRMS** (2), **PPMS** vs **RRMS** (3), **PPMS** vs **SPMS** (4). ANCOVA analysis of cognitive scores was additionally corrected for years of education. Results that would survive Bonferroni correction ($0.05/6 = 0.08$), are shown in italics. All values are reported as mean \pm standard deviation.

with **HCs**, involving the mid-anterior ($p = 0.019$), central ($p = 0.015$), mid-posterior ($p = 0.003$) and posterior ($p = 0.003$) **CC**. People with **PPMS** showed a significant decrease in density in comparison with **HCs** in the posterior **CC** ($p = 0.003$), with a significance trend for the mid-posterior **CC** ($p = 0.060$) (Figure 7.2). The results of the between-group comparisons and a direct comparison of **pwMS** subgroups are summarized in Tab. 7.1.

Relationship between **CC** density, **LV** and **GM** fraction

Accounting for the effects of age, gender and disease duration, **CC** density was significantly predicted by fraction ($R^2 = 0.194$, $p = 0.012$), with **CC LV** and hemispheric **LV** as only independent predictors ($\beta = 0.425$, $p = 0.001$, and $\beta = 0.416$, $p = 0.002$, respectively).

Relationship between **CC** damage and clinical disability

Accounting for age, gender, disease duration and years of education, the models including **CC** density, **CC LV**, hemispheric **LV** and **GM** fraction significantly predicted **BVMT** ($R^2 = 0.362$, $p = 0.013$), **CVLT** ($R^2 = 0.199$, $p = 0.027$) and **SDMT** ($R^2 = 0.309$, $p = 0.003$), with **CC** density being an independent predictor of **BVMT** ($\beta = 0.344$, $p = 0.023$) and **GM** fraction being an independent predictor of **BVMT** ($\beta =$

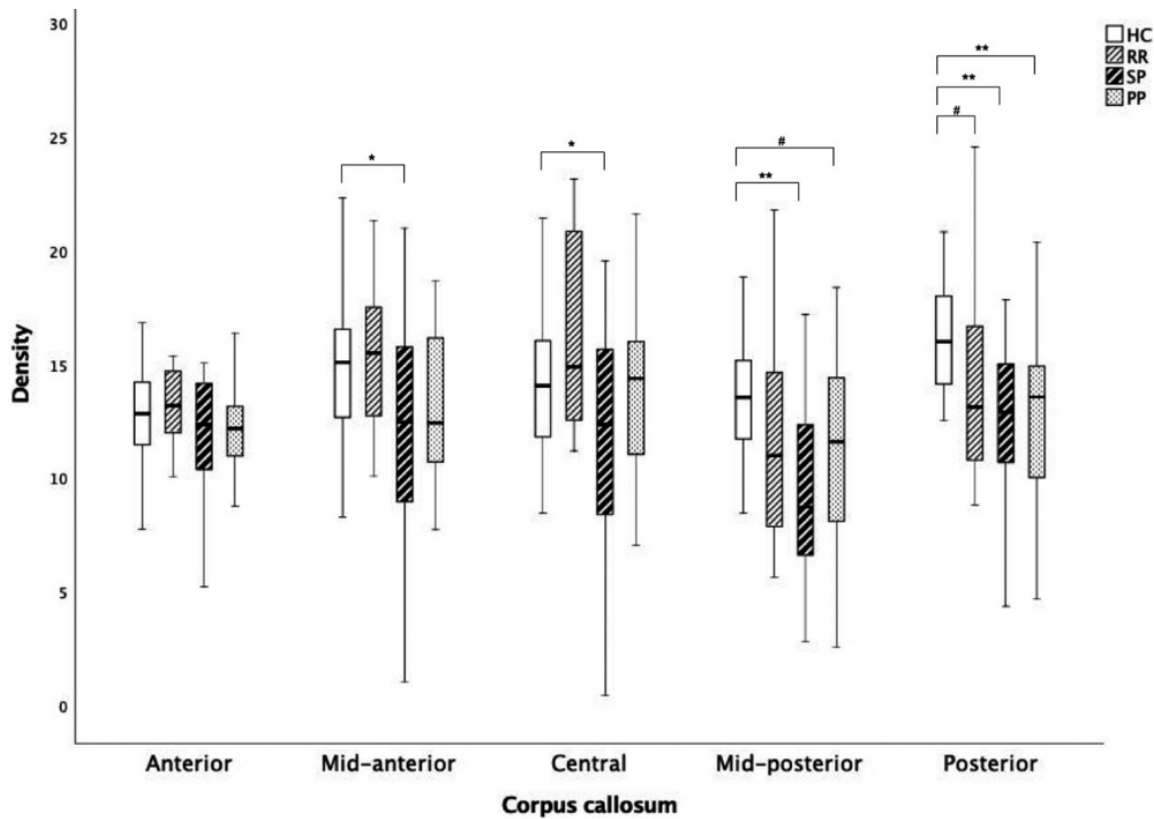


Figure 7.2 – Fibre density for pwMS and controls. Box plots displaying the 25%–75% values (boxes) \pm 95% values (whiskers) and median values (horizontal lines within boxes) of mean fibre density in the different sections of the corpus callosum. p values of the ANCOVA analysis are reported (#, significance trend, $*p < 0.05$, $**p < 0.01$).

0.540, $p = 0.001$), CVLT ($\beta = 0.319$, $p = 0.033$) and SDMT ($\beta = 0.303$, $p = 0.031$). Accounting for age, gender and disease duration, the models including CC density, CC LV, hemispheric LV and GM fraction significantly predicted EDSS ($R^2=0.239$, $p = 0.008$), 9-HPT ($R^2 = 0.270$, $p = 0.007$) and T25FWT ($R^2=0.232$, $p = 0.012$), with CC density being an independent predictor of EDSS ($\beta = 0.328$, $p = 0.018$), 9-HPT ($\beta = 0.327$, $p = 0.018$) and T25FWT ($\beta = 0.357$, $p = 0.021$), CC LV being an independent predictor of T25FWT ($\beta = 0.432$, $p = 0.002$) and GM fraction being an independent predictor of T25FWT ($\beta = 0.431$, $p = 0.017$). Detailed results of the regression models are reported in, Tab. 7.3.

	Model					Independent Predictors		
	R ²	R ² change	F	DF	P value	Beta	T value	P value
BVMT	.235	.298	2.841	8-40	.013			
CC density						.344	2.352	.023
GMF						.540	3.753	<i>.001</i>
CVLT	.199	.126	2.492	8-40	.027			
GMF						.319	2.206	.033
SDMT	.309	.130	3.689	8-40	.003			
GMF						.303	2.225	.031
EDSS	.232	.157	3.201	7-42	.008			
CC density						-.328	-2.461	.018
9-HPT	.270	.149	3.201	7-38	.007			
CC density						-.327	-2.467	.018
T25FWT	.232	.293	3.031	7-40	.012			
CC density						-.357	-2.389	.021
CCLV						.432	3.220	<i>.002</i>
GMF						-.431	-2.491	.017

Table 7.3 – Results of the hierarchical multiple linear regression analysis. Results that would survive Bonferroni correction ($0.05/4=0.01$) are shown in italics.

Topology of CC damage and phenotypic pattern

Our analysis demonstrated the presence of an inter-hemispheric disconnection in MS, mainly affecting the splenium and the posterior portion of the CC body. This finding expands previous results about the presence of microstructural CC damage in MS (Barone et al., 2018; Wahl et al., 2011), confirming the prevalent posterior involvement reported in PPMS (Margoni et al., 2019). In all phenotypes, streamline loss mainly pertained to the occipito-temporal and limbic regions, which were severely involved in PPMS and SPMS and showed a subtle involvement in RRMS, possibly as a consequence of the injury of tracts connecting GM regions more prone to atrophy or of direct axonal loss induced by macroscopic WM damage. Streamline density distribution along the CC in people with SPMS, together with the topography of damage detected in people with RRMS, seem to suggest that CC damage develops following a postero–anterior gradient. Intriguingly, this pattern seems to replicate the topography of regional GM progression over time which consistently involves cingulate and posterior regions, together with deep GM regions, earlier than anterior regions in all MS phenotypes (Eshaghi et al., 2018). The subgroup comparison of streamline density and CC LV indicated that regions other than the posterior CC showed more extensive damage fibre loss (mid-anterior and central CC) and higher LV (anterior

and mid-posterior CC) in the SPMS phenotype in comparison to the RRMS phenotype. Regarding LV, the difference between RRMS and SPMS became evident only in the anterior CC, again suggesting an initial sparing of this area, and in the mid-posterior CC, where the phenomenon of lesion repair might be hampered by virtual hypoxia occurring in fibres connecting high energy consumption regions such as the left and right precuneus (Eshaghi et al., 2018). As for the more severe fibre loss observed in the mid-anterior and central CC in the SPMS phenotype in comparison to the RRMS phenotype, it is speculated that the posterior CC, although involved early in the disease course, is less sensitive to further damage accrual along the disease course, probably because it has a higher fibre density than other CC regions. People with PPMS showed a degree of streamline density reduction in the posterior CC similar to people with SPMS, whilst presenting a lower lesion load both in the CC and hemispheric WM, which suggests that streamline density is modulated also by other factors such as, for example, GM atrophy of connected regions.

Relationship between CC density, LV and GM fraction

People with SPMS showed not only a more severe density reduction but also a higher lesion load in the hemispheric WM as well as in all CC subregions, suggesting a relationship between macroscopic damage and density reduction. On the other hand, the finding that CC involvement shows a postero–anterior gradient (similarly to GM atrophy), as well as a previous description of a correlation between GM atrophy and CC area (Klawiter et al., 2015) might suggest a relationship between streamline loss in the CC and cortical atrophy. Amongst these potential drivers, the results of our regression model point at focal WM lesions as the main correlates of CC density reduction, with an almost equal role played by local damage and Wallerian degeneration from hemispheric lesions. Whilst the involvement of specific GM regions has been interpreted as the consequence of higher energy consumption, meningeal inflammation and WM lesions (Eshaghi et al., 2018; Steenwijk et al., 2016), the posterior disconnection observed in our study seems to be related to the direct and indirect effect of macroscopic WM lesions, confirming previous longitudinal data that explored the relation between T2-weighted lesions and callosal atrophy at 5 years (Pelletier et al., 2001).

When exploring the possible influence of disease duration on CC density, no significant predictive value of disease duration was identified, suggesting that the loss of fibres is related to the accrual of GM and macroscopic WM damage over a critical value rather than to a linear effect of disease duration.

Relationship between CC damage and clinical disability

Both callosal atrophy and microstructural damage have been described as substrates of clinical impairment in RRMS and progressive MS (Barkhof et al., 1998; Barone et al., 2018; Bester et al., 2013; Bodini et al., 2013; Papathanasiou et al., 2017; Pelletier et al., 1993, 2001); therefore, CC density, which is a measure of microstructural damage that accounts for CC volume, was expected to significantly explain the clinical disability of pwMS. As CC density was highly related to WM lesions, and GM is a known predictor of disability in MS, their joint and independent contribution to motor and cognitive disability was evaluated. As expected, GM atrophy played a prevalent role in the prediction of cognitive impairment, with GM fraction being related to memory, attention and information processing speed performance. Conversely, WM damage, expressed by both callosal density and macroscopic WM lesions, was only related to information processing speed and flexibility. The relationship between processing speed, cognitive flexibility and CC damage can be explained by the role of CC in granting information flow between brain regions (Barkhof et al., 1998; Pelletier et al., 1993) and expands previous findings in people with SPMS, where moderate correlations have been identified between CC atrophy and these cognitive domains within an extensive neuropsychological battery (Papathanasiou et al., 2017). As for motor disability, an inverse scenario was observed, with an almost exclusive role of CC damage as predictor of global disability, manual dexterity and ambulation performance. Such association is presumably driven by the SPMS subgroup, for which a significant decrease in density is observable also in the anterior CC. Deficits in ambulation performance related to disconnection of premotor and motor areas have already been described in a variety of neurological conditions such as stroke and leukoaraiosis (Li et al., 2015; Moretti et al., 2005) and a similar mechanism might contribute to ambulation disability also in MS, adding to the disability induced by cerebellar and spinal involvement (Cocozza et al., 2017a; Zackowski et al., 2009).

Finally, whilst bimanual coordination relies on **CC** integrity (Bonzano et al., 2008), according to the callosal access model (Taylor et Heilman, 1980) also the execution of unilateral motor tasks requires access to the motor programmes stored in the dominant hemisphere (typically the left) and therefore requires callosal integrity in order to grant the performance of the non-dominant hand, explaining the contribution of **CC** damage to **9-HPT** performance in our study. Although it is acknowledged that our study was conducted on a small sample, limiting the power of our analysis and allowing only exploratory interpretations to be drawn, it is believed that the sound methodology applied for quantification of **CC** streamline density contributes to clarification of the mechanisms behind interhemispheric disconnection, sheds some light on its role as a factor determining clinical disability and offers an interesting hint to the presence of a topographic pattern of **WM** involvement in **MS**.

Chapter 8

Tract specific connectometry study in Fabry disease

FD is a rare X-linked lysosomal storage caused by an incomplete catabolization and subsequent intracellular accumulation of the glycosphingolipids globotriaosylceramide (Gb3), due to the defective activity of the α -galactosidase A (α -GalA) enzyme (Germain, 2010). The unmetabolized glycosphingolipid therefore accumulate in different tissues, including heart, kidney and CNS, leading to the development of clinical symptoms (Germain, 2010). With reference to CNS involvement, FD has been long considered to be a condition characterized only by major cerebrovascular events (Kolodny et al., 2015). Nevertheless, a subclinical although significant impairment of motor functions, which occurs independently from cerebrovascular involvement, is present in FD patients, characterized by the presence of poorer fine manual dexterity, slower gait and reduced hand speed (Löhle et al., 2015).

In line with these clinical findings, recent advanced MRI studies have showed the presence of a deeper and complex brain involvement in FD patients, with particular reference to the motor system (Cocozza et al., 2018b). Indeed, an alteration of the corticostriatal pathway has been described in FD patients, and a reduced functional connectivity between the motor cortex and the striatum has been described in this condition (Cocozza et al., 2017c). An additional evidence of the involvement of the extrapyramidal pathway in FD has been demonstrated in a recent study showing the presence of susceptibility and volumetric alterations affecting two of the main relay

stations of the extrapyramidal system, namely the striatum and the substantia nigra (Russo et al., 2018).

Although widespread microstructural alterations of the white matter (WM) are known to occur in FD patients, as demonstrated by different DTI studies (Albrecht et al., 2007; Coccozza et al., 2018b), to date no information about the integrity of the cortico-basal ganglia motor loop fibers are available. Given this background, aim of this study was to evaluate the microstructural integrity of the main afferences and efferences of the motor cortices to the basal ganglia motor loop in FD patients, to investigate the possible presence of structural connectivity changes in these connections, to expand the current knowledge about motor involvement in this condition.

8.1 Methods

Participants

In this retrospective cross-sectional study, part of a larger monocentric framework on the CNS involvement in FD, genetically proven patients were included along with age- and sex-comparable HC. For both groups, we evaluated male and female subjects without age limitations, with the following exclusion criteria: left handedness, co-existence of other systemic conditions or any addiction, history of stroke, head trauma or any other clinical diagnosis of diseases affecting the CNS.

For all FD patients, clinical variables of systemic organ involvement were obtained from medical records, and included the following: diabetes mellitus, hypertension, cardiac arrhythmia, left ventricular hypertrophy, renal failure (for estimated glomerular filtration rates < 90 mL/min), proteinuria (for scores > 150 mg/24 hours), cephalalgia and acroparesthesia.

The study was conducted in compliance with the ethical standard, and written informed consent was obtained from all subjects according to the Declaration of Helsinki.

MRI data acquisition

All subjects underwent an MRI scan on the same 3T scanner (Trio, Siemens Medical Systems, Erlangen, Germany), equipped with an 8-channel head coil. The MRI protocol included the following sequences: a) 3D Fluid Attenuated Inversion Recovery (FLAIR) sequence: 160 slices; TR = 6000 ms, TE = 396 ms, TI = 2200 ms; voxel size = 1.0x1.0x1.0 mm³; b) 3D T1-weighted sequence: 160 slices; TR = 1900 ms, TE = 3.4 ms, TI = 900 ms, flip angle = 9°, voxel size = 1.0x1.0x1.0 mm³; c) diffusion weighted spin echo sequence: TR = 7400 ms, TE = 88 ms, flip angle = 90°, voxel size = 2.2x2.2x2.2 mm³ with 64 directions at b=1000s/mm² in addition to nine b=0 s/mm².

MRI data analysis

For FD patients, T2-weighted hyperintense WM lesions were segmented (when present) by an observer with more than 8 years of expertise in neuroimaging data analysis, unaware of subject identity, employing a semi-automated technique¹ (Jim 7). From the segmentation procedure, lesion loads were obtained as an index of macroscopic WM damage. Furthermore, to correct for the potential impact of WM lesions in the subsequent analyses, the corresponding lesion masks were coregistered using an affine registration to the T1-weighted volumes for an in-painting procedure, as implemented in FSL², Version 5.0.10 (FMRIB Software Library), by filling the mask with the mean signal intensity values of the surrounding normal-appearing WM.

For all the subjects involved in the study, the T1-weighted volumes were segmented using the standard FreeSurfer Desikan-Killiany atlas (Desikan et al., 2006) which allowed to obtain a cortical parcellation of GM in 85 different ROIs. Along with this parcellation, the ICV was also calculated as the sum of GM, WM and cerebrospinal fluid volumes, in order to correct for differences in head sizes, which are known to occur in this condition (Pontillo et al., 2018).

DTI data were pre-processed to correct for motion and eddy currents (Andersson et Sotiropoulos, 2016). Standard DTI metrics of FA, axial diffusivity (AD), radial

1. <http://www.xinapse.com/home.php>
2. <http://www.fmrib.ox.ac.uk/fsl>

diffusivity (RD) and mean diffusivity (MD) were computed [13] using MRtrix³. To perform global anatomical constrained tractography (ACT) (Smith et al., 2012), we first co-registered the T1 and DT images using FLIRT⁴ (Jenkinson et al., 2002) with boundary based cost function (Greve et Fischl, 2009). Then we computed the fiber orientation distribution functions (Tournier et al., 2007a,b) and generated 1 million streamlines using the iFOD2 (Tournier et al., 2010) tractography algorithm from which, for each subject, we built the corresponding connectome using the FreeSurfer parcellation in 85 ROIs. From the connectomes we extracted the bundles connecting the Precentral gyrus (PrCG) with the striatum (computed as caudate nucleus plus putamen) and with the thalamus, respectively reflecting the main afferent and efferent pathways of the motor circuit within the cortico-striatal-thalamo-cortical loop (Lanciego et al., 2012; Obeso et al., 2008), as well as the CST as a representation of the pyramidal system. Thus, we built a smaller connectome using only these as ROIs (three for the left and three for the right hemisphere).

Finally, DTI metrics and connectomes were combined to carry on diffusion MRI connectometry (Yeh et al., 2013) which consists in assigning to each bundle a value that is obtained by taking the mean of the chosen metric along the streamlines composing the bundle.

An example of the reconstructed tracts is available in 8.1.

Statistical Analysis

Statistical analysis was carried out using the Statistical Package for the Social Sciences (SPSS) package (Version 23, IBM, Armonk, New York). Differences in term of age and sex were tested using a two-sample t test and a chi-squared test, respectively. A Generalized Linear Model (GLM) was employed to compare the two groups in terms of the diffusion MRI connectometry values derived from each DTI metric (FA, MD, AD, RD) on both hemispheres (left and right), including age, sex and ICV as covariates, to remove the effects of potential confounding factors not related to microstructural damage. For each DTI metric, the corresponding mean value averaged

3. <http://www.mrtrix.org>

4. <https://fsl.fmrib.ox.ac.uk>

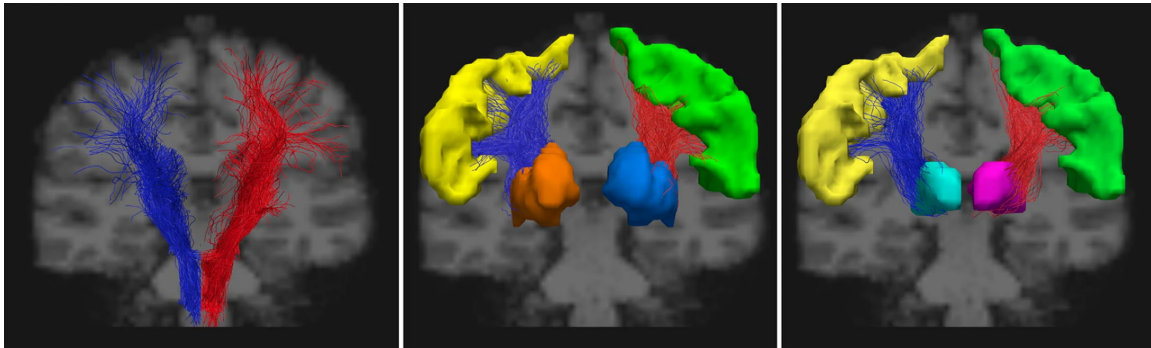


Figure 8.1 – Image showing the reconstructed tracts in a 29-year-old female healthy control. From left to right, the cortico-spinal, the cortico-striatal and thalamo-cortical tracts (red indicates the left side, blue the right side), with the green and yellow areas indicating the left and right precentral gyri, respectively. Finally, the dark blue and purple regions of interests represent the left striatum (as the sum of caudate nucleus and putamen) and the thalamus, while in orange and light blue are displayed the contralateral regions.

over the entire **WM** volume was also included in the **GLM** as a nuisance variable, in order to correct for an index of global **WM** microstructural damage.

Results were considered significant for $p < 0.05$.

8.2 Results and discussion

Forty-seven **FD** patients and forty-nine **HC** were included in this study, with the two groups being not different neither for age ($p=0.99$) nor sex ($p=0.10$). A complete list of the demographic and clinical information of the included population is available in Tab.8.2.

We found a diffuse microstructural damage of the entire **WM** highlighted by the significant difference in **FA** between **HC** and **FD** (0.238 ± 0.011 vs 0.233 ± 0.012 , $p=0.02$) (Tab.8.4) (Figure8.3), along with the presence of a microstructural involvement of cortico-striatal tracts in **FD** patients, predominantly affecting the left side compared to the contralateral (Tab.8.5) (Figure8.6). In particular, we found a significant reduction of mean **FA** values of the left cortico-striatal fibers (0.43 ± 0.02 vs 0.41 ± 0.02 for **HC** and **FD**, respectively, $p=0.001$), coupled to an in-

	HC	FD
Age (mean \pm SD)	42.3 \pm 16.3	42.3 \pm 13.1
Sex (M/F)	28/21	19/28
ERT	n.a.	35/47
ERT duration (mean \pm SD)	n.a.	33.1 \pm 30.6
Cephalalgia	n.a.	6/47
Acroparesthesia	n.a.	7/47
Hypertension	n.a.	12/47
Diabetes	n.a.	1/47
Arrhythmia	n.a.	3/47
Left ventricular hypertrophy	n.a.	23/47
Renal failure	n.a.	12/47
Proteinuria	n.a.	18/47

Figure 8.2 – Subjects demographic and clinical variables of all subjects included in the study. Age is expressed in years, while ERT duration is expressed in months FD, SD standard deviation, ERT enzyme replacement therapy, n.a. not applicable.

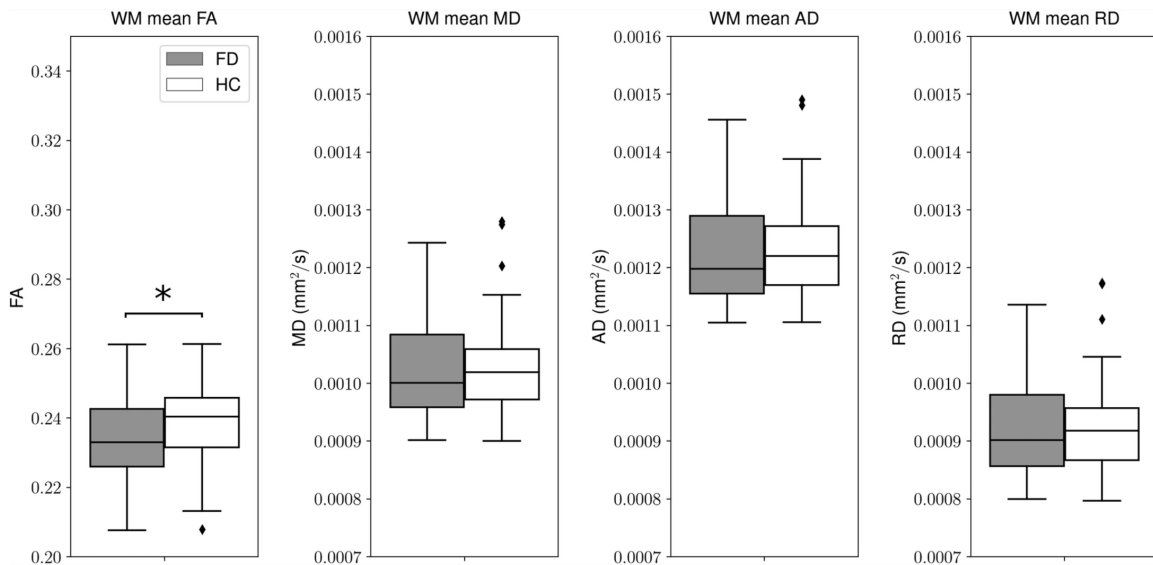


Figure 8.3 – Box and whiskers plot showing the differences in terms of mean microstructural values along the entire white matter in Fabry patients compared with healthy controls. Asterisk indicates significant differences between the two groups.

	HC	FD	<i>p</i>
FA	0.238 ± 0.011	0.233 ± 0.012	<i>0.023</i>
MD (10 ⁻³ mm ² /s)	1.032 ± 0.082	1.020 ± 0.086	0.565
AD (10 ⁻³ mm ² /s)	1.237 ± 0.083	1.122 ± 0.089	0.331
RD (10 ⁻³ mm ² /s)	0.929 ± 0.082	0.921 ± 0.086	0.711

Figure 8.4 – Mean values and standard deviations of the diffusion metrics (FA, MD, AD and RD) of the entire WM for the two groups of subjects. In the last column, the p values obtained comparing HC and FD using a GLM with age, sex, and ICV are reported (the significant difference is in italics).

crease in MD ($0.67 \cdot 10^{-3} \pm 0.02 \cdot 10^{-3} \text{mm}^2/\text{s}$ vs $0.68 \cdot 10^{-3} \pm 0.03 \cdot 10^{-3} \text{mm}^2/\text{s}$, $p=0.001$) and RD ($0.50 \cdot 10^{-3} \pm 0.02 \cdot 10^{-3} \text{mm}^2/\text{s}$ vs $0.52 \cdot 10^{-3} \pm 0.03 \cdot 10^{-3} \text{mm}^2/\text{s}$, $p<0.001$) values, while no differences emerged when AD maps were evaluated ($1.00 \cdot 10^{-3} \pm 0.03 \cdot 10^{-3} \text{mm}^2/\text{s}$ vs $1.01 \cdot 10^{-3} \pm 0.03 \cdot 10^{-3} \text{mm}^2/\text{s}$, $p=0.1109$). When evaluating cortico-striatal connection on the right side, a trend of reduced mean RD was found in FD patients compared to HC, not reaching the statistical significance (0.55 ± 0.03 vs 0.56 ± 0.04 , $p=0.09$), while no differences emerged for the remaining variables ($p=0.34$, $p=0.16$ and $p=0.14$ for FA, MD, and AD, respectively). Similarly, the thalamo-cortical tracts showed a predominant microstructural damage in FD patients for the left side compared to the contralateral. In particular we found a significant increase in MD ($0.67 \cdot 10^{-3} \pm 0.02 \cdot 10^{-3} \text{mm}^2/\text{s}$ vs $0.68 \cdot 10^{-3} \pm 0.02 \cdot 10^{-3} \text{mm}^2/\text{s}$, $p=0.01$) and RD ($0.49 \cdot 10^{-3} \pm 0.03 \cdot 10^{-3} \text{mm}^2/\text{s}$ vs $0.51 \cdot 10^{-3} \pm 0.03 \cdot 10^{-3} \text{mm}^2/\text{s}$, $p<0.001$) values, while no differences emerged when FA and AD maps were evaluated. None of the metrics showed significant differences in the right hemisphere.

Finally, when evaluating microstructural changes affecting the CST, a less pronounced lateralization was found, with results showing a similar pattern of involvement, although mainly bilateral (Tab.8.5) (Figure8.6).

In FD patients we found prominent microstructural damage of the major WM tracts implicated in both the extrapyramidal and pyramidal motor systems.

Poorer motor performance compared to age-matched HC has been described in FD patients, mainly involving functional domains (e.g. gait and hand speed) related to the extrapyramidal system (Löhle et al., 2015). Along with the evidence from ex-vivo studies of pathologic Gb3 accumulation in different neuronal populations including the substantia nigra (Kaye et al., 1988; de Veber et al., 1992), recent neuroimaging

Diffusion metric	Tract	Side	HC	FD	<i>p</i>
FA	PrCG-striatum	R	0.413 ± 0.025	0.399 ± 0.028	0.337
		L	0.434 ± 0.024	0.412 ± 0.023	<i>0.005</i>
	Thalamus-PrCG	R	0.438 ± 0.027	0.425 ± 0.028	0.482
		L	0.462 ± 0.025	0.445 ± 0.025	0.183
	CST	R	0.499 ± 0.021	0.488 ± 0.022	0.277
		L	0.529 ± 0.021	0.510 ± 0.025	<i>0.037</i>
MD (10 ⁻³ mm ² /s)	PrCG-striatum	R	0.723 ± 0.027	0.728 ± 0.034	0.162
		L	0.668 ± 0.019	0.685 ± 0.029	<i>0.001</i>
	Thalamus-PrCG	R	0.720 ± 0.024	0.724 ± 0.032	0.222
		L	0.669 ± 0.018	0.683 ± 0.024	<i>0.010</i>
	CST	R	0.749 ± 0.025	0.764 ± 0.026	<i>0.031</i>
		L	0.718 ± 0.026	0.740 ± 0.026	<i>0.002</i>
AD (10 ⁻³ mm ² /s)	PrCG-striatum	R	1.065 ± 0.034	1.059 ± 0.030	0.785
		L	1.001 ± 0.037	1.006 ± 0.035	0.092
	Thalamus-PrCG	R	1.087 ± 0.035	1.080 ± 0.029	0.813
		L	1.030 ± 0.035	1.036 ± 0.030	0.089
	CST	R	1.202 ± 0.037	1.209 ± 0.034	0.307
		L	1.190 ± 0.044	1.200 ± 0.037	0.198
RD (10 ⁻³ mm ² /s)	PrCG-striatum	R	0.551 ± 0.030	0.563 ± 0.040	0.098
		L	0.501 ± 0.021	0.525 ± 0.038	<i>0.0002</i>
	Thalamus-PrCG	R	0.536 ± 0.029	0.547 ± 0.039	0.169
		L	0.489 ± 0.021	0.507 ± 0.031	<i>0.014</i>
	CST	R	0.523 ± 0.027	0.541 ± 0.033	<i>0.018</i>
		L	0.483 ± 0.026	0.510 ± 0.031	<i>0.0004</i>

Figure 8.5 – Mean values and standard deviations of the diffusion metrics (FA, MD, AD and RD) of the three WM tracts (PrCG-striatum, thalamus-PrCG, and CST) for the two groups of subjects. The p values obtained comparing HC and FD using a GLM with age, sex, ICV, and mean values of the metric in the entire WM are reported in the last column (significant differences are in italics).

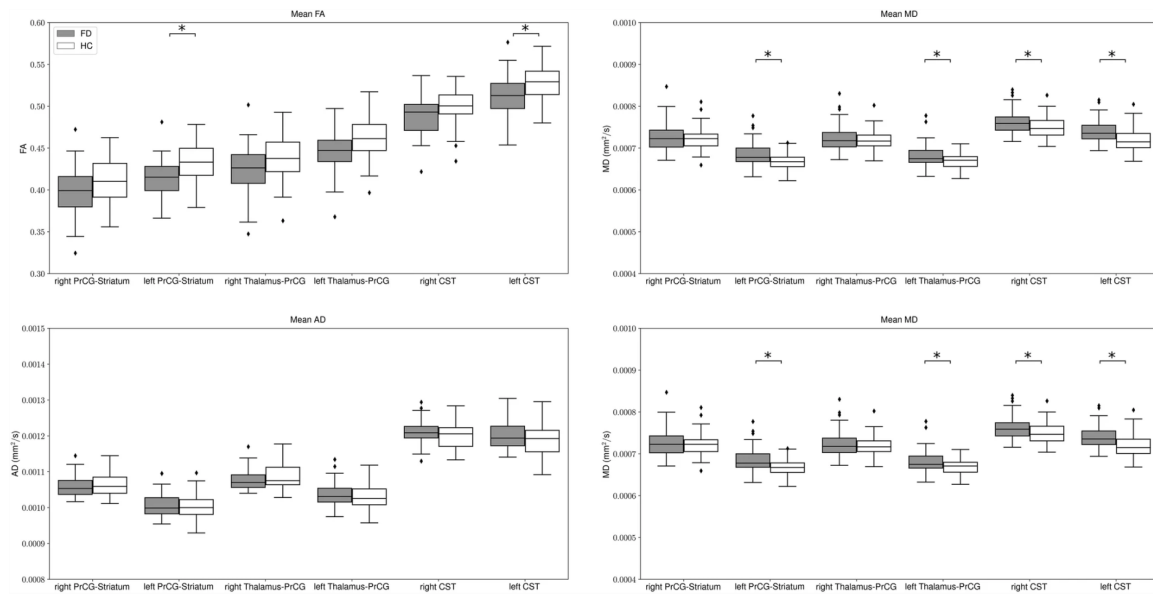


Figure 8.6 – Box and whiskers plot showing the results of the tractometry analyses, with mean diffusion metrics along the evaluated tracts in Fabry patients compared with healthy controls. Asterisk indicates significant differences between the two groups.

studies demonstrated the occurrence of neurodegenerative phenomena in two of the main hubs within the cortico-striatal-thalamo-cortical motor loop (i.e. striatum and substantia nigra), as well as functional disconnection between the motor cortex and the basal ganglia in this condition (Cocozza et al., 2017c; Russo et al., 2018). In conjunction with these previous evidences, our results may support the hypothesis of a primary neurodegenerative damage of the extrapyramidal system, occurring at least in part independently from micro- and macro-vascular pathology.

Indeed, microstructural damage of the cortico-striatal and thalamo-cortical projections may result from mechanisms of retrograde (Patel et al., 2016) and antero-grade (Kanamori et al., 2012) transneuronal axonal degeneration, respectively, caused by primary neurodegeneration of intermediate relay stations -mainly the substantia nigra- within the cortico-striatal-thalamo-cortical motor loop. In accordance with this speculation, similar alterations of DTI metrics have been demonstrated in the frontal WM of Parkinson’s disease (PD) patients (Atkinson-Clement et al., 2017; Cochrane et Ebmeier, 2013; Planetta et al., 2014). On the other hand, other tractography stud-

ies on PD patients reported opposed DTI alterations (i.e. increased FA and reduced MD) of the motor cortico-striatal and thalamo-cortical tracts (Mole et al., 2016), while concordant evidences exist on the CST showing an increase of FA (and a parallel reduction of MD) associated to PD, suggesting a reorganization of these fibers possibly reflecting a compensatory increase in axonal density due to axonal sprouting (Arkadir et al., 2014; Atkinson-Clement et al., 2017).

Furthermore, the prominent alteration of WM RD over AD showed by FD patients in our sample appears to suggest myelin damage rather than axonal degeneration (Alexander et al., 2007), so that the observed alterations may actually reflect subtle ischemic demyelination of the investigated tracts resulting from vascular pathology (Kelley, 2006; Shi et Wardlaw, 2016). Indeed, a similar pattern of DTI metrics alterations is known to characterize both white matter hyperintensities (WMH) and normal appearing white matter (NAWM) of patients with cerebral small vessel disease (SVD) (Pasi et al., 2016; Raja et al., 2019). In particular, several voxel-based DTI studies demonstrated that the occurrence of vascular parkinsonism is associated with more prominent microstructural damage of the bifrontal WM, the corona radiata and the anterior limb of internal capsule, which are the main tracts involved in movement control (Deverdun et al., 2014; Salsone et al., 2019; Van Der Holst et al., 2015; Wang et al., 2012). Indeed, it has been hypothesized that SVD disrupts the structural integrity of WM tracts, including the corticostriatal and thalamocortical fibers, thereby reducing the influence of the basal ganglia on motor, premotor, and supplementary motor cortices (Van Der Holst et al., 2015). This disconnection of the basal ganglia–thalamo-cortical circuit could possibly lead to subcortical atrophy, ultimately resulting in parkinsonism. Furthermore, SVD could also lower the threshold for developing parkinsonism symptoms, modifying the threshold for Lewy body pathology to become symptomatic (Van Der Holst et al., 2015). In this light, a similar mechanism could be theorized for FD, in which widespread WM microstructural damage has been demonstrated, not sparing the major frontal WM projection tracts (Albrecht et al., 2007; Coccozza et al., 2018a), whose prominent involvement could make FD patients more prone to the development of symptomatic or even subclinical impairment of motor functional domains, mainly related to the extrapyramidal system.

The prominence of WM microstructural damage on the left side observed in our sample of FD patients reasonably relies on the hand-dominance of the studied subjects. Indeed, an asymmetry in DTI metrics of major motor WM tracts is known to exist in HC, with higher anisotropy values in the dominant hemisphere (Angstmann et al., 2016; Catani et al., 2010; Nathan et al., 1990; Trivedi et al., 2009). Therefore, in a condition in which a widespread microstructural damage occurs, differences of DTI metrics are more likely to emerge on the dominant side. Furthermore, due to the higher level of activation and energy demand, motor WM tracts of the dominant hemisphere are theoretically more disposed to ischemic injury and excitotoxic mechanisms (Tekkök et al., 2007).

Whatever its origin, disruption of the cortico-striatal projection fibers may underlie the reduction of functional connectivity between the motor cortex and the basal ganglia observed in this condition (Cocozza et al., 2017c). Nevertheless, it is known that the relationship between structural and functional connectivity may not be straightforward, so that future dynamic effective connectivity resting-state fMRI studies are warranted in order to unravel the causal connection between motor cortex and striatum functional activation (Park et al., 2018).

Based on these observations, the question remains as to in which proportion primary neurodegenerative phenomena and cerebrovascular damage contribute to the motor functional impairment observed in FD. To disentangle this issue, further studies are needed, possibly oriented toward the direct investigation of microstructural damage at the level of substantia nigra and nigrostriatal connections, whose alterations bear the potential to represent more specific markers of primary neurodegenerative parkinsonism (Deng et al., 2018; Langley et al., 2016; Theisen et al., 2017; Zhang et al., 2001, 2015). Furthermore, the lack of clinical data also needs to be acknowledged as a limitation of our study. However, even if theoretically the correlation with clinical measures of motor impairment could have helped to elucidate the functional meaning of the observed WM alterations, it is known that neurological alterations in

FD patients are mild (Löhle et al., 2015) and thus hardly relate to findings of advanced brain MRI techniques (Cocozza et al., 2017c; Russo et al., 2018).

Although characterized by these limitations, our results confirm the presence of an

extrapyramidal involvement in [FD](#) patients, showing the presence of microstructural changes significantly affecting the cortico-striatal pathway in this condition, further confirming the presence of a deep and complex involvement of motor circuits in [FD](#).

Conclusion

The introduction of [dMRI](#) presents a cornerstone in the neuroimaging field, becoming an invaluable tool for in-vivo study of the brain structure. However, data acquisition still suffers from low resolution, artifacts and noise due to technical limitations. In this context tractography tries to describe the [WM](#) architecture by reconstructing axonal pathways based on [dMRI](#) data. The limited quality of the data, as well as the complexity of the task, yield to an “ill-posed” inverse problem characterized by non-unique solutions.

In section 5 we presented a [MCMC](#) Bayesian approach to improve signal reconstruction robustness while enhancing the estimation of parameters describing microstructural properties based on [dMRI](#) data. This is achieved by using a hierarchical approach on prior information and proved to be more appropriate for fitting across distinct tissue types while reducing noise effects characterizing voxel-by-voxel fitting methods.

In chapter 1.3 we presented how different tractography methods perform and we showed how these limitations have impact on brain connectivity studies in patients affected by [MS](#) and Fabry disease (5.2).

Then we focus on the so called “*global*” tractography algorithms, highlighting strengths and drawbacks of both *generative* and *discriminative* methods 1.3.3. We propose a novel approach developed in three different stages and representing the core of this thesis(1.4).

The first stage is presented in section 2, where we introduced a graph-based semi-global method tackling the problem of bottlenecks in streamlines reconstruction caus-

ing density inhomogeneity in correspondence of bending regions. To solve the problem, we introduced an iterative procedure that uses microstructure information and provides feedback to the shortest path tractography algorithm about the plausibility of the reconstruction.

The second stage is represented by the introduction of a global adaptive method, exploiting both the flexibility and the strengths of global reconstruction approaches, while overcoming the ROI-based nature of the previous one. Thanks to a convenient parameterization, we were able to dramatically reduce the number of parameters needed to represent the streamlines, while their trajectory were adapted using an MCMC approach informed by the observed diffusion data. The results show how the dynamic adaptation allows overcoming the limitations due to a static input, characteristic of global discriminative approaches, and further improves the reconstructions. This, in turn allows to better discriminate between valid and invalid connections, consequently promoting the removal of more false positives.

As final stage, we introduced the concept of *bundle-o-graphy*. Built upon the global adaptive approach previously described, we presented a method to directly model WM bundles, i.e., disentangling tractography reconstructions from streamline representation. By scaling-up the reconstruction process, the possibility to directly model and optimize bundles dramatically decreases the complexity of the tractography task. This, in turn, allow to exploit the potential of bundle-based reconstruction approaches while keeping a global perspective.

We believe the proposed methods could represent a step forward in characterizing and quantifying the structural connectivity by combining micro and macro-structure information, following the idea that *multi-modality*, nowadays, represents the most promising way to overcome tractography limitations.

Bibliography

- Aganj, I., Lenglet, C., Jahanshad, N., Yacoub, E., Harel, N., Thompson, P.M., Sapiro, G., 2011. A hough transform global probabilistic approach to multiple-subject diffusion mri tractography. *Medical image analysis* 15, 414–425.
- Al-Kofahi, K.A., Lasek, S., Szarowski, D.H., Pace, C.J., Nagy, G., Turner, J.N., Roysam, B., 2002. Rapid automated three-dimensional tracing of neurons from confocal image stacks. *IEEE Transactions on information technology in biomedicine* 6, 171–187.
- Albrecht, J., Dellani, P.R., Müller, M.J., Schermuly, I., Beck, M., Stoeter, P., Gerhard, A., Fellgiebel, A., 2007. Voxel based analyses of diffusion tensor imaging in fabry disease. *Journal of Neurology, Neurosurgery & Psychiatry* 78, 964–969.
- Alexander, A., Lee, J., Lazar, M., Field, A., 2007. Diffusion tensor imaging of the brain. *Neurotherapeutics: the journal of the American Society for Experimental NeuroTherapeutics* 4, 316–29.
- Alexander, D.C., 2005. Maximum entropy spherical deconvolution for diffusion mri, in: *Biennial International Conference on Information Processing in Medical Imaging*, Springer. pp. 76–87.
- Alexander, D.C., Hubbard, P.L., Hall, M.G., Moore, E.A., Ptito, M., Parker, G.J., Dyrby, T.B., 2010. Orientationally invariant indices of axon diameter and density from diffusion mri. *Neuroimage* 52, 1374–1389.
- Andersson, J.L., Sotiropoulos, S.N., 2016. An integrated approach to correction for off-resonance effects and subject movement in diffusion mr imaging. *Neuroimage* 125, 1063–1078.
- Angstmann, S., Madsen, K.S., Skimminge, A., Jernigan, T.L., Baaré, W.F., Siebner, H.R., 2016. Microstructural asymmetry of the corticospinal tracts predicts right–left differences in circle drawing skill in right-handed adolescents. *Brain Structure and Function* 221, 4475–4489.
- Arkadir, D., Bergman, H., Fahn, S., 2014. Redundant dopaminergic activity may enable compensatory axonal sprouting in parkinson disease. *Neurology* 82, 1093–1098.

- Assaf, Y., Basser, P.J., 2005. Composite hindered and restricted model of diffusion (charmed) mr imaging of the human brain. *Neuroimage* 27, 48–58.
- Assaf, Y., Blumenfeld-Katzir, T., Yovel, Y., Basser, P.J., 2008. Axc caliber: a method for measuring axon diameter distribution from diffusion mri. *Magnetic Resonance in Medicine: An Official Journal of the International Society for Magnetic Resonance in Medicine* 59, 1347–1354.
- Assaf, Y., Freidlin, R.Z., Rohde, G.K., Basser, P.J., 2004. New modeling and experimental framework to characterize hindered and restricted water diffusion in brain white matter. *Magnetic Resonance in Medicine: An Official Journal of the International Society for Magnetic Resonance in Medicine* 52, 965–978.
- Atkinson-Clement, C., Pinto, S., Eusebio, A., Coulon, O., 2017. Diffusion tensor imaging in parkinson's disease: review and meta-analysis. *Neuroimage: Clinical* 16, 98–110.
- Aydogan, D.B., Shi, Y., 2021. Parallel transport tractography. *IEEE Transactions on Medical Imaging* 40, 635–647.
- Aydogan, D.B., Souza, V.H., Lioumis, P., Ilmoniemi, R.J., 2021. Towards real-time tractography-based tms neuronavigation. *Brain Stimulation: Basic, Translational, and Clinical Research in Neuromodulation* 14, 1609.
- Barazany, D., Basser, P.J., Assaf, Y., 2009. In vivo measurement of axon diameter distribution in the corpus callosum of rat brain. *Brain* 132, 1210–1220.
- Barkhof, F., Tas, M., Valk, J., Elton, M., Lindeboom, J., Schmidt, W., Hommes, O., Polman, C., Kok, A., 1998. Functional correlates of callosal atrophy in relapsing-remitting multiple sclerosis patients. a preliminary mri study. *Journal of neurology* 245, 153–158.
- Barone, S., Caligiuri, M.E., Valentino, P., Cherubini, A., Chiriaco, C., Granata, A., Filippelli, E., Tallarico, T., Nisticò, R., Quattrone, A., 2018. Multimodal assessment of normal-appearing corpus callosum is a useful marker of disability in relapsing–remitting multiple sclerosis: an mri cluster analysis study. *Journal of Neurology* 265, 2243–2250.
- Basser, P.J., 1995. Inferring microstructural features and the physiological state of tissues from diffusion-weighted images. *NMR in Biomedicine* 8, 333–344.
- Basser, P.J., Mattiello, J., LeBihan, D., 1994. Estimation of the effective self-diffusion tensor from the nmr spin echo. *Journal of Magnetic Resonance, Series B* 103, 247–254.
- Basser, P.J., Pajevic, S., Pierpaoli, C., Duda, J., Aldroubi, A., 2000. In vivo fiber tractography using DT-MRI data. *Magnetic Resonance in Medicine* 44, 625–632.

- Bastiani, M., Shah, N.J., Goebel, R., Roebroeck, A., 2012. Human cortical connectome reconstruction from diffusion weighted MRI: The effect of tractography algorithm. *NeuroImage* 62, 1732–49.
- Battocchio, M., Girard, G., Barakovic, M., Ocampo, M., Thiran, J.P., Schiavi, S., Daducci, A., 2019. Improving graph-based tractography plausibility using microstructure information, in: *Computational Diffusion MRI*, Springer International Publishing. pp. 367–375.
- Battocchio, M., Schiavi, S., Descoteaux, M., Daducci, A., 2021. Improving tractography accuracy using dynamic filtering, in: Gyori, N., Hutter, J., Nath, V., Palombo, M., Pizzolato, M., Zhang, F. (Eds.), *Computational Diffusion MRI*, Springer International Publishing. pp. 45–54.
- Behrens, T., Berg, H.J., Jbabdi, S., Rushworth, M., Woolrich, M., 2007. Probabilistic diffusion tractography with multiple fibre orientations: What can we gain? *NeuroImage* 34, 144 – 155.
- Behrens, T.E., Sotiropoulos, S.N., Jbabdi, S., 2014. Mr diffusion tractography, in: *Diffusion MRI*. Elsevier, pp. 429–451.
- Behrens, T.E., Woolrich, M.W., Jenkinson, M., Johansen-Berg, H., Nunes, R.G., Clare, S., Matthews, P.M., Brady, J.M., Smith, S.M., 2003. Characterization and propagation of uncertainty in diffusion-weighted mr imaging. *Magnetic Resonance in Medicine: An Official Journal of the International Society for Magnetic Resonance in Medicine* 50, 1077–1088.
- Berger, A., 2002. How does it work?: Magnetic resonance imaging. *BMJ: British Medical Journal* 324, 35.
- Bester, M., Lazar, M., Petracca, M., Babb, J.S., Herbert, J., Grossman, R.I., Inglese, M., 2013. Tract-specific white matter correlates of fatigue and cognitive impairment in benign multiple sclerosis. *Journal of the neurological sciences* 330, 61–66.
- Bihan, D.L., Breton, E., Lallemand, D., Grenier, P., Cabanis, E., Laval-Jeantet, M., 1986. MR imaging of intravoxel incoherent motions: application to diffusion and perfusion in neurologic disorders. *Radiology* 161, 401–407.
- Bitar, R., Leung, G., Perng, R., Tadros, S., Moody, A.R., Sarrazin, J., McGregor, C., Christakis, M., Symons, S., Nelson, A., et al., 2006. Mr pulse sequences: what every radiologist wants to know but is afraid to ask. *Radiographics* 26, 513–537.
- Bodini, B., Cercignani, M., Khaleeli, Z., Miller, D.H., Ron, M., Penny, S., Thompson, A.J., Ciccarelli, O., 2013. Corpus callosum damage predicts disability progression and cognitive dysfunction in primary-progressive ms after five years. *Human brain mapping* 34, 1163–1172.

- Bonzano, L., Tacchino, A., Roccatagliata, L., Abbruzzese, G., Mancardi, G.L., Bove, M., 2008. Callosal contributions to simultaneous bimanual finger movements. *Journal of Neuroscience* 28, 3227–3233.
- Buchanan, C.R., Bastin, M.E., Ritchie, S.J., Liewald, D.C., Madole, J.W., Tucker-Drob, E.M., Deary, I.J., Cox, S.R., 2020. The effect of network thresholding and weighting on structural brain networks in the uk biobank. *NeuroImage* 211, 116443.
- Bullmore, E., Sporns, O., 2012. The economy of brain network organization. *Nature reviews neuroscience* 13, 336–349.
- Callaghan, P.T., 1993. Principles of nuclear magnetic resonance microscopy. Oxford University Press on Demand.
- Callaghan, P.T., Eccles, C., Xia, Y., 1988. Nmr microscopy of dynamic displacements: k-space and q-space imaging. *Journal of Physics E: Scientific Instruments* 21, 820.
- Caruyer, E., Daducci, A., Descoteaux, M., Houde, J.C., Thiran, J.P., Verma, R., 2014. Phantomas: a flexible software library to simulate diffusion mr phantoms, in: *Ismrm*.
- Catani, M., 2006. Diffusion tensor magnetic resonance imaging tractography in cognitive disorders. *Current opinion in neurology* 19, 599–606.
- Catani, M., Forkel, S., De Schotten, M.T., 2010. Asymmetry of white matter pathways. The two halves of the brain: information processing in the cerebral hemispheres. MIT Press, Cambridge , 177–210.
- Catani, M., Howard, R.J., Pajevic, S., Jones, D.K., 2002. Virtual in vivo interactive dissection of white matter fasciculi in the human brain. *NeuroImage* 17, 77 – 94.
- Catmull, E., Rom, R., 1974. A class of local interpolating splines, in: BARNHILL, R.E., RIESENFELD, R.F. (Eds.), *Computer Aided Geometric Design*. Academic Press, pp. 317–326.
- Chamberland, M., Whittingstall, K., Fortin, D., Mathieu, D., Descoteaux, M., 2014. Real-time multi-peak tractography for instantaneous connectivity display. *Frontiers in neuroinformatics* 8, 59.
- Chib, S., Greenberg, E., 1995. Understanding the Metropolis-Hastings Algorithm. *The American Statistician* 49, 327–35.
- Christiaens, D., Reisert, M., Dhollander, T., Sunaert, S., Suetens, P., Maes, F., 2015. Global tractography of multi-shell diffusion-weighted imaging data using a multi-tissue model. *NeuroImage* 123, 89–101.

- Ciccarelli, O., Catani, M., Johansen-Berg, H., Clark, C., Thompson, A., 2008. Diffusion-based tractography in neurological disorders: concepts, applications, and future developments. *The Lancet Neurology* 7, 715–727.
- Cieslak, M., Brennan, T., Meiring, W., Volz, L.J., Greene, C., Asturias, A., Suri, S., Grafton, S.T., 2018. Analytic tractography: A closed-form solution for estimating local white matter connectivity with diffusion mri. *NeuroImage* 169, 473–484.
- Clarke, E., O'Malley, C.D., 1996. *The human brain and spinal cord: A historical study illustrated by writings from antiquity to the twentieth century.* 2, Norman Publishing.
- Close, T.G., Tournier, J.D., Johnston, L.A., Calamante, F., Mareels, I., Connelly, A., 2015. Fourier tract sampling (fouts): A framework for improved inference of white matter tracts from diffusion mri by explicitly modelling tract volume. *NeuroImage* 120, 412–427.
- Cochrane, C.J., Ebmeier, K.P., 2013. Diffusion tensor imaging in parkinsonian syndromes: a systematic review and meta-analysis. *Neurology* 80, 857–864.
- Cocozza, S., Petracca, M., Mormina, E., Buyukturkoglu, K., Podranski, K., Heinig, M.M., Pontillo, G., Russo, C., Tedeschi, E., Russo, C.V., et al., 2017a. Cerebellar lobule atrophy and disability in progressive ms. *Journal of Neurology, Neurosurgery & Psychiatry* 88, 1065–1072.
- Cocozza, S., Pisani, A., Olivo, G., Saccà, F., Ugga, L., Riccio, E., Migliaccio, S., Brescia Morra, V., Brunetti, A., Quarantelli, M., Tedeschi, E., 2017b. Alterations of functional connectivity of the motor cortex in Fabry disease. *Neurology* 88, 1822–9.
- Cocozza, S., Pisani, A., Olivo, G., Saccà, F., Ugga, L., Riccio, E., Migliaccio, S., Morra, V.B., Brunetti, A., Quarantelli, M., et al., 2017c. Alterations of functional connectivity of the motor cortex in fabry disease: an rs-fmri study. *Neurology* 88, 1822–1829.
- Cocozza, S., Pontillo, G., Quarantelli, M., Saccà, F., Riccio, E., Costabile, T., Olivo, G., Brescia Morra, V., Pisani, A., Brunetti, A., et al., 2018a. Default mode network modifications in fabry disease: A resting-state fmri study with structural correlations. *Human Brain Mapping* 39, 1755–1764.
- Cocozza, S., Russo, C., Pontillo, G., Pisani, A., Brunetti, A., 2018b. Neuroimaging in fabry disease: current knowledge and future directions. *Insights into Imaging* 9, 1077–1088.
- Cointepas, Y., Poupon, C., Bihan, D.L., Mangin, J.F., 2002. A spin glass based framework to untangle fiber crossing in mr diffusion based tracking , 475–482.

- Conturo, T.E., Lori, N.F., Cull, T.S., Akbudak, E., Snyder, A.Z., Shimony, J.S., McKinstry, R.C., Burton, H., Raichle, M.E., 1999. Tracking neuronal fiber pathways in the living human brain. *Proceedings of the National Academy of Sciences* 96, 10422–10427.
- Cushing, H., 1909. A note upon the faradic stimulation of the postcentral gyrus in conscious patients. *Brain* 32, 44–53.
- Côté, M.A., Girard, G., Boré, A., Garyfallidis, E., Houde, J.C., Descoteaux, M., 2013. Tractometer: Towards validation of tractography pipelines. *Medical Image Analysis* 17, 844–857. Special Issue on the 2012 Conference on Medical Image Computing and Computer Assisted Intervention.
- Daducci, A., Dal Palu, A., Descoteaux, M., Thiran, J.P., 2016. Microstructure Informed Tractography: Pitfalls and Open Challenges. *Front Neurosci* 10, 247.
- Daducci, A., Dal Palu, A., Lemkaddem, A., Thiran, J.P., 2013. A convex optimization framework for global tractography, in: 2013 IEEE 10th International Symposium on Biomedical Imaging, IEEE. pp. 524–527.
- Daducci, A., Dal Palù, A., Lemkaddem, A., Thiran, J.P., 2015. COMMIT: convex optimization modeling for microstructure informed tractography. *IEEE Trans Med Imaging* 34, 246–57.
- Daducci, A., Gobbi, F., N, F., M, B., S, S., 2021. Blurred streamlines: a new concept to improve tractography accuracy by spatially blurring signal contributions. *Proc. Intl. Soc. Mag. Reson. Med. (ISMRM)* .
- Dejerine, J., 1895. *Anatomy of nerve centers by J. Dejerine: With the collaboration of Madame Dejèrine-Klumpke. volume 1. Rueff et Cie.*
- Dell’Acqua, F., Tournier, J.D., 2019. Modelling white matter with spherical deconvolution: How and why? *NMR in Biomedicine* 32, e3945.
- Deng, X.Y., Wang, L., Yang, T.T., Li, R., Yu, G., 2018. A meta-analysis of diffusion tensor imaging of substantia nigra in patients with parkinson’s disease. *Scientific reports* 8, 1–8.
- Descoteaux, M., Angelino, E., Fitzgibbons, S., Deriche, R., 2007. Regularized, fast, and robust analytical q-ball imaging. *Magnetic Resonance in Medicine: An Official Journal of the International Society for Magnetic Resonance in Medicine* 58, 497–510.
- Desikan, R.S., Ségonne, F., Fischl, B., Quinn, B.T., Dickerson, B.C., Blacker, D., Buckner, R.L., Dale, A.M., Maguire, R.P., Hyman, B.T., et al., 2006. An automated labeling system for subdividing the human cerebral cortex on mri scans into gyral based regions of interest. *Neuroimage* 31, 968–980.

- Deverdun, J., de Champfleury, S.M., Cabello-Aguilar, S., Maury, F., Molino, F., Charif, M., Leboucq, N., Ayrignac, X., Labauge, P., Bonafe, A., et al., 2014. Diffusion tensor imaging differentiates vascular parkinsonism from parkinsonian syndromes of degenerative origin in elderly subjects. *European journal of radiology* 83, 2074–2079.
- Dijkstra, E.W., 1959. A note on two problems in connexion with graphs. *Numer. Math.* 1, 269–71.
- Dobryakova, E., Rocca, M.A., Valsasina, P., DeLuca, J., Filippi, M., 2017. Altered neural mechanisms of cognitive control in patients with primary progressive multiple sclerosis: An effective connectivity study. *Human brain mapping* 38, 2580–2588.
- Douek, P., Turner, R., Pekar, J., Patronas, N., Le Bihan, D., 1991. Mr color mapping of myelin fiber orientation. *J Comput Assist Tomogr* 15, 923–929.
- Dyrby, T.B., Sogaard, L.V., Hall, M.G., Ptito, M., Alexander, D.C., 2013. Contrast and stability of the axon diameter index from microstructure imaging with diffusion mri. *Magnetic resonance in medicine* 70, 711–721.
- Einstein, A., 1905. Über die von der molekularkinetischen theorie der wärme geforderte bewegung von in ruhenden flüssigkeiten suspendierten teilchen. *Annalen der Physik* 322, 549–560.
- Eshaghi, A., Marinescu, R.V., Young, A.L., Firth, N.C., Prados, F., Jorge Cardoso, M., Tur, C., De Angelis, F., Cawley, N., Brownlee, W.J., et al., 2018. Progression of regional grey matter atrophy in multiple sclerosis. *Brain* 141, 1665–1677.
- Essayed, W.I., Zhang, F., Unadkat, P., Cosgrove, G.R., Golby, A.J., O'Donnell, L.J., 2017. White matter tractography for neurosurgical planning: A topography-based review of the current state of the art. *NeuroImage: Clinical* 15, 659–672.
- Fick, A., 1855. Ueber diffusion. *Annalen der Physik* 170, 59–86.
- Fick, R.H., Wassermann, D., Deriche, R., 2019. The dmipy toolbox: Diffusion mri multi-compartment modeling and microstructure recovery made easy. *Frontiers in neuroinformatics* 13, 64.
- Fillard, P., Descoteaux, M., Goh, A., Gouttard, S., Jeurissen, B., Malcolm, J., Ramirez-Manzanares, A., Reisert, M., Sakaie, K., Tensaouti, F., Yo, T., Mangin, J.F., Poupon, C., 2011. Quantitative evaluation of 10 tractography algorithms on a realistic diffusion mr phantom. *NeuroImage* 56, 220–34.
- Fillard, P., Poupon, C., Mangin, J.F., 2009. A Novel Global Tractography Algorithm Based on an Adaptive Spin Glass Model, in: *International Conference on Medical Image Computing and Computer-Assisted Intervention*, pp. 927–34.

- Fischl, B., van der Kouwe, A., Destrieux, C., Halgren, E., Ségonne, F., Salat, D.H., Busa, E., Seidman, L.J., Goldstein, J., Kennedy, D., Caviness, V., Makris, N., Rosen, B., Dale, A.M., 2004a. Automatically Parcellating the Human Cerebral Cortex. *Cerebral Cortex* 14, 11–22.
- Fischl, B., Salat, D.H., Busa, E., Albert, M., Dieterich, M., Haselgrove, C., Van Der Kouwe, A., Killiany, R., Kennedy, D., Klaveness, S., et al., 2002. Whole brain segmentation: automated labeling of neuroanatomical structures in the human brain. *Neuron* 33, 341–355.
- Fischl, B., Salat, D.H., Van Der Kouwe, A.J., Makris, N., Ségonne, F., Quinn, B.T., Dale, A.M., 2004b. Sequence-independent segmentation of magnetic resonance images. *Neuroimage* 23, S69–S84.
- Flouri, D., Owen, D., Aghwane, R., Mufti, N., Maksym, K., Sokolska, M., Kendall, G., Bainbridge, A., Atkinson, D., Vercauteren, T., et al., 2020. Improved fetal blood oxygenation and placental estimated measurements of diffusion-weighted mri using data-driven bayesian modeling. *Magnetic resonance in medicine* 83, 2160–2172.
- Fornito, A., Zalesky, A., Bullmore, E.T., 2016. Chapter 11 - statistical connectomics, in: *Fundamentals of Brain Network Analysis*. Academic Press, pp. 383–419.
- Fourier, J.B.J., Darboux, G., et al., 1822. *Théorie analytique de la chaleur*. volume 504. Didot Paris.
- Freidlin, R., Kakareka, J., Pohida, T., Komlosh, M., Basser, P., 2012. A spin echo sequence with a single-sided bipolar diffusion gradient pulse to obtain snapshot diffusion weighted images in moving media. *Journal of Magnetic Resonance* 221, 24–31.
- Frenet, F., 1852. Sur les courbes à double courbure. *Journal de mathématiques pures et appliquées* , 437–447.
- Garey, L.J., 1999. *Brodmann’s’ localisation in the cerebral cortex’*. World Scientific.
- Garg, N., Reddel, S.W., Miller, D.H., Chataway, J., Riminton, D.S., Barnett, Y., Masters, L., Barnett, M.H., Hardy, T.A., 2015. The corpus callosum in the diagnosis of multiple sclerosis and other cns demyelinating and inflammatory diseases. *Journal of Neurology, Neurosurgery & Psychiatry* 86, 1374–1382.
- Garyfallidis, E., Brett, M., Correia, M., Williams, G., Nimmo-Smith, I., 2012. Quickbundles, a method for tractography simplification. *Frontiers in Neuroscience* 6, 175.
- Germain, D.P., 2010. Fabry disease. *Orphanet journal of rare diseases* 5, 1–49.
- Girard, G., Descoteaux, M., 2012. Anatomical tissue probability priors for tractography. *International Conference on Medical Image Computing and Computer Assisted Intervention (MICCAI’12)-Computational Diffusion MRI Workshop* , 174–185.

- Girard, G., Whittingstall, K., Deriche, R., Descoteaux, M., 2014. Towards quantitative connectivity analysis: reducing tractography biases. *NeuroImage* 98, 266–78.
- Granberg, T., Martola, J., Bergendal, G., Shams, S., Damangir, S., Aspelin, P., Fredrikson, S., Kristoffersen-Wiberg, M., 2015. Corpus callosum atrophy is strongly associated with cognitive impairment in multiple sclerosis: results of a 17-year longitudinal study. *Multiple Sclerosis Journal* 21, 1151–1158.
- Gray, H., 1918. Anatomy of the human body. *Annals of surgery* 68, 564–566.
- Green, P.J., 1995. Reversible jump markov chain monte carlo computation and bayesian model determination. *Biometrika* 82, 711–732.
- Greve, D.N., Fischl, B., 2009. Accurate and robust brain image alignment using boundary-based registration. *Neuroimage* 48, 63–72.
- Gross, C.G., 1987. Neuroscience, early history of. *Encycl. Neurosci* , 843–847.
- H, D.D., K, P.T., 1973. Algorithms for the reduction of the number of points required to represent a digitized line or its caricature. *Cartographica: The International Journal for Geographic Information and Geovisualization* 10, 112–22.
- Hagmann, P., Cammoun, L., Gigandet, X., Meuli, R., Honey, C.J., Wedeen, V.J., Sporns, O., 2008. Mapping the structural core of human cerebral cortex. *PLoS biology* 6, e159.
- Hahn, E.L., 1950. Spin echoes. *Physical review* 80, 580.
- Hamilton, W.R., 1828. Theory of systems of rays. *The Transactions of the Royal Irish Academy* , 69–174.
- Harms, R.L., Roebroek, A., 2018. Robust and fast markov chain monte carlo sampling of diffusion mri microstructure models. *Frontiers in neuroinformatics* 12, 97.
- Hastings, W.K., 1970. Monte carlo sampling methods using markov chains and their applications. *Biometrika* 57, 97–109.
- He, Y., Dagher, A., Chen, Z., Charil, A., Zijdenbos, A., Worsley, K., Evans, A., 2009. Impaired small-world efficiency in structural cortical networks in multiple sclerosis associated with white matter lesion load. *Brain* 132, 3366–3379.
- Hofman, M.A., 2014. Evolution of the human brain: when bigger is better. *Frontiers in neuroanatomy* 8, 15.

- Honey, C.J., Kötter, R., Breakspear, M., Sporns, O., 2007. Network structure of cerebral cortex shapes functional connectivity on multiple time scales. *Proceedings of the National Academy of Sciences* 104, 10240–10245.
- Honey, C.J., Sporns, O., Cammoun, L., Gigandet, X., Thiran, J.P., Meuli, R., Hagmann, P., 2009. Predicting human resting-state functional connectivity from structural connectivity. *Proceedings of the National Academy of Sciences* 106, 2035–2040.
- Horsfield, M.A., Jones, D.K., 2002. Applications of diffusion-weighted and diffusion tensor mri to white matter diseases—a review. *NMR in Biomedicine: An International Journal Devoted to the Development and Application of Magnetic Resonance In Vivo* 15, 570–577.
- Ianuș, A., Carvalho, J., Fernandes, F.F., Cruz, R., Chavarrias, C., Palombo, M., Shemesh, N., 2022. Soma and neurite density mri (sandi) of the in-vivo mouse brain and comparison with the allen brain atlas. *NeuroImage* 254, 119135.
- Inglese, M., Petracca, M., 2018. Mri in multiple sclerosis: Clinical and research update. *Current opinion in neurology* 31, 249–255.
- Inglis, B., Bossart, E., Buckley, D., Wirth III, E., Mareci, T., 2001. Visualization of neural tissue water compartments using biexponential diffusion tensor mri. *Magnetic Resonance in Medicine: An Official Journal of the International Society for Magnetic Resonance in Medicine* 45, 580–587.
- Iturria-Medina, Y., Canales-Rodríguez, E., Melie-García, L., Valdés-Hernández, P., Martínez-Montes, E., Alemán-Gómez, Y., Sánchez-Bornot, J., 2007. Characterizing brain anatomical connections using diffusion weighted MRI and graph theory. *NeuroImage* 36, 645–60.
- Jbabdi, S., Bellec, P., Toro, R., Daunizeau, J., Péligrini-Issac, M., Benali, H., 2008. Accurate anisotropic fast marching for diffusion-based geodesic tractography. *International journal of biomedical imaging* 2008.
- Jbabdi, S., Johansen-Berg, H., 2011. Tractography: Where Do We Go from Here? *Brain Connectivity* 1, 169–83.
- Jbabdi, S., Woolrich, M., Andersson, J., Behrens, T., 2007. A bayesian framework for global tractography. *NeuroImage* 37, 116–29.
- Jenkinson, M., Bannister, P., Brady, M., Smith, S., 2002. Improved optimization for the robust and accurate linear registration and motion correction of brain images. *Neuroimage* 17, 825–841.
- Jespersen, S.N., Kroenke, C.D., Østergaard, L., Ackerman, J.J., Yablonskiy, D.A., 2007. Modeling dendrite density from magnetic resonance diffusion measurements. *Neuroimage* 34, 1473–1486.

- Jeurissen, B., Descoteaux, M., Mori, S., Leemans, A., 2019. Diffusion mri fiber tractography of the brain. *NMR in Biomedicine* 32, e3785.
- Jeurissen, B., Leemans, A., Tournier, J.D., Jones, D.K., Sijbers, J., 2012. Investigating the prevalence of complex fiber configurations in white matter tissue with diffusion magnetic resonance imaging. *Human Brain Mapping* 34, 2747–2766.
- Jeurissen, B., Tournier, J.D., Dhollander, T., Connelly, A., Sijbers, J., 2014. Multi-tissue constrained spherical deconvolution for improved analysis of multi-shell diffusion mri data. *NeuroImage* 103, 411–426.
- Johansen-Berg, H., Behrens, T.E., 2013. Diffusion MRI: from quantitative measurement to in vivo neuroanatomy. Academic Press.
- Johansen-Berg, H., Rushworth, M.F., 2009. Using diffusion imaging to study human connective anatomy. *Annual review of neuroscience* 32, 75–94.
- Jones, D.K., 2003. Determining and visualizing uncertainty in estimates of fiber orientation from diffusion tensor mri. *Magnetic Resonance in Medicine: An Official Journal of the International Society for Magnetic Resonance in Medicine* 49, 7–12.
- Jones, D.K., 2010. Diffusion mri. Oxford University Press.
- Jones, D.K., Knösche, T.R., Turner, R., 2013. White matter integrity, fiber count, and other fallacies: the do's and don'ts of diffusion mri. *Neuroimage* 73, 239–254.
- Kaden, E., Kelm, N.D., Carson, R.P., Does, M.D., Alexander, D.C., 2016a. Multi-compartment microscopic diffusion imaging. *NeuroImage* 139, 346–359.
- Kaden, E., Kruggel, F., Alexander, D.C., 2016b. Quantitative mapping of the per-axon diffusion coefficients in brain white matter. *Magnetic Resonance in Medicine* 75, 1752–1763.
- Kanamori, A., Catrinescu, M.M., Belisle, J.M., Costantino, S., Levin, L.A., 2012. Retrograde and wallerian axonal degeneration occur synchronously after retinal ganglion cell axotomy. *The American journal of pathology* 181, 62–73.
- Kaye, E.M., Kolodny, E.H., Logigian, E.L., Ullman, M.D., 1988. Nervous system involvement in fabry's disease: clinicopathological and biochemical correlation. *Annals of Neurology: Official Journal of the American Neurological Association and the Child Neurology Society* 23, 505–509.
- Kelley, R.E., 2006. Ischemic demyelination. *Neurological research* 28, 334–340.

- Klawiter, E.C., Ceccarelli, A., Arora, A., Jackson, J., Bakshi, S., Kim, G., Miller, J., Tauhid, S., von Gizycki, C., Bakshi, R., et al., 2015. Corpus callosum atrophy correlates with gray matter atrophy in patients with multiple sclerosis. *Journal of Neuroimaging* 25, 62–67.
- Kocevar, G., Stamile, C., Hannoun, S., Cotton, F., Vukusic, S., Durand-Dubief, F., Sappey-Marinié, D., 2016. Graph theory-based brain connectivity for automatic classification of multiple sclerosis clinical courses. *Frontiers in neuroscience* 10, 478.
- Koh, D.M., Collins, D.J., Orton, M.R., 2011. Intravoxel incoherent motion in body diffusion-weighted mri: reality and challenges. *American Journal of Roentgenology* 196, 1351–1361.
- Kolodny, E., Fellgiebel, A., Hilz, M.J., Sims, K., Caruso, P., Phan, T.G., Politei, J., Manara, R., Burlina, A., 2015. Cerebrovascular involvement in fabry disease: current status of knowledge. *Stroke* 46, 302–313.
- Koubiyr, I., Besson, P., Deloire, M., Charre-Morin, J., Saubusse, A., Tourdias, T., Brochet, B., Ruet, A., 2019. Dynamic modular-level alterations of structural-functional coupling in clinically isolated syndrome. *Brain* 142, 3428–3439.
- Kreher, B., Mader, I., Kiselev, V., 2008. Gibbs tracking: A novel approach for the reconstruction of neuronal pathways. *Magn Reson Med* 60, 953–63.
- Kubik, S., Abernathy, C.D., et al., 1990. *Atlas of the Cerebral Sulci*. Thieme Medical Publishers.
- Lanciego, J.L., Luquin, N., Obeso, J.A., 2012. Functional neuroanatomy of the basal ganglia. *Cold Spring Harbor perspectives in medicine* 2, a009621.
- Langley, J., Huddleston, D.E., Merritt, M., Chen, X., McMurray, R., Silver, M., Factor, S.A., Hu, X., 2016. Diffusion tensor imaging of the substantia nigra in parkinson’s disease revisited. *Human brain mapping* 37, 2547–2556.
- Lassmann, H., 2018. Multiple sclerosis pathology. *Cold Spring Harbor perspectives in medicine* 8, a028936.
- Lauterbur, P.C., 1973. Image formation by induced local interactions: examples employing nuclear magnetic resonance. *nature* 242, 190–191.
- Lazar, M., Alexander, A.L., 2003. An error analysis of white matter tractography methods: synthetic diffusion tensor field simulations. *Neuroimage* 20, 1140–1153.
- Le Bihan, D., 1991. Molecular diffusion nuclear magnetic resonance imaging. *Magnetic resonance quarterly* 7, 1–30.

- Le Bihan, D., Breton, E., 1985. In vivo magnetic resonance imaging of diffusion. *Comptes Rendus des Seances de l'Academie des Sciences. Serie 2* 301, 1109–1112.
- Le Bihan, D., Breton, E., Lallemand, D., Aubin, M., Vignaud, J., Laval-Jeantet, M., 1988. Separation of diffusion and perfusion in intravoxel incoherent motion (ivim) mr imaging. *Radiology* , 497–505.
- Le Bihan, D., Turner, R., Douek, P., 1993. Is water diffusion restricted in human brain white matter? an echo-planar nmr imaging study. *Neuroreport* 4, 887–890.
- Lee, S., Lee, H.Y., Lee, I.F., Tseng, C.Y., 2004. Ink diffusion in water. *European Journal of Physics* 25, 331–336.
- Lemkaddem, A., Skiöldebrand, D., Dal Palú, A., Thiran, J.P., Daducci, A., 2014. Global Tractography with Embedded Anatomical Priors for Quantitative Connectivity Analysis. *Frontiers in Neurology* 5, 232.
- Li, Y., Jewells, V., Kim, M., Chen, Y., Moon, A., Armao, D., Troiani, L., Markovic-Plese, S., Lin, W., Shen, D., 2013. Diffusion tensor imaging based network analysis detects alterations of neuroconnectivity in patients with clinically early relapsing-remitting multiple sclerosis. *Human brain mapping* 34, 3376–3391.
- Li, Y., Wu, P., Liang, F., Huang, W., 2015. The microstructural status of the corpus callosum is associated with the degree of motor function and neurological deficit in stroke patients. *PLoS One* 10, e0122615.
- van Lieshout, M.N.M., 2000. *Markov Point Processes and Their Applications*. Imperial College Press. pp. 1–8.
- Lieshout, M.N.M.V., 1994. Stochastic annealing for nearest-neighbour point processes with application to object recognition. *Advances in Applied Probability* 26, 281–300.
- Lipp, I., Parker, G.D., Tallantyre, E.C., Goodall, A., Grama, S., Patitucci, E., Heveron, P., Tomassini, V., Jones, D.K., 2020. Tractography in the presence of multiple sclerosis lesions. *NeuroImage* 209, 116471.
- Llufriu, S., Martinez-Heras, E., Solana, E., Sola-Valls, N., Sepulveda, M., Blanco, Y., Martinez-Lapiscina, E.H., Andorra, M., Villoslada, P., Prats-Galino, A., et al., 2017. Structural networks involved in attention and executive functions in multiple sclerosis. *NeuroImage: Clinical* 13, 288–296.
- Löhle, M., Hughes, D., Milligan, A., Richfield, L., Reichmann, H., Mehta, A., Schapira, A.H., 2015. Clinical prodromes of neurodegeneration in anderson-fabry disease. *Neurology* 84, 1454–1464.

- Ludwig, E., Klingler, J., 1956. Page/index/vorwort, in: Atlas cerebri humani. Karger Publishers, pp. 1–6.
- Magphail, E.M., Bolhuis, J.J., 2001. The evolution of intelligence: adaptive specializations versus general process. *Biological Reviews* 76, 341–364.
- Maier-Hein, K.H., Neher, Peter and, ., Stieltjes, B., Descoteaux, M., 2017. The challenge of mapping the human connectome based on diffusion tractography. *Nature Communications* 5.
- Mandonnet, E., Sarubbo, S., Petit, L., 2018. The nomenclature of human white matter association pathways: proposal for a systematic taxonomic anatomical classification. *Frontiers in neuroanatomy* , 94.
- Mangin, J.F., Fillard, P., Cointepas, Y., Bihan, D.L., Frouin, V., Poupon, C., 2013. Toward global tractography. *NeuroImage* 80, 290–6.
- Manza, P., Zhang, S., Li, C.S.R., Leung, H.C., 2016. Resting-state functional connectivity of the striatum in early-stage parkinson’s disease: Cognitive decline and motor symptomatology. *Human brain mapping* 37, 648–662.
- Margoni, M., Petracca, M., Schiavi, S., Fabian, M., Miller, A., Lublin, F., Inglese, M., 2019. Axonal water fraction as marker of white matter injury in primary-progressive multiple sclerosis: A longitudinal study. *European Journal of Neurology* 26, 1068–1074.
- Maunsell, J., van Essen, D.C., 1983. The connections of the middle temporal visual area (mt) and their relationship to a cortical hierarchy in the macaque monkey. *Journal of Neuroscience* 3, 2563–2586.
- Mercadante, A.A., Tadi, P., 2020. Neuroanatomy, gray matter .
- Metropolis, N., Rosenbluth, A.W., Rosenbluth, M.N., Teller, A.H., Teller, E., 1953. Equation of state calculations by fast computing machines. *The Journal of Chemical Physics* 21, 1087–1092.
- Mole, J.P., Subramanian, L., Bracht, T., Morris, H., Metzler-Baddeley, C., Linden, D.E., 2016. Increased fractional anisotropy in the motor tracts of parkinson’s disease suggests compensatory neuroplasticity or selective neurodegeneration. *European radiology* 26, 3327–3335.
- Moretti, M., Carlucci, G., Di Carlo, A., Fonda, C., Prieto, M., Mugnai, S., Bracco, L., Piccini, C., Pracucci, G., Inzitari, D., 2005. Corpus callosum atrophy is associated with gait disorders in patients with leukoaraiosis. *Neurological Sciences* 26, 61–66.
- Mori, S., Crain, B.J., Chacko, V.P., Van Zijl, P.C.M., 1999. Three-dimensional tracking of axonal projections in the brain by magnetic resonance imaging. *Annals of Neurology* 45, 265–69.

- Nathan, P., SMITH, M.C., Deacon, P., 1990. The corticospinal tracts in man: course and location of fibres at different segmental levels. *Brain* 113, 303–324.
- Neal, R.M., et al., 2011. Mcmc using hamiltonian dynamics. *Handbook of markov chain monte carlo* 2, 2.
- Nigro, S., Passamonti, L., Riccelli, R., Toschi, N., Rocca, F., Valentino, P., Nisticò, R., Fera, F., Quattrone, A., 2015. Structural ‘connectomic’ alterations in the limbic system of multiple sclerosis patients with major depression. *Multiple Sclerosis Journal* 21, 1003–1012.
- Northcutt, R.G., Kaas, J.H., 1995. The emergence and evolution of mammalian neocortex. *Trends in neurosciences* 18, 373–379.
- Novikov, D.S., Fieremans, E., Jespersen, S.N., Kiselev, V.G., 2019. Quantifying brain microstructure with diffusion mri: Theory and parameter estimation. *NMR in Biomedicine* 32, e3998.
- Obeso, J.A., Rodríguez-Oroz, M.C., Benitez-Temino, B., Blesa, F.J., Guridi, J., Marin, C., Rodríguez, M., 2008. Functional organization of the basal ganglia: therapeutic implications for parkinson’s disease. *Movement disorders: official journal of the Movement Disorder Society* 23, S548–S559.
- Ocampo-Pineda, M., Schiavi, S., Rheault, F., Girard, G., Petit, L., Descoteaux, M., Daducci, A., 2021a. Hierarchical microstructure informed tractography. *Brain connectivity* 11, 75–88.
- Ocampo-Pineda, M., Schiavi, S., Rheault, F., Girard, G., Petit, L., Descoteaux, M., Daducci, A., 2021b. Hierarchical microstructure informed tractography. *Brain Connectivity* 11, 75–88.
- Orton, M.R., Collins, D.J., Koh, D.M., Leach, M.O., 2014. Improved intravoxel incoherent motion analysis of diffusion weighted imaging by data driven bayesian modeling. *Magnetic resonance in medicine* 71, 411–420.
- Ozturk, A., Smith, S., Gordon-Lipkin, E., Harrison, D., Shiee, N., Pham, D., Caffo, B., Calabresi, P., Reich, D., 2010. Mri of the corpus callosum in multiple sclerosis: association with disability. *Multiple Sclerosis Journal* 16, 166–177.
- Pagani, E., Rocca, M.A., De Meo, E., Horsfield, M.A., Colombo, B., Rodegher, M., Comi, G., Filippi, M., 2020. Structural connectivity in multiple sclerosis and modeling of disconnection. *Multiple Sclerosis Journal* 26, 220–232.
- Pajevic, S., Basser, P.J., 2003. Parametric and non-parametric statistical analysis of dt-mri data. *Journal of magnetic resonance* 161, 1–14.

- Palombo, M., Ianus, A., Guerreri, M., Nunes, D., Alexander, D.C., Shemesh, N., Zhang, H., 2020. Sandi: a compartment-based model for non-invasive apparent soma and neurite imaging by diffusion mri. *NeuroImage* 215, 116835.
- Palotai, M., Cavallari, M., Koubiyr, I., Morales Pinzon, A., Nazeri, A., Healy, B.C., Glanz, B., Weiner, H.L., Chitnis, T., Guttmann, C.R., 2020. Microstructural fronto-striatal and temporo-insular alterations are associated with fatigue in patients with multiple sclerosis independent of white matter lesion load and depression. *Multiple Sclerosis Journal* 26, 1708–1718.
- Panagiotaki, E., Chan, R.W., Dikaios, N., Ahmed, H.U., O’Callaghan, J., Freeman, A., Atkinson, D., Punwani, S., Hawkes, D.J., Alexander, D.C., 2015. Microstructural characterization of normal and malignant human prostate tissue with vascular, extracellular, and restricted diffusion for cytometry in tumours magnetic resonance imaging. *Investigative radiology* 50, 218–227.
- Panagiotaki, E., Schneider, T., Siow, B., Hall, M.G., Lythgoe, M.F., Alexander, D.C., 2012. Compartment models of the diffusion mr signal in brain white matter: A taxonomy and comparison. *NeuroImage* 59, 2241–54.
- Papathanasiou, A., Messinis, L., Zampakis, P., Papathanasopoulos, P., 2017. Corpus callosum atrophy as a marker of clinically meaningful cognitive decline in secondary progressive multiple sclerosis. impact on employment status. *Journal of Clinical Neuroscience* 43, 170–175.
- Pardini, M., Yaldizli, Ö., Sethi, V., Muhlert, N., Liu, Z., Samson, R.S., Altmann, D.R., Ron, M.A., Wheeler-Kingshott, C.A., Miller, D.H., et al., 2015. Motor network efficiency and disability in multiple sclerosis. *Neurology* 85, 1115–1122.
- Park, H.J., Friston, K.J., Pae, C., Park, B., Razi, A., 2018. Dynamic effective connectivity in resting state fmri. *NeuroImage* 180, 594–608.
- Parker, G.J.M., Wheeler-Kingshott, C.A.M., Barker, G.J., 2002. Estimating distributed anatomical connectivity using fast marching methods and diffusion tensor imaging. *IEEE Trans Med Imaging* 21, 505–12.
- Pasi, M., van Uden, I.W., Tuladhar, A.M., de Leeuw, F.E., Pantoni, L., 2016. White matter microstructural damage on diffusion tensor imaging in cerebral small vessel disease: clinical consequences. *Stroke* 47, 1679–1684.
- Patel, K.R., Ramsey, L.E., Metcalf, N.V., Shulman, G.L., Corbetta, M., 2016. Early diffusion evidence of retrograde transsynaptic degeneration in the human visual system. *Neurology* 87, 198–205.

- Pelletier, J., Habib, M., Lyon-Caen, O., Salamon, G., Poncet, M., Khalil, R., 1993. Functional and magnetic resonance imaging correlates of callosal involvement in multiple sclerosis. *Archives of Neurology* 50, 1077–1082.
- Pelletier, J., Suchet, L., Witjas, T., Habib, M., Guttmann, C., Salamon, G., Lyon-Caen, O., Chérif, A.A., 2001. A longitudinal study of callosal atrophy and interhemispheric dysfunction in relapsing-remitting multiple sclerosis. *Archives of neurology* 58, 105–111.
- Pereira, J.B., van Westen, D., Stomrud, E., Strandberg, T.O., Volpe, G., Westman, E., Hansson, O., 2017. Abnormal Structural Brain Connectome in Individuals with Preclinical Alzheimer’s Disease. *Cerebral Cortex* 28, 3638–3649.
- Perrin, G., Descombes, X., Zerubia, J., 2005. Adaptive simulated annealing for energy minimization problem in a marked point process application, in: *Energy Minimization Methods in Computer Vision and Pattern Recognition*, pp. 3–17.
- Pestilli, F., Yeatman, J.D., Rokem, A., Kay, K.N., Wandell, B.A., 2014. Evaluation and statistical inference for human connectomes. *Nature Methods* 11, 1058.
- Petracca, M., Schiavi, S., Battocchio, M., El Mendili, M.M., Fleysher, L., Daducci, A., Inglese, M., 2020. Streamline density and lesion volume reveal a postero–anterior gradient of corpus callosum damage in multiple sclerosis. *European Journal of Neurology* 27, 1076–1082.
- Petracca, M., Zaaraoui, W., Cocozza, S., Vancea, R., Howard, J., Heinig, M.M., Fleysher, L., Oesingmann, N., Ranjeva, J.P., Inglese, M., 2018. An mri evaluation of grey matter damage in african americans with ms. *Multiple sclerosis and related disorders* 25, 29–36.
- Pierpaoli, C., Basser, P.J., 1996. Toward a quantitative assessment of diffusion anisotropy. *Magnetic resonance in Medicine* 36, 893–906.
- Planetta, P.J., McFarland, N.R., Okun, M.S., Vaillancourt, D.E., 2014. Mri reveals brain abnormalities in drug-naive parkinson’s disease. *Exercise and sport sciences reviews* 42.
- Poliakov, A.V., Albright, E., Hinshaw, K.P., Corina, D.P., Ojemann, G., Martin, R.F., Brinkley, J.F., 2005. Server-based approach to web visualization of integrated three-dimensional brain imaging data. *Journal of the American Medical Informatics Association* 12, 140–151.
- Polman, C.H., Reingold, S.C., Banwell, B., Clanet, M., Cohen, J.A., Filippi, M., Fujihara, K., Havrdova, E., Hutchinson, M., Kappos, L., et al., 2011. Diagnostic criteria for multiple sclerosis: 2010 revisions to the mcdonald criteria. *Annals of neurology* 69, 292–302.

- Pontillo, G., Cocozza, S., Brunetti, A., Brescia Morra, V., Riccio, E., Russo, C., Saccà, F., Tedeschi, E., Pisani, A., Quarantelli, M., 2018. Reduced intracranial volume in fabry disease: evidence of abnormal neurodevelopment? *Frontiers in neurology* , 672.
- Poulin, P., Rheault, F., St-Onge, E., Jodoin, P.M., Descoteaux, M., 2018. Bundle-wise deep tracker: Learning to track bundle-specific streamline paths. *Proc. of the Int. Society for Magnetic Resonance in medicine ISMRM-ESMRMB* .
- Poupon, C., Mangin, J.F., Clark, C.A., Frouin, V., Régis, J., Le Bihan, D., Bloch, I., 2001. Towards inference of human brain connectivity from mr diffusion tensor data. *Medical Image Analysis* 5, 1–15.
- Poupon, C., Mangin, J.F., Frouin, V., Régis, J., Poupon, F., Pachot-Clouard, M., Bihan, D.L., Bloch, I., 1998. Regularization of mr diffusion tensor maps for tracking brain white matter bundles, in: *International Conference on Medical Image Computing and Computer-Assisted Intervention*, Springer. pp. 489–498.
- Pujol, S., Wells, W., Pierpaoli, C., Brun, C., Gee, J., Cheng, G., Vemuri, B., Commowick, O., Prima, S., Stamm, A., et al., 2015. The dti challenge: toward standardized evaluation of diffusion tensor imaging tractography for neurosurgery. *Journal of Neuroimaging* 25, 875–882.
- Raja, R., Rosenberg, G., Caprihan, A., 2019. Review of diffusion mri studies in chronic white matter diseases. *Neuroscience letters* 694, 198–207.
- Reisert, M., Kiselev, V., Dihtal, B., Kellner, E., Novikov, D., 2014. MesoFT: Unifying Diffusion Modelling and Fiber Tracking, in: *Med Image Comput Comput Assist Interv*, pp. 201–8.
- Reisert, M., Mader, I., Anastasopoulos, C., Weigel, M., Schnell, S., Kiselev, V., 2011. Global fiber reconstruction becomes practical. *NeuroImage* 54, 955–62.
- Rheault, F., Poulin, P., Caron, A.V., St-Onge, E., Descoteaux, M., 2020. Common misconceptions, hidden biases and modern challenges of dmri tractography. *Journal of neural engineering* 17, 011001.
- Rheault, F., St-Onge, E., Sidhu, J., Maier-Hein, K., Tzourio-Mazoyer, N., Petit, L., Descoteaux, M., 2019. Bundle-specific tractography with incorporated anatomical and orientational priors. *NeuroImage* 186, 382 – 398.
- Roberts, J.D., 1959. *Nuclear magnetic resonance: applications to organic chemistry*. McGraw-Hill Book Company, Inc.
- Rockland, K.S., Pandya, D.N., 1979. Laminar origins and terminations of cortical connections of the occipital lobe in the rhesus monkey. *Brain research* 179, 3–20.

- Romascano, D., Meskaldji, D.E., Bonnier, G., Simioni, S., Rotzinger, D., Lin, Y.C., Menegaz, G., Roche, A., Schluep, M., Pasquier, R.D., et al., 2015. Multicontrast connectometry: A new tool to assess cerebellum alterations in early relapsing-remitting multiple sclerosis. *Human brain mapping* 36, 1609–1619.
- Roth, G., Dicke, U., 2012. Chapter 20 - evolution of the brain and intelligence in primates, in: Hofman, M.A., Falk, D. (Eds.), *Evolution of the Primate Brain*. Elsevier. volume 195 of *Progress in Brain Research*, pp. 413–430.
- Rubinov, M., Sporns, O., 2010. Complex network measures of brain connectivity: uses and interpretations. *Neuroimage* 52, 1059–1069.
- Russo, C., Pontillo, G., Pisani, A., Saccà, F., Riccio, E., Macera, A., Rusconi, G., Stanzione, A., Borrelli, P., Morra, V.B., et al., 2018. Striatonigral involvement in fabry disease: A quantitative and volumetric magnetic resonance imaging study. *Parkinsonism & Related Disorders* 57, 27–32.
- Salzone, M., Caligiuri, M.E., Vescio, V., Arabia, G., Cherubini, A., Nicoletti, G., Morelli, M., Quattrone, A., Vescio, B., Nisticò, R., et al., 2019. Microstructural changes of normal-appearing white matter in vascular parkinsonism. *Parkinsonism & related disorders* 63, 60–65.
- Savadjiev, P., Campbell, J.S., Descoteaux, M., Deriche, R., Pike, G.B., Siddiqi, K., 2008. Labeling of ambiguous subvoxel fibre bundle configurations in high angular resolution diffusion mri. *NeuroImage* 41, 58–68.
- Scannell, J.W., Blakemore, C., Young, M.P., 1995. Analysis of connectivity in the cat cerebral cortex. *Journal of Neuroscience* 15, 1463–1483.
- Schiavi, S., Lu, P.J., Weigel, M., Lutti, A., Jones, D.K., Kappos, L., Granziera, C., Daducci, A., 2022. Bundle myelin fraction (bmf) mapping of different white matter connections using microstructure informed tractography. *NeuroImage* 249, 118922.
- Schiavi, S., Ocampo-Pineda, M., Barakovic, M., Petit, L., Descoteaux, M., Thiran, J.P., Daducci, A., 2020a. A new method for accurate in vivo mapping of human brain connections using microstructural and anatomical information. *Science Advances* 6.
- Schiavi, S., Petracca, M., Battocchio, M., El Mendili, M.M., Paduri, S., Fleysher, L., Inglese, M., Daducci, A., 2020b. Sensory-motor network topology in multiple sclerosis: Structural connectivity analysis accounting for intrinsic density discrepancy. *Human Brain Mapping* 41, 2951–2963.
- Schilling, K., Gao, Y., Janve, V., Stepniewska, I., Landman, B.A., Anderson, A.W., 2018. Confirmation of a gyral bias in diffusion mri fiber tractography. *Human brain mapping* 39, 1449–1466.

- Schilling, K.G., Rheault, F., Remedios, S., Pierpaoli, C., Anderson, A.W., Anderson, A.W., Landman, B.A., Descoteaux, M., 2020. Brain connections derived from diffusion MRI tractography can be highly anatomically accurate—if we know where white matter pathways start, where they end, and where they do not go. *Brain Structure and Function* .
- Schmahmann, J.D., Pandya, D.N., 2007. Cerebral white matter—historical evolution of facts and notions concerning the organization of the fiber pathways of the brain. *Journal of the History of the Neurosciences* 16, 237–267.
- Selden, N.R., Gitelman, D.R., Salamon-Murayama, N., Parrish, T.B., Mesulam, M.M., 1998. Trajectories of cholinergic pathways within the cerebral hemispheres of the human brain. *Brain: a journal of neurology* 121, 2249–2257.
- Serret, J., 1851. On some formulas relating to the theory of a double curvature curves. *Journal of Pure and Applied Mathematics* , 193–207.
- Sethian, J., 2001. Evolution, implementation, and application of level set and fast marching methods for advancing fronts. *Journal of Computational Physics* 169, 503–555.
- Sherbondy, A., Dougherty, R., Ananthanarayanan, R., Modha, D., Wandell, B., 2009. Think global, act local; projectome estimation with BlueMatter, in: *Med Image Comput Comput Assist Interv*, pp. 861—8.
- Shi, Y., Wardlaw, J.M., 2016. Update on cerebral small vessel disease: a dynamic whole-brain disease. *Stroke and vascular neurology* 1.
- Shu, N., Liu, Y., Li, K., Duan, Y., Wang, J., Yu, C., Dong, H., Ye, J., He, Y., 2011. Diffusion tensor tractography reveals disrupted topological efficiency in white matter structural networks in multiple sclerosis. *Cerebral cortex* 21, 2565–2577.
- Sinke, M.R., Otte, W.M., Christiaens, D., Schmitt, O., Leemans, A., van der Toorn, A., Sarabdjitsingh, R.A., Joëls, M., Dijkhuizen, R.M., 2018. Diffusion mri-based cortical connectome reconstruction: dependency on tractography procedures and neuroanatomical characteristics. *Brain Structure and Function* 223, 2269–2285.
- Smith, R., Raffelt, D., Tournier, J.D., Connelly, A., 2020. Quantitative streamlines tractography: methods and inter-subject normalisation .
- Smith, R.E., Tournier, J.D., Calamante, F., Connelly, A., 2012. Anatomically-constrained tractography: improved diffusion mri streamlines tractography through effective use of anatomical information. *Neuroimage* 62, 1924–1938.

- Smith, R.E., Tournier, J.D., Calamante, F., Connelly, A., 2013. SIFT: Spherical-deconvolution informed filtering of tractograms. *NeuroImage* 67, 298–312.
- Smith, R.E., Tournier, J.D., Calamante, F., Connelly, A., 2015a. SIFT2: Enabling dense quantitative assessment of brain white matter connectivity using streamlines tractography. *NeuroImage* 119, 338–51.
- Smith, R.E., Tournier, J.D., Calamante, F., Connelly, A., 2015b. The effects of SIFT on the reproducibility and biological accuracy of the structural connectome. *NeuroImage* 104, 253–65.
- Smith, S.M., Jenkinson, M., Woolrich, M.W., Beckmann, C.F., Behrens, T.E., Johansen-Berg, H., Bannister, P.R., De Luca, M., Drobnjak, I., Flitney, D.E., et al., 2004. Advances in functional and structural mr image analysis and implementation as fsl. *Neuroimage* 23, S208–S219.
- Sobotta, Johannes, 1908. *Textbook and Atlas of Human Anatomy*.
- Son, S.J., Kim, J., Park, H., 2017. Structural and functional connectional fingerprints in mild cognitive impairment and alzheimer’s disease patients. *PloS one* 12, e0173426.
- Song, S.K., Sun, S.W., Ju, W.K., Lin, S.J., Cross, A.H., Neufeld, A.H., 2003. Diffusion tensor imaging detects and differentiates axon and myelin degeneration in mouse optic nerve after retinal ischemia. *Neuroimage* 20, 1714–1722.
- Song, S.K., Sun, S.W., Ramsbottom, M.J., Chang, C., Russell, J., Cross, A.H., 2002. Dysmyelination revealed through mri as increased radial (but unchanged axial) diffusion of water. *Neuroimage* 17, 1429–1436.
- Song, S.K., Yoshino, J., Le, T.Q., Lin, S.J., Sun, S.W., Cross, A.H., Armstrong, R.C., 2005. Demyelination increases radial diffusivity in corpus callosum of mouse brain. *Neuroimage* 26, 132–140.
- Sotiropoulos, S.N., Zalesky, A., 2019. Building connectomes using diffusion mri: why, how and but. *NMR in Biomedicine* 32, e3752.
- Sporns, O., Tononi, G., Kötter, R., 2005. The human connectome: a structural description of the human brain. *PLoS computational biology* 1, e42.
- St-Onge, E., Girard, G., Whittingstall, K., Descoteaux, M., 2015. Surface tracking from the cortical mesh complements diffusion mri fiber tracking near the cortex, in: *Proceedings of the ISMRM Meeting*.
- Steenwijk, M.D., Daams, M., Pouwels, P.J., J. Balk, L., Tewarie, P.K., Geurts, J.J., Barkhof, F., Vrenken, H., 2015. Unraveling the relationship between regional gray matter atrophy and pathology in connected white matter tracts in long-standing multiple sclerosis. *Human brain mapping* 36, 1796–1807.

- Steenwijk, M.D., Geurts, J.J., Daams, M., Tijms, B.M., Wink, A.M., Balk, L.J., Tewarie, P.K., Uitdehaag, B.M., Barkhof, F., Vrenken, H., et al., 2016. Cortical atrophy patterns in multiple sclerosis are non-random and clinically relevant. *Brain* 139, 115–126.
- Stejskal, E.O., Tanner, J.E., 1965. Spin diffusion measurements: spin echoes in the presence of a time-dependent field gradient. *The journal of chemical physics* 42, 288–292.
- Tallinen, T., Chung, J.Y., Rousseau, F., Girard, N., Lefèvre, J., Mahadevan, L., 2016. On the growth and form of cortical convolutions. *Nature Physics* 12, 588–593.
- Taylor, D., Bushell, M., 1985. The spatial mapping of translational diffusion coefficients by the nmr imaging technique. *Physics in medicine & biology* 30, 345.
- Taylor, H.G., Heilman, K.M., 1980. Left-hemisphere motor dominance in righthanders. *Cortex* 16, 587–603.
- Tekkök, S.B., Ye, Z., Ransom, B.R., 2007. Excitotoxic mechanisms of ischemic injury in myelinated white matter. *Journal of Cerebral Blood Flow & Metabolism* 27, 1540–1552.
- Tewarie, P., van Dellen, E., Hillebrand, A., Stam, C.J., 2015. The minimum spanning tree: an unbiased method for brain network analysis. *Neuroimage* 104, 177–188.
- Theisen, F., Leda, R., Pozorski, V., Oh, J.M., Adluru, N., Wong, R., Okonkwo, O., Dean III, D.C., Bendlin, B.B., Johnson, S.C., et al., 2017. Evaluation of striatonigral connectivity using probabilistic tractography in parkinson’s disease. *NeuroImage: Clinical* 16, 557–563.
- Tournier, J.D., Calamante, F., Connelly, A., 2007a. Robust determination of the fibre orientation distribution in diffusion mri: non-negativity constrained super-resolved spherical deconvolution. *Neuroimage* 35, 1459–1472.
- Tournier, J.D., Calamante, F., Connelly, A., 2007b. Robust determination of the fibre orientation distribution in diffusion MRI: Non-negativity constrained super-resolved spherical deconvolution. *NeuroImage* 35, 1459–72.
- Tournier, J.D., Calamante, F., Connelly, A., 2010. Improved probabilistic streamlines tractography by 2nd order integration over fibre orientation distributions. *Proc. Intl. Soc. Mag. Reson. Med. (ISMRM)* 18.
- Tournier, J.D., Calamante, F., Connelly, A., 2012. Mrtrix: Diffusion tractography in crossing fiber regions. *Int J Imaging Syst Technol* 22, 53–66.
- Tournier, J.D., Calamante, F., Gadian, D.G., Connelly, A., 2004. Direct estimation of the fiber orientation density function from diffusion-weighted mri data using spherical deconvolution. *Neuroimage* 23, 1176–1185.

- Trivedi, R., Agarwal, S., Rathore, R.K.S., Saksena, S., Tripathi, R.P., Malik, G.K., Pandey, C.M., Gupta, R.K., 2009. Understanding development and lateralization of major cerebral fiber bundles in pediatric population through quantitative diffusion tensor tractography. *Pediatric research* 66, 636–641.
- Tsitsiklis, J.N., 1995. Efficient algorithms for globally optimal trajectories. *IEEE transactions on Automatic Control* 40, 1528–1538.
- Tuch, D.S., 1999. High angular resolution diffusion imaging of the human brain, in: *Proceedings of the 7th Annual Meeting of ISMRM, Philadelphia, 1999*.
- Tuch, D.S., Reese, T.G., Wiegell, M.R., Makris, N., Belliveau, J.W., Wedeen, V.J., 2002. High angular resolution diffusion imaging reveals intravoxel white matter fiber heterogeneity. *Magnetic Resonance in Medicine: An Official Journal of the International Society for Magnetic Resonance in Medicine* 48, 577–582.
- Tuch, D.S., Salat, D.H., Wisco, J.J., Zaleta, A.K., Hevelone, N.D., Rosas, H.D., 2005. Choice reaction time performance correlates with diffusion anisotropy in white matter pathways supporting visuospatial attention. *Proceedings of the national academy of sciences* 102, 12212–12217.
- Turk, E., Scholtens, L.H., van den Heuvel, M.P., 2016. Cortical chemoarchitecture shapes macroscale effective functional connectivity patterns in macaque cerebral cortex. *Human brain mapping* 37, 1856–1865.
- Udin, S.B., Fawcett, J.W., 1988. Formation of topographic maps. *Annual review of neuroscience* 11, 289–327.
- Ugolini, G., 2010. Advances in viral transneuronal tracing. *Journal of neuroscience methods* 194, 2–20.
- Van Der Holst, H.M., van Uden, I.W., Tuladhar, A.M., de Laat, K.F., van Norden, A.G., Norris, D.G., Van Dijk, E.J., Esselink, R.A., Platel, B., de Leeuw, F.E., 2015. Cerebral small vessel disease and incident parkinsonism: the run dmc study. *Neurology* 85, 1569–1577.
- Van Essen, D.C., Donahue, C.J., Glasser, M.F., 2018. Development and evolution of cerebral and cerebellar cortex. *Brain, behavior and evolution* 91, 158–169.
- Van Essen, D.C., Jbabdi, S., Sotiropoulos, S.N., Chen, C., Dikranian, K., Coalson, T., Harwell, J., Behrens, T.E., Glasser, M.F., 2014. Mapping connections in humans and non-human primates: aspirations and challenges for diffusion imaging, in: *Diffusion MRI*. Elsevier, pp. 337–358.
- Van Essen, D.C., Smith, S.M., Barch, D.M., Behrens, T.E., Yacoub, E., Ugurbil, K., 2013. The wu-minn human connectome project: An overview. *NeuroImage* 80, 62–79.

- Van Wijk, B.C., Stam, C.J., Daffertshofer, A., 2010. Comparing brain networks of different size and connectivity density using graph theory. *PLoS one* 5, e13701.
- de Veber, G.A., Schwarting, G.A., Kolodny, E.H., Kowall, N.W., 1992. Fabry disease: immunocytochemical characterization of neuronal involvement. *Annals of Neurology: Official Journal of the American Neurological Association and the Child Neurology Society* 31, 409–415.
- Wahl, M., Hübers, A., Lauterbach-Soon, B., Hattingen, E., Jung, P., Cohen, L.G., Ziemann, U., 2011. Motor callosal disconnection in early relapsing-remitting multiple sclerosis. *Human brain mapping* 32, 846–855.
- Wang, H.C., Hsu, J.L., Leemans, A., 2012. Diffusion tensor imaging of vascular parkinsonism: structural changes in cerebral white matter and the association with clinical severity. *Archives of neurology* 69, 1340–1348.
- Wassermann, D., Makris, N., Rathi, Y., Shenton, M., Kikinis, R., Kubicki, M., Westin, C.F., 2016. The white matter query language: a novel approach for describing human white matter anatomy. *Brain Struct Funct* 221, 4705–4721.
- Wasserthal, J., Neher, Peter F. and Maier-Hein, K.H., 2018. Tract orientation mapping for bundle-specific tractography, Springer International Publishing. pp. 36–44.
- Wasserthal, J., Neher, P.F., Hirjak, D., Maier-Hein, K.H., 2019. Combined tract segmentation and orientation mapping for bundle-specific tractography. *Medical Image Analysis* 58, 101559.
- Wedeen, V.J., Hagmann, P., Tseng, W.Y.I., Reese, T.G., Weisskoff, R.M., 2005. Mapping complex tissue architecture with diffusion spectrum magnetic resonance imaging. *Magnetic resonance in medicine* 54, 1377–1386.
- van Wijk, B.C.M., J.Stam, C., Daffertshofer, A., 2010. Comparing brain networks of different size and connectivity density using graph theory. *PLOS ONE* 5, 1–13.
- Yeh, F.C., Tang, P.F., Tseng, W.Y.I., 2013. Diffusion mri connectometry automatically reveals affected fiber pathways in individuals with chronic stroke. *NeuroImage: Clinical* 2, 912–921.
- Yuan, M., Lin, Y., 2006. Model selection and estimation in regression with grouped variables. *Journal of the Royal Statistical Society: Series B (Statistical Methodology)* 68, 49–67.
- Zackowski, K.M., Smith, S.A., Reich, D.S., Gordon-Lipkin, E., Chodkowski, B.A., Sambandan, D.R., Shteyman, M., Bastian, A.J., Van Zijl, P.C., Calabresi, P.A., 2009. Sensorimotor dysfunction in multiple sclerosis and column-specific magnetization transfer-imaging abnormalities in the spinal cord. *Brain* 132, 1200–1209.

- Zalesky, A., 2008. DT-MRI Fiber Tracking: A Shortest Paths Approach. *IEEE Trans Med Imaging* 27, 1458–71.
- Zalesky, A., Fornito, A., Cocchi, L., Gollo, L.L., van den Heuvel, M.P., Breakspear, M., 2016. Connectome sensitivity or specificity: which is more important? *NeuroImage* 142, 407–20.
- Zalesky, A., Sarwar, T., Ramamohanarao, K., 2019. A cautionary note on the use of sift in pathological connectomes. *Magnetic Resonance in Medicine* 83, 791–794.
- Zhang, F., Daducci, A., He, Y., Schiavi, S., Seguin, C., Smith, R., Yeh, C.H., Zhao, T., O'Donnell, L.J., 2022. Quantitative mapping of the brain's structural connectivity using diffusion mri tractography: a review. *NeuroImage* , 118870.
- Zhang, H., Hubbard, P.L., Parker, G.J., Alexander, D.C., 2011. Axon diameter mapping in the presence of orientation dispersion with diffusion mri. *Neuroimage* 56, 1301–1315.
- Zhang, H., Schneider, T., Wheeler-Kingshott, C.A., Alexander, D.C., 2012. Noddi: Practical in vivo neurite orientation dispersion and density imaging of the human brain. *NeuroImage* 61, 1000–1016.
- Zhang, Y., Brady, M., Smith, S., 2001. Segmentation of brain mr images through a hidden markov random field model and the expectation-maximization algorithm. *IEEE transactions on medical imaging* 20, 45–57.
- Zhang, Y., Wu, I.W., Buckley, S., Coffey, C.S., Foster, E., Mendick, S., Seibyl, J., Schuff, N., 2015. Diffusion tensor imaging of the nigrostriatal fibers in parkinson's disease. *Movement Disorders* 30, 1229–1236.

Appendix A

Collaborations and Doctoral activities

A.1 Collaborations

- **Joint PhD University of Verona - University of Sherbrooke, Canada**

In April 2019 I've had the opportunity to move to one of the most well known laboratory in the field, the Sherbrooke Connectivity Imaging Laboratory ([SCIL](#)) at University of Sherbrooke, headed by Prof. Maxime Descoteaux. This is enclosed in an international collaboration providing qualifications recognized in two different countries, Italy and Canada, and where the two university institutions share the responsibilities of supervising, coordinating and examining the researcher's work towards the PhD degree.

- Diffusion connectivity application to study the cortico-striatal integrity in Fabry disease - University of Verona, University "Federico II", Naples

Recent evidences suggested the presence of an alteration of the extrapyramidal system in [FD Coccozza et al. \(2017b\)](#), a rare X-linked lysosomal storage disorders long considered to be characterized by major cerebrovascular events only. In particular, an alteration of the cortico-striatal pathway has been described in these patients, with a reduced functional connectivity between the motor cortex and the striatum, bilaterally. Although a widespread alteration of the microstructural integrity of [WM](#) has been described in [FD](#) patients, to date no direct investigation of the possible damage of the cortico-striatal fibers has been performed. Given this knowledge, aim of the work was to study the microstructural integrity of the cortico-striatal connections in [FD](#) patients, compared to a group of [HC](#), to investigate the possible presence of structural connectivity changes in these connections and expand the current knowledge about motor involvement in [FD](#).

- Using microstructure informed tractography to reduce discrepancy in the density of structural connectomes - University of Verona, Icahn School of Medicine at Mount Sinai, New York

Graph theory is a valuable framework to study brain connectivity and has been widely applied to investigate neurological conditions such as [MS](#). However, especially when comparing healthy subjects with patients affected by brain diseases, graph measures may be influenced by the discrepancy in density [Fornito et al. \(2016\)](#); [van Wijk. et al. \(2010\)](#). In the case of structural connectomes this discrepancy can be related to the known biases in tractography [Girard et al. \(2014\)](#). Even though it is known that reducing this effect will highlight the true differences in graph's topology between groups of subjects, up to date there is no common strategy to deal with this issue. We proposed to use microstructure informed tractography to directly account for such density differences and provide a fair comparison between [MS](#) patients and [HC](#).

- Exploring the presence and clinical impact of interhemispheric disconnection in progressive multiple sclerosis - University of Verona, Icahn School of Medicine at Mount Sinai, New York

We explored the presence and clinical impact of interhemispheric disconnection in [PMS](#) through a tractography-based approach, quantifying the number of streamlines passing through callosal subregions. In [PMS](#), we identified a reduced number of streamlines in the splenium and the anterior portion of the [CC](#) body. Patients with primary and secondary progressive phenotype presented different patterns of [CC](#) involvement. The reduced number of streamlines in central and anterior [CC](#) was related to motor disability and fatigue, while loss of the integrity in the posterior portion of [CC](#) was the main feature of cognitively impaired patients.

A.2 Journal publications

- **Battocchio, M.**, Girard, G., Barakovic, M., Ocampo, M., Thiran, J.P., Schiavi, S., Daducci, A., 2019. *Improving graph-based tractography plausibility using microstructure information*. Computational Diffusion MRI, Springer International Publishing. pp. 367–375.
- Cocozza, S., Pontillo, G., **Battocchio, M.**, Riccio, E., Caccavallo, S., Russo, C., Di Risi, T., Pisani, A., Daducci, A., Brunetti, A., 2019. *Microstructural damage of the cortico-striatal and thalamo-cortical fibers in fabry disease: a diffusion mri tractometry study*. *Neuroradiology*, 1432–1920
- Petracca, M., Schiavi, S., **Battocchio, M.**, El Mendili, M.M., Fleysher, L., Daducci, A., Inglese, M., 2020. *Streamline density and lesion volume reveal a postero–anterior gradient of corpus callosum damage in multiple sclerosis*. *European Journal of Neurology* 27, 1076–1082
- Schiavi, S., Petracca, M., **Battocchio, M.**, El Mendili, M.M., Paduri, S., Fleysher, L.,

- Inglese, M., Daducci, A., 2020. *Sensory-motor network topology in multiple sclerosis: Structural connectivity analysis accounting for intrinsic density discrepancy*. Human Brain Mapping 41, 2951–2963
- **Battocchio, M.**, Schiavi, S., Descoteaux, M., Daducci, A., 2021. *Improving tractography accuracy using dynamic filtering*. Computational Diffusion MRI, Springer International Publishing. pp. 45–54.
 - Powell, E., **Battocchio, M.**, Parker, C.S., Sator, P.J., 2021. *Generalised hierarchical bayesian microstructure modelling for diffusion mri*. Computational Diffusion MRI, Springer. pp. 36–47
 - Gabusi, I., Pontillo, G., Petracca, M., **Battocchio, M.**, Bosticardo, S., Costabile, T., Daducci, A., Pane, C., Riccio, E., Pisani, A., Brunetti, A., Schiavi, S., and Coccozza S., 2022. *Structural disconnection and functional reorganization in Fabry Disease: a multimodal MRI study*. Brain Communications (accepted)
 - **Battocchio, M.**, Schiavi, S., Descoteaux, M., Daducci, A., 2022. *Bundle-o-graphy: improving structural connectivity estimation with adaptive microstructure-informed tractography* (under review)

A.3 Conference abstracts

- Matteo Battocchio, Gabriel Girard, Muhamed Barakovic, Mario Ocampo, Jean-Philippe Thiran, Simona Schiavi and Alessandro Daducci, September 2018. “*Graph based microstructure informed tractography*”, poster Medical Image Computing and Computer Assisted Intervention Society ([MICCAI](#)).
- Matteo Battocchio, Sirio Coccozza , Simona Schiavi , Giuseppe Pontillo , Camilla Russo , Antonio Pisani , Alessandro Daducci and Arturo Brunetti, May 2019. “*Microstructural changes of the cortico-striatal pathway in Fabry disease: a diffusion MRI connectometry study*”, abstract International Society for Magnetic Resonance in Medicine ([ISMRM](#)) and Italian chapter [ISMRM](#).
- Sirio Coccozza, Matteo Battocchio, Giuseppe Pontillo, Simona Schiavi, Camilla Russo, Antonio Pisani, Alessandro Daducci and Arturo Brunetti, 2019. “*Microstructural damage of fibers connecting anterior and posterior nodes of the DMN in Fabry disease*”, abstract OHBM.
- Sirio Coccozza, Matteo Battocchio, Giuseppe Pontillo, Simona Schiavi, Camilla Russo, Antonio Pisani, Alessandro Daducci and Arturo Brunetti, 2019. “*A diffusion connectometry study of the cortico-striatal pathway integrity in Fabry Disease*”, abstract OHBM 2019.
- Simona Schiavi , Maria Petracca , Matteo Battocchio , Mohamed Mounir El Mendili , Matilde Inglese and Alessandro Daducci, 2019. “*Using microstructure informed tractography to reduce discrepancy in the density of structural connectomes. An application to Multiple Sclerosis*”, abstract [ISMRM](#).

- Maria Petracca, Simona Schiavi, Matteo Battocchio, Mohamed Mounir El Mendili, Swetha Paduri, Lazar Fleysler, Alessandro Daducci and Matilde Inglese, 2019. “*Motor network topology in MS: structural connectivity changes accounting for density reduction*”, abstract OHBM and Italian chapter [ISMRM](#) 2019.
- Maria Petracca , Matteo Battocchio , Simona Schiavi , Mohamed Mounir El Mendili , Lazar Fleysler , Alessandro Daducci and Matilde Inglese. “*Investigating the contribution of interhemispheric disconnection to disability and fatigue in Progressive Multiple Sclerosis*”, abstract [ISMRM](#) 2019.
- Matteo Battocchio , Simona Schiavi, Maxime Descoteaux and Alessandro Daducci. “*Improving tractography accuracy using dynamic filtering*”, oral at [MICCAI](#) September 2020.
- Matteo Battocchio, Simona Schiavi, Maxime Descoteaux and Alessandro Daducci. “*Bundle-o-graphy*” Educational oral [ISMRM](#) 2021, Magna Cum Laude Merit Award.
- Matteo Battocchio, Simona Schiavi, Maxime Descoteaux and Alessandro Daducci. “*Testing the feasibility and effectiveness of bundle-based global tractography (bundle-o-graphy) in real human brain data*”, abstract [ISMRM](#) 2022.
- G Girard, J Rafael-Patino, R Truffet, D Baran Aydogan, N Adluru, V A Nair, V Prabhakaran, B B Bendlin, A L Alexander, S Bosticardo, I Gabusi, M Ocampo-Pineda, M Battocchio, Z Piskorova, P Bontempi, S Schiavi, A Daducci, A Stafiej, D Ciupek, F Bogusz, T Pieciak, M Frigo, S Sedlar, S Deslauriers-Gauthier, I Kojcic, M Zucchelli, H Laghrissi, Y Ji, R Deriche, K G Schilling, B A Landman, A Cacciola, G A Basile, S Bertino, N Newlin, P Kanakaraj, F Rheault, P Filipiak, T Shepherd, Y C Lin, D G Placantonakis, F E Boada, S H Baete, E Hernández-Gutiérrez, A Ramírez-Manzanares, R Coronado-Leija, P Stack-Sánchez, L Concha, M Descoteaux, S Mansour L, C Seguin, A Zalesky, K Marshall, E J Canales-Rodríguez, Y Wu, S Ahmad, P T Yap, A Théberge, F Gagnon, F Massi, J L Villarreal Haro, M Pizzolato, E Caruyer, and J P Thiran. *Structural connectivity estimates are accurate: the outcome of diffusion-simulated connectivity (DiSCo) challenge*, abstract [ISMRM](#) 2022.
- Ilaria Gabusi, Giuseppe Pontillo, Simona Schiavi, Sara Bosticardo, Maria Petracca, Matteo Battocchio, Antonio Pisani, Arturo Brunetti, Alessandro Daducci, and Sirio Coccozza. *Combined structural and functional connectivity changes in Fabry disease*, abstract [ISMRM](#) 2022.

A.4 Attended Conferences and Workshops

- [MICCAI](#) 16 - 20 September 2018, Granada, Spain
[MICCAI](#) is dedicated to the promotion, preservation and facilitation of research, education and practice in the field of medical image computing and computer assisted medical interventions including biomedical imaging and robotics, through the organization and operation

of regular high quality international conferences and publications which promote and foster the exchange and dissemination of advanced knowledge, expertise and experience in the field produced by leading institutions and outstanding scientists, physicians and educators around the world.

- [ISMRM](#) 11 -16 May 2019, Montréal, Canada
[ISMRM](#) is an international, nonprofit, scientific association whose purpose is to promote communication, research, development, and applications in the field of magnetic resonance in medicine and biology and other related topics and to develop and provide channels and facilities for continuing education in the field.
- Multi-Scale Imaging of the White Matter Anatomy, 17 May 2019, Montreal, Canada
Researchers from around the world specialized in diffusion MRI gathered to discuss neuroanatomy observed at multiple scales, from large-scale network connectivity to to axonal microstructures.
- MIDL 6- 9 July 2020, Montréal, Canada
The MIDL conference aims to be a forum for deep learning researchers, clinicians and health-care companies to take a leap in the application of deep learning based automatic image analysis in disease screening, diagnosis, prognosis, treatment selection and treatment monitoring.
- Brainhack Micro2Macro, January 2021
The Brainhack Micro2Macro 2021 is an official satellite event of the International Global Brainhack 2020. The goal of this hackathon is to bring together researchers with disparate backgrounds to collaborate on open science projects in neuroimaging, with a focus on the link between brain macrostructure and microstructure. During the event I contributed to the development of a hierarchical bayesian approach for microstructure modelling.
- [ISMRM](#) 7 -12 May 2022, London, England